Development of Stable and Efficient Perovskite Light Emitting Diodes and Photovoltaics

Thesis submitted to be The University of Nottingham for the degree of

Doctor of Philosophy

Shuo Ding

20318791

Supervised by

Dr Hao Chen

Dr Xinyu Zhang

Dr Chaoyu Xiang

September 2024

Preface

This thesis is an original work of Shuo Ding under the supervision of Dr Hao Chen, Dr Xinyu Zhang, and Dr Chaoyu Xiang.

Major publications related to this thesis:

- S. Ding, Q. Wang, W. Gu, Z. Tang, B. Zhang, C. Wu, X. Zhang, H. Chen, X. Zhang, R. Cao, T. Chen, L. Qian, C. Xiang, Phase dimensions resolving of efficient and stable perovskite light-emitting diodes at high brightness, Nat. Photonics 18 (2024) 363–370. https://doi.org/10.1038/s41566-023-01372-0.
- Q. Wang, S. Ding, S. He, T. Zhang, L. Qian, P. Xiao, T. Chen, C. Xiang, Improving the Operational Stability of Near-Infrared Quasi-2D Perovskite Light-Emitting Diodes by Cation Engineering, Adv. Opt. Mater. 11 (2023) 2201778. https://doi.org/10.1002/adom.202201778.
- B. Zhang, S. Ding, X. Zhang, L. Qian, C. Xiang, Enhancing the performance of Quasi-2D perovskite blue light emitting diodes via a WS2 energy matching layer, Chem. Phys. Lett. 826 (2023) 140671. https://doi.org/10.1016/j.cplett.2023.140671.
- S. Ding, Z. Kong, Y. Shen, P. Shen, C. Wu, L. Qian, X. Zhang, L. Hu, H. Chen, C. Xiang, Phase stabilization via A-site ion anchoring for ultra-stable

perovskite light emitting diodes, Mater. Horizons (2024). https://doi.org/10.1039/D4MH00701H.

- W. Li, S. Ding, J. Xu, C. Wu, X. Li, L. Qian, H. Chen, X. Zhang, K. Kang, C. Xiang, Ammonium Thiocyanate Enhanced High-Performance Quasi-Two-Dimensional Perovskite Solar Cells, ACS Appl. Energy Mater. 7 (2024) 1120–1127. https://doi.org/10.1021/acsaem.3c02624.

Other works of Shuo Ding during the PhD program are listed in Appendix as Appendix 4.

Abstract

Metal halide perovskites (MHPs), a subclass of perovskite materials, have emerged as one of the most promising candidates for the next generation optoelectronic technologies due to their exceptional electronic and optical characteristics. The applications of MHPs have been broadened considerably from their initial deployment in photovoltaic cells (PVs) to multiple optoelectronic devices such as light emitting diodes (LEDs), photodetectors, scintillators, and photolytic systems. Despite the wide range of applications, there persists an urgent need for the development of highly stable and efficient MHP-based optoelectronic devices, a prerequisite to meet the rigorous standards of industry scale mass production. However, the exact origins of the inefficiency and instability issues in perovskite materials remain inadequately understood, thus impeding the comprehensive solutions to enhance their efficiency and operational stability. This thesis, therefore, begins with the objective to elucidate the fundamental mechanisms underlying the inefficiency and instability issues in perovskite materials and devices, and proposes efficacious solutions for the development of highly stable and efficient optoelectronic devices, including LEDs and PVs.

Perovskite light emitting diodes (PeLEDs) are fabricated via the quantum confinement of conventional bulk MHPs, which improves the exciton binding energy and facilitates the exciton recombination process. Three strategies have been proposed to improve exciton binding and device efficiency: nano three-dimensional (nano 3D) perovskite fabrication, perovskite nanocrystal synthesis, and quasi-two-dimensional (quasi-2D) perovskite formation. Of all three strategies, quasi-2D perovskite formation has demonstrated unique advantages due to its well-confined excitons within multi-quantum-well structures, simple fabrication processes, and broad functionalization potentials. As a result, quasi-2D PeLEDs have achieved the highest reported external quantum efficiency (EQE) among all PeLEDs to date. However, intrinsic issues related to EQE, and stability remain to be addressed, particularly with regards to the operational stability. Therefore, it is necessary to conduct a comprehensive analysis of the causes of instability and inefficiency in quasi-2D PeLEDs, while corresponding solutions should be proposed to address these issues, as listed below.

1. Phase dimensions. Quasi-2D perovskites exhibit unique multi-quantum-well structure with mixed phase dimensions, where the thickness of a single quantum well can be described with the n value (n represents the number of the lead-centred octahedra along the thickness direction in a

single quantum well). In quasi-2D perovskites, excitons can transfer from large band gap low n components to small band gap larger n phases. Therefore, the control of phase dimensions has become eminently critical for efficient inter-phase energy transfer and consequent high luminescent efficiency. To resolve the phase dimensions, in-depth characterizations have figured out that the low n phases were the origin of perovskite instability and deficiency, and a simple and novel mixed solvent post-treatment, "solvent sieve" method, was developed to selectively remove the low n phases and facilitate the energy transfer process. As a result, highly stable and efficient PeLEDs were fabricated with the solvent sieve method, demonstrating not only high EQE and half-lifetime T_{50} of 29.5% and 18.67 h at 12,000 cd/m^2 (equivalent over 50,317 h or 5.7 years at 100 cd/m^2), respectively, but also extraordinary resistance to air and moisture, maintaining over 75% of film photoluminescence quantum yield and 80% of device EQE after stored in the ambient for 100 days. The simple solvent sieve method confirmed the feasibility of MHPs for luminescence applications and unleashes the efficiency and stability potentials of PeLEDs for future commercial applications.

2. Defects. Defects inside MHPs trigger non-radiative exciton recombination and lead to higher reactivity and severe ion transportation,

which deteriorate the efficiency and stability of PeLEDs. Therefore, effective control of defects should be conducted to improve the efficiency and stability of PeLEDs. In this study, a sweet coordination strategy was proposed to optimize the perovskite growth process and significantly suppress the defect formation. Therefore, highly efficient, and stable PeLEDs were fabricated with a maximum EQE of 31.3% and an operating half-life over 76.9 hours at an initial luminance of 10,000 cd/m^2 (equivalent over 211,800 hours or 24.2 years at 100 cd/m^2). This work paves the road towards future applications of PeLEDs in display and lighting industries.

3. Ion migration. Ion migration effect originating from the soft deformable lattice of MHPs has been considered as one of the main causes for the limited lifetime of PeLEDs. However, due to the complexity of the perovskite components, simple methods to spontaneously suppress the migration of all perovskite ions are still challenging. Therefore, a highly fluorinated molecule, 1H,1H-perfluorohexylamine (PFHA), was selected to spontaneously form strong coordination with all perovskite ions and significantly suppress the ion migration process. As a result, ultra-stable and efficient green PeLEDs was fabricated with a champion EQE of 27.1% and a T_{50} lifetime of 103.17 hours at 10,000 cd/m^2 (equivalent to over

326,252 hours or 37.2 years at 100 cd/m^2), setting a record for PeLEDs operational stability. This work confirms the stability potential of PeLEDs and sheds light on the possibility that PeLEDs can be commercialized in the future display and lighting industries.

Quasi-2D perovskites are also used as perovskite photovoltaic cells (PePVs), where the ligands inside the quasi-2D perovskites can stabilise the perovskite structures and improve the stability of the PePVs. However, problems still hinder the progress of quasi-2D PePVs, including severe interfacial problems between the perovskite and the charge transporting layers. Therefore, modification of the interface should be conducted to improve the performance of quasi-2D PePVs.

4. Interface. The interfaces between the perovskite and the charge transporting layers determine the exciton transportation process within PePVs. The buried interface between the perovskite and the bottom electron transporting layer in conventional PePVs is also critical for perovskite growth and film quality. Therefore, a multifunctional passivator ammonium thiocyanate (NH_4SCN) was used to treat the SnO_2/perovskite interface of quasi-2D perovskite solar cells. This interfacial modification method effectively passivated the interfacial

defects and regulated the energy levels, with significant improvement in the wettability of perovskite precursors on tin oxide films and the quality of the perovskite films. This strategy of NH_4SCN interfacial modification achieved high efficiency and stable quasi-2D PePVs with a maximum power conversion efficiency (PCE) of 21.96% and an impressive stability of maintaining 90% of the initial PCE after 3,000 h in the ambient atmosphere.

In summary, this thesis has introduced four critical issues for both PeLEDs and PePVs and four corresponding solutions to resolve the issues. As a result, highly stable and efficient PeLEDs and PePVs have been developed. All these solutions have demonstrated a bright future for the industrialisation of perovskite optoelectronic devices.

Acknowledgements

After four years of learning and researching for my PhD programme, I have gained an invaluable wealth of lifelong experience. At this pivotal moment, I would like to express my heartfelt gratitude to people who have provided indispensable assistance throughout the preparation of this thesis.

Foremost, I would express my profound appreciation to Professor Hao Chen, my first supervisor. Your insights and dedication as a scholar have shaped my academic gratitude. Meanwhile, your consistent support during the PhD programme has granted me an exciting, enriching, and fruitful doctoral journey. Then, I am also solely indebted to my second supervisor, Professor Xinyu Zhang. Your help during the annual reports and thesis was highly instrumental. Next, I am also deeply thankful to Professor Chaoyu Xiang, my third supervisor at Ningbo Institute of Materials Technology and Engineering, CAS. With your help, we have significantly extended the frontiers of perovskite optoelectronics. Finally, this thesis was also dedicated in memory of Professor Lei Qian, my former third supervisor, who was also a great mentor, colleague, and friend. Throughout his illustrious and prolific career, he has made indelible scientific contributions that continue to resonate, which will forever be commemorated and celebrated.

Also, I would thank my former PhD supervisors at both UNNC and NC State University, including Professor Franky So, Professor Zhikuan Chen, Professor Fei Chen, etc. All of you have played distinct roles in my study and career.

Subsequently, I would extend my heartfelt thanks to my cherished friends and esteemed collaborators, particularly Dr Shichen Yin, Dr Chunyan Wu, Dr Zhaobing Tang, Xuanyu Zhang, Wencui Gu, Zhiwei Yao, Piaoyang Shen, Qiangqiang Wang, Wenqiang Li, Bo Zhang, Dr Carr Hoi Yi Ho, Dr Xiangyu Fu, Siliang He and Yusen Pei. Thank you all for your invaluable support and companionship throughout this challenging yet fulfilling journey.

Finally, I owe an immense debt of thanks to my beloved parents and other cherished friends. Your unwavering support, and invaluable perspectives have sustained me through the arduous process of completing this thesis and have provided me with precious memories of my life. Your backing has been the foundation upon which I have built this academic milestone.

I love you all.

Nomenclature

Symbol	Designation	Unit
T_x	Lifetime, the time it takes for the value to decrease to x% of its initial value.	Time unit, second, minute or hour, etc.
J	Current density	mA/cm^2
V	Voltage	V
L	Luminance	cd/m^2
V_{oc}	Open circuit voltage	V
J_{sc}	Short circuit current density	mA/cm^2
FF	Fill factor	-
C	Capacitance	F
F	Frequency	Hz

Abbreviations

[6,6]-phenyl-C61-butyric acid methyl ester (PCBM)

1H,1H-perfluorohexylamine (PFHA)

1-naphthylmethylammonium iodide (NMAI)

1-naphthylmethylammonium ion (NMA^+)

2-(4-(9,10-di(naphthalen-2-yl) anthracen-2-yl)phenyl)-1-phenyl-1H-benzo[d]imidazole (ADN-PBIP or ZADN)

2,4,6-Tris(3'-(pyridin-3-yl)biphenyl-3-yl)-1,3,5-triazine (TmPPPyTz)

2',2''-(1,3,5-benzinetriyl)-trwas(1-phenyl-1-H-benzimidazole) (TPBi)

4-fluoro-phenethylammonium bromide (FPEABr)

4-tert-butylpyridine (tBP)

Air mass (AM)

Ammonium thiocyanate (NH_4SCN)

Atomic force microscopy (AFM)

Augmented reality (AR)

Bis(trifluoromethane)sulfonimide lithium salt (Li-TFSI)

Branched polyethylenimine (PEI)

Caesium bromide (CsBr)

Caesium iodide (CsI)

Caesium lead bromide ($CsPbBr_3$)

Caesium lead iodide ($CsPbI_3$)

Cambridge Sequential Total Energy Package (CASTEP)

Carbon tetrachloride (CT)

Charge transporting layers (CTLs)

Chlorobenzene (CB)

Conduction band minimum (CBM)

Current efficiency (CE)

Cyclamate sodium (Cyc Na)

Density functional theory (DFT)

D-glucose (D-Glc)

Dimethyl sulfoxide (DMSO)

Diphenyl phosphine chloride (DPPOCl)

Electroluminescence (EL)

Electron transporting layers (ETLs)

Electron transporting materials (ETMs)

Ethylenediamine (EDA)

External quantum efficiency (EQE)

Fluorine doped tin oxide (FTO)

Formamidine hydrobromide (FABr)

Formamidine hydrochloride (FACl)

Formamidinium ion (FA+)

Formamidinium lead bromide ($FAPbBr_3$)

Fourier transform infrared spectra (FTIR)

Full width at half maximum (FWHM)

Generalized gradient approximation (GGA)

Grazing incidence wide angle X-ray scattering (GIWAXS)

Hexylamine (HA)

High photoluminescence quantum yield (PLQY)

Hole transporting layers (HTLs)

Hole transporting materials (HTMs)

Hydrobromic acid (HBr)

Hypophosphorous acid (H_3PO_2)

Indium tin oxide (ITO)

Integrating sphere (IS)

International Commission on Illumination / Commission Internationale de l´Eclairage (CIE)

Isopropanol (IPA)

Lead bromide ($PbBr_2$)

Lead iodide (PbI_2)

Lead oxide (PbO)

Ligand-site (L-site)

Light emitting diodes (LEDs)

Liquid crystal display (LCD)

Lithium fluoride (LiF)

Maximum power point (MPP)

Metal halide perovskites (MHPs)

Methylammonium chloride (MACl)

Methylammonium iodide (MAI)

Methylammonium ion (MA^+)

Micro light emitting diode (micro-LED)

Multi-quantum-well (MQW)

N, N-dimethylformamide (DMF)

Nano three-dimensional (nano 3D)

National Renewable Energy Laboratory (NREL)

Near-infrared (NIR)

Nickel oxide (NiO_x)

Nitrobenzene (NB)

N-methyl pyrrolidone (NMP)

Nuclear magnetic resonance (NMR)

On the fly generated (OTFG)

One-dimensional (1D)

Optical intensity (OD)

Organic light emitting diode (OLED)

Perdew Burke Ernzerhof (PBE)

Perovskite light emitting diodes (PeLEDs)

Perovskite photovoltaic cells (PePVs)

Perovskite quantum dot LEDs (PeQLEDs)

Perovskite quantum dots PVs (PeQDPVs)

Phenethyl ammonium bromide (PEABr)

Phenethyl ammonium ion (PEA^+)

Phenyl butylammonium iodide (PBAI)

Photoluminescence (PL)

Photovoltaic cells (PVs)

Polyvinyl pyrrolidone (PVP)

Polyvinylidene fluoride (PVDF)

Potassium chloride (KCl)

Potassium iodide (KI)

Potassium trifluoromethanesulfonate (CF_3SO_3K)

Power conversion efficiency (PCE)

Quantum dot emitting diode (QLED)

Quasi-two-dimensional (quasi-2D)

Reduced-dimensional perovskites (RDPs)

Revolutions per minute (rpm)

Saccharin (Sacc)

Scanning electron microscopy with energy dispersive X-ray spectroscopy (SEM-EDX)

Space-charge-limited current (SCLC)

Thermal evaporation (TE)

Time-of-flight secondary ion mass spectrometry (TOF-SIMS)

Tin oxide (SnO_2)

Transient absorption (TA)

Transient absorption spectroscopy (TAS)

Trap-filling-limited voltage (V_{TFL})

Two-dimensional (2D)

UV photoelectron spectrometer (UPS)

Virtual reality (VR)

Visualization for Electronic and Structural Analysis software (VESTA)

X-ray photoelectron spectroscopy (XPS)

Zero-dimensional (0D)

List of Tables

List of Figures

Contents

Chapter 1. Introduction

1.1 Background

Optoelectronic materials and devices have garnered significant attention from both academia and industry due to their importance in various applications, including power generation, lighting, display, and sensing [1–3]. The development of stable and efficient optoelectronic materials and devices has been a lifelong pursuit to achieve reliable and efficient optoelectronic applications [4, 5]. For example, as for the display technology, the performance of display devices has significantly improved as the technology has evolved from liquid crystal display (LCD) to organic light emitting diode (OLED) and micro light emitting diode (micro-LED), and even quantum dot emitting diode (QLED), as shown in Figure 1.1 [6]. The evolution of display technologies has boosted almost all the display properties, including colour gamut, colour purity, viewing angle, resolution, refresh rate, luminescent efficiency, and operational stability of display screens [7]. Nevertheless, the search for new capabilities in next generation display materials and devices are still urgently demanded to further enhance display performance and meet the requirements of emerging display applications such as virtual reality (VR) and augmented reality (AR) [8].

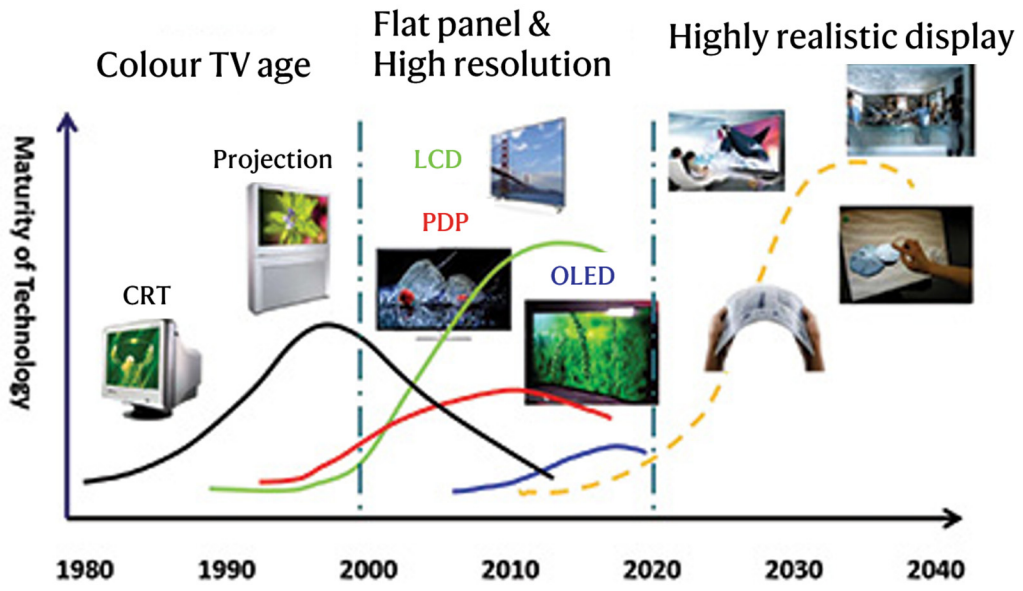

Figure 1.1 | Evolution of display technologies [6].

Meanwhile, the advances in optoelectronic devices are closely determined by the development of emerging optoelectronic materials [9]. Therefore, to date, perovskite has emerged as a promising optoelectronic material, leading to significantly increased investigation of perovskite-based devices such as perovskite light-emitting diodes (PeLEDs) and photovoltaic cells (PePVs) [10, 11].

The typical structure of conventional perovskite optoelectronic devices, including PeLEDs and PePVs, is based on the structure of diodes, as presented in Figure 1.2a, where the core effective layers made of semiconducting materials MHPs, are sandwiched between charge transporting layers (CTLs) and electrodes (anodes and cathodes). Meanwhile, some structures based on

other categories of semiconductor devices are also employed, such as resistor and transistor, as shown in Figure 1.2b [12]. However, due to the convenience of fabrication and simple integration with semiconductor industry, the diode-like structure is still mostly applied according to the literature [12].

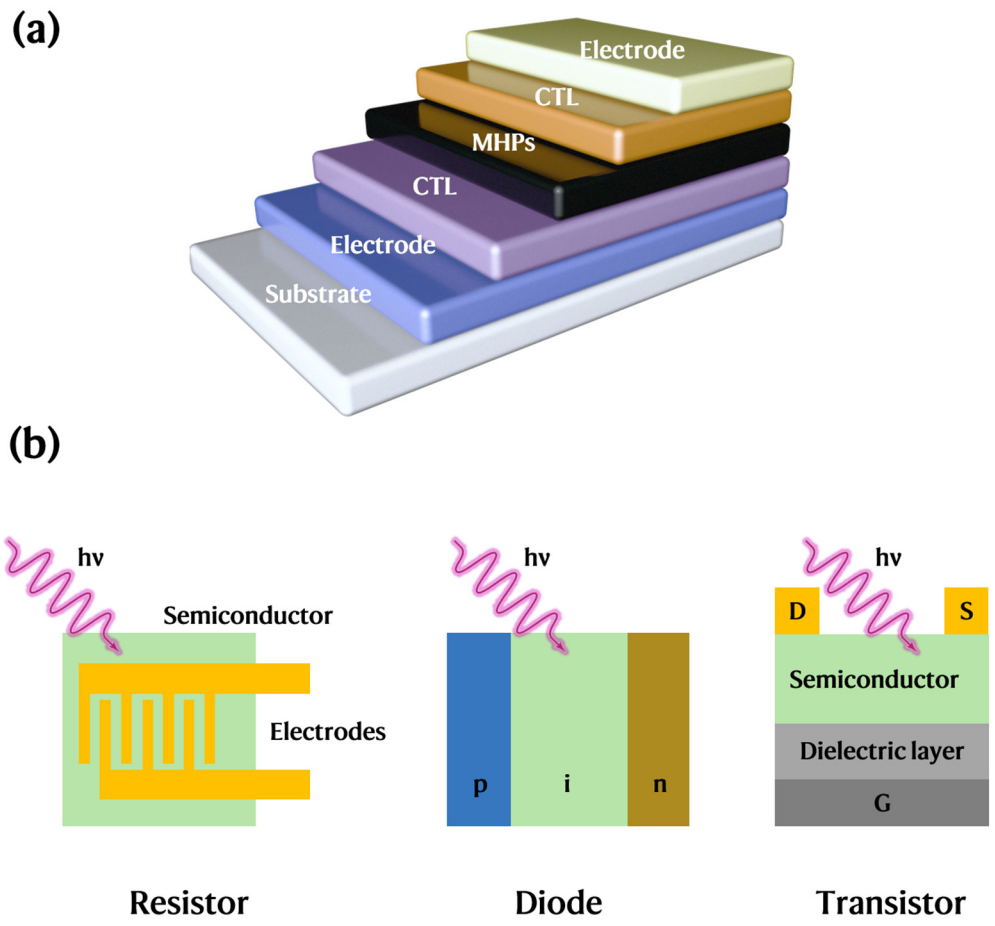

Figure 1.2 | (a) The typical structures of conventional perovskite optoelectronic devices (diode). (b) The typical structures of other perovskite optoelectronic devices [12].

Specifically, in PeLEDs, both positive and negative charge carriers (holes and electrons) are injected from the electrodes through the charge transport layers, including electron transporting layers (ETLs) and hole transporting layers (HTLs), into the MHP active layers, form excitons and emit light by the radiative exciton recombination process [7, 11, 13], converting electricity to light. In PePVs, however, the entire process is reversed, where excitons are formed upon light irradiation, then dissociate under the impact of built-in potentials and generate electricity, enabling energy conversion from light to electricity [14]. The typical energy levels and directions of carriers' motion are shown as Figure 1.3. Therefore, the critical requirements for highly stable and efficient PeLEDs and PePVs can be intrinsically different due to the discrepancy in operational mechanism and device structures.

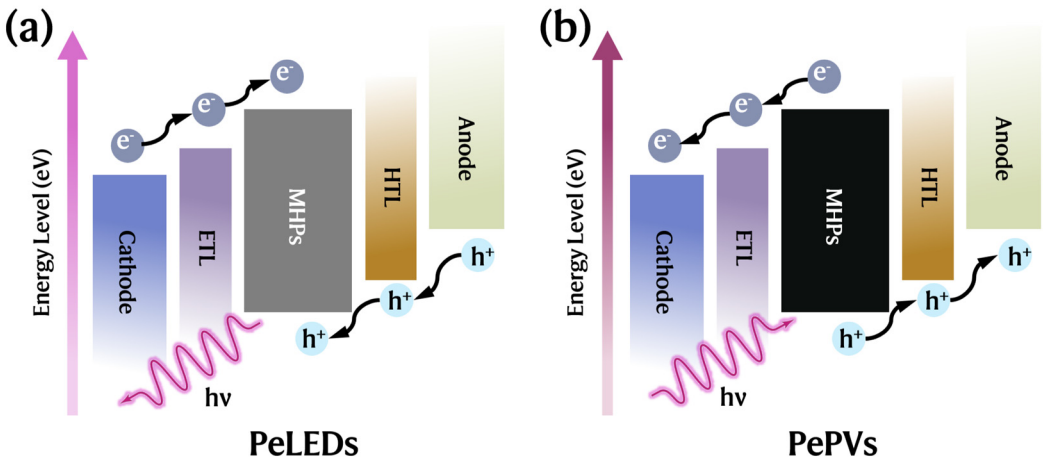

Figure 1.3 | (a) The typical energy levels and directions of carriers' motion in PeLEDs. (b) The typical energy levels and directions of carriers' motion in PePVs.

To quantify the advantages of MHP-based optoelectronic devices, key parameters to describe the device performance are introduced. One of the most important parameters to evaluate device performance is the device efficiency, which is defined as the conversion efficiency between light and electricity for optoelectronic devices. Specifically, for PeLEDs, the external quantum efficiency (EQE) is the relative ratio of emitted photons to injected electrons [7]. For PePVs, the power conversion efficiency (PCE) is the relative ratio of generated electricity to the total energy of incident light [15]. Therefore, comparisons of both EQEs for PeLEDs and PCEs for PePVs have become one of the most direct milestones for MHPs based optoelectronic devices.

Another critical parameter for MHP-based optoelectronic devices is the operational lifetime, which describes the robustness and operational stability of devices under certain working conditions. Usually, T_X is employed to mark the device's operational lifetime, where x is the percentage of initial value. For instance, T_{50} refers to the half-life, which is the time it takes for the value to decrease to 50% of its initial value. Meanwhile, by alternating the value of x, other critical lifetime parameters are also employed to evaluate the stability of MHP-based optoelectronic devices for different applications, such as T_{95}, T_{90}, or T_{80} for highly stable PeLEDs [16] or PePVs [17, 18].

Overall, the rapid advances in device performance of MHP-based optoelectronic devices have demonstrated the potential of MHPs as the next generation of optoelectronic materials. The advances on efficiency and operational lifetime for both PeLEDs and PePVs are summarized in Figure 1.4. As presented in Figure 1.4a [11], since the first report of room-temperature PeLEDs with EQE no more than 0.4% in 2014 [19], the efficiencies of PeLEDs have been improved dramatically in the past decade, reaching 30% in 2023 with the assistance of optimized optical outcoupling design [20]. Therefore, such progresses in device EQE have proven the potentials of MHPs as electroluminescent materials. However, the advances of the other critical parameter, the operational lifetime, have fallen behind. According to Figure 1.4b, at an initial luminance of 100 cd/m^2, which represents the standard display brightness for contemporary electronic devices, the reported operational lifetimes of the most advanced PeLEDs have hardly even surpassed a 20-hour lifetime threshold. This significantly constrained operational durability not only imposes limitations on the current practical applications of PeLED technology, but also undermines their potential prospects for commercialization in the future.

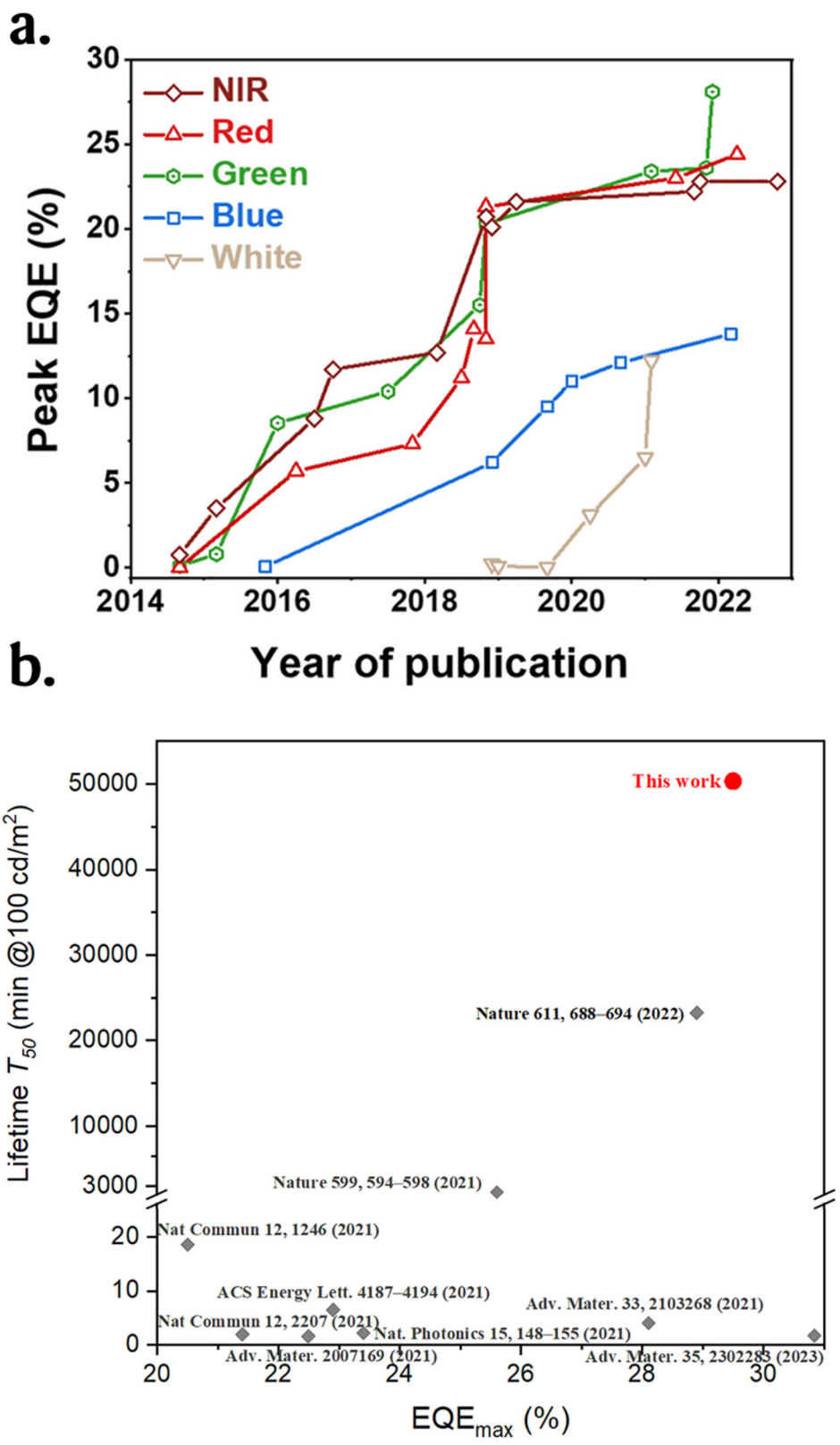

Figure 1.4 | (a) Advances on device EQEs of PeLEDs [11]. (b) Advances on device EQEs and operational lifetimes of green PeLEDs (data listed in Table A1-1).

Simultaneously, the underlying rationale and potential mechanism for the limited operational stability of PeLEDs remain intricate and controversial. A variety of contributory factors have been proposed as representative causes for this limited stability, including but not limited to ion migration effects [21, 22], chemical instability [23, 24], lattice distortion [25]. However, a comprehensive understanding of the intrinsic causes is yet to be established. More critically, despite the substantial efforts invested in enhancing the operational lifetime of PeLEDs, efficacious solutions that could yield significant improvements to the final device performance are still awaiting, with limited advances on the device operational lifetime capable of meeting current commercialization standards [26].

As for PePVs, significant strides have also been accomplished over the past decade, particularly in terms of PCEs. As depicted in Figure 1.5 [27], the highest PCE achieved by single-junction PePVs has surpassed the 26% mark, placing them among the most efficient photovoltaic materials across all categories. Concurrently, substantial advancements have been made in enhancing the operational stability of these devices, culminating in an extended operational lifetime, as measured by T_{90}, reaching thousands of hours [28, 29]. Meanwhile, studies on industrial-scale fabrication processes of PePVs have also drawn great attention, with considerable research efforts directed towards exploring and optimizing manufacturing methodologies

such as blade coating [30, 31], ink-jet printing [32–34], roll to roll fabrication [35, 36], etc. However, apart from the rapid development of representative three-dimensional PePVs, the advances of other types of PePVs, such as quasi-two-dimensional PePVs, have fallen behind [37] and more issues at device level remain relatively underexplored.

In conclusion, the advancements in optoelectronic devices are fundamentally contingent upon the discovery and development of novel optoelectronic materials. The advent of MHPs has opened new avenues for the next generation optoelectronic devices, including PeLEDs and PePVs. Both efficiency and operational lifetime serve as pivotal metrics to assess the device performance. To date, PeLEDs have demonstrated remarkable strides in efficiency. However, pressing demands are needed to address critical improvements in their operational lifetimes. As for PePVs, substantial enhancements have been achieved in both PCEs and operational stability, yet certain subclasses of PePVs remain underexplored, meriting further exploration and investigation.

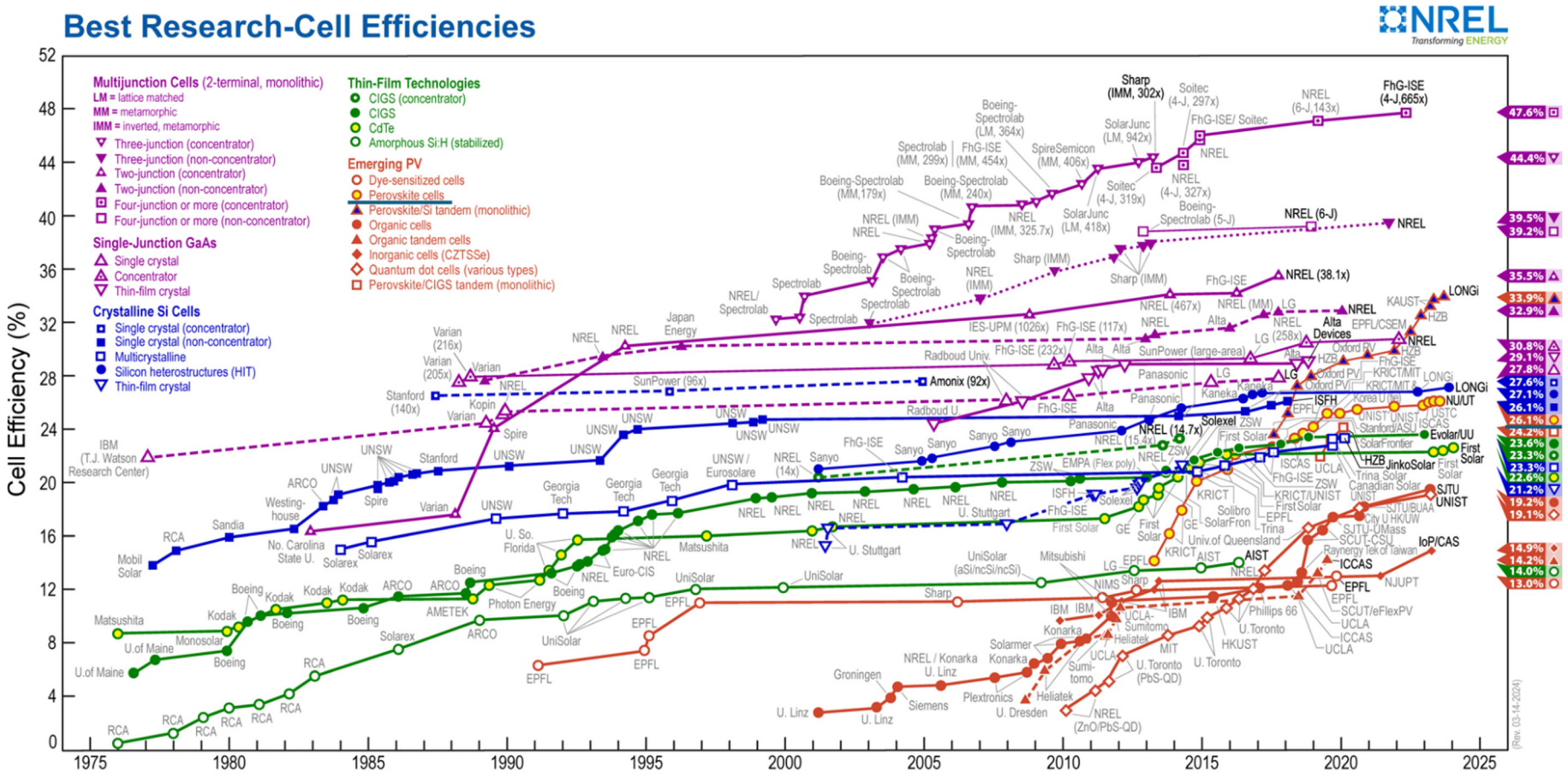

Figure 1.5 | PCE evolution of PePVs [27].

1.2 Aims and Objectives

In light of the multifaceted issues and challenges encountered in MHP-based optoelectronic devices, this thesis endeavours to explore the potential for further enhancing efficiency and operational stability. The principal objective is to solve the underlying issues of MHP-based optoelectronic devices and develop stable and efficient PeLEDs and PePVs.

To achieve this challenging goal, the following specific objectives have been set:

- Comprehensive literature review: a meticulous literature review is undertaken to consolidate the critical aspects regarding both device efficiency and operational stability.
- In-depth property and mechanism analysis: extensive studies of the intrinsic properties and behaviour of perovskites are performed to gain profound understandings of the fundamental mechanisms underlying the deficiency and instability issues in current PeLEDs and quasi-two-dimensional PePVs.
- Mechanism-based strategy development: efficacious strategies are employed to address these issues grounded on the mechanism analysis, thereby leading to significant advancements in the operational lifetime and efficiency metrics of the devices.

- Device fabrication and applications: highly stable and efficient perovskite optoelectronic devices, including PeLEDs and PePVs, have been developed, underscoring the promising future for the industry scale application and commercialization of perovskite optoelectronic technology.

By meeting these objectives, this thesis seeks to contribute valuable insights into the improvement of MHP-based optoelectronic devices, paving the way for their broader applications in optoelectronics.

1.3 Thesis structure

In this thesis, Chapter 1 delivers a systematic introduction of MHP materials as well as MHP-based optoelectronic devices, particularly PeLEDs and PePVs. Pivotal performance parameters quantifying the performance of PeLEDs and PePVs are also introduced, and critical issues especially the operational lifetime that bottlenecked the commercial applications of PeLEDs and PePVs are also summarized.

Chapter 2 provides a meticulous literature review on perovskite materials and essential perovskite structures, succeeded by an in-depth examination of critical challenges for both PeLEDs and PePVs, where the principal challenges for PeLEDs are summarized as phase dimensions control, defects management, and ion migration suppression, whereas the interface engineering plays a crucial role in improving the performance of PePVs. Also, summary of basic film fabrication techniques, such as solution process and thermal evaporation, are reviewed in this chapter.

Chapter 3 introduces the primary methodologies and techniques employed throughout the research, including general material synthesis process and characterization means, as well as first-principles simulation and optical simulation methods. All the primary materials fabrication, characterization, and theoretical simulation methodologies and techniques have led to

comprehensive understandings of underlying mechanisms and reproducible fabrication of perovskite materials and optoelectronic devices.

Subsequently, Chapters 4 to 7 present the main results in this thesis. Chapter 4 describes the development of a solvent sieve method to tackle the issue of phase dimensions, thereby realizing efficient and stable quasi-2D PeLEDs. Chapter 5 introduces a sweet coordination strategy aimed at comprehensive defect passivation, with further improvements on device performance. Chapter 6 elucidates the employment of an ion pinning strategy that effectively hinders ion migration within the perovskite structure, significantly enhancing the operational lifetime of PeLEDs, thus paving the way for highly stable and efficient devices suitable for industrialization. For PePVs, Chapter 7 implements a novel interfacial modification technique to facilitate defect passivation and enhance film quality.

Finally, Chapter 8 consolidates the conclusions in this thesis and Chapter 9 outlines the prospective directions for further research.

Chapter 2. Literature Review

2.1 Perovskite

The term, "perovskite," originally described a specific type of mineral with the chemical formula of $CaTiO_3$. However, since Miyasaka et al.'s pioneering report in 2009 [38] on lead halide perovskite photovoltaic cells (PePVs), MHPs have garnered significant attention as prospective next-generation optoelectronic materials due to their exceptional optoelectronic attributes and economically favourable fabrication costs [19, 39–42], as summarized in Figure 2.1 [43–45]. Specifically, MHPs now represent a category of nanostructured compounds with the general formula ABX_3, where A denotes organic cations (e.g., methylammonium ion (MA^+) or formamidinium ion (FA^+)) or large inorganic cations (such as caesium ions Cs^+), B signifies divalent metal cations commonly Pb^{2+} or Sn^{2+}, and X symbolizes a halide anion including Cl^-, Br^-, or I^-, etc., as presented in Figure 2.2.

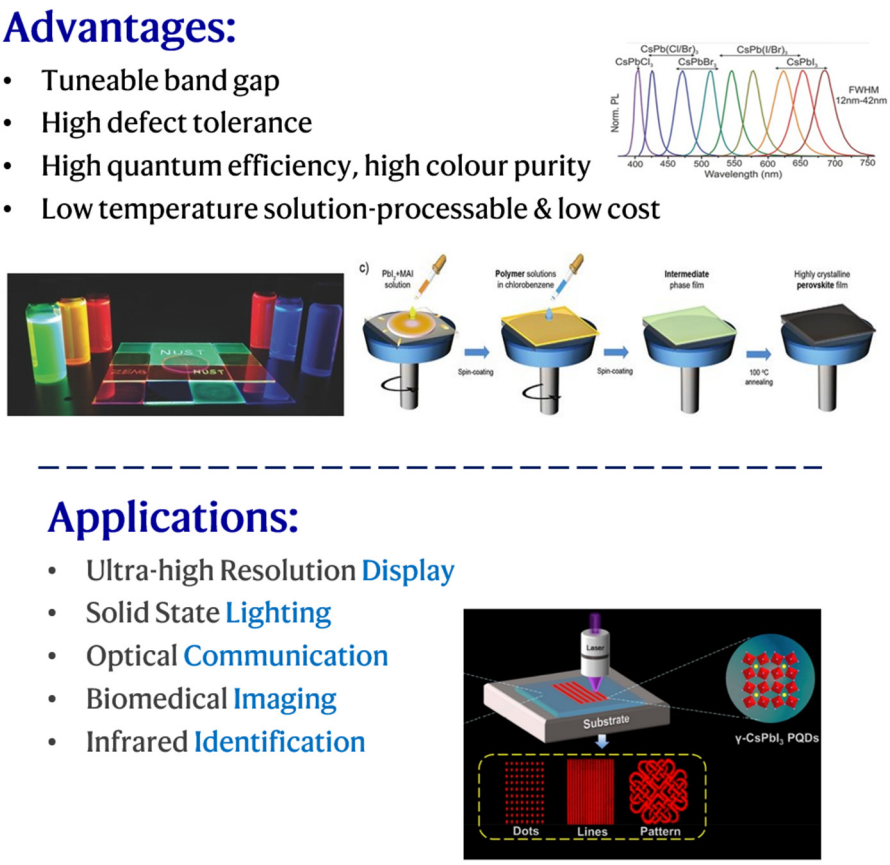

Figure 2.1 | Representative advantages [44, 46] and critical applications [45] for MHP based optoelectronic devices.

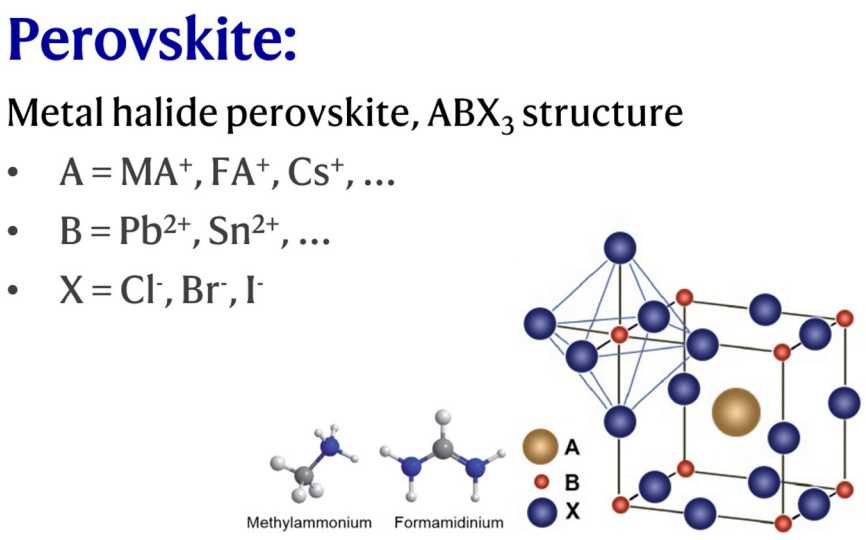

Figure 2.2 | The scheme of representative perovskite lattice structure.

The crystal structure of MHPs is formed by a lattice built up with corner-sharing BX_6 octahedra, with A-site cations occupying the cubic octahedral interstitial sites. Notably, within the perovskite lattice ABX_3, various ions can spontaneously inhabit the same site, leading to doping through ion substitution. Yet, when the cation substitution ratio between A and A' (or B and B') approximates 0.5, it results in the formation of double perovskite compounds with the formula $AA'B_2X_6$ (or $A_2BB'X_6$) [47, 48], as presented in Figure 2.3 [47]. This phenomenon significantly broadens the compositional scope of the perovskite family, thereby giving rise to unique structural configurations and properties [49, 50].

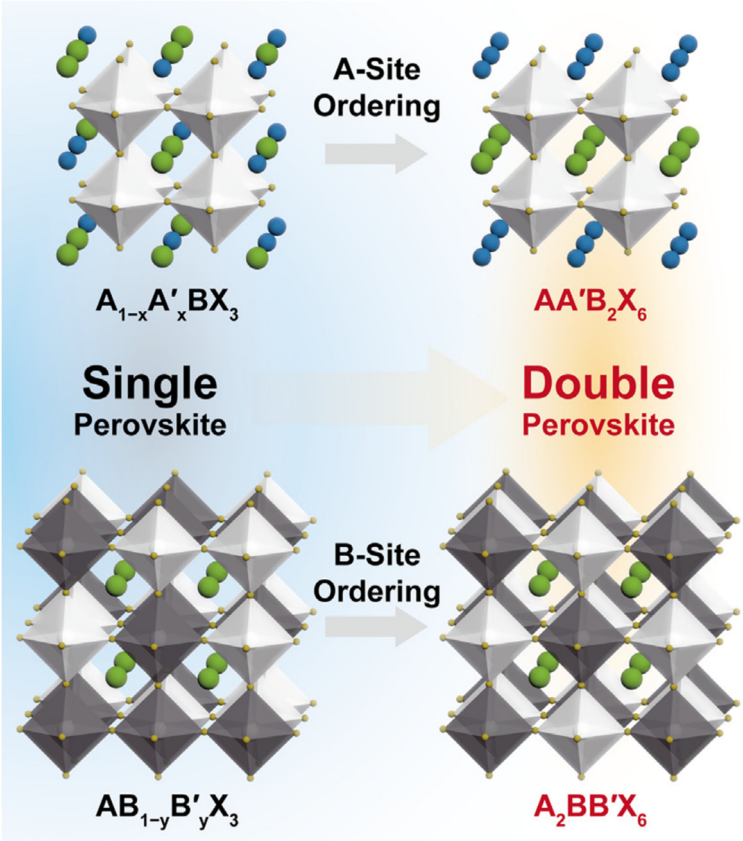

Figure 2.3 | The structure of double perovskite [47].

The exceptional optoelectronic properties of MHPs directly come from their distinctive perovskite structures. The three-dimensional network of corner-sharing BX_6 octahedra allows for the rotation or tilting of the octahedra, resulting in strong electron-phonon interactions [51–53]. As a result, MHPs have demonstrated their potential as high-performance optoelectronic materials. MHPs exhibit easily tuneable direct band gaps that can cover the entire visible light spectrum by adjusting the ratio of different halide anions (Cl^-, Br^-, and I^-) [54–56]. This property makes MHPs suitable for a wide range of optoelectronic devices that operate in the visible light and near-infrared (NIR) range. Secondly, MHPs exhibit distinct defect tolerance. The most easily formed point defects result in shallow defects near the band edges, which only slightly alter the emitting photon energy. This leads to minimal trap-assisted exciton recombination and narrow bandwidth light emission [57, 58]. For instance, when compared to the typical full width at half maximum (FWHM) of approximately 70 nm in conventional OLEDs [59], PeLEDs exhibit an FWHM of less than 20 nm. This results in a high level of colour purity that is suitable for display screen applications [60–62]. Thirdly, MHPs are typically fabricated using low-temperature solution processes, such as spin-coating [63], blade-coating [31, 64], large-scale inkjet printing [32, 34], and roll-to-roll processing techniques [35, 36]. These methods significantly reduce fabrication costs and enable the mass production and industrialization of perovskite optoelectronic devices. To date, MHPs have

been applied to almost all types of optoelectronic devices, as shown in Figure 2.4 [12], including PeLEDs and PePVs.

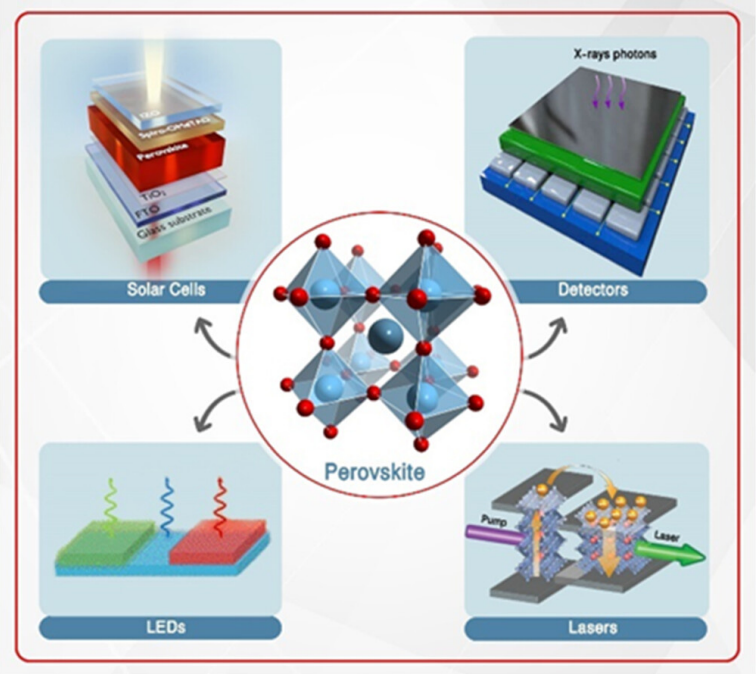

Figure 2.4 | Typical applications of MHP optoelectronic devices [12].

2.2 Perovskite light emitting diodes (PeLEDs).

Perovskite light emitting diodes are a class of optoelectronic devices that convert electricity into light. Excitons recombine inside PeLEDs effectively, generating light. However, conventional bulk MHPs are not preferred for luminescence applications due to their relatively low exciton binding energy [65, 66]. Therefore, quantum confinement of conventional bulk MHPs is usually employed to improve the exciton binding energy and facilitate the exciton recombination process. To date, at least three efficient strategies,

namely nano 3D perovskites, nanocrystals and quasi-2D perovskites, have been proposed to achieve substantial quantum confinement, resulting in high efficiency for PeLEDs, as summarized in Figure 2.5.

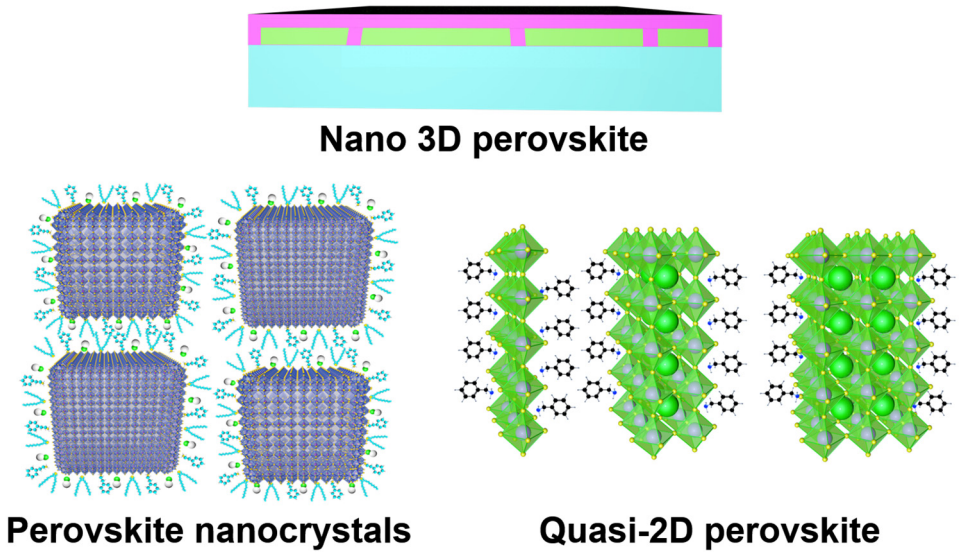

Figure 2.5 | The scheme of three strategies for quantum confined MHPs for PeLEDs application.

The strategies that facilitate the exciton recombination are usually achieved with modification on the nanostructures of MHPs, and the representative milestone-level works are summarized as Figure 2.6 [19, 42, 67–69].

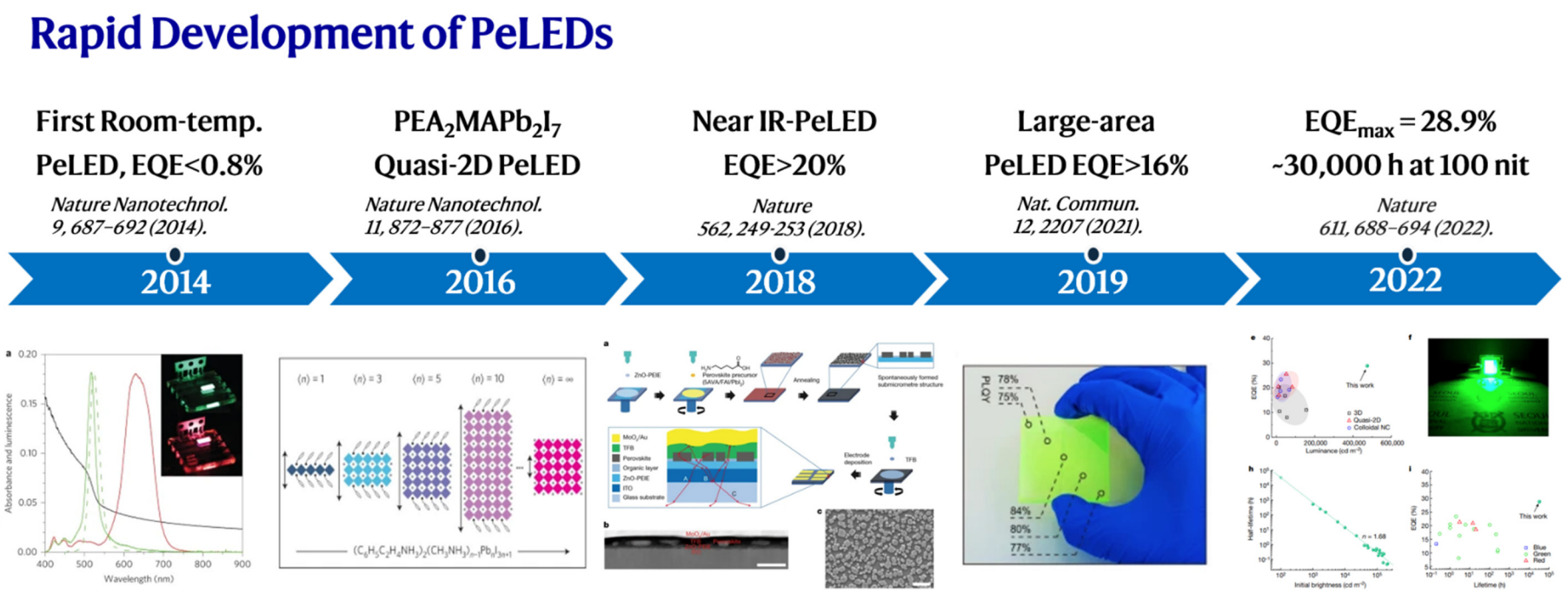

Figure 2.6 | The revolution and representative works of PeLEDs [19, 42, 67–69].

Firstly, decreasing the grain size in conventional bulk perovskite can confine excitons within the grains and facilitate the exciton recombination and light generation. This has led to the proposal of dedicated nano 3D PeLEDs [39, 67]. Secondly, colloidal perovskite quantum dots have been synthesized using methods as conventional II-IV group quantum dots and have been applied as perovskite quantum dot LEDs (PeQLEDs) [70, 71]. Thirdly, two-dimensional (2D) or quasi-two-dimensional (quasi-2D) perovskites have become a unique strategy in perovskite material systems due to their multi-quantum-well structures, energy funnelling processes, and well-confined excitons. The designs for quantum-confined MHPs not only improved device performance but also allowed for wide performance tunability in the design and fabrication of PeLEDs [72, 73], such as the functionalisation of low-dimensional PeLEDs and consequent novel chiral PeLEDs [74–76].

Among all the strategies mentioned above, quasi-2D perovskites have demonstrated unique superiority due to their well-confined excitons within multi-quantum-well structures, broad functionalization potentials, and a simple fabrication process. Quasi-2D perovskite materials exhibit unique properties arising from their structural characteristics, which are significantly different from those of conventional 3D bulk and common 2D perovskite materials. To simplify, quasi-2D perovskites are mixed phase dimension material systems containing a series of 2D and 3D bulk phases. The

formation of these quantum wells is achieved with the employment of bulky organic cations to partially substitute traditional small A-site cations, which disrupts the inherent continuous 3D lattice structure and generates stable quasi-2D configurations [77], as presented in Figure 2.7 [78]. Quasi-2D perovskites adopt a chemical formula of $A'_2A_{n-1}B_nX_{3n+1}$ (where $1 \leq n \leq \infty$), with A' as a bulky organic cation like monoammonium ($R\text{-}NH^{3+}$) or diammonium cations ($^+H_3N\text{-}R\text{-}NH_3^+$), where R represents an alkyl chain or an aromatic ligand. These materials are constituted by a sequence of alternating inorganic and organic derivations [79]. The introduced large organic amine molecules won't penetrate into the perovskite lattice due to large steric hindrance but occupy the A-site position, thereby hindering the expansion of the lead centred octahedra network along out-of-plane orientations and forming stable multiple quantum well structures [80].

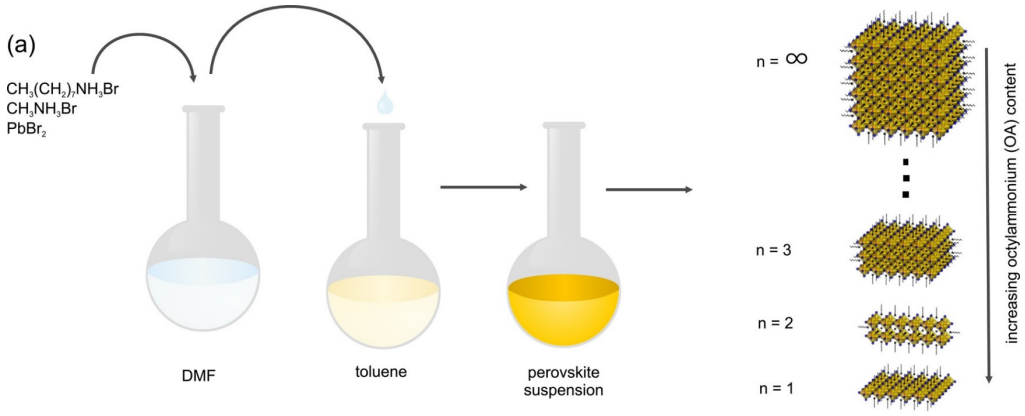

Figure 2.7 | Schematic of the synthesis process of the perovskite quantum wells [78].

The quantum confinement of quasi-2D perovskites is achieved by the intrinsic structure. In quasi-2D perovskite, the inorganic lead centred octahedra are encapsulated between two layers of bulky organic spacers with comparably lower dielectric constants, as shown in Figure 2.8 [55]. Herein, the inorganic lead centred octahedra layers behave like "quantum wells", while the organic capping layers serve as the "barriers", resulting in a natural formation of quantum-well architectures in quasi-2D perovskites with a sharp atomic boundary between "barriers" and "wells". Such quantum confinement and dielectric confinement effects elevate the exciton binding energy of quasi-2D perovskites above their 3D counterparts [81]. Meanwhile, the carrier wave functions are spatially confined in the finite width quantum wells, thus restricting carrier mobility, and enhancing exciton binding energy and the phase bandgap. As a result, both electrons and holes are confined within the quantum well, fostering the creation of stable room-temperature excitons and improving radiative recombination efficiency [68]. Therefore, the quantum confinement of quasi-2D perovskites is significantly enhanced, which further ensures the broad applications of quasi-2D perovskites in light emission applications that require high exciton binding energy for efficient exciton recombination.

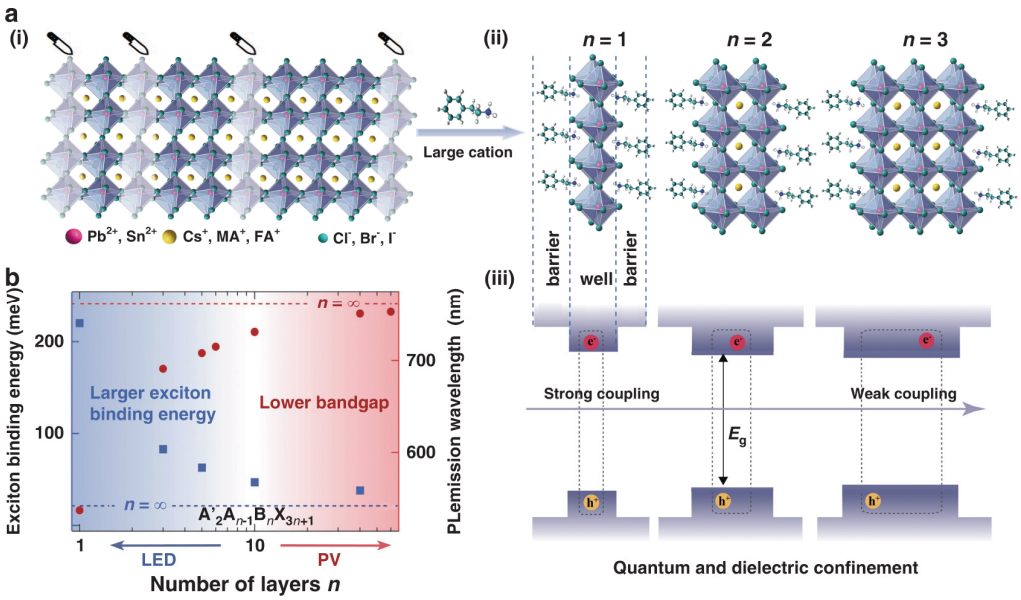

Figure 2.8 | The structure and consequent quantum confinement of quasi-2D perovskites [55].

Those 2D phases are described by the thickness with the “n value”, the number of lead-centred octahedra in a single well for reduced-dimensional perovskites (RDPs), as shown in Figure 2.9 [82–84]. To form quasi-2D perovskites, bulky cations (ligands, as usually named in chemical synthesis) such as phenethyl ammonium ion (PEA^+) and 1-naphthylmethylammonium ion (NMA^+) are introduced into perovskite precursor solutions [44]. And during the film formation process, these bulky cations usually coordinate at A-site, terminate the growth of 3D bulk perovskite phases, and form mixed 2D phases.

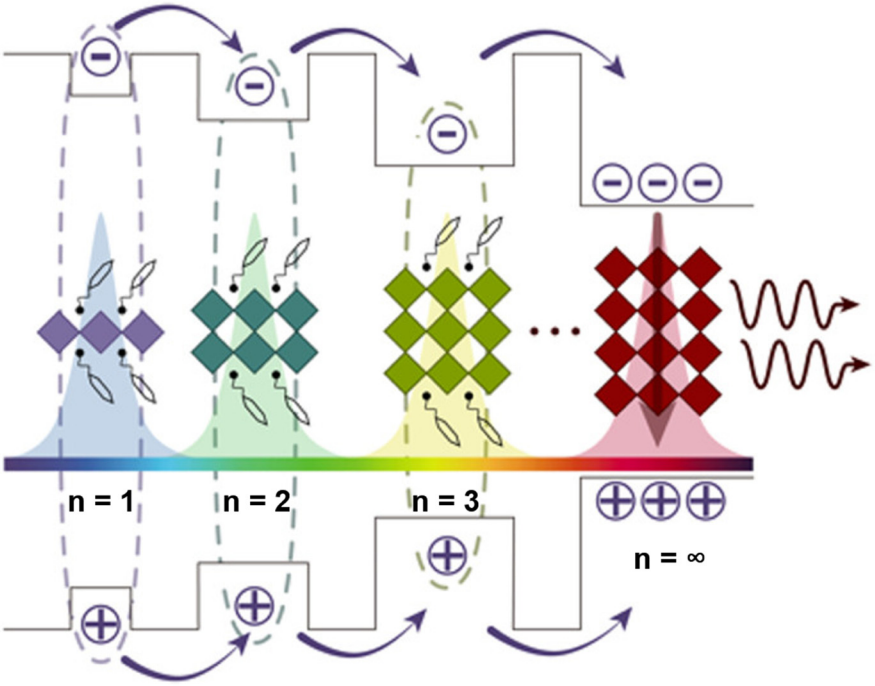

Figure 2.9 | Representative structure of quasi-2D perovskites and consequently scheme of energy funnelling [84].

The development of quasi-2D MHPs has been propelled by several advantageous attributes. Firstly, the mixed 2D phases inside quasi-2D perovskites engenders natural quantum well structures, thereby eliciting both dielectric and quantum confinement effects [85–87]. These strong confinements of excitons lead to a significant enhancement of exciton binding energies. Secondly, the inherent compositional complexity of quasi-2D perovskites contributes to their high tuneability. For instance, quasi-2D perovskites exhibit a remarkable degree of spectral tunability that can be readily manipulated through composition adjustments and phase dimensional engineering. In conventional 3D perovskites, the shift of the

emission spectrum via alternation of halide content often risks phase segregation, halide redistribution and stability issues [88]. While for quasi-2D perovskites, the tuning of emission spectra can be achieved by simply changing the n value without phase segregation issues, as shown in Figure 2.10 [89, 90]. Consequently, quasi-2D perovskite material systems have facilitated a seamless tunability of photoluminescence wavelengths spanning the entire visible spectrum from violet to the NIR region [38, 61, 91, 92]. Additionally, the presence of exchangeable ligands (L-site ions) endows quasi-2D perovskites with facile functionalization possibilities [44].

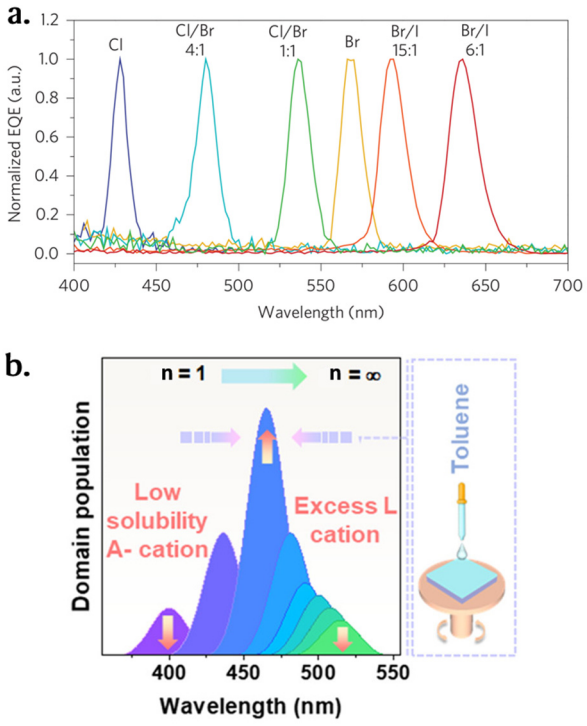

Figure 2.10 | Strategies to tune the emission peaks of MHPs. (a) Changing conventional 3D perovskites emission spectrum with mixed halide [89]. (b) Tuning the emission spectra of quasi-2D perovskites with modification of n value [90].

Finally, unlike perovskite nanocrystals that necessitate additional complicated synthesis stages [70], quasi-2D perovskites can generally be deposited in a single step film formation process, contributing to lower production costs. Thus, quasi-2D PeLEDs have become the most commonly reported high efficiency devices (with EQE > 20%) among all PeLED categories, and also achieved the highest reported EQE to date [20, 72, 73], as presented in Figure 2.11.

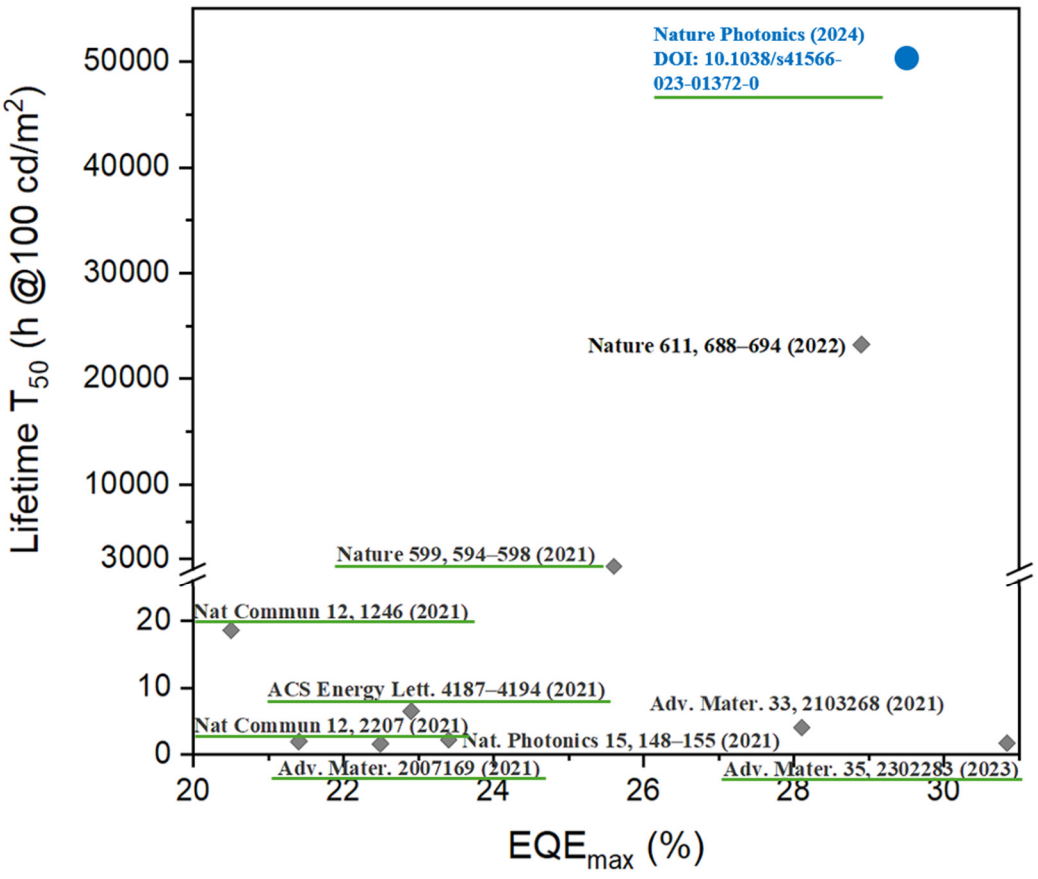

Figure 2.11 | Advances on device EQEs and operational lifetimes of green PeLEDs (quasi-2D PeLEDs are underlined in green, and the author's own work is in blue).

Despite the significant progresses achieved in quasi-2D PeLEDs technology, there remains a pressing need to address the inherent challenges pertaining to both device EQE and stability, particularly limited operational lifetimes. More importantly, the causes of limited operational stability remain complicated [22], restricting the PeLED performance. Hence, it is imperative to conduct a thorough examination of the factors responsible for instability and inefficiency in quasi-2D PeLEDs, followed by the identification and implementation of targeted solutions to mitigate these issues, as outlined subsequently.

2.2.1 Phase dimensions

Among all categories of perovskite materials, quasi-2D perovskites exhibit a strikingly unique intrinsic characteristic: they embody a distinctive multi-quantum-well (MQW) architecture with a blend of diverse dimensional phases. This MQW structure serves as a pivotal factor that fundamentally governs their intrinsic properties, and thereby provides a strategic routine to tailor and optimize the performance of quasi-2D PeLEDs.

The phase dimensions of quasi-2D perovskites predominantly govern the inter-phase energy funnelling process, which plays a crucial role in the luminescence process of quasi-2D perovskites. The energy funnelling process originates from the graded band structure of the mixed n value

phases inside quasi-2D perovskite [81], where excitons can transfer from large band gap low n components to small band gap larger n phases [68]. This unique structure and process effectively functions as a carrier concentrating mechanism, improving the carrier density at the recombination centres. Conversely, in conventional 3D perovskites, excitons formed and undergo recombination at the same position, owing to an absence of additional influences on charge carrier transportation. However, in quasi-2D perovskites, the excitons initialized within the low-n domains do not recombine locally. Instead, they migrate to the small band gap larger n phases and recombine due to the energy levels of different quantum wells. Such a process increases the carrier density at the luminescent larger n phases and is named as carrier concentrating mechanism. As a result, it partially hinders the impact of shallow trap states via photo-passivating, significantly hindering trap assisted nonradiative recombination processes by supplementing extra excitons to fill in the traps in luminescent larger n phases [93]. This facilitated energy funnelling or transfer process subsequently boosts radiative recombination, enabling quasi-2D perovskite films to display high photoluminescence quantum yield (PLQY) even at minimal carrier densities. Thus, gaining profound insights into the energy transfer kinetics and effectively manipulating these processes with advanced phase dimension controls are critical for fabricating efficient quasi-2D PeLEDs.

To date, the probing of the carrier recombination kinetics inside quasi-2D perovskite is generally performed with some ultrafast spectroscopy methods. Remarkably, transient absorption (TA) spectra can clearly distinguish different bleaching peaks of different quantum well phases and attribute them to different n values. Figure 2.12 illustrates a representative transient absorption spectrum of quasi-2D perovskite. The contribution of divergent phases in quasi-2D perovskite films can be estimated directly from transient absorption spectroscopy. Meanwhile, since the optical intensity (OD) of absorption spectrum marks the intensity of absorption and corresponding exciton density, the evolution of relative peak intensities for different n value phases can exhibit the carriers' migration process from phases with smaller n values to those with larger n values, as shown in Figure 2.12 [94]. Also, the transfer rate can be calculated from the growth period of ground state bleach for different components, wherein the OD of low n phases usually reaches the maximum first and begin to decay rapidly comparing to the higher n phases, showing an exciton funnelling process from low n phases to higher n phases. As Figure 2.13 shows [94], the transfer periods of smaller n value phases to higher n value ones are usually at the order of picosecond, signifying an ultrafast energy transfer process.

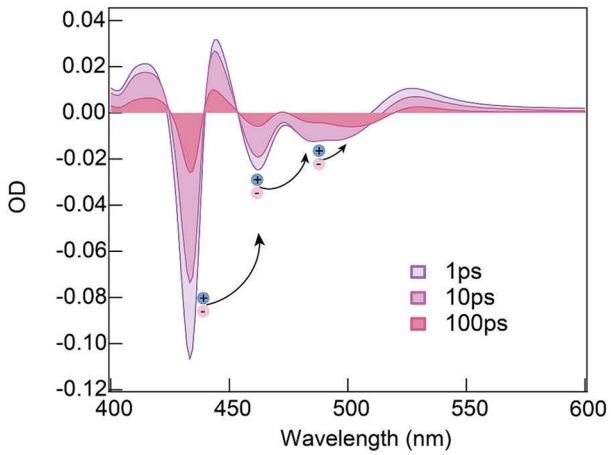

Figure 2.12 | Transient absorption spectra of a representative quasi-2D perovskite film [94].

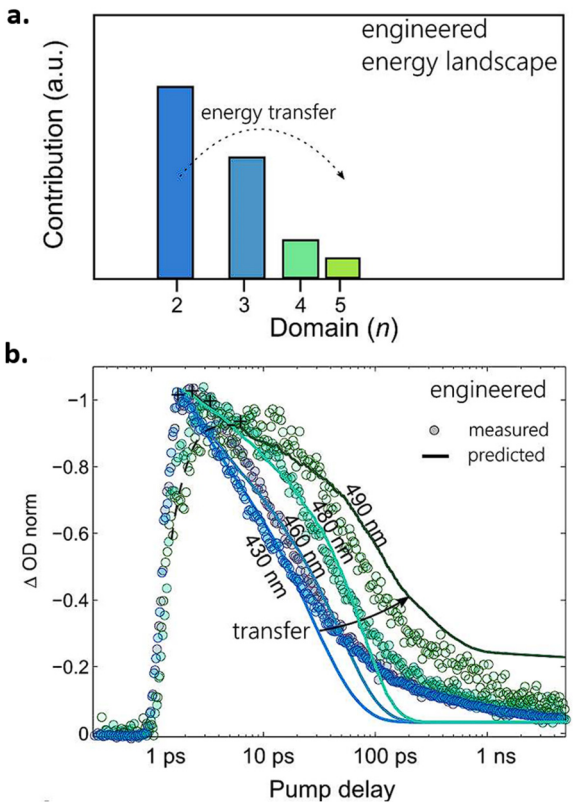

Figure 2.13 | (a) Contribution of divergent phases in quasi-2D perovskite films as estimated from transient absorption spectroscopy. (b) Experimental and predicted time dependent transient absorption changes for quasi-2D perovskites at different wavelengths [94].

Thus, regulating phase dimensions is important for efficient inter-phase energy transfer and high luminescent efficiency [72], as illustrated in Figure 2.14 [95]. Despite its importance, the exact mechanisms governing the manipulation of phase dimensions remain largely elusive. The most conventional method for phase control in quasi-2D perovskite is tuning the average n value or the stoichiometry of the perovskite film precursor, as reported by extensive studies [13, 96–98]. For instance, diminishing the average n value of the perovskite film precursor usually leads to intense quantum confinement effect and broad bandgap and spectral blueshift, as Figure 2.15 shows [96]. As a consequence, the selection of a proper large organic cation ratio inside the perovskite precursor is critical for both effective quantum confinement and emission spectrum of PeLEDs [96].

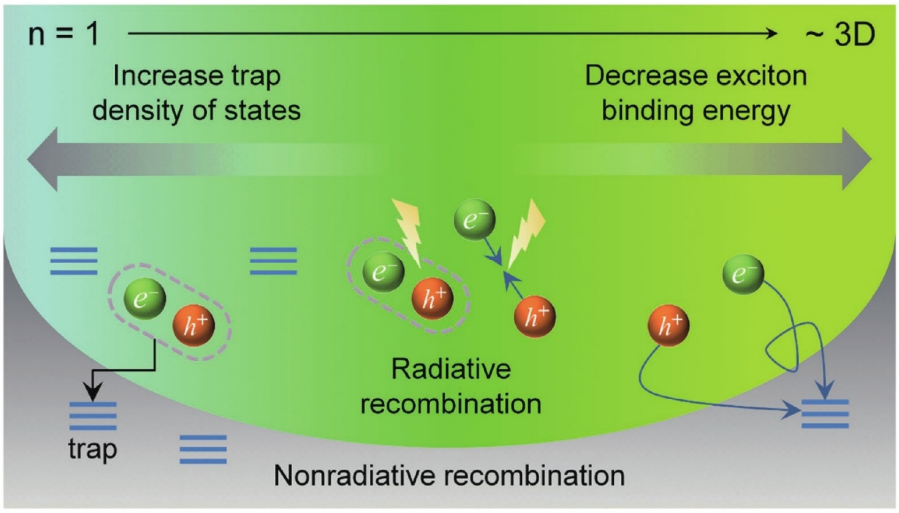

Figure 2.14 | Principle for designing phase dimensions with different n values inside quasi-2D perovskites [95].

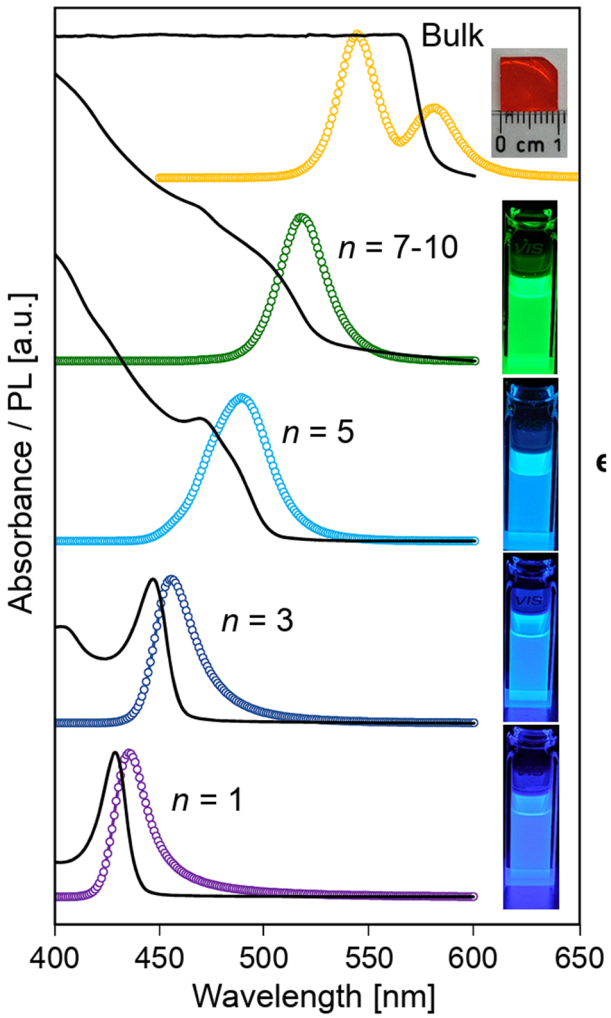

Figure 2.15 | Absorption and PL spectra of perovskites with different n values [96].

However, such a method of altering the average n value or the stoichiometry of the perovskite film precursor, especially the large organic cation ratio, can only change the relative ratio of different n value phases on some occasions, which is not enough for full scale manipulation of phase dimensions. Meanwhile, even though improving the proportion of large organic cations can progressively reduce the n value in principle, this does not automatically

guarantee that quasi-2D perovskite films with lower n values will generate effective light emission. Excessive generation of low n-value phases resulting from increased large organic cation content can compromise energy transfer efficiency and degrade optical performance [99]. Furthermore, excess insulating organic cations can undermine charge transporting properties, while pronounced electron-phonon coupling and exciton-exciton annihilation at small n values introduce nonradiative recombination channels, further deteriorating the optical characteristics [51]. However, reducing the proportion of large organic cations (improving the average n value of perovskite precursor) does not guarantee effective light emission as well, leading to lower exciton confinement and resulting lower PLQYs, as presented in Figure 2.16 [100]. Thus, the limitation of alternating the average n value or the stoichiometry of the perovskite film precursor has hindered the progress of efficacious phase dimensions manipulation and improvements of quasi-2D PeLEDs.

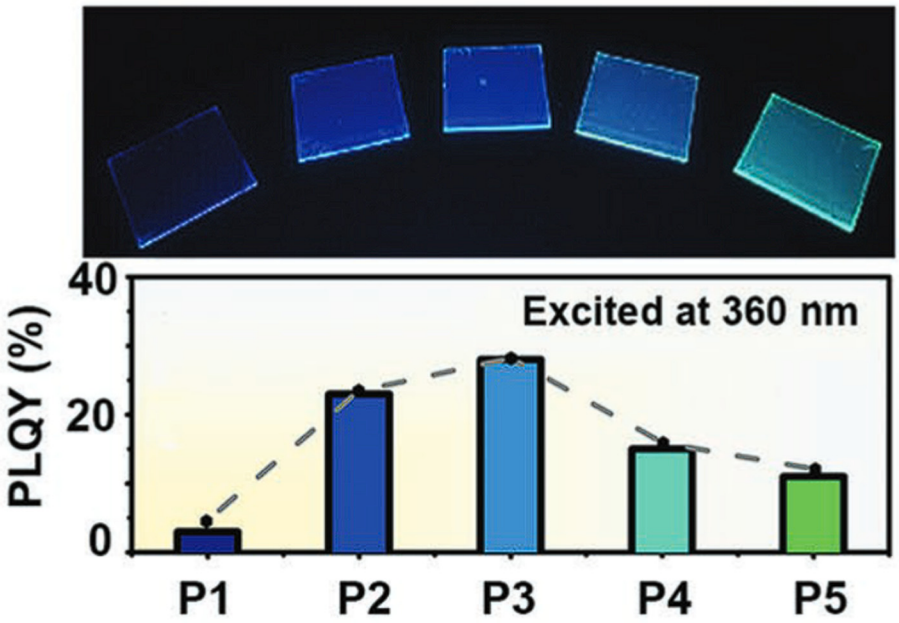

Figure 2.16 | Photos and corresponding PLQYs of perovskite films with different n values [100].

Despite the relatively constrained existing methodologies for effective control over the phase dimensions in quasi-2D perovskites, to date, the relationship between phase dimensions and perovskite stability is not even well understood with contradicted reports. For instance, the stability of low n phases is controversial, with proposal that quasi-2D perovskite degradation originated from the edge of low n value phases (Figure 2.17a [101]), but theoretical calculation results showing low n phases exhibit higher formation energy and stability comparing to higher n ones, as shown in Figure 2.17b [102]. Such contradictions have hindered the solutions of phase dimension issues. Additionally, current strategies for effectively controlling phase dimensions with post-treatment methods are limited. Due to the ultra-small

dimensions of quantum wells at the nanometre level, conventional methods such as mechanical separation are hardly effective in controlling quasi-2D phase dimensions. Therefore, developing an effective strategy to resolve the phase dimension issues of quasi-2D perovskites is urgently required to achieve stable and efficient PeLEDs.

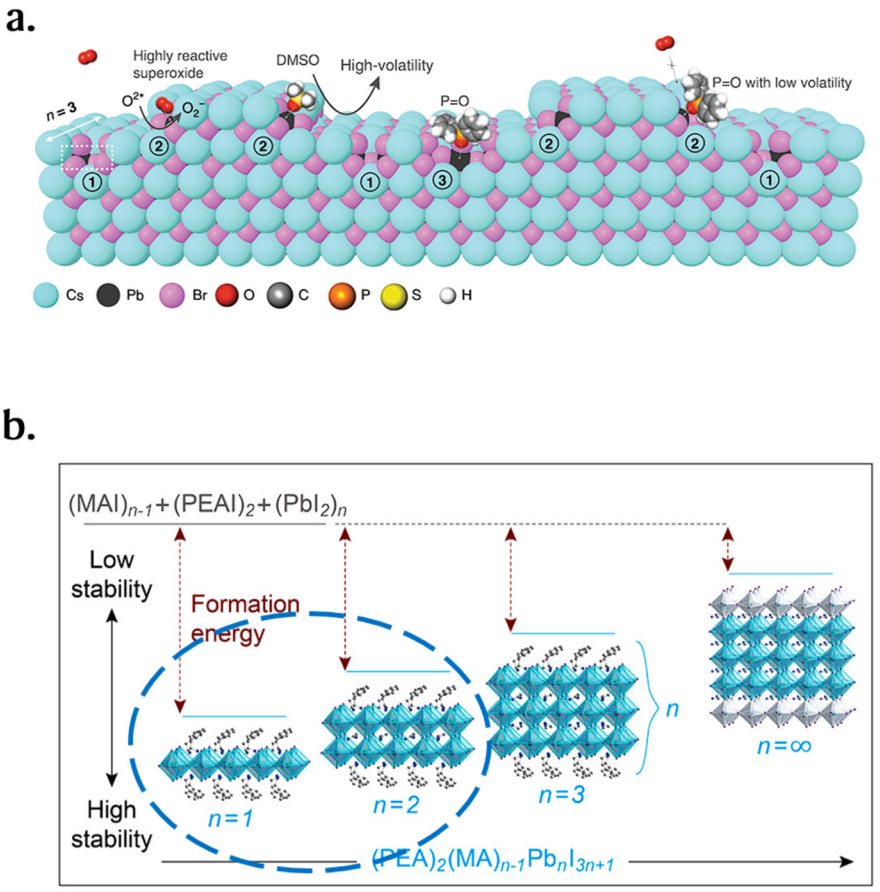

Figure 2.17 | (a) Scheme of the quasi-2D perovskite degradation process that originated from the edge of low n value phases [101]. (b) Simulation results showing low n phases possess higher formation energy and consequent higher stability [102].

2.2.2 Defects

Defects constitute a critical factor for the physicochemical properties of semiconductor materials. Through the regulation of type, distribution, and quantity of defects, it is possible to refine materials and significantly improve the performance of semiconductor devices. Therefore, throughout the development of perovskite technology, the studies of defect behaviour have been widely reported with remarkable advancements on MHP based optoelectronic device applications.

The types of defects inside perovskites can be categorized by their dimensions from zero-dimensional (0D) defects (Figure 2.18c, Figure 2.18d and Figure 2.18f [103]) to high dimensional defects including one-dimensional (1D), two dimensional (2D) and three dimensional (3D) ones (Figure 2.18d and Figure 2.18g [103]).

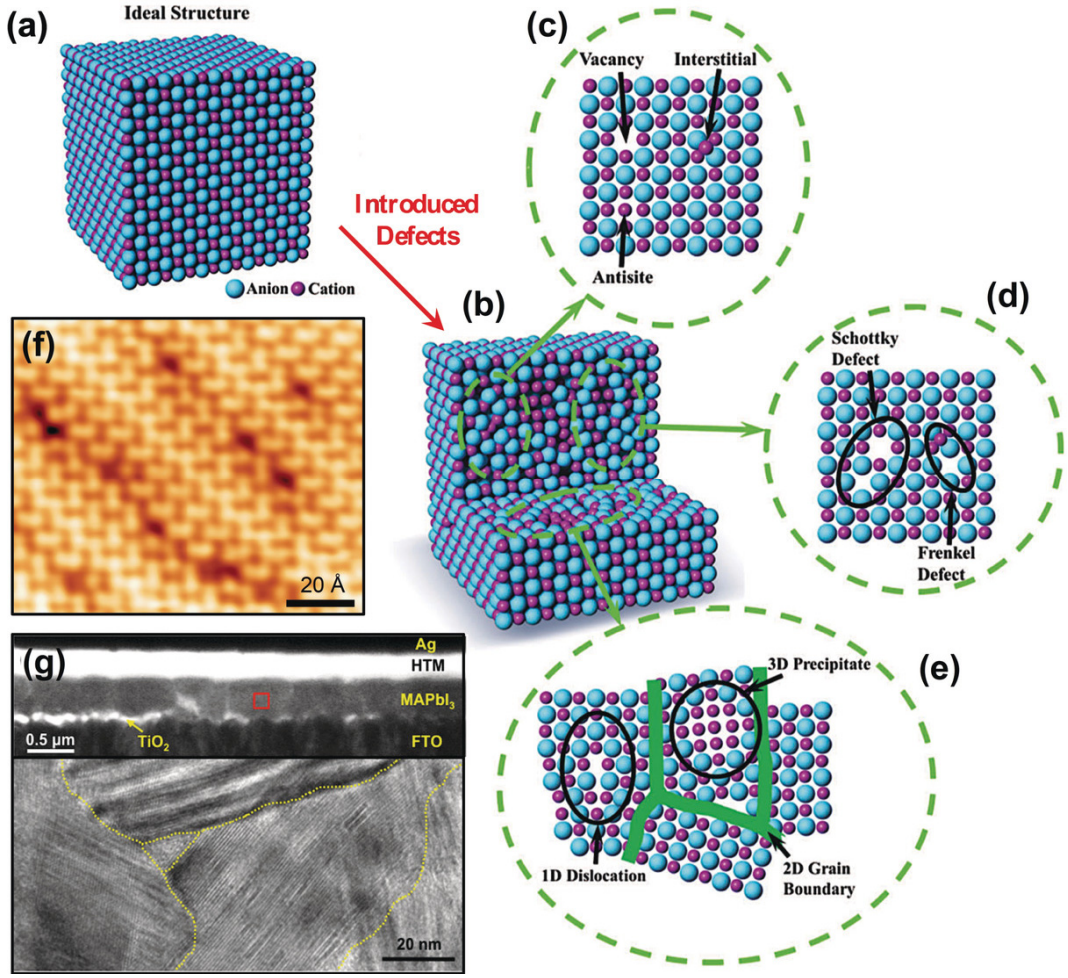

Figure 2.18 | Some representative defect types inside perovskite films, from 0D defects to 3D ones [103]. (a) Ideal perovskite structure. (b) Real perovskite structure. (c) (d) Point defects. (e) 1D to 3D defects. (f) Observed point defects in perovskite lattice with microscopy. (g) Observed 1D to 3D defects in perovskite film with microscopy.

0D defects usually involve common point defects and defect pairs. Based on thermodynamics, 0D defects can emerge naturally or through the incorporation of foreign atoms [104–106]. For MHPs with the ABX_3 structure, point defects encompass vacancies (V_A, V_B, V_X), interstitials (A_i, B_i, X_i), and

anti-site defects (AB, AX, BA, BX, XA, XB) [107], as illustrated in Figure 2.19a [108]. These defects can introduce electronic energy levels within the semiconductor band gaps. If these defect levels lie above the conduction band edge or below the valence band edge, they are not harmful to carrier transport and recombination processes, classified as shallow defects. However, if these trap states are situated in the middle of the bandgap, they are designated as deep defects that deteriorate the carrier transportation and recombination process, as illustrated in Figure 2.19b [107]. It is commonly agreed that many point defects possess low formation energies and generate shallow defects, enabling MHPs with defect tolerance [109, 110], while some intrinsic point defects can also exhibit both deep defect energy levels and high formation energies [111].

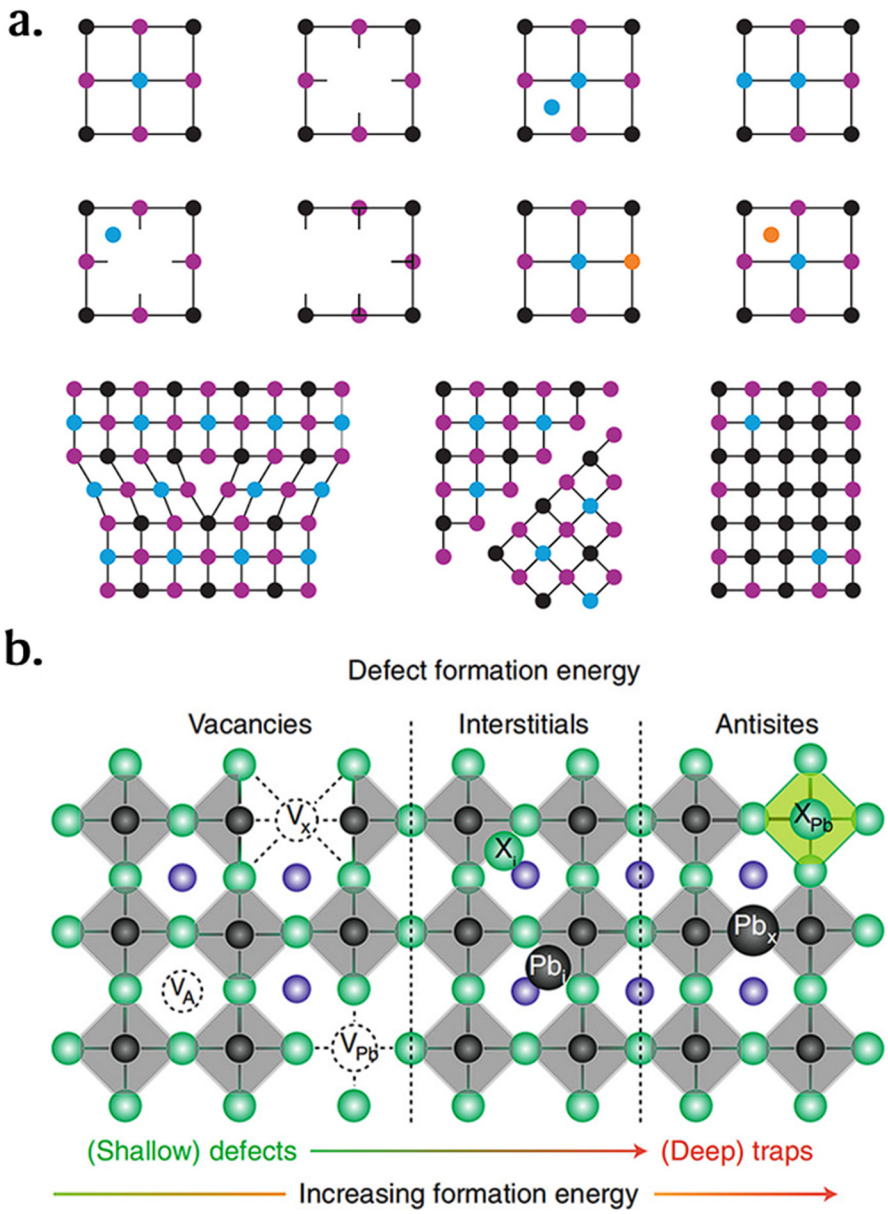

Figure 2.19 | (a) Defects in the perovskite lattice, including (0D) point defects, defect pairs, (1D) dislocation, (2D) grain boundary and (3D) precipitate [108]. (b) Typical point defects, formation energy and trap depth [107].

Apart from individual point defects, defect pairs are also prevalent in MHPs. The most common defect pairs in MHPs are Frenkel defects and Schottky defects, where Frenkel defects consist of a pair of vacancies and interstitials

of the same ion and Schottky defects involve two vacancies with different charges [112]. The formation and elimination processes of defect pairs are complicated. It has been reported that defect pairs can form during the crystallization process of MHPs and migrate under applied electric and light fields, highly correlated with halide segregation phenomena [113], as presented in Figure 2.20 [114]. Also, light illumination can facilitate the annihilation of Frenkel defect pairs, thereby eliminating carrier trapping states [115]. The generation of defect pairs can also deteriorate the optoelectronic performance of MHPs. For example, the formation of interstitial sites of Frenkel defects introduces deep trap states into the bandgap of MHPs and results in non-radiative recombination and reduction of PLQYs [114], with further accelerated device degradation [116].

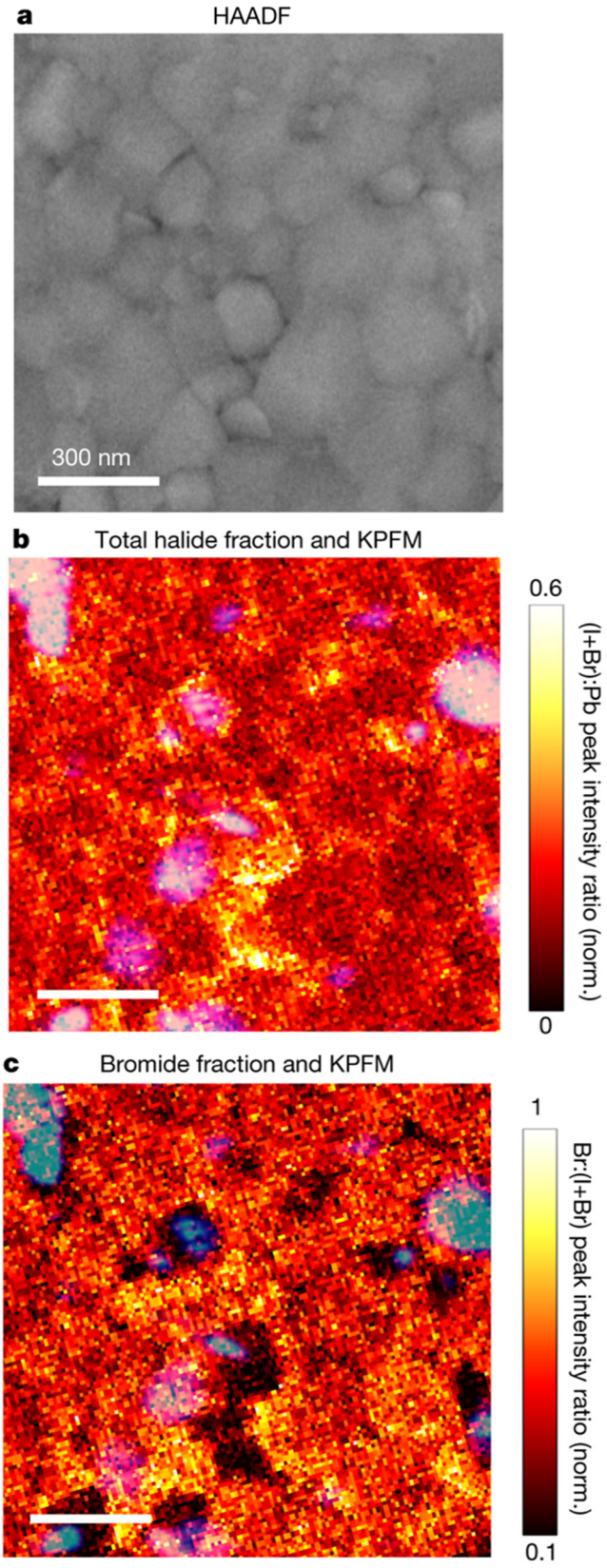

Figure 2.20 | Direct observation of halide segregation phenomena inside MHP film [114].

Higher dimensional defects can be generated from the proliferation of 0D point defects and defect pairs, such as 1D dislocations, 2D grain boundaries, and 3D defects including precipitates or voids inside perovskite films [103]. Typically, 1D linear defects occur in the crystal when the halide perovskite lattice mismatches the substrate (in Figure 2.21 [117]), as the same phenomena during the epitaxial growth of conventional semiconductor films. As for 2D defects, the grain boundary defects originate from the polycrystalline nature of MHP materials generally used in PeLEDs. The impacts of grain boundaries inside MHPs have been reported as grain boundaries can induce very shallow tap levels near the VB edge, impeding carrier diffusion [118], and promoting nonradiative recombination [119]. Beyond grain boundaries and interfaces, 3D precipitates and voids can also lead to trap assisted nonradiative recombination processes, deteriorating optoelectronic properties and facilitating film decomposition [120].

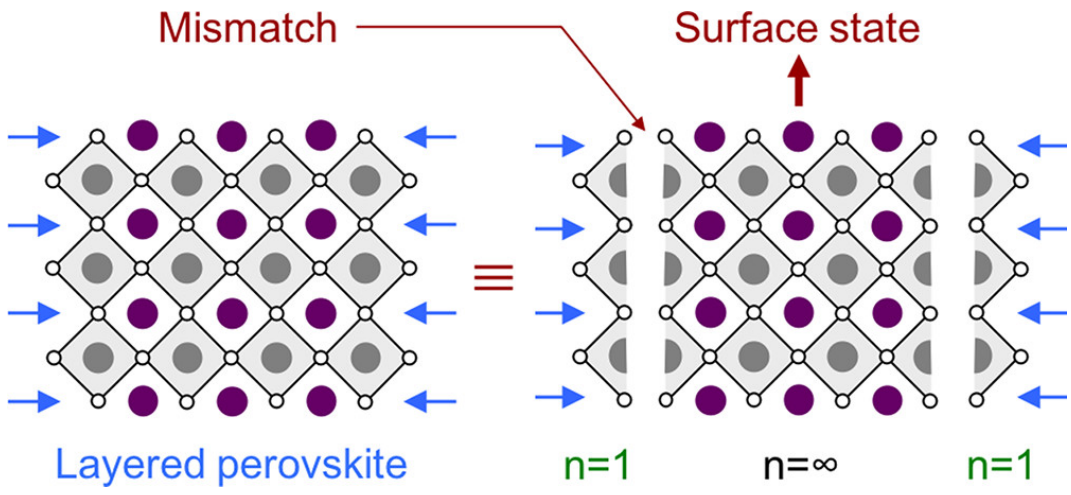

Figure 2.21 | Lattice mismatches and 1D defects in MHPs [117].

The formation of defects inside MHP films is also extremely complicated. In a perfect crystal, each atom occupies a definitive site within the ordered lattice structure. However, defects typically manifest when the periodicity of the lattice is disrupted, especially for MHPs with inherently soft structural features [121]. In general, the defects originate from either intrinsic or extrinsic factors. Intrinsic factors typically revolve during the formation processes of MHPs, such as nucleation, crystal growth, and annealing, which significantly determines the overall quality of the MHP film [122]. For example, a rapid crystal growth or improper annealing process can usually lead to uncontrollable defects formation, wherein ions can hardly fit in ideal lattice sites due to limited ion diffusion conditions. While the extrinsic factors also play a crucial role in the creation of defects. Research has demonstrated that certain levels of moisture or oxygen exposure can potentially enhance perovskite performance, although these environmental elements can also undermine the long-term stability of perovskite-based devices [123]. Since MHP based optoelectronic devices often operate under persistent external factors, such as light irradiation, electric field, and heat, the complex interactions between these external factors and the defects within the materials are important for further in-depth investigation.

The impacts of defects to MHPs can be summarized as two aspects. In MHPs, defects can cause trap-assisted non-radiative exciton recombination (as

Figure 2.22 shows [111]), as well as higher reactivity and severe ion transportation, which reduce the efficiency and stability of PeLEDs [82, 85, 91]. Therefore, effective suppression and passivation of defects are necessary to improve the efficiency and stability of PeLEDs. Unfortunately, MHPs are frequently fabricated with multiple defects as a result of the rapid and less controllable crystal formation process at room temperature. Therefore, it is crucial to suppress defects via optimizing the MHPs formation techniques. However, the mixed ion nature of MHPs significantly increases the difficulty of suppressing defects comprehensively [46, 124], and spontaneous coordination with both cations and anions is required to effectively optimize ion behaviour and avoid defect formation.

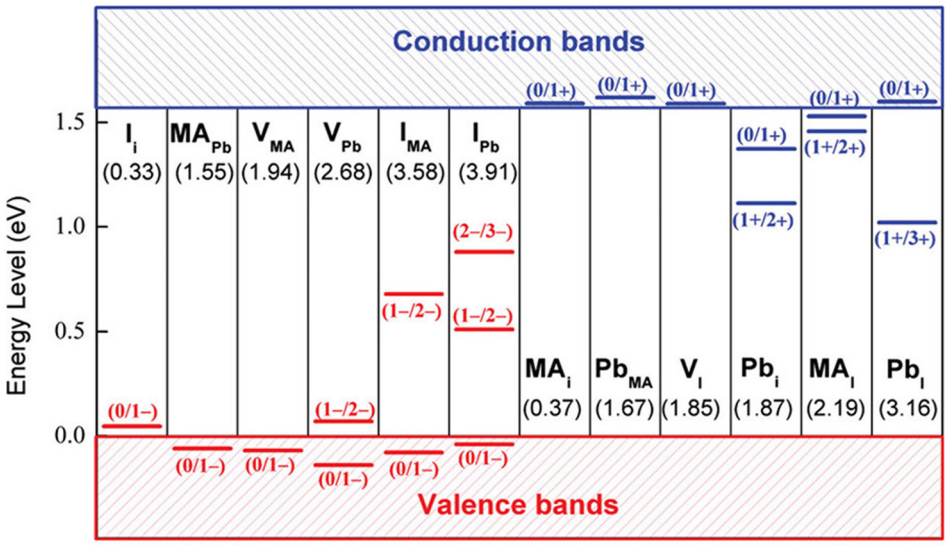

Figure 2.22 | Trap states caused by defects inside representative $MAPbI_3$ MHPs [111].

2.2.3 Ion migration.

The ion migration effect is particularly significant in MHPs compared to other conventional semiconductors. The process and consequence of ion migration in MHP films is summarized as Figure 2.23 [125], including Ion migration, electrode corrosion, electrochemical reactions, and interfacial reactions.

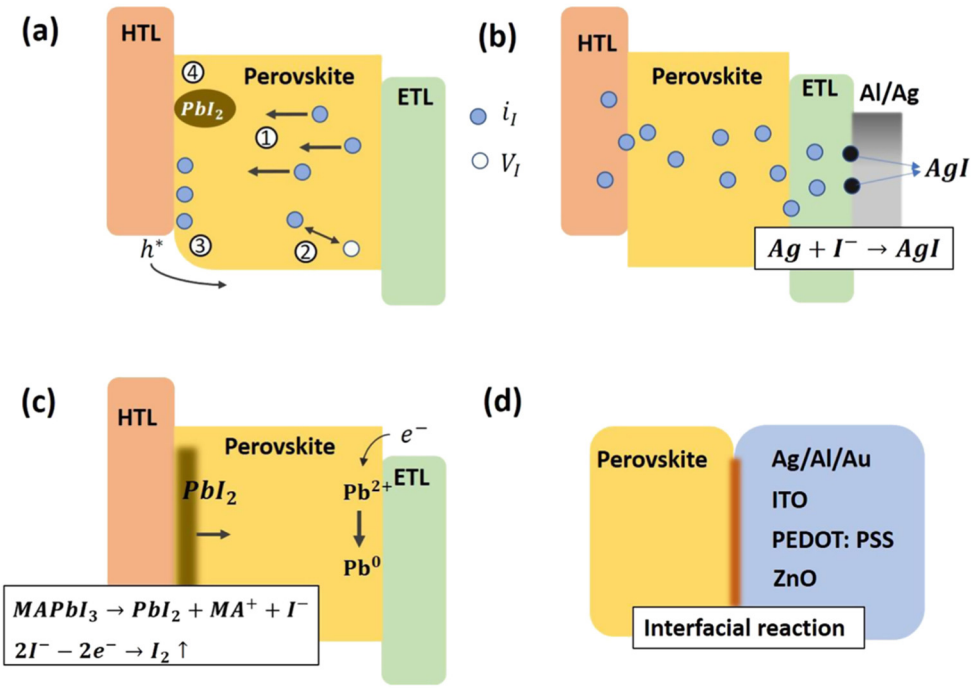

Figure 2.23 | Scheme of the process and consequence of ion migration in MHP films [125]. (a) Ion migration. (b) Ion migration leads to electrode corrosion. (c) Electrochemical reactions. (d) Interfacial reactions.

The ion migration effect can be attributed to the intrinsic structure of MHPs [126], which is unique due to their soft ionic structure unlike conventional

semiconductors like silicon or GaAs [127, 128]. This structure allows for high mobility and flexibility of ions within the perovskite material. Furthermore, MHPs also present a mixed electronic and ionic conductivity with ion migration routine across the MHP lattice, as presented in Figure 2.24 [129]. The migration abilities of different ions in perovskites vary due to their different sites within the perovskite structure. Theoretical studies have shown that halide anions (I^-) have a relatively high migration trend, with an activation energy calculated as low as 0.1 eV [129–131], while A-site cations such as MA^+ have a higher activation energy of about 0.5 eV [105, 132, 133]. Also, it is usually believed that the migration of B-site ions, such as Pb^{2+}, shows a too high migration activation energy to be mobile [129].

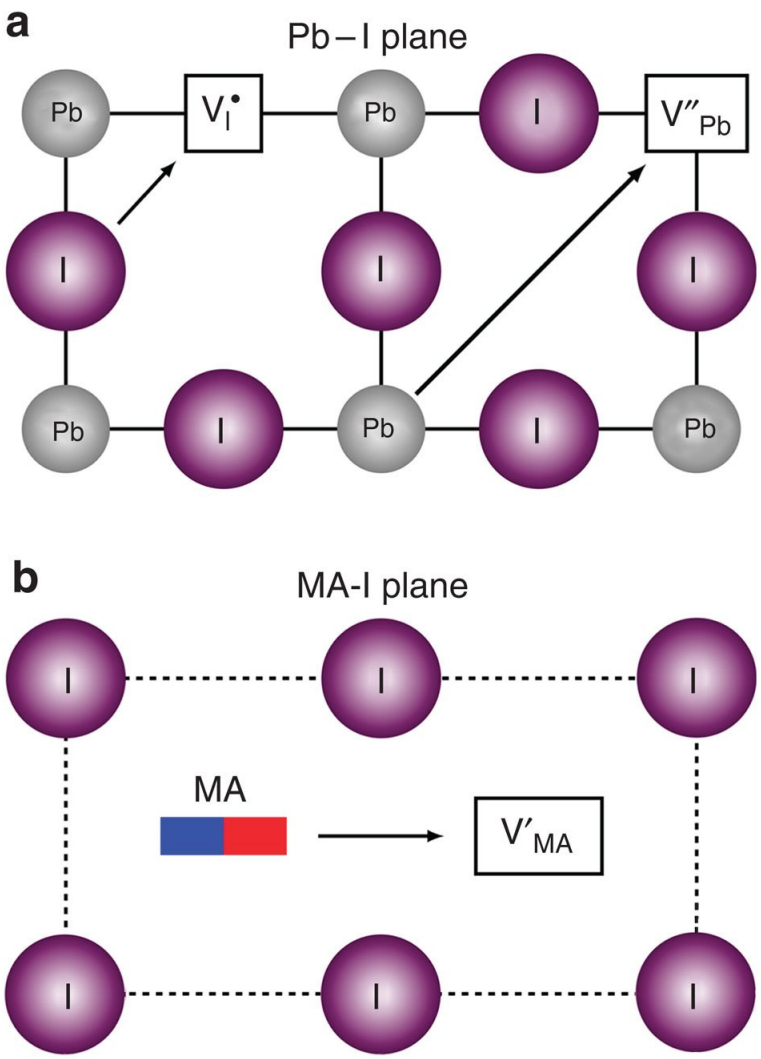

Figure 2.24 | Ion migration routine in typical MHP structure [129].

In MHP films and devices, the low activation energy of ion migration has been figured as inherent causes of limited device performance and stability. It has been widely reported that ion migration effect can cause diverse microscale effects, such as defect formation and migration [134–137], creation and annihilation of Frenkel defects for halide ions [138–142], distortion of MHPs lattice [136, 142, 143], changes of charge injection at interfaces [144–148], and severe electrode corrosion [149–154]. Meanwhile, some interesting

macroscale phenomena are also extensively reported to be the direct consequence of ion migration, such as: (1) The hysteresis effect in MHP-based optoelectronic devices including PeLEDs and PePVs, as Figure 2.25 presents, respectively [155, 156], leading to inconsistent power output and reduced overall efficiency. (2) The giant switchable photovoltaic effect [157] with potential applications as electrically and optically readable memristors and circuits. (3) Fluorescence intermittency or "blinking" behaviour [158] (Figure 2.26b [159]), undesirable properties for lighting and display applications due to random fluctuations of ions. (4) Photo or electrically induced enhancements in PLQYs via halide redistribution [138]. (5) Phase segregation [159], often caused by long range accumulative ion migration and compositional changes within MHP films, as listed in Figure 2.26a [159]. These diverse effects have all highlighted the necessity of efficacious control over the ion migration effect for the advancement of optoelectronic applications.

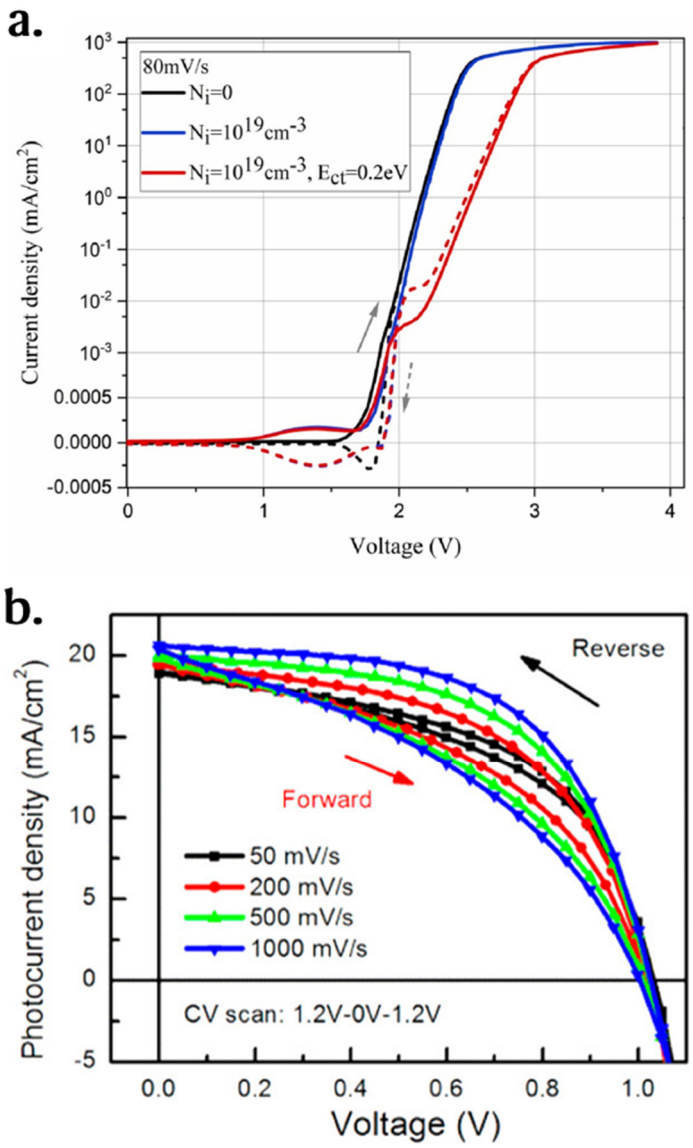

Figure 2.25 | Hysteresis effect of (a) PeLEDs [155] and (b) PePVs [156].

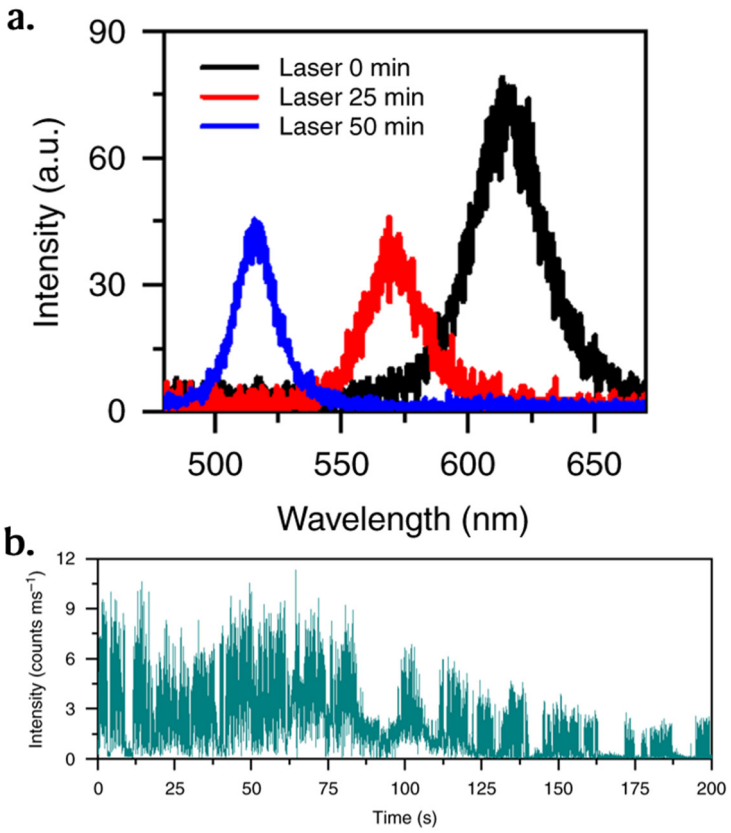

Figure 2.26 | (a) Phase segregation phenomena lead to changes in the PL spectrum. (b) Fluorescence intermittency or "blinking" behaviour [159].

The most critical consequence of the ion migration effect has been reported as the main cause of PeLEDs instability [22]. All consequences of ion migration have led to a severe deterioration in the stability of PeLEDs, as well as a decrease in long-term efficiency throughout the lifespan of PeLED devices. Therefore, it is crucial to effectively inhibit the ion migration effect to achieve highly stable PeLEDs, especially for halide anions and A-site cations. To date, a large variety of methodologies have been developed to suppress the ion migration effect in quasi-2D MHPs [160]. Compositional

engineering like ions doping into MHP lattice can improve the migration barrier of ions. For instance, yttrium (III) chloride (YCl_3) dopants into the precursor solution of blue quasi-2D PeLEDs can improve the migration activation energy of halide ions, achieving significant suppression effect of ion migration and corresponding enhanced spectral stability and operational stability [161]. Meanwhile, some small organic molecules can function as effective inhibitors to ion migration due to strong interaction with B-site lead and X-site halide ions, leading to bright, narrowband, and spectrally stable blue quasi-2D PeLEDs, as shown in Figure 2.27 [162].

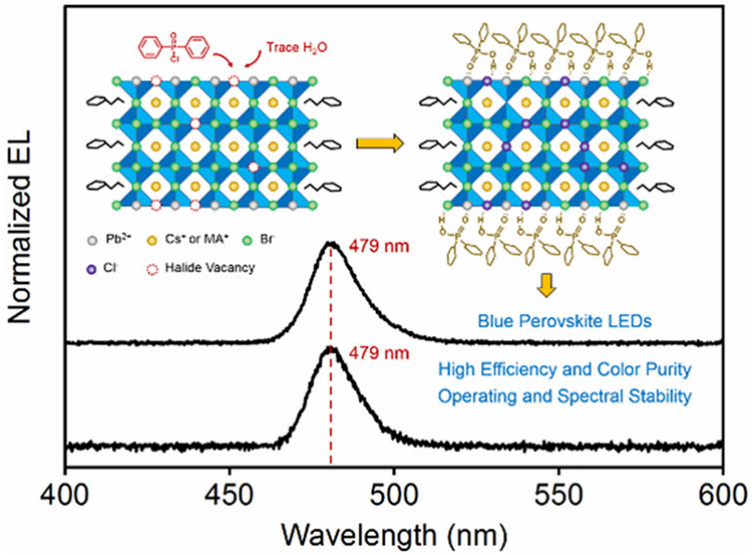

Figure 2.27 | Ion migration suppression with small organic molecules diphenyl phosphine chloride (DPPOCl) [162] led to improved spectra stability.

Also, additional surface passivation methods can hinder the surface assisted and inter-layer ion migration Figure 2.28a [163], improving the operational

lifetime of PeLEDs, as Figure 2.28b illustrates [163]. However, the existing research remains inadequate due to the overall limited operational lifetime of PeLEDs [73], with most state-of-art studies reporting operational lifetime no more than 20 hours at the conventional luminance of 100 cd/m^2, far behind the basic requirements for industrialization. Thereby, further exploration and improvements on PeLEDs operational lifetime have been urgently demanded.

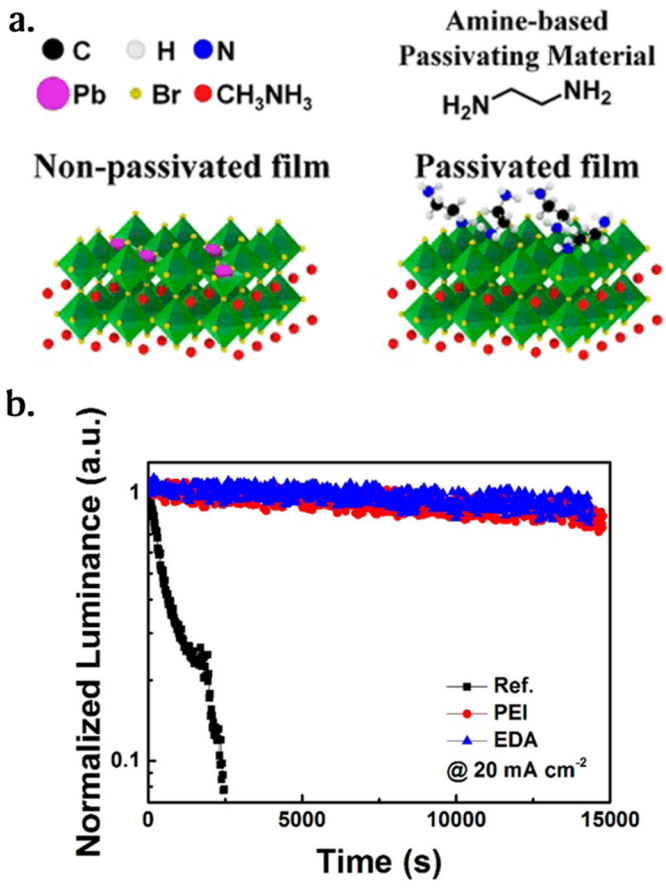

Figure 2.28 | (a) Scheme of surface passivation method. (b) Improved operational lifetime of PeLEDs based on the surface passivation method (PEI: branched polyethylenimine, EDA: ethylenediamine) [163].

As introduced above, the efficacious ion migration suppression is still lacking to meet the industrialization requirements of PeLEDs, necessitating an operational lifetime of at least several years for display screens. One of the main obstacles is rendered from the complex ionic components inside MHPs. Current approaches of ion coordination mainly concentrate on the formation of strong interactions with B-site lead and X-site halide ions. But maintaining strong coordination to all kinds of ions spontaneously remains a critical challenge. Meanwhile, the electrochemical stability issue generated along with the ion migration is also critical during the long-term operation of PeLEDs, still demanding further investigation.

In summary, PeLEDs are optoelectronic devices that convert electricity into light through efficient exciton recombination induced by quantum confinement. Till now, nano-3D PeLEDs, PeQLEDs, and quasi-2D PeLEDs have been developed to achieve effective quantum confinement. Among PeLED devices, quasi-2D PeLEDs have been considered particularly successful, setting the performance record of EQE and lifetime across all categories of PeLEDs. However, the limited operational stability of PeLEDs has raised critical challenges, such as phase dimensions, defects, and ion migration issues, and addressing these issues is urgently required to achieve highly stable and efficient PeLEDs for potential industrialisation. Therefore, in this thesis, three corresponding strategies, solvent sieve method, sweet

coordination strategy, and ion pinning strategy, have been proposed and successfully employed to tackle these major challenges, as introduced in Chapter 4 to 6 below.

2.3 Perovskite photovoltaic cells (PePVs).

The initial room temperature optoelectronic application of MHPs was reported in 2009 as photovoltaic cells as Figure 2.29 [38], with an initial design as dye sensitized solar cells [38]. In just 15 years, the record power conversion efficiency (PCE) of PePVs has increased from about 3% to over 26%, as reported by the National Renewable Energy Laboratory (NREL) certification (Figure 1.5 [27]), approaching the theoretical limit of PCEs of about 30% for PePVs [164]. Meanwhile, PePVs have achieved impressive stability, sustaining over 90% of their initial PCEs for several thousand hours under complicated conditions [165–170].

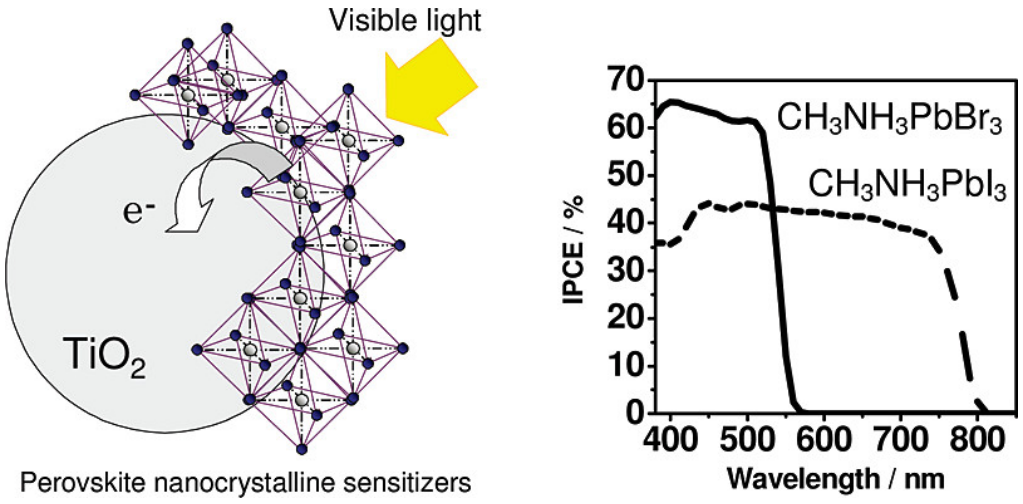

Figure 2.29 | First reported PePVs in 2009 [38].

The strategies for improving the performance of PePVs diverge from those employed in from those employed for PeLEDs due to the reverse operational condition, despite some unique but less efficient light-emitting solar cells, as shown in Figure 2.30 [171]. While PeLEDs necessitate quantum confinement effects to govern the exciton recombination processes, PePVs operate via the photo-induced dissociation of excitons into free charge carriers and resulting electrical power generation [172]. Therefore, the nanostructures optimized for exciton confinement and recombination in PeLEDs are not directly applicable to PePV technology. Meanwhile, critical challenges for PePVs arise not only from the MHP materials themselves but also from the delicate device structure [173].

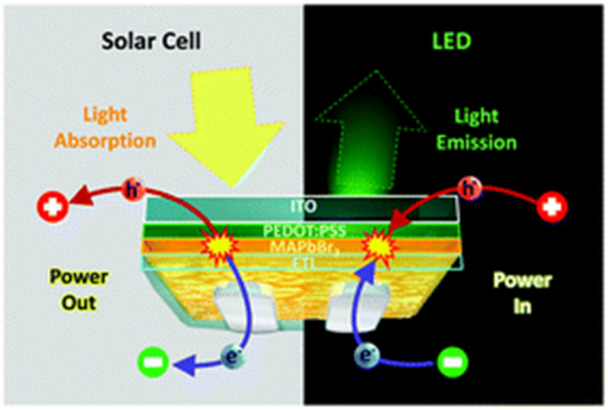

Figure 2.30 | Different operation processes of PeLEDs and PePVs in a light-emitting solar cell [171].

The development of PePVs has spun from fundamental material synthesis to the encapsulation of complete photovoltaic modules. Despite the

comprehensive nature of these developments, this thesis focuses on a specific and crucial aspect, the interfacial issue inside two-step quasi-2D PePVs. Compared with conventional 3D perovskites, quasi-2D perovskites have enlarged band gaps, which hinders the interfacial energy level matching [63, 174, 175]. Meanwhile, the two-step method represents a unique fabrication process involving the immersion or spin-coating of a PbI_2 film with organic salts solution such as methylammonium iodide (MAI) [176], whereupon crystallization ensues following the interaction between the organic and inorganic components, as Figure 2.31 presents [174]. Unlike conventional one-step method which often encounters surface coverage and uniformity issues due to less controllable film crystallization process [177], two-step method has boasted benefits of facile fabrication and reliable reproducibility due to the easily controlled reaction mechanism of Figure 2.32 [174]. Also, the PCE of the two-step method has caught up with the one-step method with over 25% at lower temperature [178]. The two-step method fabrication of other optoelectronic devices like perovskite photodetectors has also been reported [179], indicating the great potential in the preparation of highly efficient and stable PePVs and other optoelectronic devices.

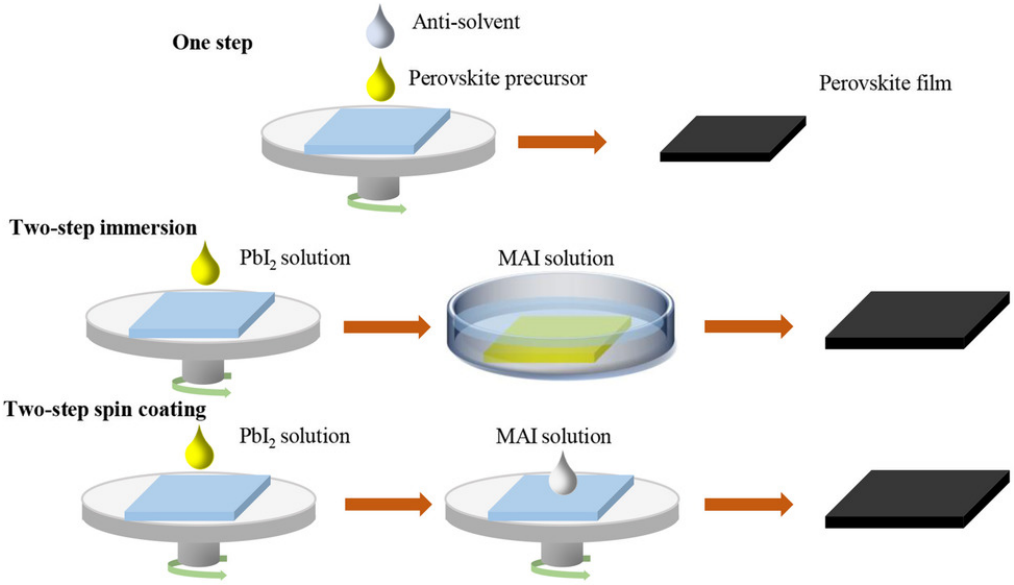

Figure 2.31 | Schematic illustration of perovskite fabrication process of one-step method and two-step method [174].

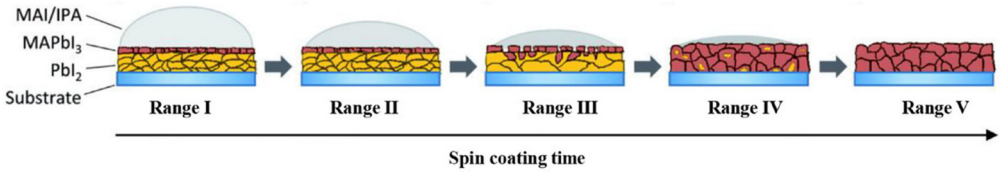

Figure 2.32 | Scheme of the reaction mechanism of the two-step method [174].

Despite the superiority of fabrication reproducibility compared to one-step method, the two-step method does not automatically solve the interfacial issues in PePVs. Till now, the interfacial issues have imposed a significant problem for PePV device structure, particularly for quasi-2D PePVs with enlarged band gaps [180–183]. Considering the complexity of carrier dynamics inside PePVs (Figure 2.33 [184]), interfacial energy level mismatching between the MHPs and the charge transporting layers can

hinder charge extraction and cause severe interfacial recombination, resulting in deduction of PCEs of PePVs. Additionally, the quality of the interface, such as the interfacial defect density, is critical for the PCEs and long-term operational lifetime of PeLEDs [185, 186].

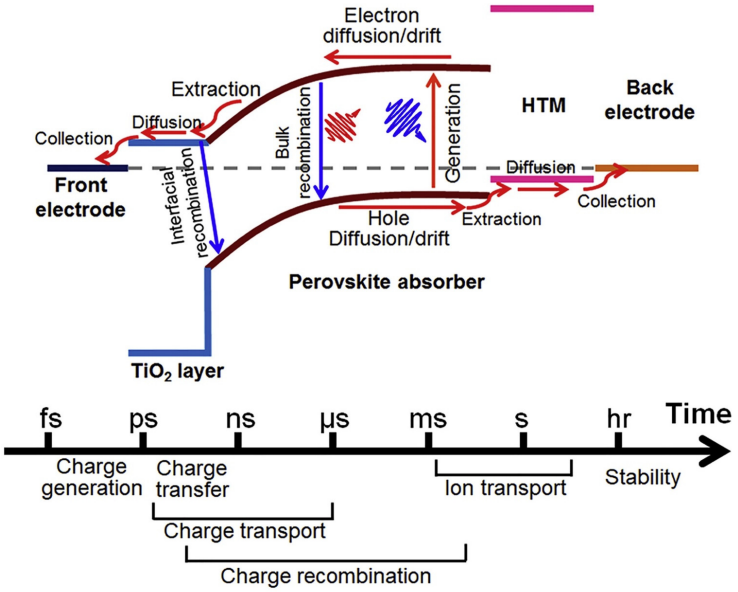

Figure 2.33 | Carrier dynamics processes and corresponding timescale inside PePVs [184].

Therefore, to improve the performance of quasi-2D PePVs, modification of the interface is necessary. The most convenient method for interfacial energy level matching is to optimize the interface materials themselves, with a large selection of both electron transporting materials (ETMs) and hole transporting materials (HTMs) listed in Figure 2.34 [187]. Additionally, the buried interface between the perovskite and the charge transporting layers

on the bottom side strongly determines the nucleation and growth process of MHPs, becoming eminently critical for optimal perovskite growth and high film quality [18, 188–190]. Through a simple lift-off process, researchers can directly observe the film quality difference of the surface and the buried interface (Figure 2.35 [191]).

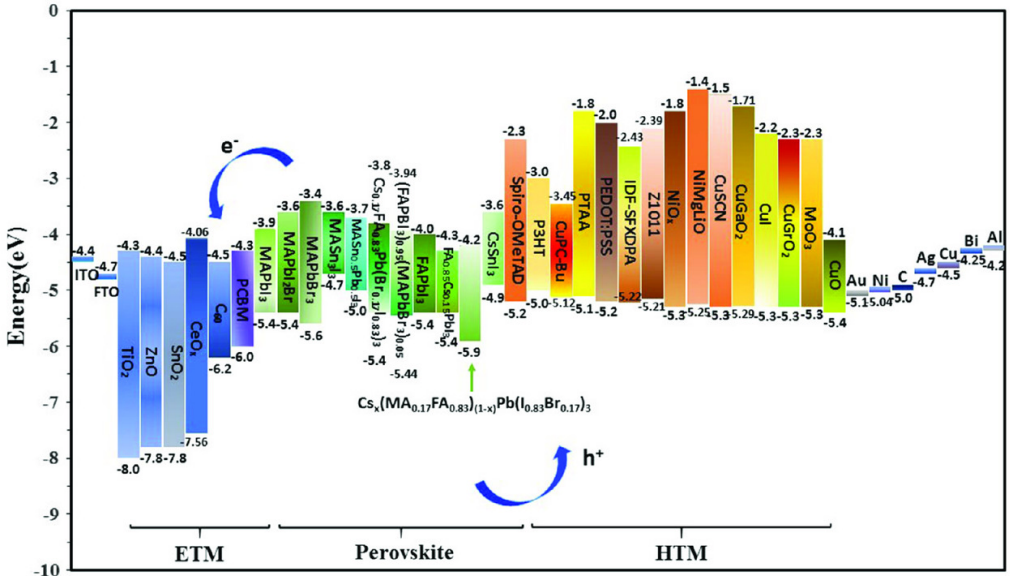

Figure 2.34 | The energy level diagram of widely employed materials in PePVs [187].

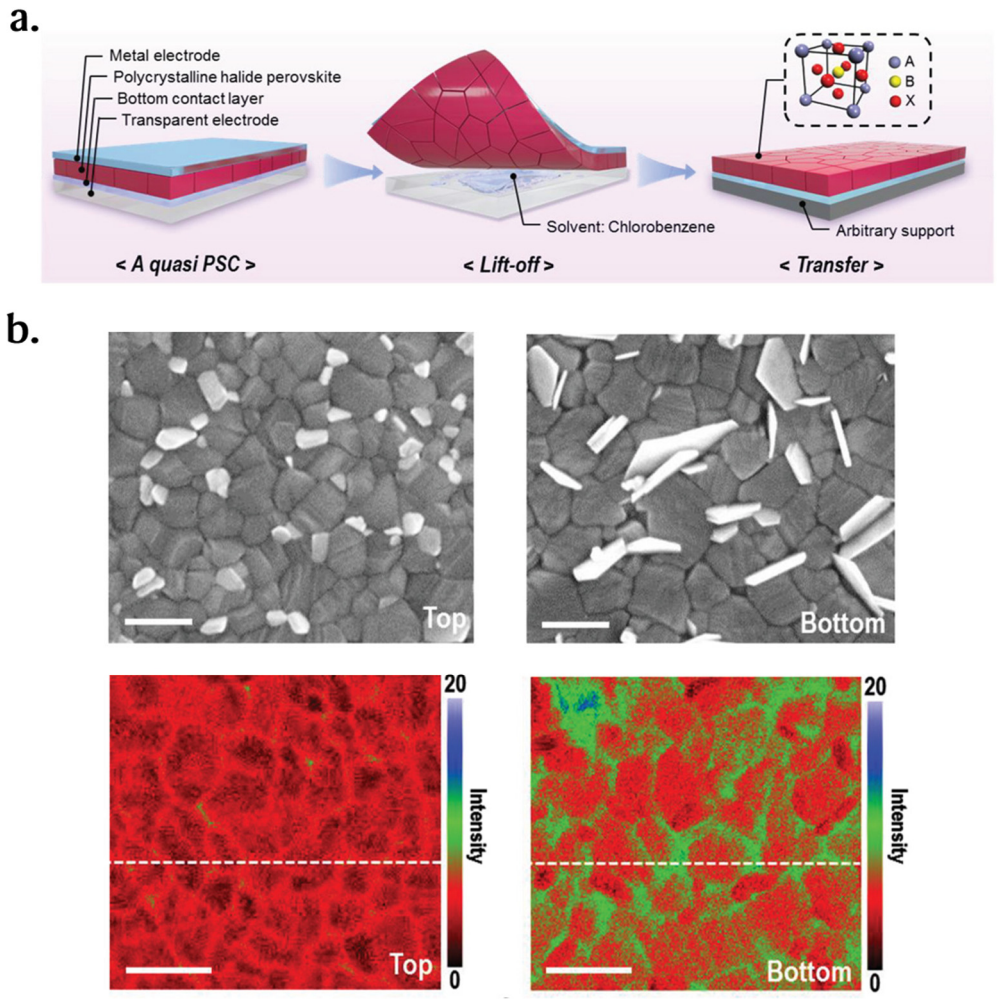

Figure 2.35 | (a) The lift-off process for direct characterization of the buried interface for PePVs. (b) Difference in film quality of top surface and buried interface [191].

Therefore, improving interfaces can significantly enhance the performance of PePVs and contribute to the industrialization of perovskite photovoltaic panels, and an ammonium thiocyanate based interfacial modification method have been introduced to spontaneously passivate interfacial defects and improve perovskite film quality, and introduced detailed in Chapter 7.

2.4 Basic fabrication techniques of PeLEDs and PePVs

For MHP based optoelectronic devices including PeLEDs and PePVs, the fabrication process generally includes solution process, where solution form precursors are made into thin film with spin-coating, and thermal evaporation.

The spin-coating process is illustrated as Figure 2.36a. Spin-coating, a thin film formation technique that has been widely utilized for decades, represents depositing a small volume of the coating material precursor onto the central region of a substrate, followed by spinning it with a precisely controlled high-speed rotation. During this procedure, the substrate revolves about an axis perpendicular to the plane of the coating zone. The coating materials are radially dispersed and eventually overflows the edge of the substrate, resulting in the formation of a uniform thin film coating on the substrate surface, as Figure 2.36b shows [192].

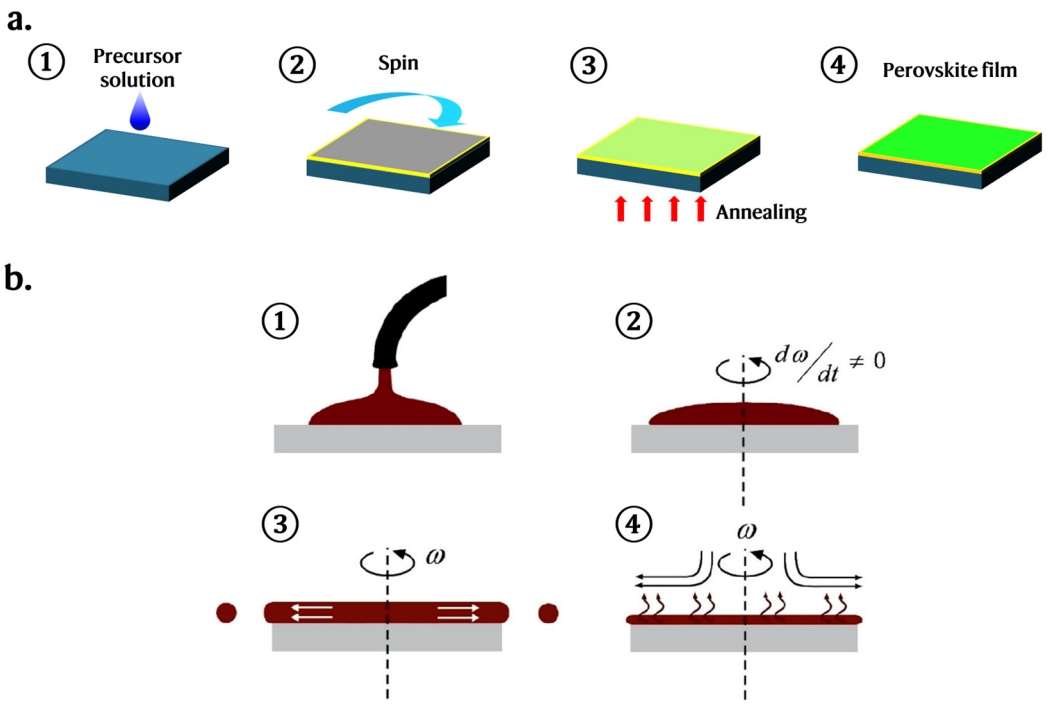

Figure 2.36 | (a) Fabrication process of MHPs via spin-coating process. (b) Four stages of the spin-coating process [192].

The film deposited by spin-coating method can be simply tuned via parameters control. Generally, the final thickness and other attributes of spin-coated film are determined by complex interactions between the physicochemical properties of the coating material precursor itself, including viscosity, drying kinetics, solid content ratio, surface tension, and other factors, as well as the operational parameters during the spin coating process, particularly the rotation velocity and acceleration rate. The fine tuning of these parameters allows for precise control over the film's characteristics and performance.

As mentioned, numerous factors have significant influence on the spin coating deposition process. Some parameters such as spin velocity, acceleration rate, dwell time, or vacuum-assisted solvent removal process have played critical roles on the final film quality. However, due to the broad variability of precursor materials and the heterogeneous nature of substrates, no universally standardized protocols have been established for the spin coating procedure beyond some fundamental guidelines [193]. However, some basic defects formed during the spin-coating process should be prohibited via systematic control and regulation of precursor optimization and spin-coating parameters, as listed in Figure 2.37 [193].

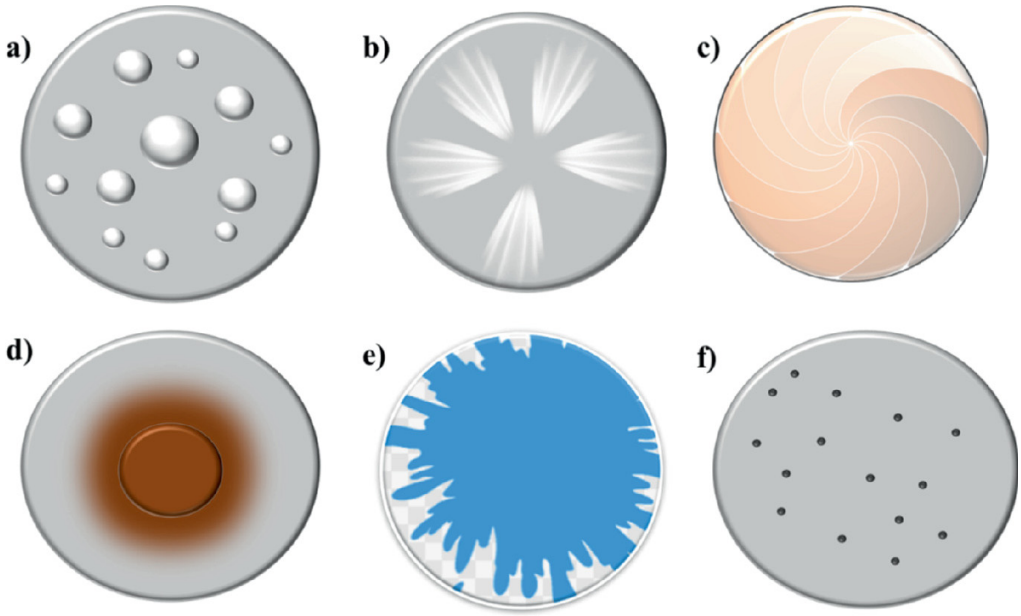

Figure 2.37 | The defects formed during the spin coating process: (a) Air bubble. (b) Comets. (c) Swirl pattern. (d) Coffee ring. (e) Non-deposited area. (f) Pin holes [193].

Meanwhile, some other solution fabrication processes are also applied for MHP based optoelectronic devices including PeLEDs and PePVs: blade-coating, slot-die coating, and spray coating of MHP materials, as presented in Figure 2.38 [192]. All the fabrication methodologies are usually employed to fabricate large area MHP films with high uniformity and have opened a gate for the mass production and industrialization of MHP based optoelectronic devices.

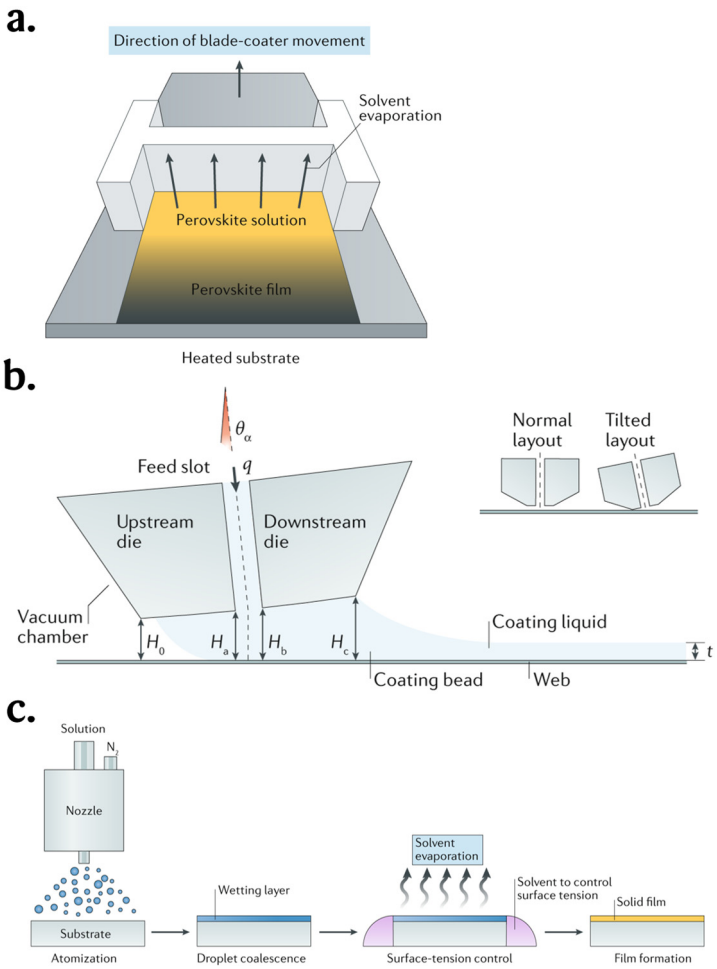

Figure 2.38 | Solution fabrication processes of MHPs: (a) Blade-coating and (b) Slot-die coating process. (c) Spray coating [192].

Thermal evaporation (TE), an early established and extensively employed thin film deposition technology, is a physicochemical process wherein source materials are heated, vaporized, and subsequently condensed onto substrates within a high vacuum environment, as Figure 2.39 presents [194]. This method has gained profound applications across the semiconductor industry, successfully employed in commercial products, such as OLEDs and thin-film photovoltaic devices [195]. Therefore, thermal evaporation has become a compelling option for large scale and high-throughput industrial manufacturing due to its maturity [196].

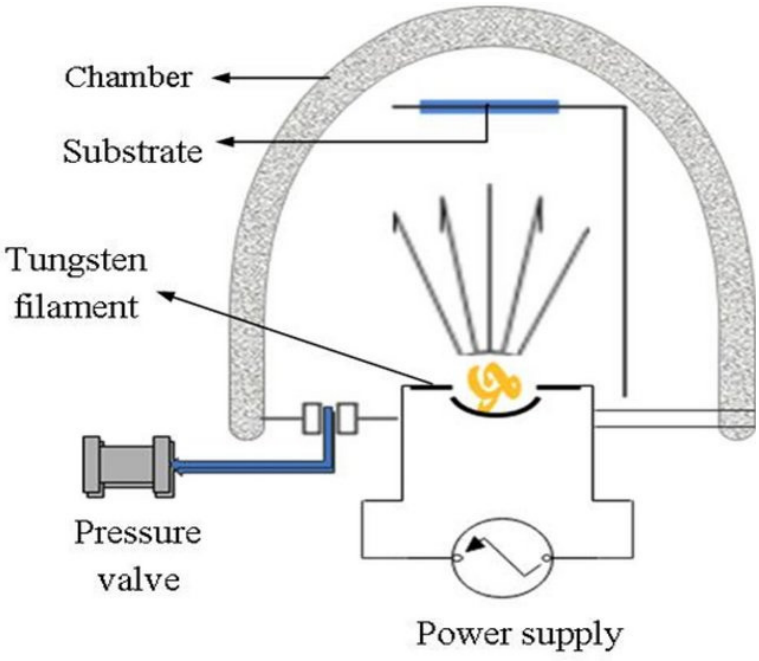

Figure 2.39 | Scheme of a representative thermal evaporation method process [194].

In this thesis, thermal evaporation has been applied for the deposition process of conventional organic carrier transporting layers and metal electrodes. Meanwhile, thermal evaporation fabrication process has been widely employed for MHP materials to date [197], with multiple strategies from multi-step deposition to one-step single source evaporation, as illustrated in Figure 2.40 [198].

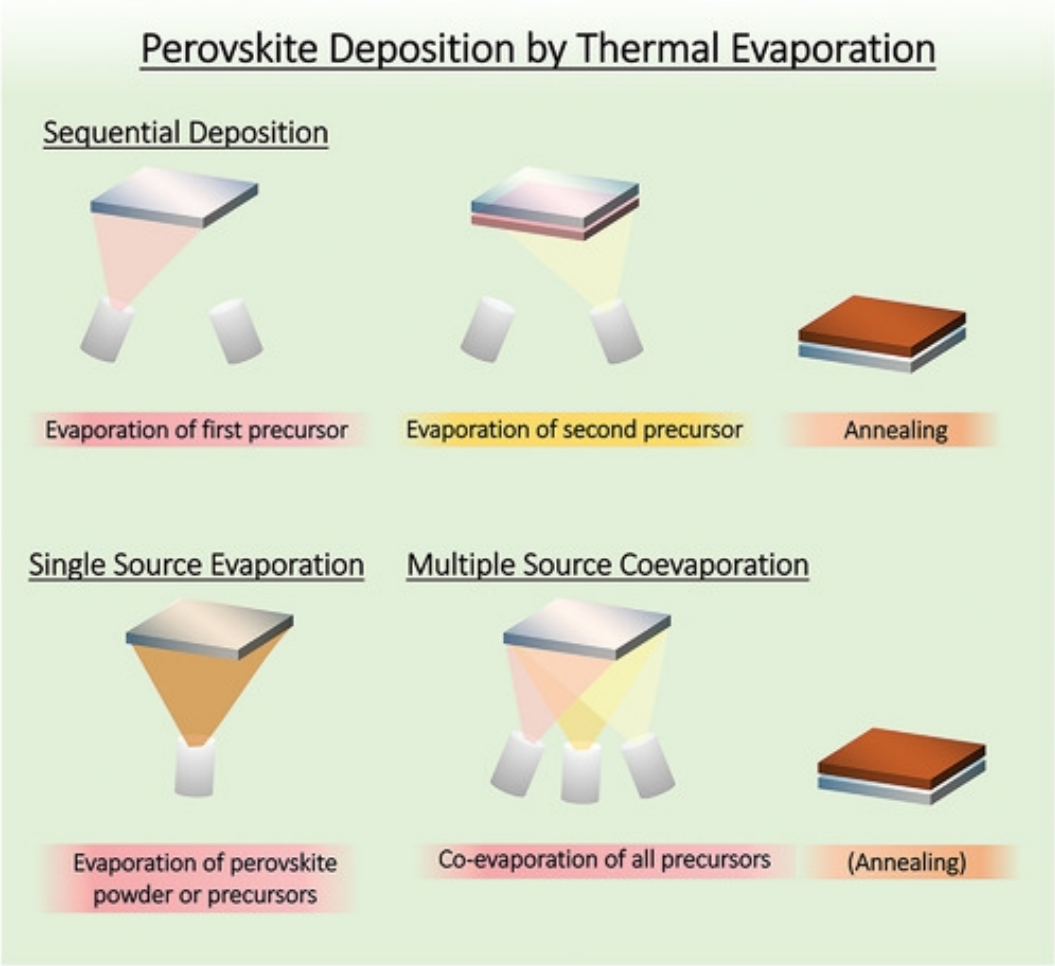

Figure 2.40 | Thermal evaporation of MHP materials [198].

2.5 Summary

In this chapter, a thorough literature review on fundamental properties of perovskite materials and their key structure have been performed. Subsequently, an in-depth summary of principal challenges for both PeLEDs and PePVs has been introduced. For PeLEDs, phase dimensions control, defects management, and ion migration suppression have become eminent issues, whereas the interface engineering plays a crucial role in improving the performance of PePVs. To overcome these challenges, extensive investigations into the underlying mechanisms and effective solutions accordingly should be undertaken, as presented in the following Chapter 4 to 7. Furthermore, basic fabrication techniques of PeLEDs and PePVs such as solution process and thermal evaporation are also introduced.

Chapter 3. Methodology

3.1 Materials

In this thesis, perovskite materials are synthesized via the solution state reactions in polar solvent such as dimethyl sulfoxide (DMSO) or N-methyl pyrrolidone (NMP), and the major reaction during the Pb-based perovskite formation is:

$$AX + PbX_2 \rightarrow APbX_3 \quad 3.1$$

Wherein A represents A-site cations, and X represents halides.

Specifically, for PeLEDs, lead bromide ($PbBr_2$, 99.999%), caesium bromide (CsBr, 99.999%), caesium iodide (CsI, 99.99%), polyvinyl pyrrolidone (PVP, average molecular weight 40,000), N, N-dimethylformamide (DMF, 99.8%) and ethanolamine (99.5%) are purchased from Sigma. Formamidine hydrobromide (FABr, 99%), phenethyl ammonium bromide (PEABr, 99%), methylammonium chloride (MACl, 99%), 2',2'-(1,3,5-benzinetriyl)-trwas(1-phenyl-1-H-benzimidazole) (TPBi, 99%), lithium fluoride (LiF, 99.9%), PEDOT:PSS (Clevious PVP AI 4083), [6,6]-phenyl-C61-butyric acid methyl ester (PCBM), and phenyl butylammonium iodide (PBAI, 99%) are purchased from Xi'an Polymer Light. Lead iodide (PbI_2, ≥ 99.999%), 1-naphthylmethylammonium iodide (NMAI), chlorobenzene (CB, 99.8%), hypophosphorous acid (H_3PO_2, 50% in H_2O), formamidine hydrochloride (FACl, 96%), D-glucose (D-Glc, 99%), and potassium trifluoromethanesulfonate (CF_3SO_3K, 98%) are purchased from Macklin.

Nickel acetate tetrahydrate (99.9%) is purchased from Acros. Hexylamine (HA, 99%) is purchased from TCI. Saccharin (Sacc, 98%), cyclamate sodium (Cyc Na, 99%), NMP (99.9%), phenethylamine (98%), nitrobenzene (NB, 99.5%), hydrobromic acid (HBr, 48 weight% in H_2O, 99.99% metals basis) and lead oxide (PbO, Aladdin, 99%) are purchased from Aladdin. Ethanol (99.5%) is purchased from Meryer. PTAA is purchased from Hangzhou LinkZill Technology Co., Ltd. 2,4,6-Tris(3'-(pyridin-3-yl)biphenyl-3-yl)-1,3,5-triazine (TmPPPyTz) and 2-(4-(9,10-di(naphthalen-2-yl) anthracen-2-yl)phenyl)-1-phenyl-1H-benzo[d]imidazole (ADN-PBIP or ZADN) are purchased from Lumtec. All chemicals are used as received without purification.

For PePVs, SnO_2 colloid (tin oxide (IV), 15% in H_2O colloidal dispersion) is purchased from Alfa Aesar. FK209 Co(III) TFSI salt and spiro-OMeTAD are sourced from Xi'an Polymer Light Technology Corp. Bis(trifluoromethane)sulfonimide lithium salt (Li-TFSI), 4-tert-butylpyridine (tBP), isopropanol (IPA) and acetonitrile are obtained from Sigma-Aldrich.

3.2 Preparation of perovskite precursor

For PeLEDs, the organometal green perovskite precursor solution is prepared by dissolving PEABr, FABr, and $PbBr_2$ (0.5 mmol/mL) and MACl, with a molar ratio of 2:3:4:0.1 in NMP. 3 mg/ml CF_3SO_3K is added as solid in the solution. For saccharin perovskites, 10 mg/ml Sacc is added as solid together

with other solids. Then, the solution is stirred overnight and filtered with a 0.22 μm PTFE filter before use. The inorganic green perovskite precursor solution is prepared by dissolving CsBr, $PbBr_2$ (0.3 mmol/mL), PEABr, and MACl, with a molar ratio of 1.2:1:0.4:0.05 in DMSO. 2 mg/ml PVP is added in the solution. For saccharin perovskites, 5 mg/ml Sacc is added as solid together with other contents. Then, the solution is stirred at 60 °C for 2 hours to ensure that all the contents are fully dissolved and filtered with a 0.22 μm PTFE filter before use. The inorganic pure red perovskite precursor solution is prepared by dissolving CsI, PBAI, NMAI, and PbI_2 with the molar ratios of 1.2:1:1:2 in DMF with Pb^{2+} molar concentration of 0.1 M, respectively. For saccharin-added solution, 10 mg/mL saccharin is added with the same contents in the precursor solution. The solutions are stirred at room temperature before use.

3.3 Device fabrication

For organometal green PeLEDs (Chapter 4, Chapter 5, and Chapter 6), pre-patterned fluorine doped tin oxide (FTO) glass substrates (HT14, 14 Ω/sq., Liaoning Advanced Election Technology Co., Ltd) are cleaned using ultrasonication in deionized water, acetone, and isopropanol for 15 min, respectively. The substrates are dried with nitrogen flow, followed by ultraviolet ozone treatment for 15 minutes. Nickel oxide (NiOx) is fabricated by spin-coating precursor (made by dissolving nickel acetate tetrahydrate

(24.886 mg/mL), ethanolamine (6.108 µL/mL) in ethanol and stirred at 65 °C for 2 h) onto the FTO-coated glass substrates at 6,000 revolutions per minute (rpm) and annealing at 500 °C for one hour. PVP is then spin-coated from solution (2 mg/mL in DMF) at 8,000 rpm and is annealed at 120 °C for 10 min. Subsequently, the substrates are transferred to a nitrogen-filled glovebox, and the perovskite film is spin-coated from the precursor at 4,000 rpm for 180 s at a controlled temperature of 16±1 °C and annealed at 90 °C for 10 min. During the spin-coating of perovskite film, 200 µL of CB is gently dropped as anti-solvent in 1 s after 45 s of spinning with 200 µL pipette. Then, 100 µL of HA dissolved in CB (2% by volume) is dripped onto the perovskite film for 2 s, spin-coated at 10,000 rpm for 60 s to remove extra solvent sieve, and then annealed at 90 °C for 10 min to remove all the residual solvent. Finally, the substrates are transferred into a vacuum chamber and TmPPPyTz (0.1 Å/s, 5 nm), ADN-PBIP (0.3 Å/s, 40 nm), LiF (0.05 Å/s, 1 nm), Al (1 Å/s, 80 nm) and Ag (0.2 Å/s, 20 nm) are sequentially evaporated through a shadow mask. The effective area is 0.04 cm^2, defined by the overlapping area of FTO and metal electrodes.

For inorganic green PeLEDs (Chapter 5), NiOx and PVP layer are fabricated on pre-cleaned patterned FTO glass substrates (HT14, 14 Ω/sq., Liaoning Advanced Election Technology Co., Ltd). Nickel oxide (NiO_x) is fabricated by spin-coating precursor (made by dissolving nickel acetate tetrahydrate

(24.886 mg/mL), ethanolamine (6.108 μL/mL) in ethanol and stirred at 65 °C for 2 h) onto the FTO-coated glass substrates at 6,000 rpm and annealing at 500 °C for one hour. PVP is then spin-coated from solution (2 mg/mL in DMF) at 8,000 rpm and is annealed at 120 °C for 10 min. Subsequently, the substrates are transferred to a nitrogen-filled glovebox, and the perovskite film is spin-coated from the precursor at 3500 rpm for 90 s at a controlled temperature of 20±1 °C and annealed at 90 °C for 10 min. Then, the substrates are transferred into a vacuum chamber and TPBi (0.3 Å/s, 40 nm), LiF (0.05 Å/s, 1 nm), Al (1 Å/s, 80 nm) and Ag (0.2 Å/s, 20 nm) are sequentially evaporated through a shadow mask. The effective area is 0.04 cm^2, defined by the overlapping area of FTO and metal electrodes.

For inorganic pure red PeLED (Chapter 5), indium tin oxide (ITO) coated glass substrates (15 Ω/sq., Liaoning Advanced Election Technology Co., Ltd) are cleaned by deionized water, acetone, and alcohol under the ultrasonic bath in sequence. After they are dried, ITO substrates are treated with O_2 plasma for 15 min before spin-coating HILs. PEDOT: PSS is spin-coated on ITO substrates at 4,000 rpm for 40 s and then baked at 150 °C for 15 min. Then PTAA (5 mg/mL) is spin-coated at 10,000 rpm for 30 s and annealing at 125 °C for 15 min. After this, perovskite films are prepared by spin-coating the precursor solution onto the HTLs at 4,000 rpm for 60 s in the N_2 glovebox, followed by annealing at 80 °C for 15 min. Finally, the substrates are

transferred into a nitrogen glovebox, TPBi (40 nm), LiF (1 nm), and Al electrode (100 nm) is deposited in a thermal evaporation system. The effective area is 0.04 cm^2.

For PePVs (Chapter 7), the ITO glass substrates are sonicated in ITO cleaner, with deionized water, acetone, and IPA for 15 minutes each to ensure thorough cleaning. Prior to usage, the ITO glass substrate undergoes a 15-minute treatment with a UV ozone device. The SnO_2 solution (2.67%, diluted with deionized water) is spin-coated onto the ITO glass substrate at 4,000 rpm for 30 seconds, followed by annealing at 150 °C for 30 minutes in ambient air. Afterwards, the substrate undergoes a 10-minute UV ozone cleaning process to enhance surface wettability with UV-ozone cleaner BZS250GF-TC. For comparison, NH_4SCN solution (0.05-0.2 mg in 1 ml H_2O) is spin-coated onto SnO_2 at 5,000 rpm for 30 seconds and subsequently thermally annealed at 100 °C for 10 minutes under ambient air conditions. Afterwards, a 1.3 M PbI2 solution in DMF: DMSO (9:1) solvent is spin-coated onto SnO_2 at 1,000 rpm. for 30 seconds, then annealed at 70 °C for 1 minute and cooled to room temperature. For perovskite film deposition, FAI: MAI: MACl: PEAI (78 mg:5.54 mg:7.8 mg:2 mg in 1 ml IPA) solution is spin-coated onto PbI_2 at a spin rate of 1500 rpm for 30 s and then thermally annealed at 150 °C for 15 min under ambient air conditions (30-40% humidity). For comparison, 3mg/ml NH_4SCN is added into perovskite precursor as additive

[199]. Following perovskite formation, the samples are transferred to a glove box filled with nitrogen for subsequent processing. A solution of spiro-OMeTAD is deposited onto the perovskite layer with a spin rate of 3,000 rpm for 30 seconds. The solution consists of 72.3 mg spiro-OMeTAD, 35 µL lithium LiTFSI stock solution (260 mg LiTFSI in1ml acetonitrile), 10µl FK209 (tris(2-(1H-pyrazol-1-yl)-4-tert-butylpyridine)-cobalt(III) tris(bis(trifluoromethylsulfonyl) solution (300 mg FK209 in 1 ml acetonitrile), 30 µL 4-tert-butylpyridine, and 1 ml chlorobenzene. An 80 nm-thick Au film is thermally evaporated, employing a shadow mask to serve as the counter electrode.

In summary, the fabricated PeLEDs and PePVs are devices with multi-layer thin films. The representative PeLEDs and PePVs structures are shown as Figure 3.1a and Figure 3.1b, respectively. Both devices exhibit similar thin film stacking structure, with main differences of materials selection for charge transporting layers and notable MHP layer thickness. PeLEDs usually have a MHP thickness of no more than 100 nm for efficient light outcoupling [7], while the MHP thickness for PePVs typically exceeds several hundred nanometres to ensure light absorption and utilization.

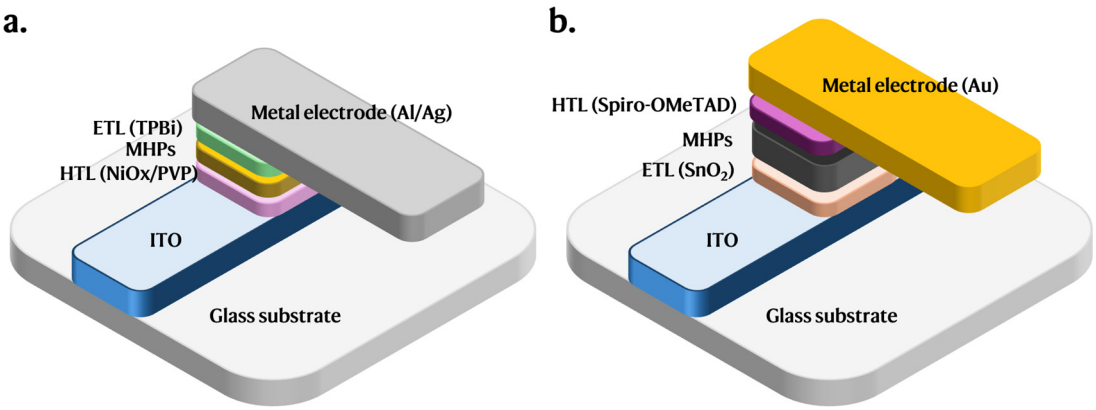

Figure 3.1 | Representative device structures of (a) PeLEDs and (b) PePVs.

3.4 Monocrystal synthesis

The monocrystals are synthesized following the previous reported method [200]. PbO (2 mol/l), FACl and phenethylamine is mixed in the stoichiometry of 1:0:2 (n=1) or 2:1:2 (n=2) in a mixture of hydrobromic acid (HBr, 48 weight% in H_2O) and hypophosphorous acid (H_3PO_2, 50% in H_2O). The solution is heated to a temperature of 220 ℃ under continuous stirring until all the precursors are dissolved, and the solution starts to boil. Then, the solution is left cooling down to room temperature and the monocrystals start to crystallize. The monocrystal powders are then collected and washed with CB. The quality and phase purity of the synthesized powders are verified by x-ray diffraction at the wavelength of λ=1.54189 Å, step size of 0.1 degree, and 2-theta range from 5 to 30 degree.

3.5 Characterization

For PeLEDs, the sheet resistivity is measured with 4D Model 280 DI four-point

probe. The absorption spectra are measured with the PerkinElmer LAMBDA 1050+ UV/Vis/NIR Spectrophotometer. Grazing incidence wide angle X-ray scattering (GIWAXS) experiments are performed using a Xenocs Xeuss 3.0 laboratory beamline at the Vacuum Interconnected Nanotech Workstation (Nano-X) of Suzhou Institute of Nano-Tech and Nano-Bionics, Chinese Academy of Sciences. An X-ray wavelength of λ=1.54189 Å and a beam size of (0.9×0.9) mm^2 is employed for the measurements. The scattered intensities are collected using a Dectris EIGER2 R 1M detector at a sample to detector distance of 100 mm, with an incident angle of 0.2 degree. PL and PLQY is measured by Hamamatsu C9920-2 absolute PL quantum yield spectrometer. Transient PL is measured by Hitachi F-4600 fluorescence spectrophotometer with a total activation energy of 1 pJ. X-ray photoelectron spectroscopy (XPS) spectra are acquired with Kratos AXIS ULTRA X-ray photoelectron spectrometer. Transient absorption spectroscopy (TAS) results are acquired on a Helios setup, where a nondegenerate pump–probe configuration is applied to probe the transient dynamics (50 fs to 7 ns). Additionally, the pump and probe laser pulses are generated by frequency doubling the fundamental output (Coherent Vitesse, 80 MHz, Ti-sapphire laser) and white light is generated with a sapphire plate, respectively. The pump wavelength is 360 nm. Fourier transform infrared spectra (FTIR) is performed with Thermal Fisher IS50 Fourier transform infrared spectrometer. In-situ UV-Vis absorption is conducted with Ocean Optics QE Pro spectrometer, deuterium

tungsten halogen light source and optical fibres during spin-coating. The integration time of the spectrometer is 0.2 s. Solubility is measured by a dynamic method, where powders are added into continuous stirred solvents under water bath of 16 °C. The refractive index of our perovskite is obtained from the ellipsometry measurement with M-2000DI ellipsometer, J. A. Woollam Inc.

The electroluminescence performance of devices is measured with a photodiode-based setup [201]. Electroluminescence spectra are obtained using an Ocean Optics USB 2000+ spectrometer with the devices driven at a constant current with a Keithley 2400 source meter. The *J-V-L* characteristics of the devices are taken under ambient conditions with a Keithley 2400 source meter measuring the sweeping voltages and currents and a Keithley 6485 Picoammeter together with a calibrated silicon detector (Edmund) measuring light intensities. Luminance is calibrated using a photometer (Spectra Scan PR655) with the assumption of Lambertian emission pattern of all devices. The EQEs are cross-checked with an integrating sphere (IS, XP-EQE-Adv, Guangzhou Xipu Optoelectronics), which calibrated with a standard light source HL-3P-INT-CAL, Ocean Insight Inc. (serial number: 7003P2143). Angular dependent electroluminescence (EL) intensity is measured with our EQE setup and a swivel bracket on the optical platform, and the device is operated under a fixed bias of 3.6 V. The operational lifetime

test is conducted under ambient conditions at room temperature (20±2 °C) using a commercialized lifetime test system (Guangzhou Jinghe Equipment Co., Ltd). The devices are encapsulated with Nagase UV epoxy resin XNR5516Z(C)-SA1 and capping glasses.

For PePVs, the SEM images are acquired using a field-emission SEM Verios G4 UC with an accelerating voltage of 3 kV. AFM images are obtained using a Dimension ICON 8 in tapping mode. The XRD patterns are characterized on a German Brooke polycrystalline X-ray diffractometer using a Cu K_{α}. The time-of-flight secondary ion mass spectrometry (TOF-SIMS) is performed by TOF.SIMS5-100 at the Vacuum Interconnected Nanotech Workstation (Nano-X) of Suzhou Institute of Nano-Tech and Nano-Bionics, Chinese Academy of Sciences. Steady-state photoluminescence (PL) measurements are conducted using an integrated confocal microscopy system (FL3-111) with laser excitation at a wavelength of 450 nm and a fluence of approximately 0.1 μJ/cm^2. The *J*–*V* curves are characterized under simulated air mass (AM) 1.5G illumination using a solar simulator (Enlitech SS-F5-3A, 100 mW/cm^2) and a Keithley 2400 source meter. The solar cells are measured under reverse scan (+1.5 V to −0.1 V) and forward scan (−0.1 V to +1.5 V) with a step size of 0.02 V and a delay time of 100 ms. The EQE is measured using an integrated system from Enlitech (QE-R3011). The capacitance of devices is measured under dark conditions. The maximum power point (MPP) tracking tests of different

devices are performed on the setup of CRYSCO P3000 in the ambient atmosphere at 25°C and 65°C, where devices are encapsulated with YK003 UV seal glue and capping glass.

3.6 Simulation

To evaluate the interactions between different molecules and perovskite materials, *Ab initio* simulation is performed with Cambridge Sequential Total Energy Package (CASTEP, version 20.1.1) [202]. All the geometry optimization processes are conducted with generalized gradient approximation (GGA) type Perdew Burke Ernzerhof (PBE) exchange-correlation functional [203] with Koelling-Harmon relativistic treatment, and on the fly generated (OTFG) ultrasoft pseudopotential is applied for better accuracy and consistency. Also, the plane wave basis cut-off energy is set at 680 eV, and the self-consistent convergence total energy is chosen to be as 5×10^{-7} eV/atom where maximum force, maximum displacement and maximum stress are set to be as 0.01 eV/Å, 5×10^{-4} Å and 0.02 GPa respectively unless specified. 5×5×5 Monkhorst-Pack k-point grids are applied for perovskite lattice and molecules geometry optimization, while 2×2×4 superlattice surface models with 30 Å vacuum slab are further geometrically optimized by 3×3×1 k-point sampling. The formation energy is defined be the formula of

$$E_{Formation} = |E_{Perovskites\ with\ molecule} - (E_{Molecule} + E_{Perovskite})| \qquad 3.2$$

All the atomic structures are visualized with Visualization for Electronic and

Structural Analysis software (VESTA, version 3.5.8) [204].

For optical simulation, the outcoupling efficiency are obtained from the calculated Poynting vectors at each interface of our PeLED structure of glass (n=1.45, incoherent)/FTO (n=1.96, 360 nm)/NiOx (n=1.89, 20 nm)/PVP (n=1.53, 3 nm)/perovskite/TmPPPyTz (n=1.9, 5 nm)/AND-PBIP (n=1.9, 40 nm)/LiF (n=1.39, 1 nm)/Al (n from literature [205], 120 nm), using a recently proposed method [206, 207]. This method has considered the photon recycling effect of perovskite film, wherein the photons absorbed by perovskite film can be re-emitted due to the high PLQY of MHP materials. Therefore, the maximum outcoupling efficiency with photon recycling effect are obtained at each perovskite thickness by integrating the results for dipoles with different wavelengths, orientations (vertical and horizontal), polarisations (s and p) and positions (10 positions uniformly distributed over the perovskite layer).

Chapter 4. Resolving Phase Dimensions with Solvent Sieve Method

4.1 Introduction

In this chapter, a formamidinium-based organometal quasi-2D perovskite material system and corresponding PeLED devices are investigated. The quasi-2D perovskites are then fabricated by spin-coating the precursors with a composition of phenethylammonium bromide (PEABr), formamidinium bromide (FABr) and lead bromide ($PbBr_2$) in a molar ratio of 2:3:4 [208], with a typical chemical formula of $PEA_2FA_{n-1}Pb_nX_{3n+1}$. Similar as Equation 3.1, the main chemical reaction happened during the film fabrication process is:

$$2PEAX + (n-1)FAX + nPbX_2 \rightarrow PEA_2FA_{n-1}Pb_nX_{3n+1} \quad 4.1$$

Wherein X represents halide and n represents the n value. As illustrated in Chapter 2, the n values of different quantum wells are critical for perovskite properties. Therefore, the stability difference between different n valued phases is firstly investigated.

4.2 Instability of low-n phases inside quasi-2D perovskites

The stability of different n valued phases is firstly compared via the ambient stability test. For quantum wells with smaller n values, the band gaps of quantum wells are enlarged due to their stronger quantum confinement. Therefore, the low n phases have larger band gaps and corresponding blue shifted absorption peaks compared to higher n phases, enabling convenient identification through absorption spectroscopy. Figure 4.1 showed that the absorption peaks of low n phases (such as 400 nm for n=1) disappeared firstly,

indicating that the degradation of quasi-2D perovskites starts from the decomposition of low-n phases. Therefore, the instability of low-n phases inside quasi-2D perovskites is confirmed, which originates from the different crystallization processes and corresponding different structures of low-n phases inside quasi-2D perovskites from the ideal cases.

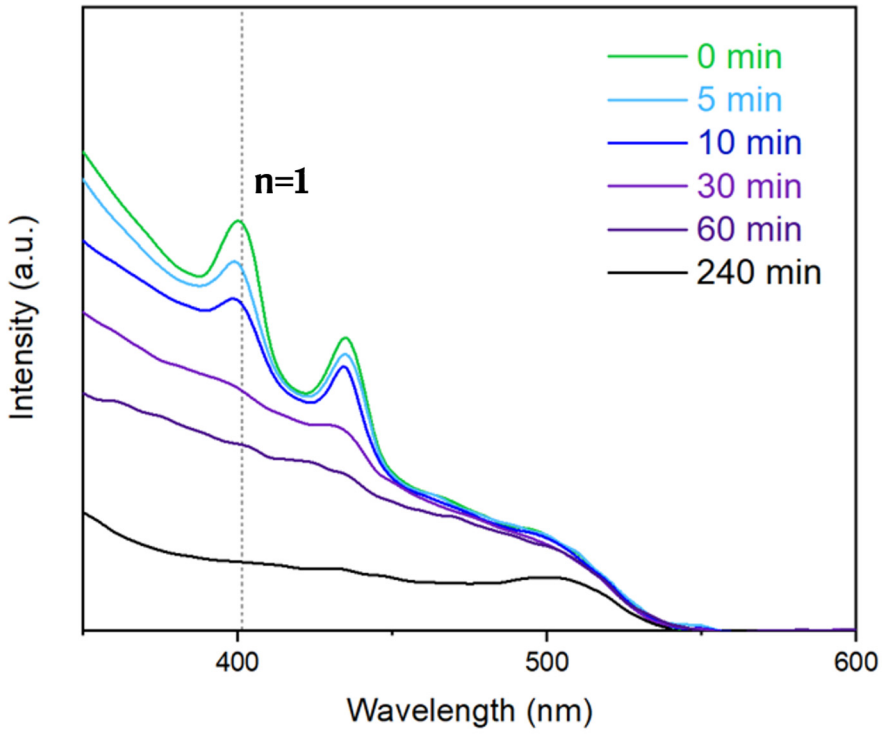

Figure 4.1 | Ambient stability of low n phases inside quasi-2D perovskites.

However, the finding of low n phase instability above doesn't solve the "contradiction" raised in Chapter 2.2.1", wherein our experimental observations seemingly diverge from some theoretical results. Meanwhile, the critical concern of the foundational mechanism dictating the stability

difference between the different n valued phases are still not unveiled. Therefore, more analysis about the phase stability inside and outside the quasi-2D perovskites shall be performed.

First, the differences between low n phases inside quasi-2D perovskites and pure 2D perovskites (n=1 monocrystals with ideal 2D structure [200]) are checked. The key difference between quasi-2D perovskites and n=1 monocrystals is the crystallization processes. With in-situ absorption measurement, the formation process of low n phases in quasi-2D perovskites are tracked. Herein, t=0 s represents the dripping of anti-solvent. As shown in Figure 4.2, low n phases in quasi-2D perovskites formed immediately after anti-solvent dripping (~3 s), and the intensity reached the maximum within 20 s, indicating that most of low n phases formed rapidly and are likely to be low-quality and defective due to limited period for ion diffusion. While for n=1 monocrystals, overnight cooling (cooling rate set to ~0.5 °C/min, >400 min) is required to ensure a much slower crystallization rate and substantial time for ion diffusion to get high-quality 2D n=1 monocrystals. Therefore, the significant difference in the crystallization process between low n phases inside quasi-2D perovskites and 2D perovskites led to a significant difference in the crystal quality, especially in the defect density, where low n phases inside quasi-2D perovskites are much more defective than ideal 2D perovskites due to the rapid crystallization process.

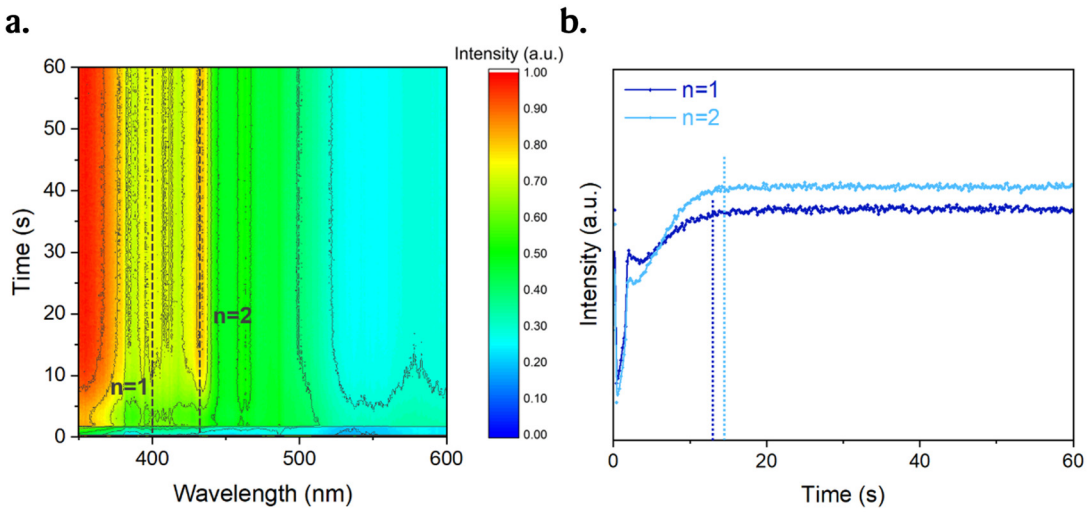

Figure 4.2 | (a) In-situ absorption measurement of quasi-2D perovskite formation during spin-coating. (b) Intensity changes at different wavelengths for divergent phases.

The rapid crystallization process leads to inferior crystal quality with more defects for low n phases inside quasi-2D perovskites, compared with 2D n=1 monocrystals. From the XRD patterns (Figure 4.3), the n=1 monocrystals show very narrow and mono-distributed diffraction patterns, consistent with the ideal crystal structure of n=1 monocrystals. However, for quasi-2D perovskite film, the diffraction peaks for low n phases are highly diffused with irregular side peaks, in good accordance with their inferior crystallinity, significant lattice distortion and high defect density.

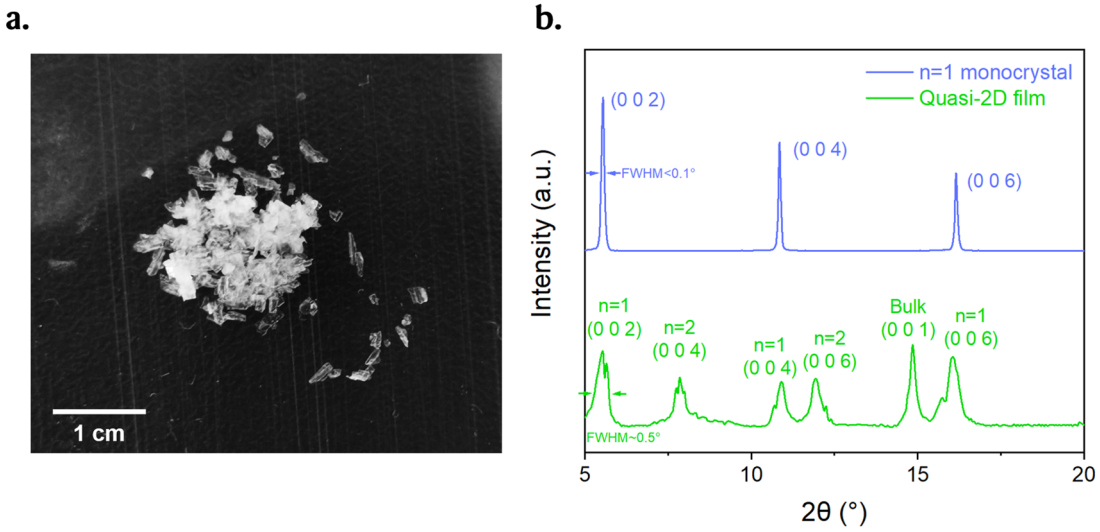

Figure 4.3 | (a) Photograph and (b) X-ray diffraction patterns of synthesized n=1 monocrystals and quasi-2D perovskite films.

Furthermore, a spectroscopic analysing method like transient absorption spectroscopy (TAS) is also employed to compare the defect densities. The kinetics are fitted by a triple-exponential function:

$$\Delta A(t) = A_1 e^{-\frac{t-t_0}{\tau_1}} + A_2 e^{-\frac{t-t_0}{\tau_2}} + A_3 e^{-\frac{t-t_0}{\tau_3}} \quad 4.2$$

where A_1, A_2, and A_3 are amplitudes, t_0 is initial time constant, τ_1, τ_2 and τ_3 are decay time constants. Only the decay processes are fitted, and all the intensities are normalized for direct comparison. Herein, the first order constants A_1 and τ_1 mainly describe the process of trap assisted recombination [209] and are listed in the inset to compare the defect density. Based on the fitting, the A_1 of n=1 phases inside quasi-2D perovskite is much higher than that of 2D n=1 monocrystal, meaning that the exciton decay process in n=1 phases of quasi-2D perovskite is dominated by trap assisted

recombination, Therefore, the low n phases of quasi-2D perovskite are much more defective than 2D n=1 monocrystals.

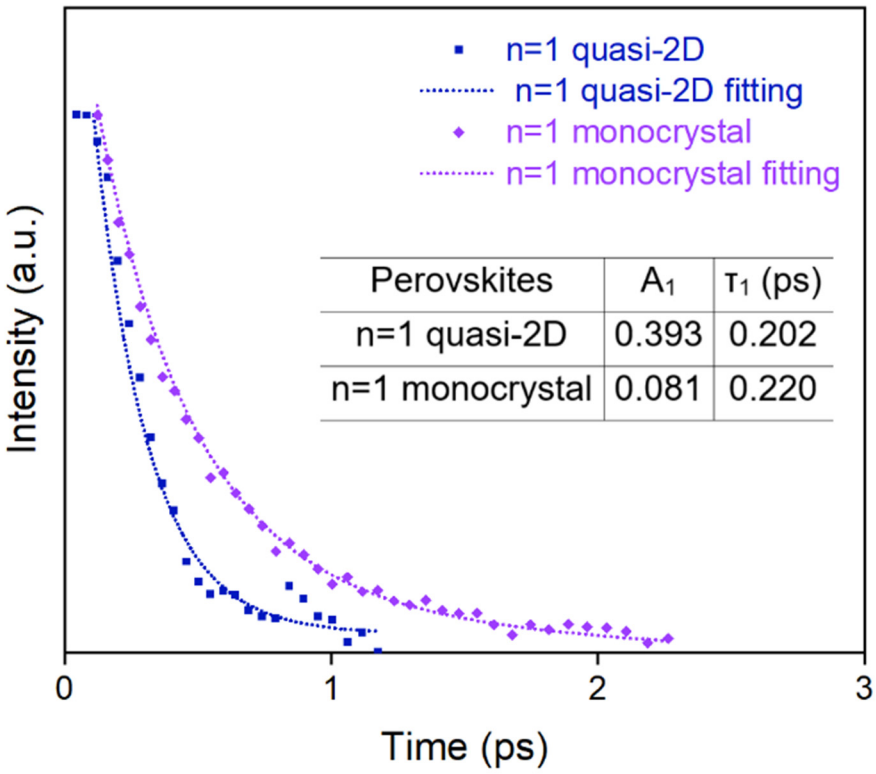

Perovskites	A_1	τ_1 (ps)
n=1 quasi-2D	0.393	0.202
n=1 monocrystal	0.081	0.220

Figure 4.4 | TAS photobleaching features for quasi-2D perovskites and 2D n=1 monocrystals (402 nm) and fitted first-order decay time constants (τ_1) and corresponding amplitudes (A_1) of fitting curves (inset).

The highly defectiveness of low n phases inside quasi-2D perovskites leads to poor stability. The ambient stability of 2D n=1 monocrystals is tracked by measuring the UV-Vis absorption spectra changes during storing both films in the atmosphere (50±10% humidity, 22±2 °C), as shown in Figure 4.5. The 2D n=1 monocrystals are extremely stable during storage period with almost no

changes in absorption spectra during the 240 minutes, presenting much better stability than low n phases in quasi-2D perovskites (Figure 4.1). This indicate that low n phases inside quasi-2D perovskites degrade firstly in the ambient and trigger the full degradation of quasi-2D perovskites, in good accordance with the theory in the literature that the degradation of quasi-2D perovskites starts from the edge of the low n phases [101].

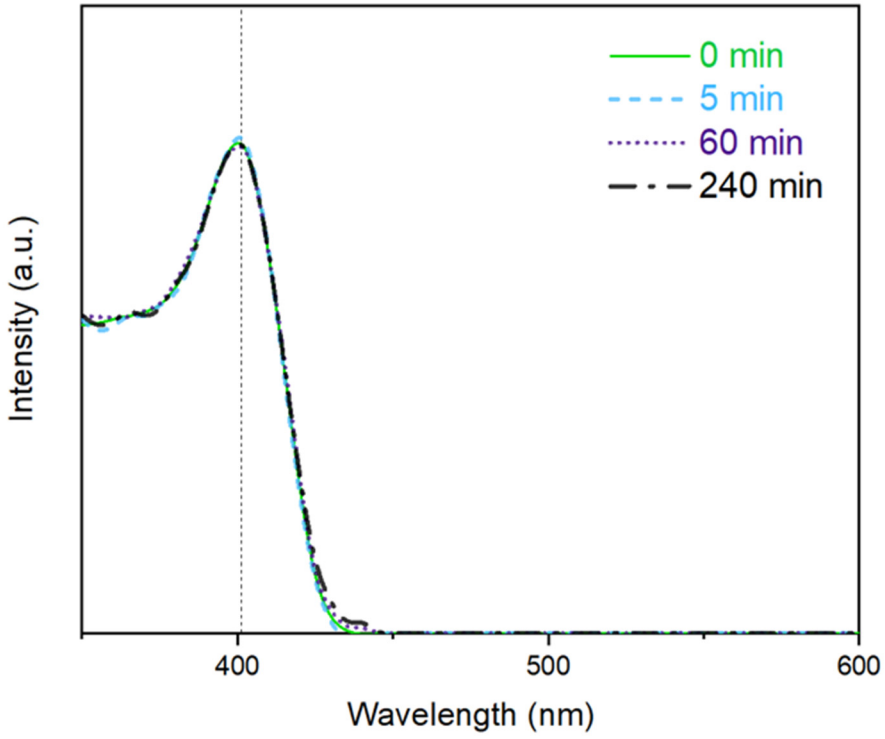

Figure 4.5 | Ambient stability of 2D n=1 monocrystals.

In summary, the observed "contradiction" regarding low n phase stability between the experiment and theoretical results stems from differences in their structural characteristics of low n phases. Theoretical simulations

utilize idealized structures of low n phases, leading to computation results that suggest low n phases possess higher binding energies and consequent stability compared to those higher n counterparts. Conversely, in real quasi-2D perovskite systems, the rapid crystallization process during spin-coating results in highly defective and distorted low n phases, which diverge significantly from the ideal cases. Thereby, the low n phases inside quasi-2D perovskites become the origin of instability and shall be removed thoroughly to improve the perovskite stability.

4.3 High-quantum-yield perovskites by solvent sieve method

To selectively remove those undesirable low-n phases, a novel "solvent sieve" method is developed. The solvent sieve is composed of mixing a polar solvent and nonpolar anti-solvent together, and the treatment is performed by pouring mixed solvent directly onto perovskite films, as shown in Figure 4.6.

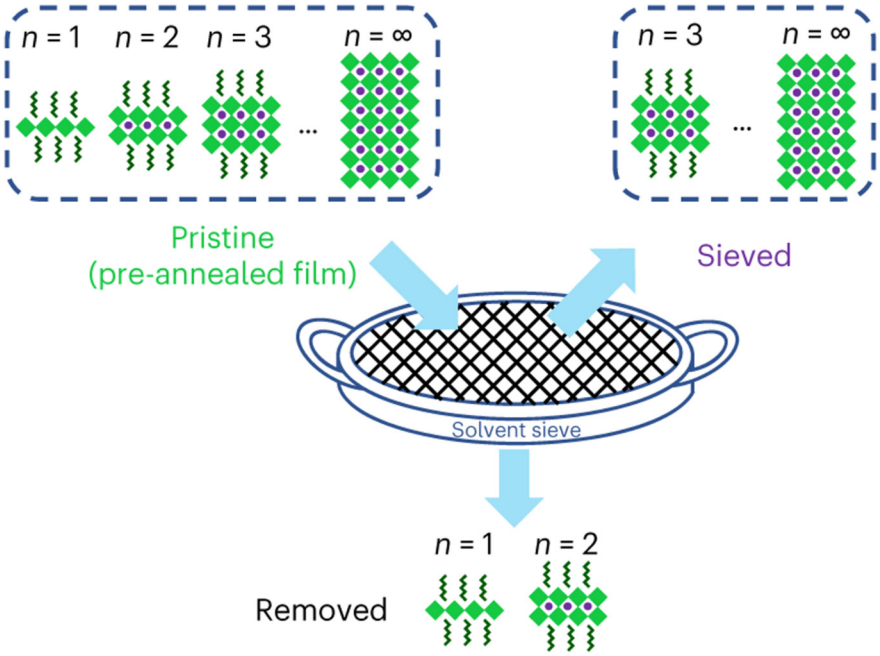

Figure 4.6 | Scheme of solvent sieve method.

Herein the polar solvent serves as the mesh of the solvent sieve, interacting with perovskites, whereas the nonpolar solvent serves as the framework part, without the sieving effect on perovskites. Due to their ionic crystal property, perovskites can be dissolved in some polar solvents but resist nonpolar anti-solvents. A vast range of polar and nonpolar solvent combinations can serve as solvent sieves (some typical combinations and corresponding device EQEs listed in Table 4.1). One of the most efficient solvent sieve systems employed in this study (consists of hexylamine (HA) and chlorobenzene (CB), as Figure 4.7 shows).

Table 4.1 | Some solvent sieves assessed in this study.

Polar content (2% vol)	Nonpolar content	EQE_{max} of fabricated PeLEDs (%)
-	-	12.5
Butylamine	Chlorobenzene	6.1
Amylamine	Chlorobenzene	17.8
Hexylamine	Chlorobenzene	29.5
Heptamine	Chlorobenzene	17.2
Octylamine	Chlorobenzene	9.7
Hydroxy hexylamine	Chlorobenzene	0.3
Hexylamine	Toluene	24.3
Hexylamine	Ethyl acetate	16.9
Hexanoic acid	Chlorobenzene	0.0
Dimethyl sulfoxide	Chlorobenzene	0.0
Hexylamine	Chlorobenzene	17.7 (nanocrystal pinning)

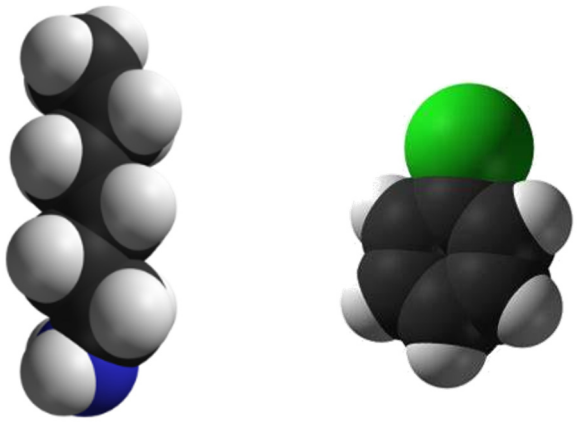

Hexylamine (HA) Chlorobenzene (CB)

Figure 4.7 | Chemical structure of HA and CB. Atoms: H (white), C (black), N (blue), Cl (green).

When the concentration of polar HA content in the solvent sieve increases from 0 to 5%, the thickness of treated film decreases from over 70 nm to approximately 40 nm correspondingly, implying that the solvent sieve has significant dissolving effect on the perovskite film, and part of the perovskite films have been effectively removed, as shown in Figure 4.8.

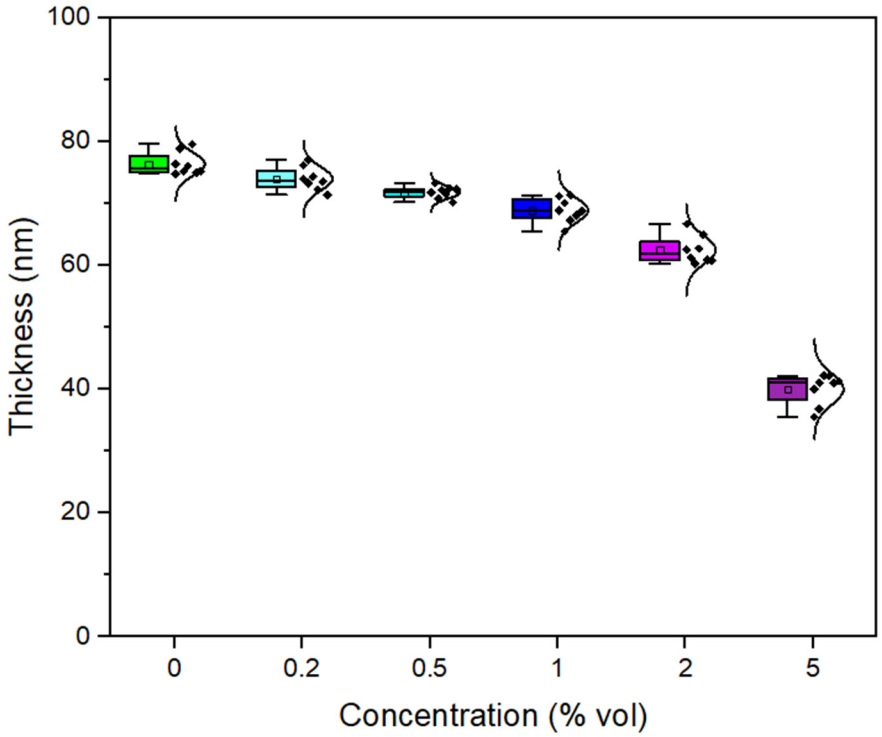

Figure 4.8 | Perovskite film thickness box plots after being sieved with solvent sieve (HA/CB) of different polar solvent concentrations. In the box plots, the black dots represent the data points, and the curves show the distribution trends; the middle bar represents the median, and the box represents the interquartile range; bars extend to 1.5× the interquartile range.

The selectivity of solvent sieves on perovskite phase dimensions is determined by the polar content concentration. The phase selectivity is demonstrated via optical and structural analysis. Figure 4.9 shows the absorption spectra of perovskites sieved with different polar solvent concentrations. Even when sieved at a relatively low polar solvent ratio (0.5% vol, for example), the low-n (n = 1, 2) absorption peaks of the quasi-2D perovskites diminish selectively. As the concentration of polar content

increases, most of the n = 1 phase is removed after 0.5% HA/CB solvent sieving, and all of the n = 1 and most of the n = 2 phases are removed after 2% HA/CB solvent sieving, which indicates the removal of target phases with proper polar content concentration within this range.

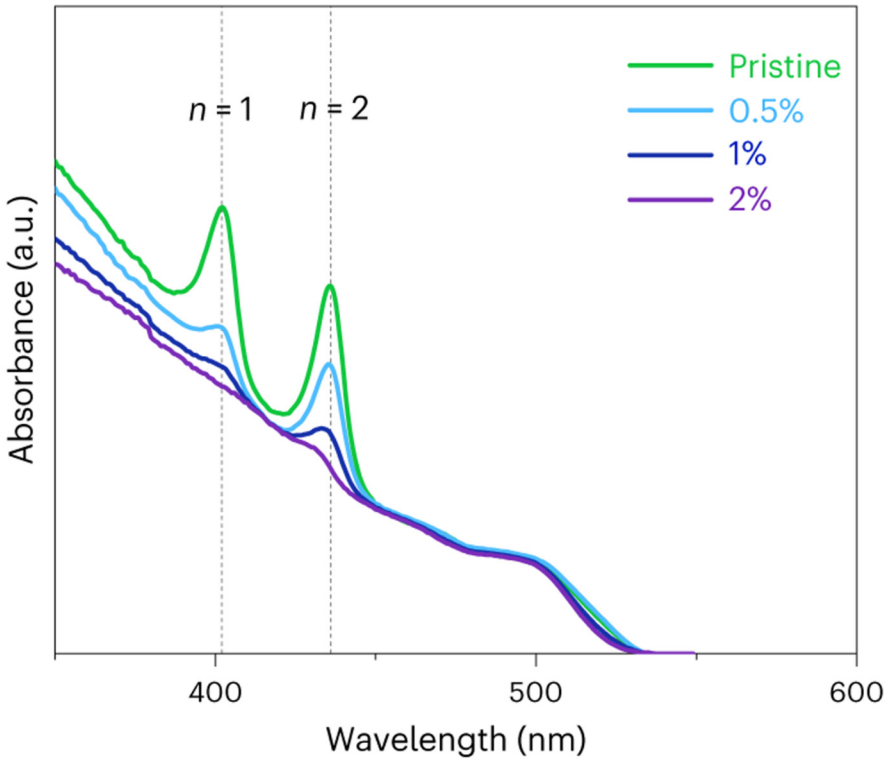

Figure 4.9 | Absorption spectrum of perovskite films solvent-sieved at different polar solvent concentrations.

Herein the polarity and donor ability of the solvent sieve played an important role in phase selectivity [200] and film quality. For the low-quality low-n phases in quasi-2D perovskites, rapid dissolution happens within just a few seconds (Figure 4.10). Therefore, effective removal of low-n phases from

quasi-2D perovskites could be achieved during the spin-coating process. The short-period processing of solvent sieve method is promising for large scale fabrication in the industry.

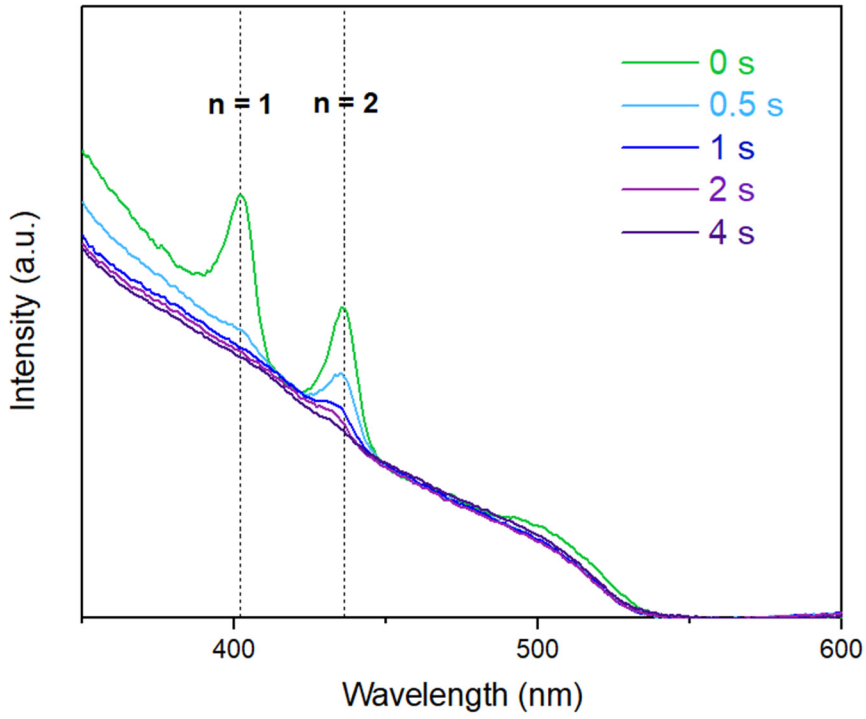

Figure 4.10 | In-situ UV-Vis absorption results during the solvent sieve process.

More detailed structure information is given by the grazing- incidence wide-angle X-ray scattering (GIWAXS) characterization (Figure 4.11). In pristine quasi-2D perovskites, strong low-n value peaks are observed, and highly corrugated orientation structures are also observed from the points-like GIWAXS pattern. After being sieved (2% by volume), perovskites show almost no low-n peaks. All the n = 1 phases, and most of the n = 2 phases, are removed. Moreover, the expanding arc form of the GIWAXS pattern indicates that the

orientation of 2D phases distributes more evenly, beneficial for the overall charge transfer in PeLEDs.

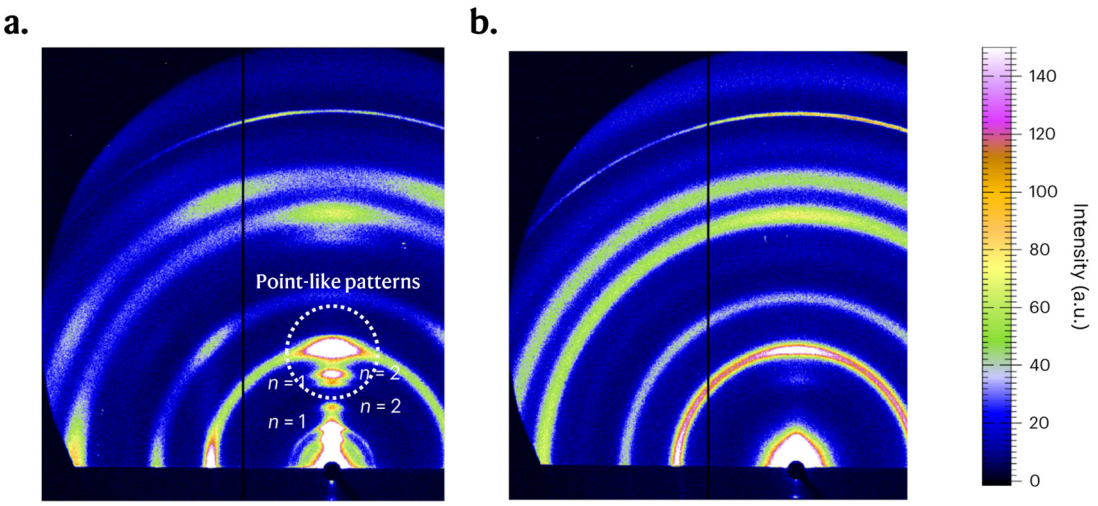

Figure 4.11 | GIWAXS pattern of (a) Pristine and (b) Solvent-sieved perovskite films.

The surface roughness of the perovskite films is also greatly reduced after solvent sieving (Figure 4.12). It is observed that the peaks and ridges of the pristine samples are removed after the solvent sieving treatment. More details of thin film surface morphology are further unveiled with SEM, as Figure 4.13 presents. It can be discovered that the pristine film contains some high-contrast bars and particles, which are usually considered as lead bromide crystals. While for solvent sieved samples, the surface is highly uniform and smooth, indicating an excellent film quality as well. The smooth surface of the solvent-sieved sample contributes to better contacts with the

top layers, enabling low interfacial energy losses and high efficiency for PeLED devices.

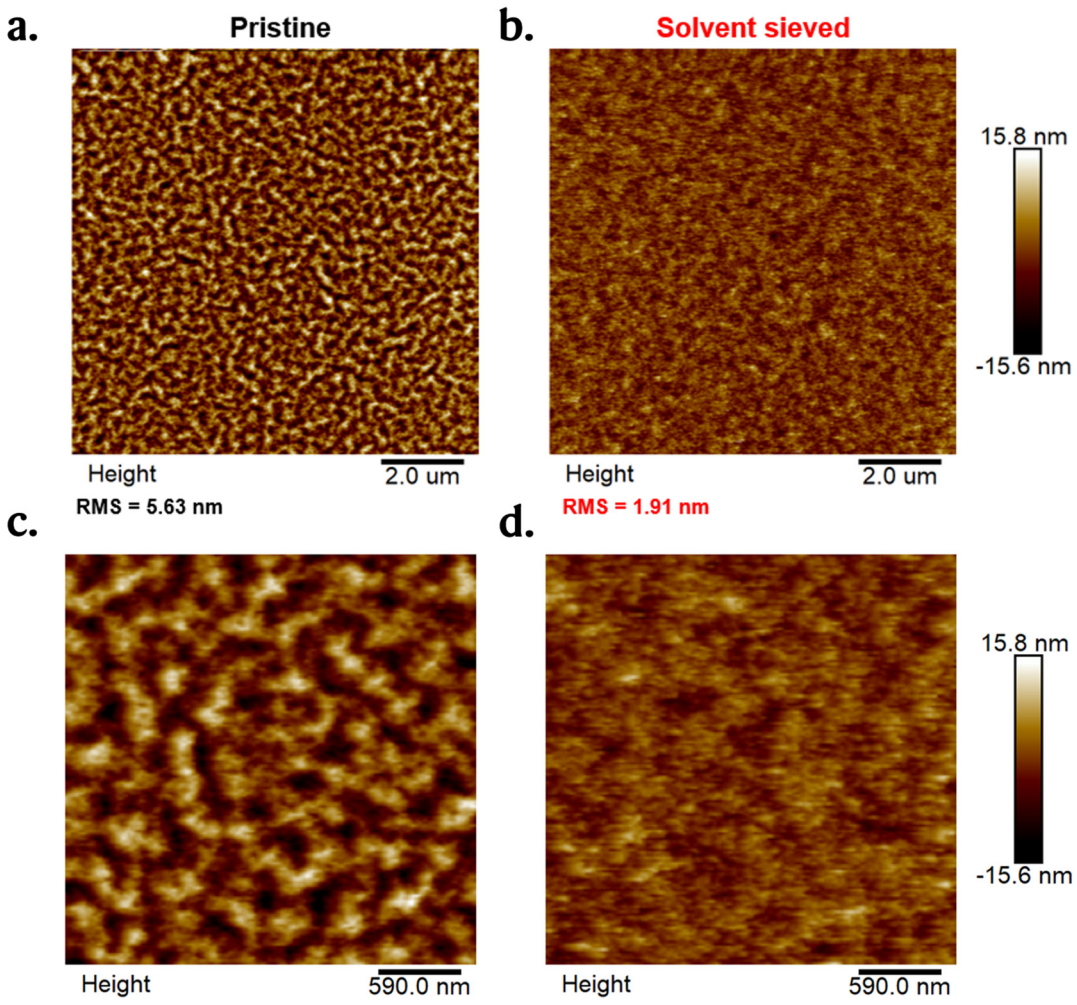

Figure 4.12 | surface morphology of (a) (c) Pristine and (b) (d) Solvent sieved perovskite film by atomic force microscope. The much smoother surface of solvent sieved perovskite contributes to better contact and film stability.

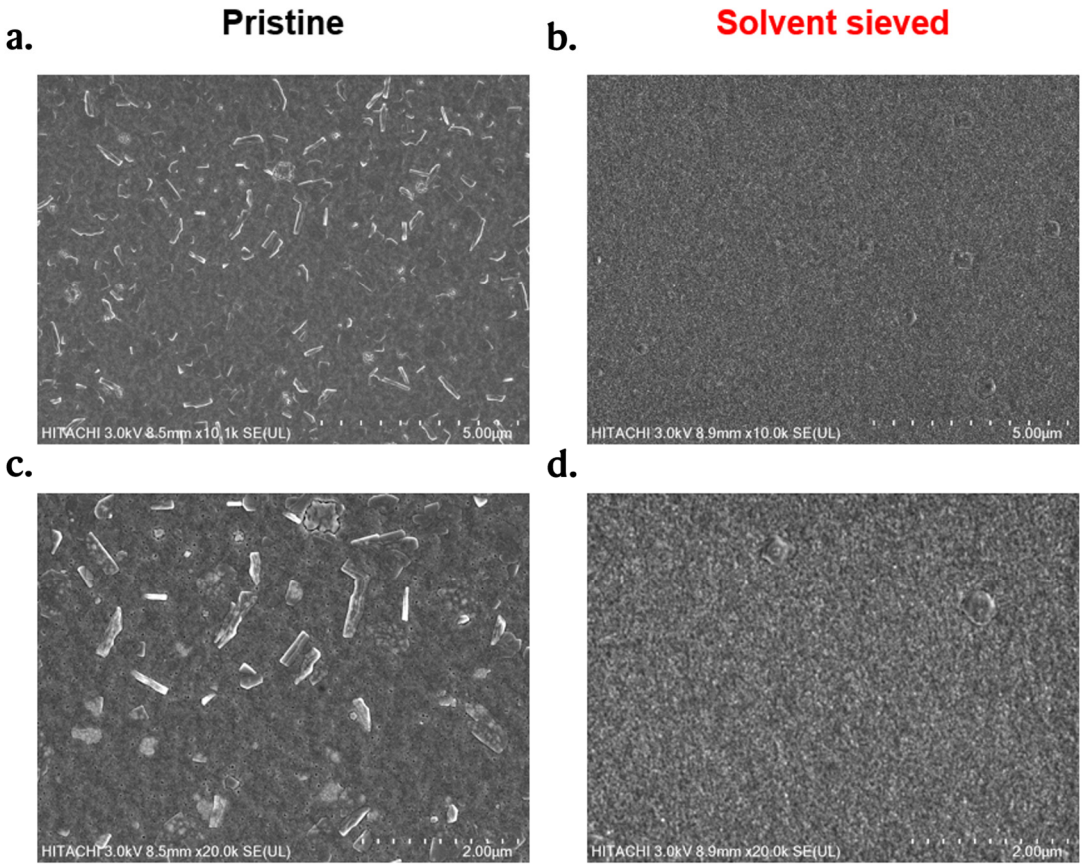

Figure 4.13 | Surface SEM images of (a) (c) Pristine and (b) (d) Solvent sieved perovskite films.

The optical properties of perovskites can be improved by the solvent sieve method. The typical photoluminescent spectra of pristine and solvent-sieved perovskite films are shown in Figure 4.14. Both films show the emission peaks of around 528 nm, while solvent sieved film have a smaller FWHM compared to the pristine one, indicating a better radiative phase purity. As shown in Figure 4.15, solvent-sieved perovskites have higher PLQYs than pristine perovskites within a broad range of 0.5% to 3% polar content. The improved PLQYs from 0 to 2% indicate decreased non-radiative rates and

corresponding decreased trap densities inside solvent-sieved perovskites. When the polar solvent ratio was too large (like 3%), the perovskite was dissolved and the PLQY began to drop.

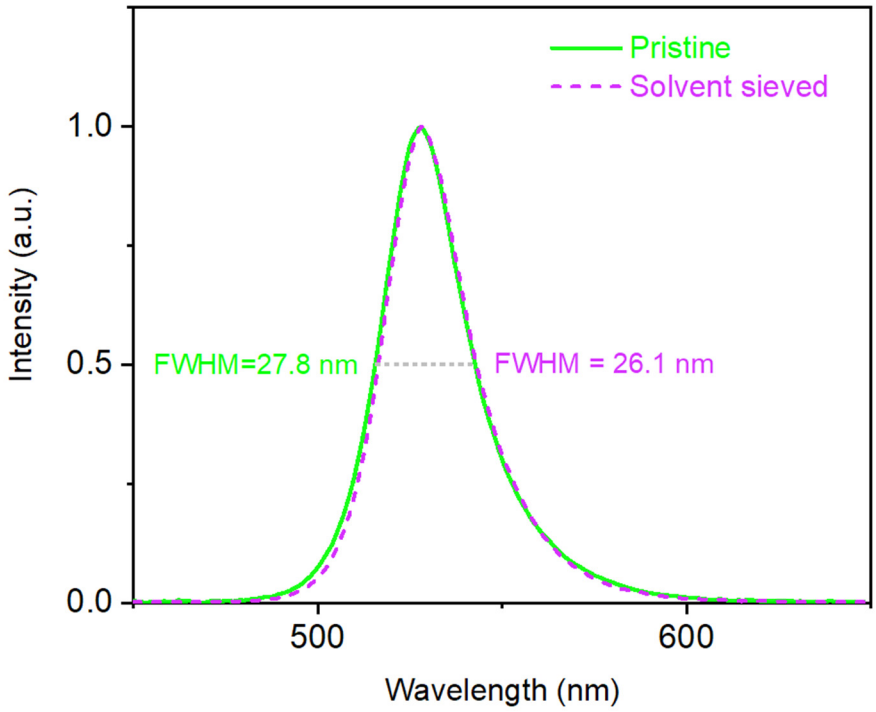

Figure 4.14 | Photoluminescent spectrum of pristine and solvent sieved perovskites.

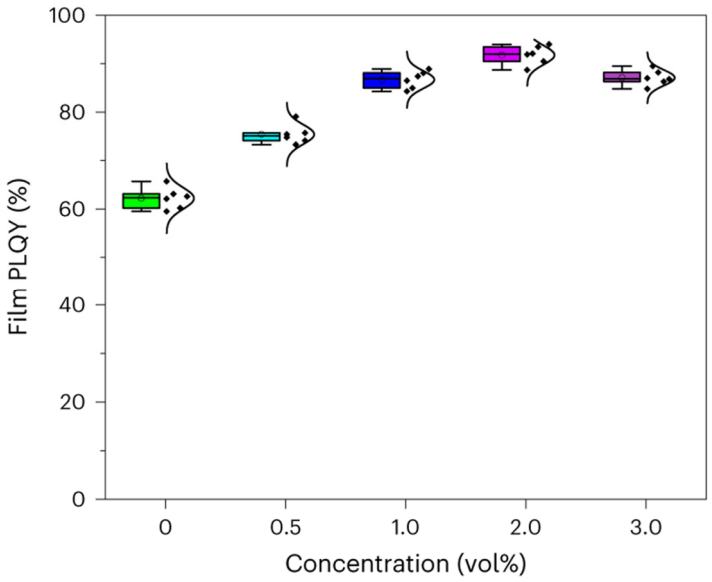

Figure 4.15 | PLQY box plots for pristine and solvent-sieved perovskites. In the box plots, the black dots represent the data points, and the curves show the distribution trends; the middle bar represents the median, and the box represents the interquartile range; bars extend to 1.5× the interquartile range.

Transient photoluminescence measurements are also conducted to characterize the exciton decay lifetime of perovskites. In a typical measurement (Figure 4.16), a sieved perovskite has much longer decay lifetime than a pristine one. Since the trap density is inversely correlated with the transient photoluminescence decay lifetime [210], the longer photoactivated carrier decay lifetime reveals lower trap density of solvent-sieved perovskites. Together with the structure characterizations, the solvent sieve method demonstrates its efficient removal of defects with high energy in perovskites.

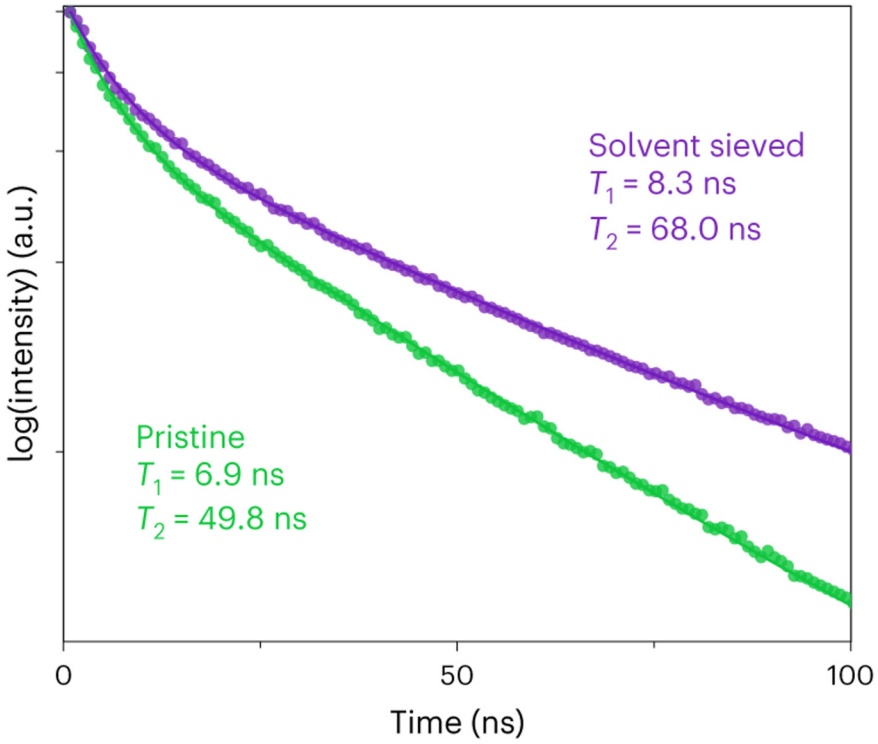

Figure 4.16 | Representative transient photoluminescence results of pristine and solvent-sieved perovskites. a.u., arbitrary units.

4.4 Intrinsic stable perovskites and excellent energy funnelling

The phases of quasi-2D perovskites are greatly purified by selectively screening out undesirable defect-rich low-n phases via solvent sieve methods, thus unleashing the stability potential of quasi-2D perovskites. The solvent-sieved perovskites show strong chemically stability while exposed to humid air, as confirmed by X-ray photoelectron spectroscopy (XPS) results. Figure 4.17 compares the XPS spectra of pristine and solvent-sieved perovskites. It is believed that the decomposition of nitrogen-containing organics is a main cause of perovskites degradation [211]. For nitrogen element, hardly any

changes can be seen after 28 days of continuous exposure to ambient air (50±10% humidity) for the solvent-sieved sample, whereas dramatic change is observed in the pristine sample. No CH_3-group signal at 0.9 ppm chemical shift is observed in 1H nuclear magnetic resonance (NMR) results in both pristine and solvent-sieved samples (Figure 4.18), meaning that no measurable HA molecules are attached to the perovskite films.

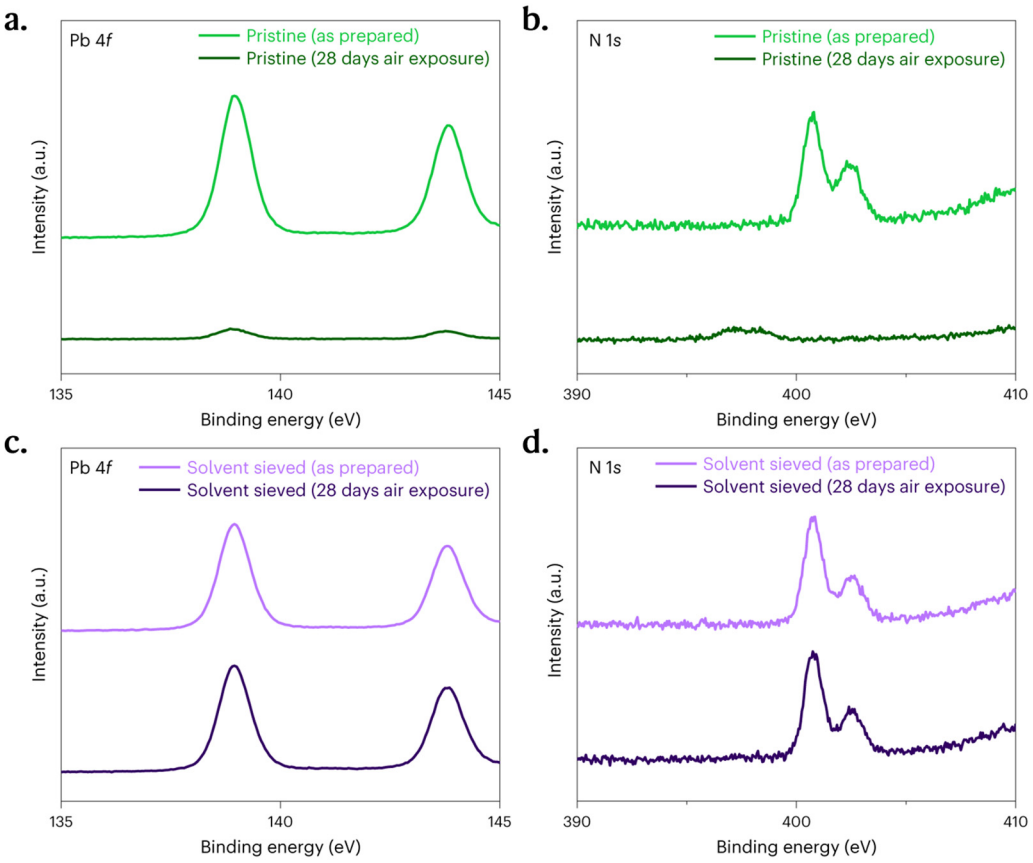

Figure 4.17 | XPS spectra of Pb and N in (a, b) pristine and (c, d) solvent-sieved perovskite films.

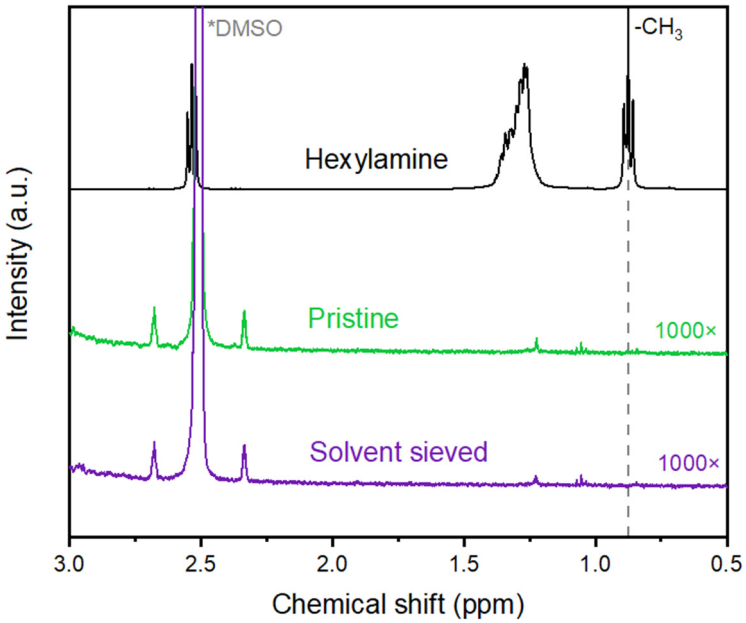

Figure 4.18 | ^{1}H NMR results of spectra of hexylamine, pristine and solvent sieved perovskite films. The materials are dissolved in d_6-DMSO. The concentration of hexylamine is 20% vol, and for perovskites, 3×3 cm^2 perovskite films are fully dissolved in 0.5 ml d_6-DMSO.

In quasi-2D perovskites, the multi-quantum-well nature leads to an energy transfer from large-bandgap, low-n phases to small-bandgap, higher-n phases [68]. Herein, transient absorption spectroscopy measurements are conducted to gain a deeper insight into the energy transfer process inside quasi-2D perovskites. The decay kinetics of domains with different n values of both samples are given in Figure 4.19. It is shown that in the solvent-sieved perovskites, the intensity changes for $n > 4$ phases (at around 518 nm) reach their maximum in 1 ps, much faster than pristine ones (over 3 ps), indicating a much faster energy funnelling process from low-n phases to higher-n

phases in solvent-sieved perovskites, as shown in Figure 4.20. Furthermore, in pristine perovskites, strong n = 1 and 2 peaks (around 402 and 435 nm) are observed, indicating a long and complicated energy transfer path; however, in solvent-sieved samples, almost all the low-dimensional peaks disappear, indicating that the exciton decay routine is greatly shortened.

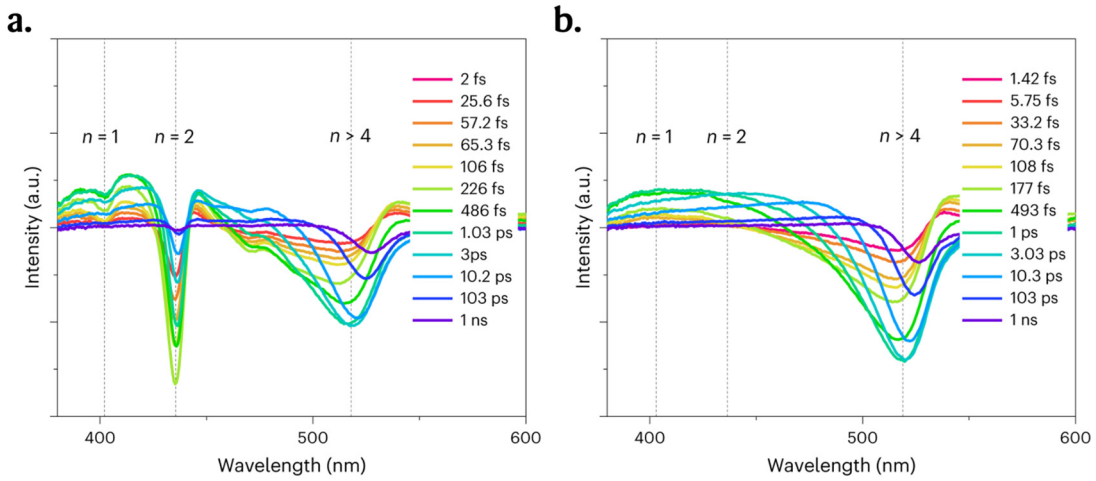

Figure 4.19 | Transient absorption spectroscopy results of (a) Pristine and (b) Solvent-sieved samples.

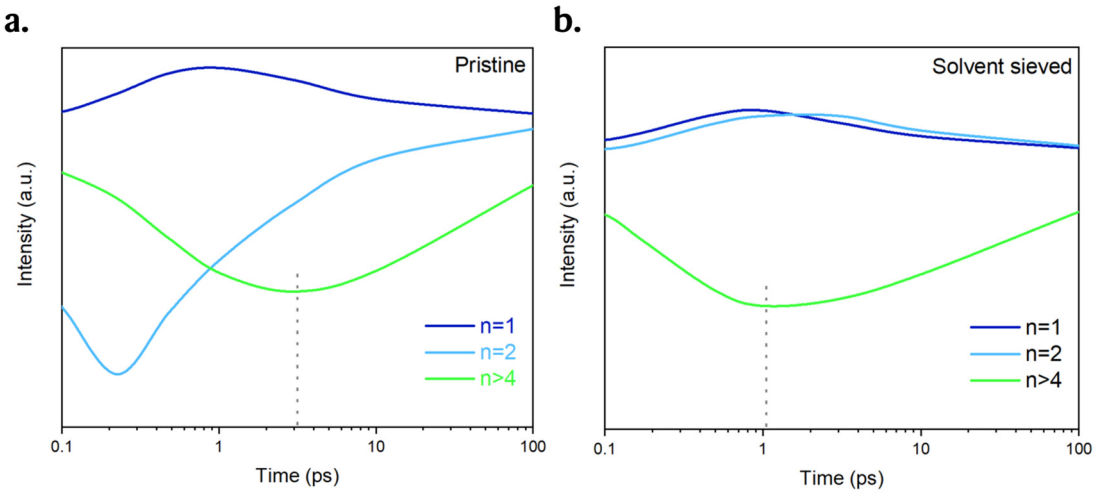

Figure 4.20 | TAS photobleaching features for (a) Pristine and (b) Solvent sieved samples.

Further exciton dynamics analysis is conducted through fitting the decay process of TAS with a triple-exponential model (Equation 4.2), as shown in Figure 4.21. It can be found that the A_1 of low-n phases (n = 1 and n = 2) is much higher than that of n > 4 phases in both pristine and solvent-sieved perovskites, showing that the exciton decay process in low-n phases is dominated by trap-assisted recombination, which indicates that the low-n phases are even more defective than higher-n phases, proving the effectiveness of solvent sieve method in reducing the perovskite film defect density.

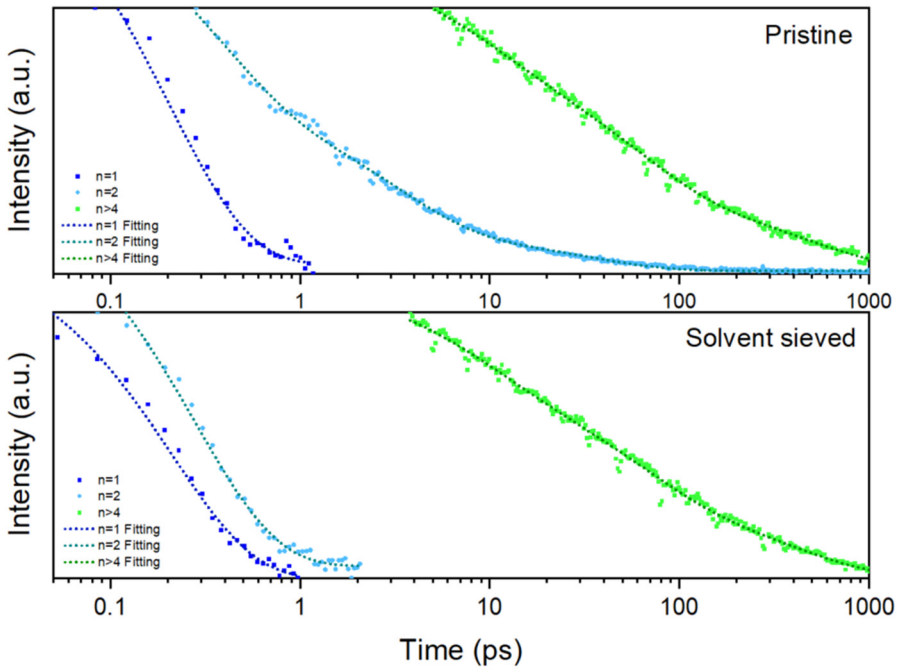

Figure 4.21 | Fitting curves of TAS photobleaching kinetics for different phases (402 nm for n=1, 435 nm for n=2 and 518 nm for n>4 phases).

Table 4.2 | TAS photobleaching kinetics for pristine and solvent sieved perovskite films.

Perovskite film		A_1	τ_1 (ps)
Pristine	n=1	0.393	0.202
	n=2	0.317	0.346
	n>4	0.194	7.904
Solvent sieved	n=1	0.389	0.212
	n=2	0.335	0.380
	n>4	0.173	8.051

4.5 Performance of PeLED device

With the removal of defects and significantly enhanced energy funnelling, high-performance PeLED devices are fabricated. The PeLED device structure in this study is FTO / NiO_x / PVP / perovskites / TmPPPyTz / LiF/ Al, as shown in Figure 4.22.

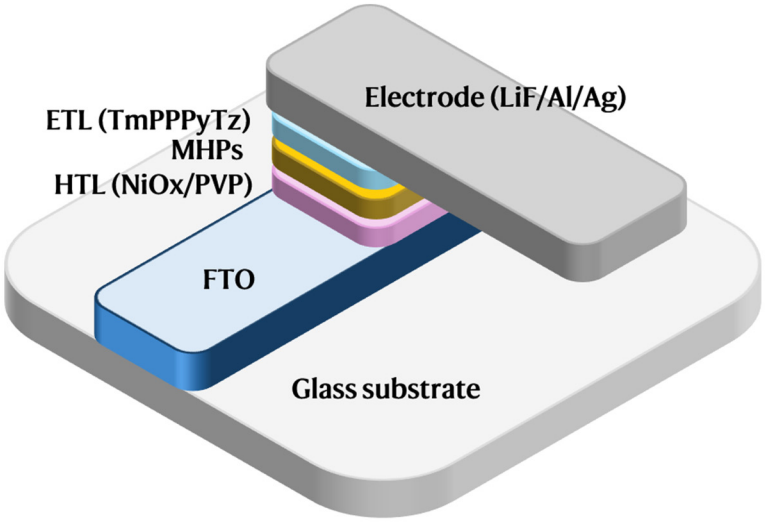

Figure 4.22 | Device structure of PeLED device.

The electroluminescence intensity follows a Lambertian distribution (the standard diffuse reflection model, Figure 4.24), indicating that the PeLEDs are normal LED devices without extra optical outcoupling. The electroluminescence spectra, current density–voltage–luminance (*J*–*V*–*L*) and the EQE characteristics are plotted in Figure 4.23. The pristine and solvent-sieved PeLEDs show emission peaks at 530 nm and 531 nm, a FWHM of 24.0 and 22.1 nm, and CIE coordination at (0.193, 0.760) and (0.192, 0.764), respectively. The *J-V-L* curve of solvent sieved PeLED exhibits much higher current density and luminance than the pristine one, in good accordance with the improved energy funnelling and luminescent properties of solvent sieved perovskites (Figure 4.23b).

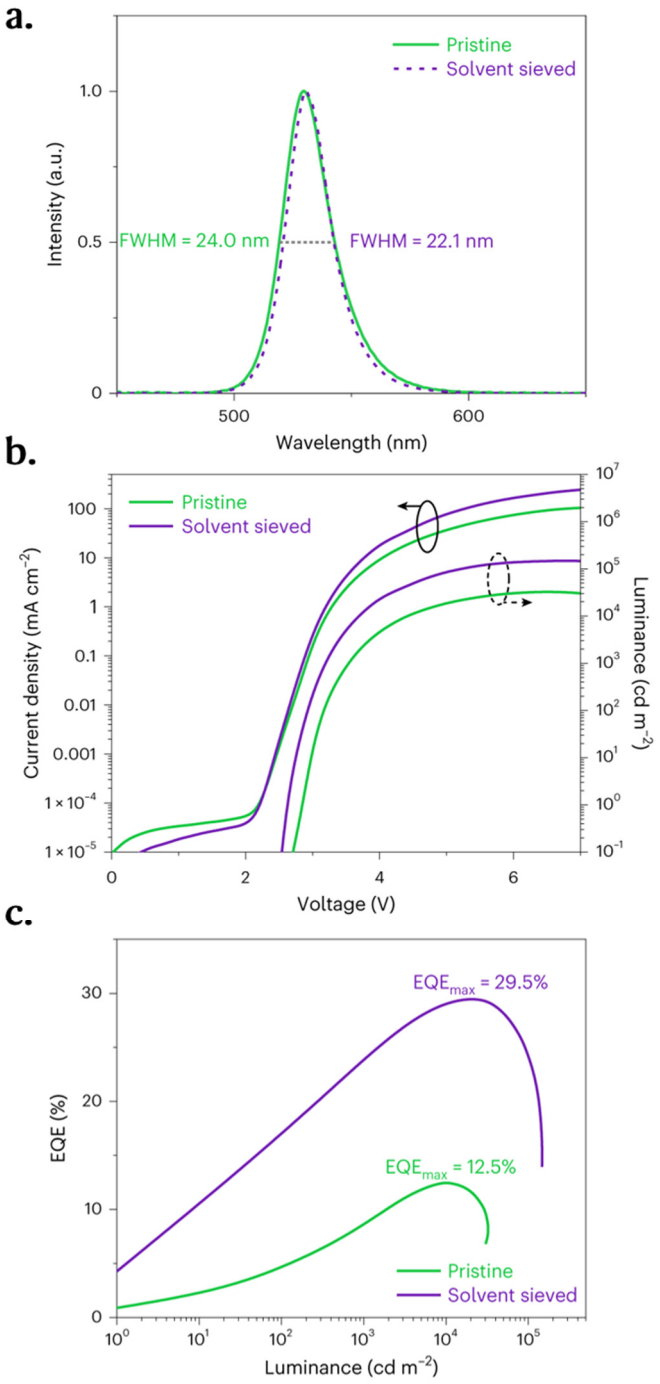

Figure 4.23 | PeLEDs performance. (a) Representative electroluminescence spectra of PeLED devices. The grey dashed line marks the FWHM. (b) *J*–*V*–*L* data of champion PeLED devices. (c) The EQE of champion devices based on pristine and solvent-sieved perovskite films, respectively (statistical data of over 30 devices available in Figure 4.26).

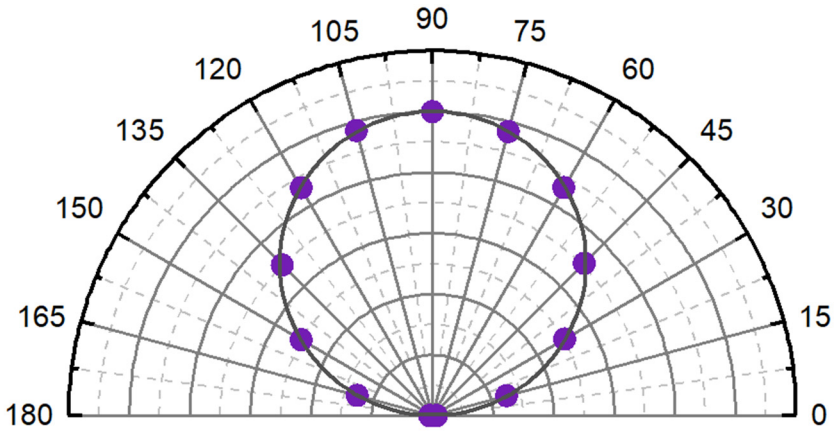

Figure 4.24 | Angular dependent electroluminescence (EL) intensity of solvent sieved PeLED.

As a result, the solvent-sieved PeLEDs possess a highest EQE of 29.5% (Figure 4.23c) and corresponding current efficiency (CE) of 124.0 cd A^{-1} (Figure 4.25), with an average EQE of 26.5 ± 1.4% over 30 devices (Figure 4.26)—over an order of magnitude higher than the pristine EQE_{max} of 12.5%. Meanwhile, the maximum luminance of the solvent-sieved device reaches a record brightness of 147,872.8 cd m^{-2} for highly efficient quasi-2D PeLEDs. The high luminance of solvent sieved PeLEDs shows enormous potential in the applications of display and lighting.

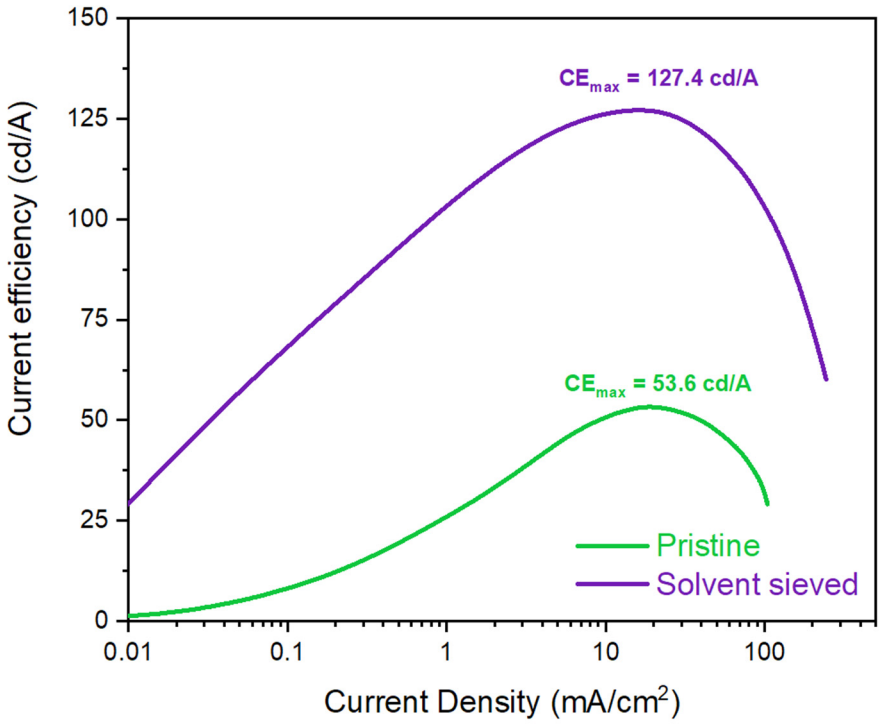

Figure 4.25 | Current efficiency versus current density for best-performance PeLED devices.

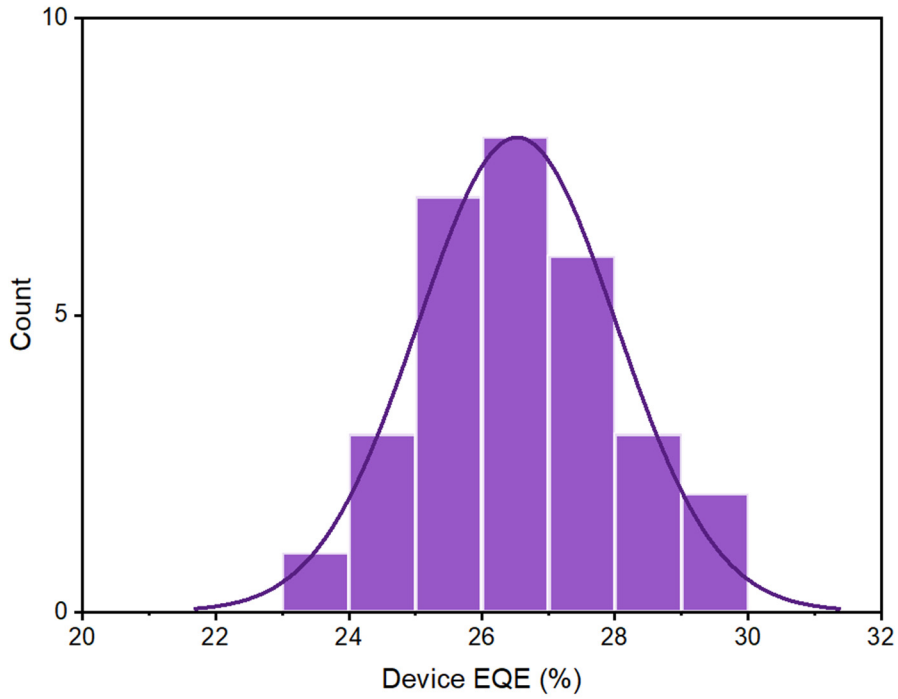

Figure 4.26 | Statistical device EQE_{max} of solvent sieved PeLEDs. 30 devices are measured in total.

The PeLED device performance is further confirmed with both our EQE measurement set-up and integrating sphere (Figure 4.27) [212]. The consistent crosscheck results with different setups have ensured the reliability of our EQE measurements.

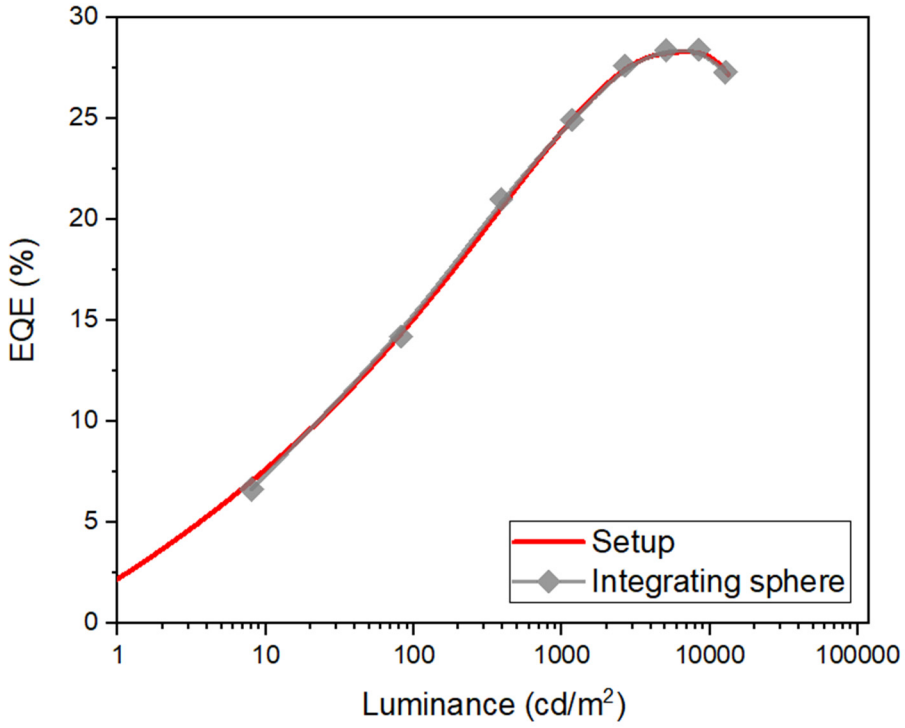

Figure 4.27 | EQE for the same device measured by our setup and an integration sphere (XP-EQE-Adv). The EQE_{max} of this device is measured to be 28.30% (setup) and 28.39% (integrating sphere).

Then, the optical simulation results, with the measured refractive index of perovskite film, are also appended (Figure 4.28) using the transfer matrix method code, oledpy. Over 30% theoretical outcoupling efficiency can be theoretically achieved with active layer thickness from 20 to 80 nm according

to the simulation. The theoretical outcoupling efficiency is 33.9% at a perovskite thickness of 60 nm.

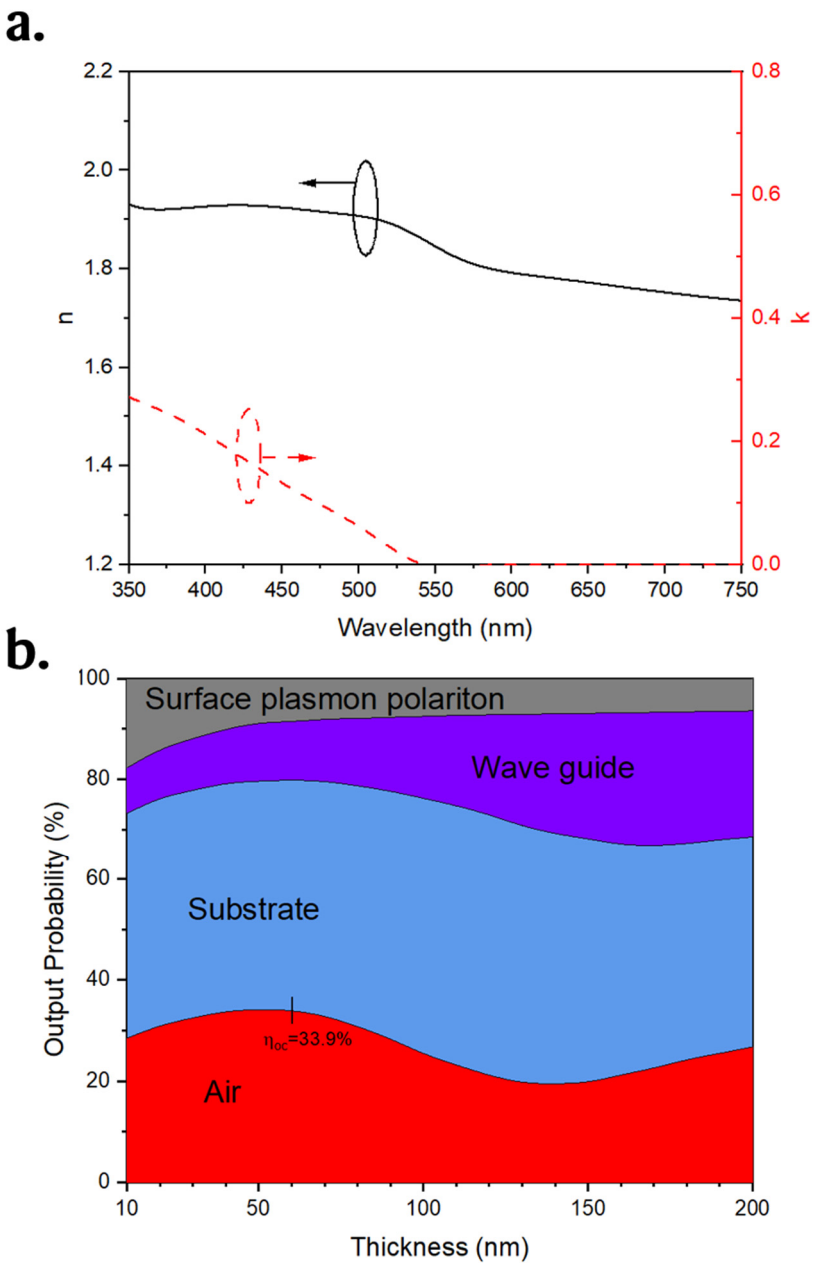

Figure 4.28 | (a) Refractive index *n* and extinction coefficient *k* of the perovskite emissive layer. (b) Outcoupling probability distribution as the function of perovskite layer thickness.

The operational lifetime of PeLED devices is presented in Figure 4.29. The initial luminance is tuned to 12,000 cd m^{-2} and all the devices are measured at constant current density mode. The champion T_{50} (the time at which the luminance drops to the 50% of initial value) of solvent-sieved PeLED devices reaches 18.67 h (which is equivalent to over 50,317 h or 5.7 years at 100 cd m^{-2}; see Figure 4.30 and Table A1-1)—nearly two orders of magnitudes higher than the pristine devices (only 0.67 h). Meanwhile, the spectrum stability of PeLED devices is essential for industrialized application of display screens to maintain stable colour presentation. No notable change to the electroluminescence spectra is observed before and after the lifetime test (Figure 4.31), which also confirms the extraordinary device stability of solvent sieved PeLEDs.

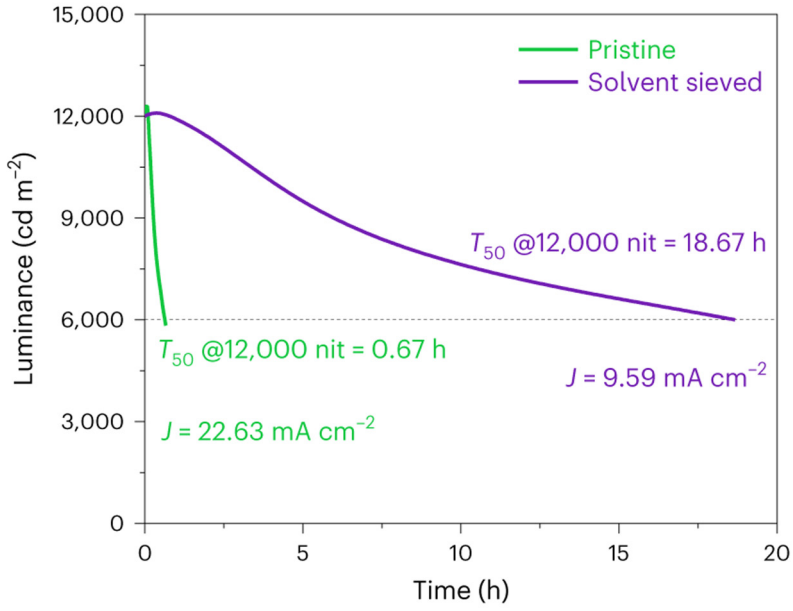

Figure 4.29 | Champion operational lifetime of PeLEDs. The black dashed line marks the position of T_{50}.

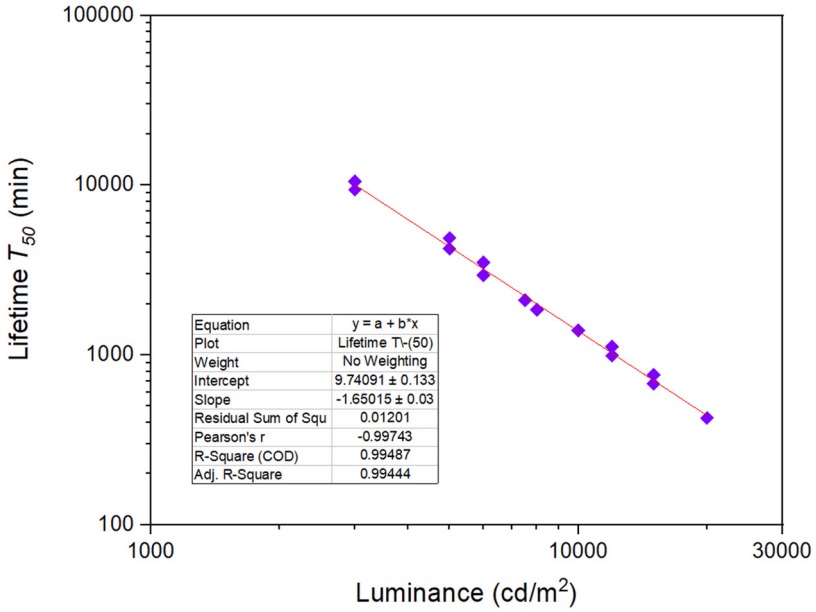

Figure 4.30 | Maximum T_{50} lifetime of PeLEDs at different initial luminance. The calculated T_{50} lifetime at 100 cd/m^2 is about 3,019,027.6 min for the slope of -1.65.

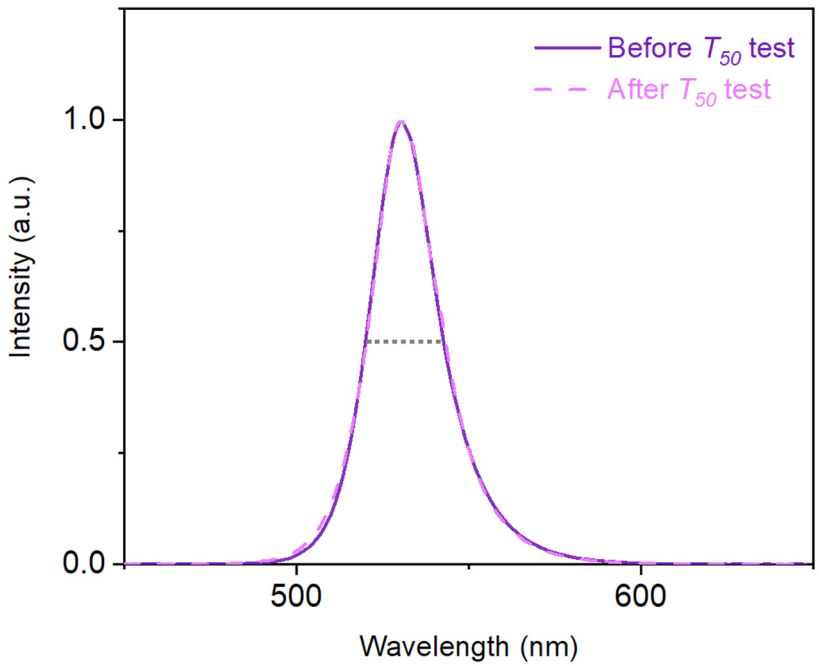

Figure 4.31 | EL spectra change after operational lifetime T_{50} test. No meaningful change of EL spectra is observed after the lifetime test.

A low trap density in the emitting layer is crucial to LED operation lifetime [212]. The reduction of trap density can not only reduce joule heating but also suppress the ion migration effect, which contributes to a higher device operational stability [125, 213]. Lower trap density in solvent-sieved perovskites is further confirmed by space-charge-limited current (SCLC) measurement, and herein the hole-only devices are fabricated with a structure of FTO / NiO_x / PVP / perovskite / molybdenum oxide (MoO_x) / Au [72, 214]. According to the SCLC model [215], the defect density is proportional to the trap-filling-limited voltage (V_{TFL}), representing the voltage that all the electric traps inside materials are filled with charges, and can be given by the slope change points of the curves in Figure 4.32. The trap density in the solvent-sieved sample is much lower than untreated one, which contributes to an improvement in the operational lifetime. The SCLC results also show that the solvent-sieved perovskites have better conductivity, in agreement with the *J*–*V* curve in Figure 4.23b.

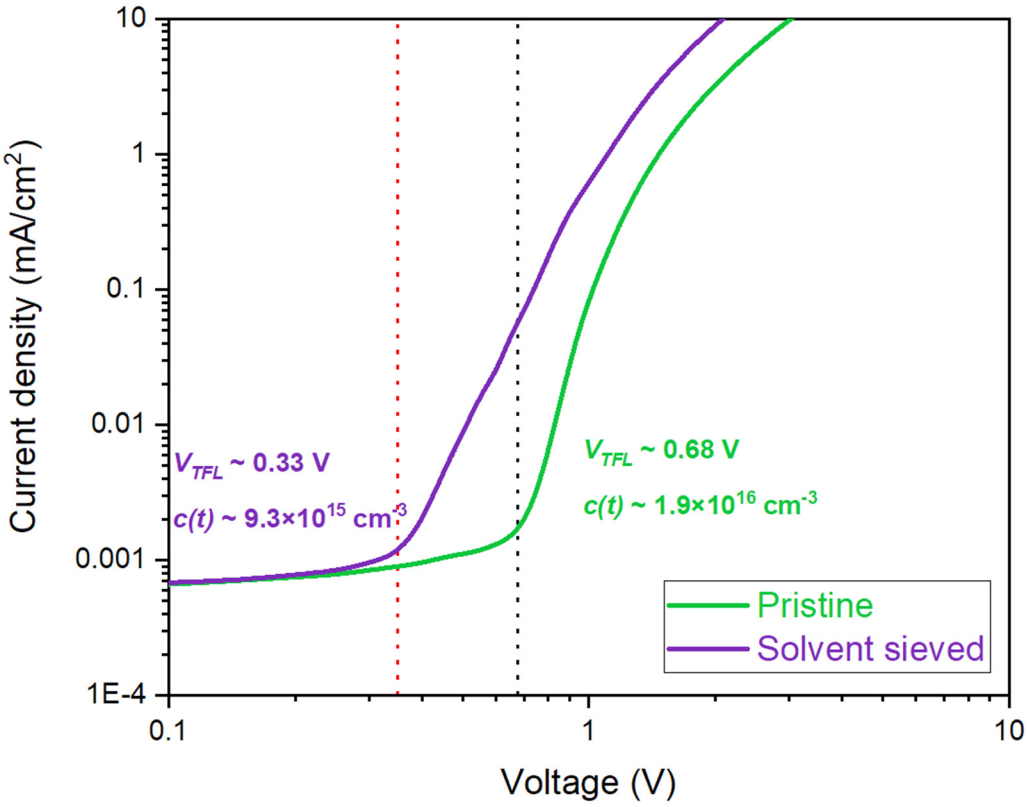

Figure 4.32 | Current density versus voltage curve for hole-only devices. The solvent sieved perovskites have much lower V_{TFL} and higher conductivity.

4.6 Long-term stable solvent-sieved perovskites and PeLEDs

Due to the removal of defective phases and improved radiative phase purity [216], the solvent-sieved perovskite films exhibit impressive stability under ambient conditions. As PLQY is extremely sensitive to crystal distortion or defects of perovskites, the maintenance of optical properties under high humidity and air is particularly important. The optical change with time for pristine and solvent-sieved perovskite films is studied in ambient air, with a relatively high humidity of 50 ± 10%, and without any encapsulation. Figure 4.33a presents the photos of pristine and solvent-sieved perovskite films

exposed to humid air after 100 days. The PLQY changes over 100 days are shown in Figure 4.33b. The solvent-sieved perovskite film can maintain 75% of its initial PLQY for over 100 days on average (Table A1-2), whereas the pristine perovskites lose most of their PLQY after exposure to humid air for 1 h. GIWAXS results indicated that the pristine samples fully decomposed, whereas the solvent-sieved samples maintain clear scattering patterns after 28 days storage in the ambient air, as shown in Figure 4.34. It can be found that pristine samples are fully decomposed, while the solvent sieved samples are stable.

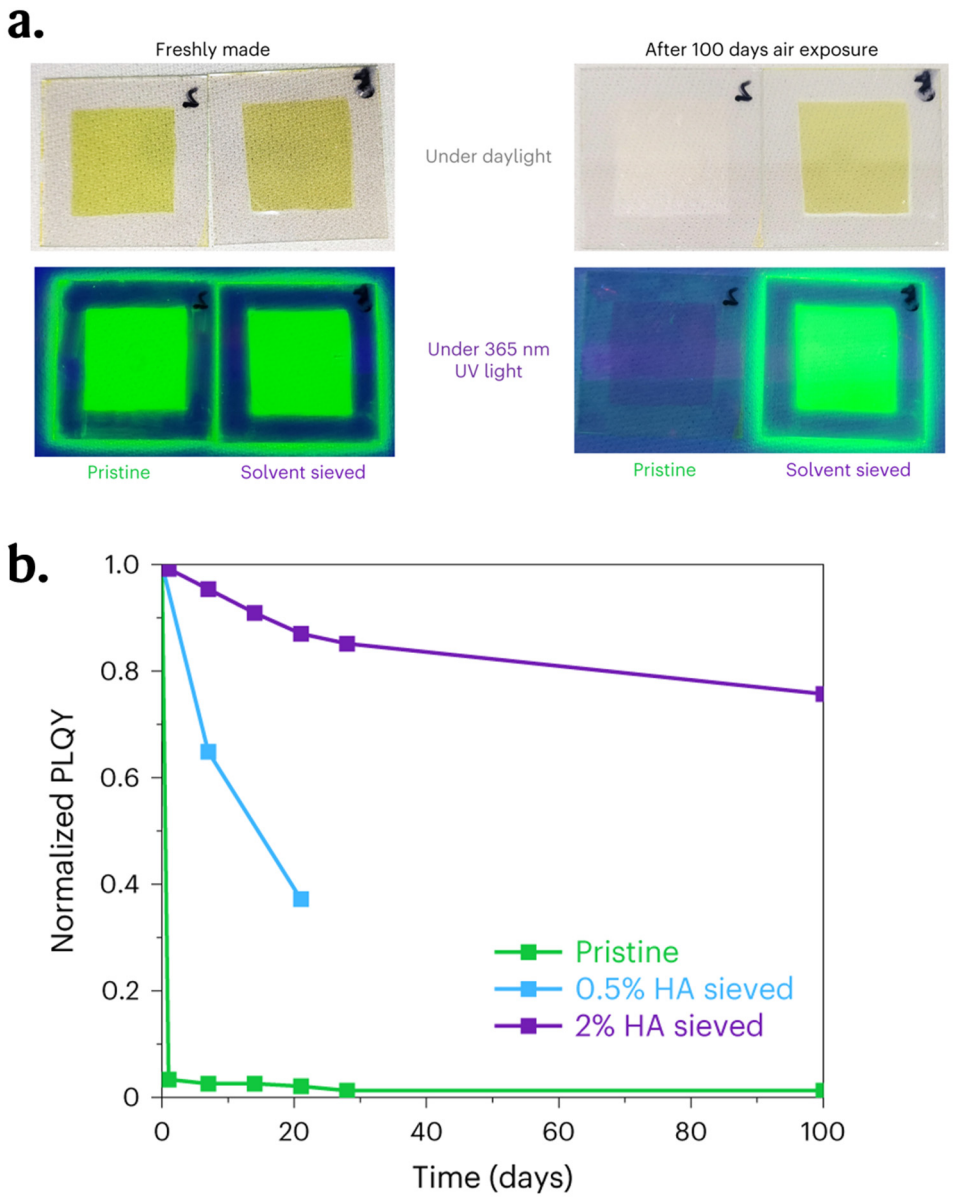

Figure 4.33 | Stability of PeLEDs. (a) Photos of pristine and solvent-sieved perovskite films exposed to humid air after 100 days. (b) Representative PLQY changes with time for pristine and solvent-sieved perovskite films in ambient air.

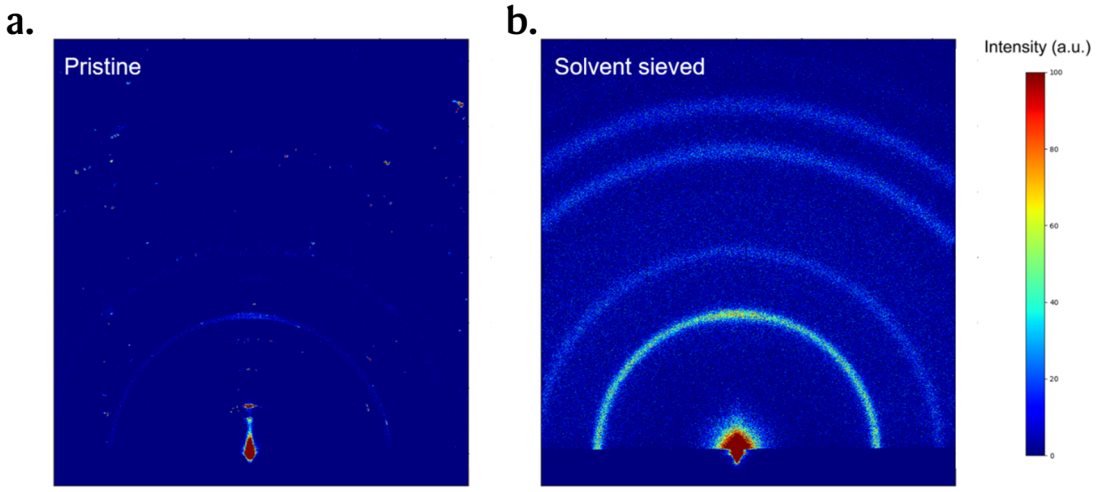

Figure 4.34 | GIWAXS pattern of (a) pristine and (b) solvent-sieved perovskite films after 28 days storage in the ambient condition (controlled humidity of 50±10%).

The ambient air stability of sieved quasi-2D perovskites is also confirmed by fabricating previous humid air exposed perovskite films into PeLED devices. Figure 4.35 shows that solvent-sieved perovskites maintain as high as 80% of device EQE after being stored in ambient air at moderate humidity for 100 days. The excellent resistance of solvent-sieved perovskites to ambient air is not only beneficial to cost-effective encapsulants, but also shows immense potential as a platform material for broad luminescence applications such as down-conversion optical films, where high-energy photons are converted into lower-energy photons through film absorption and re-emission that requires remarkable material stability.

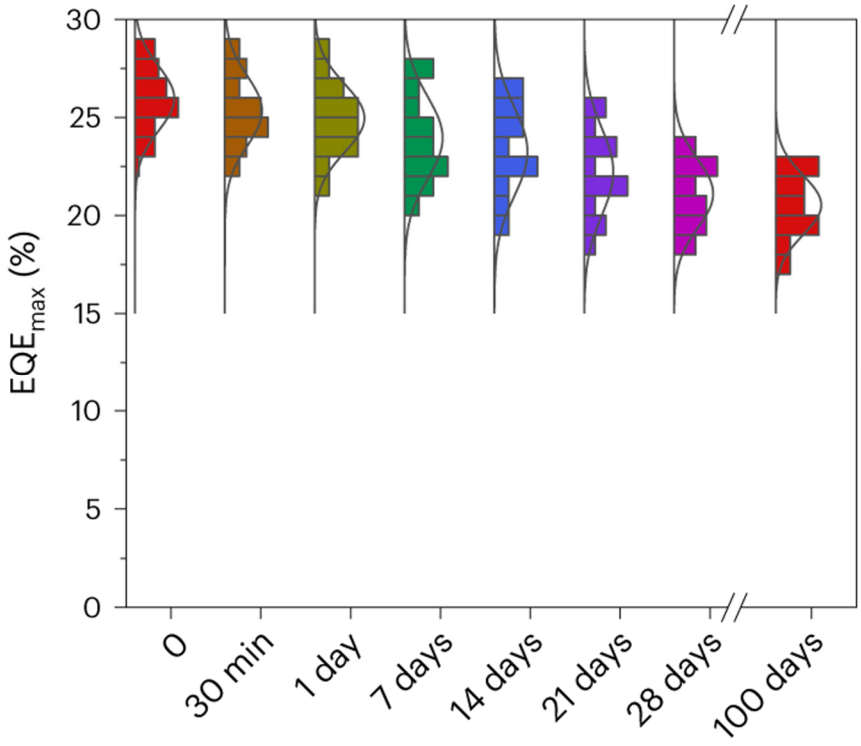

Figure 4.35 | Maximum EQE of PeLEDs made with perovskite films stored at ambience for different lengths of time.

4.7 Discussion

In this chapter, the instability of perovskite low-n phases inside quasi-2D perovskites is firstly investigated, and an innovative solvent sieve method has been proposed to achieve high-quantum-yield and intrinsic stable perovskite films with enhanced energy funnelling, followed by the fabrication of stable and efficient PeLEDs. This project has established a comprehensive framework from the analysis of mechanism, the optimization of materials to the fabrication of devices.

The first critical issue this study has solved is the fundamental mechanisms underlying the limited stability of perovskite materials and PeLEDs. Our work for the first time directly evidences that the low n phases are the critical source of perovskite instability (Figure 4.1), providing deeper insights of the correlations between perovskite nanostructures and stability. Straightforwardly, it moves beyond the conventional, less discerning approaches that attribute instability broadly to defects without clear differentiation of the fine structures [137, 217, 218]. By identifying the instability of these low n phases, our discovery paves the way for targeted strategies to enhance the stability of both perovskite materials and PeLEDs, as well as other MHP-based optoelectronic devices like PePVs, which will be discussed as Table 7.1.

Furthermore, this research has successfully resolved the enduring "contradiction" surrounding the supposed low n phase stability issues (Figure 2.17). Through meticulous examination of crystallization mechanisms in both quasi-2D perovskites and monocrystals (Figure 4.2), alongside the resultant perovskite crystallinity (Figure 4.3), our work has affirmed the evident differences in material structures. Specifically, low n phases inside quasi-2D perovskites exhibit diminished crystallinity and as well as severe lattice distortion, therefore exhibiting inferior material stability (Figure 4.1). Conversely, perovskite monocrystals display an ideal

lattice structure as well as remarkable stability, as illustrated in Figure 4.5. This resolving of the "contradiction" underscores the significance of considering real-world structural complexities in understanding and predicting material properties, especially when theoretical models based on idealized structures may not fully encapsulate the intricacies of experimental realities.

The mechanism of the solvent sieve method is based on the solubility difference of divergent phases in polar solvent, wherein the low n phases possess higher surface-to-volume ratio and more defects, and they are easily dissolved in polar solvent compared to the higher n counterparts. So far, the most successful polar/nonpolar solvent combination is HA/CB (Figure 4.7) in this work. However, the combination of polar and nonpolar solvents offers a myriad of possible combinations. While several solvent sieve formulations have been developed and examined, as illustrated in Table 4.1, a lot of unexplored combinations await further investigation, holding the prospect of discovering even more efficacious sieving systems with enhanced performance. Presently, the choice of polar solvents is largely confined to a narrow range of amines, with attempts using alternatives such as DMSO yielding diminished perovskite performance instead of improvement. Concerning nonpolar solvents, while their influence may be less pronounced, variations in outcomes have been observed between chlorobenzene, toluene,

and ethyl acetate. Therefore, more research endeavours shall be directed towards identifying more efficacious solvent sieves, facilitated by experimental screening or employing advanced artificial intelligence algorithms [11] to efficiently navigate throughout the vast combination space. Meanwhile, a systematic summary of how the different chemical functional groups of solvents relate to their sieving ability is crucial. Unravelling the underlying mechanisms governing this relationship is instrumental in guiding the rational design of remarkable solvent sieves, thereby accelerating the applications of this technology for advanced MHP-based optoelectronics.

The post-synthesis refinement of perovskites, targeting the selectively removal of low-quality components or phases, holds broad value for refining MHP-based optoelectronic devices across various applications. As an example, our solvent sieve method stands out as a highly selective technique with great phase dimensions sensitivity, independent of the perovskite composition. In another word, unlike approaches confined by specific material constituents, our method has transcended the perovskite contents limitations. Therefore, expanding our prior achievements in green light emitting bromide-based PeLEDs, this universal strategy has been employed to fabricate exceptionally stable infrared-emitting iodide-based PeLEDs with large organic cation engineering to hinder the ion migration issues, with

significant improvements on device operational lifetime of almost two orders of magnitude, as shown in Figure 4.36a [16].

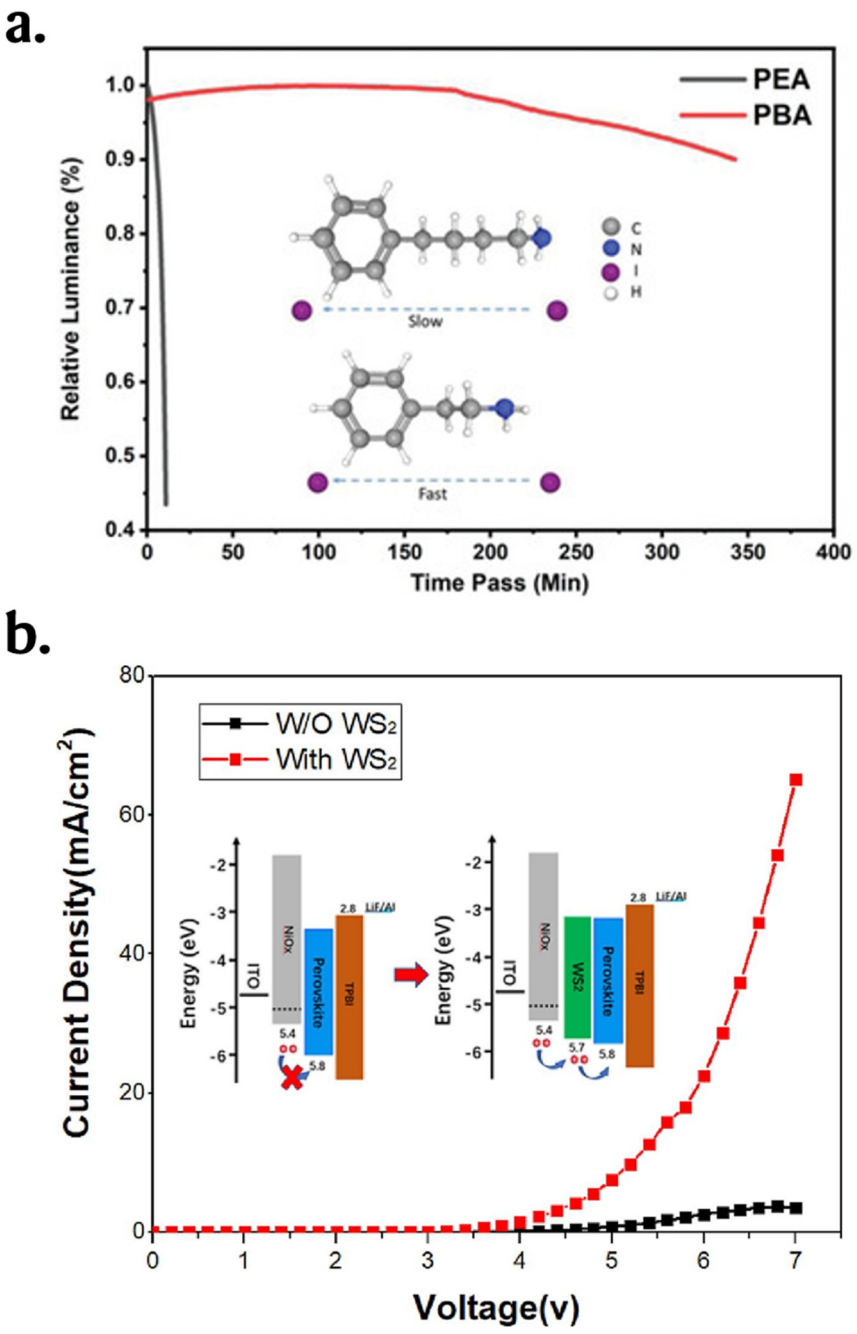

Figure 4.36 | (a) highly stable infrared PeLEDs based on solvent sieve method [16]. (b) High efficiency organometal blue PeLEDs [219] based on solvent sieve method.

Furthermore, high-efficiency, chloride- and bromide-containing organometallic blue PeLEDs are also fabricated with unique 2D tungsten disulfide (WS_2) energy level matching layers, with remarkable HTL energy level matching to perovskites and enhanced hole injection, achieving an improvement on EQE of one order of magnitude, as depicted in Figure 4.36b [219]. This generalizability underscores the broad applicability and potential of the solvent sieve method across diverse halide perovskite systems as a general and powerful toolkit, pushing the boundaries of perovskite based optoelectronic device development.

Finally, the discovery of the rapid crystallization process of low n phases inside quasi-2D perovskite (Figure 4.2) has also inspired alternative methodologies aimed at decelerating this crystal formation process. Currently, 2D perovskite monocrystals find notable applications such as detectors [220] and transistors [221] due to their relatively ideal structure and low defect densities. However, this is not to suggest that pure 2D perovskites are unsuitable for PeLEDs, but the complicated and protracted synthesis processes for obtaining pure 2D perovskite single crystals pose a hindrance to their implementation in PeLED technology. Therefore, two avenues warrant exploration: firstly, the development of facile and practical synthesis methods for pure 2D perovskite single crystals designed for PeLEDs holds promise for achieving perovskite films of high quality with an ideal

structure. Secondly, the development of any strategy capable of decelerating the crystallization kinetics of quasi-2D perovskites has become imperative. To this end, some studies have employed high boiling point solvents, such as NMP [222] or dimethylpropyleneurea (DMPU) [223], to decelerate solvent evaporation, with limited success in achieving crystal qualities comparable to those of single crystals. Phenomenological control strategies, including cold antisolvent bathing [224], have also been attempted, falling short of meeting the critical standards for industrial scalability. Consequently, more investigation shall be performed to refine the crystallization processes for perovskites, pushing towards optimization that fulfils industrial demands, and an example of the sweet coordination strategy on crystallization optimization and defect suppression will be introduced in Chapter 5.

4.8 Summary

Overall, this chapter introduces an innovative and efficacious post-treatment solvent sieve method, which not only dramatically enhances the luminescent performance and stability of PeLEDs, but also constitutes a foundational step towards the ongoing industrialization of perovskites with distinctive nanostructures and excellent luminescence performance. Specifically, Perovskite multi-quantum-well structures are greatly improved by selectively screening out undesirable defect-rich low-n phases; thus, a high-performance green quasi-2D PeLED device with a highest EQE of 29.5% and T_{50}

lifetime of 18.67 h at 12,000 cd m^{-2} (equivalent over 50,317 h or 5.7 years at 100 cd m^{-2}) is achieved, with a maximum luminance of 147,872.8 cd m^{-2}. The solvent-sieved perovskites present extraordinary resistance to air and moisture due to the efficient removal of unstable phases, maintaining over 75% of film PLQY and 80% of device EQE after being stored at ambience for 100 days. This work opens a gate for spontaneously improving the efficiency and stability of PeLEDs at high brightness, which could benefit future mass production and commercialization of PeLEDs and other luminescence applications.

More importantly, the solvent sieve method operates independently of the material composition, relying solely on the perovskite phase dimensions. Thus, our developed solvent sieve method has emerged as a universal toolset enabling precise control over the phase dimensions of quasi-2D perovskites, thereby resulting in remarkable improvements in PeLED performance metrics. Moreover, this methodology can be further employed to address similar phase dimension challenges in other MHP based optoelectronic devices, including PePVs and MHP-based photodetectors. Consequently, it opens a new avenue and broadens the prospects for the continuous development and industrialization of MHP materials and devices.

Chapter 5. Suppressing Defects with Sweet Coordination Strategy

5.1 Introduction

In this chapter, a similar formamidinium-based organometal quasi-2D perovskite material system and corresponding PeLED devices are investigated, as studied in Chapter 4. The quasi-2D perovskites are also fabricated by spin-coating the precursors with a composition of phenethylammonium bromide (PEABr), formamidinium bromide (FABr) and lead bromide ($PbBr_2$) in a molar ratio of 2:3:4 [208], with a typical chemical formula of $PEA_2FA_{n-1}Pb_nX_{3n+1}$., with the same main chemical reaction as Equation 4.1.

The only critical difference between PeLED devices in Chapter 4 and this chapter is the device structure, wherein the bilayer ETL structure (TmPPPyTz/ AND-PBIP) was employed in this chapter instead of single layer one (TmPPPyTz), as Figure 5.1 shows. The bilayer ETL structure was reported in the literature to further improve the PeLED stability [67, 71]

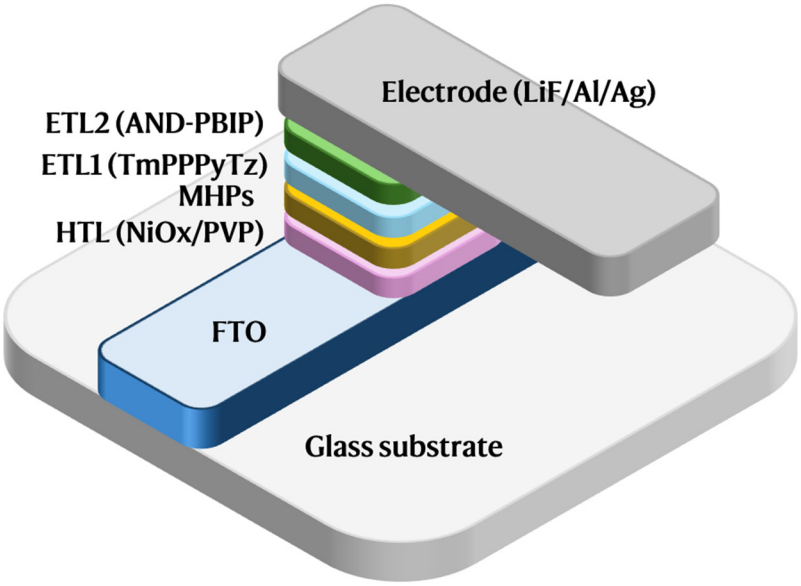

Figure 5.1 | Device structure of PeLEDs in this chapter.

Then, a novel and simple coordination strategy will be presented to tailor these non-radiative phases and suppress the defects formation. In contrast to post-treatment methods, it is more important to coordinate lead ions in their precursor with stronger coordinating molecules than solvent to inhibit the formation of unwanted defective non-radiative phases without degrading the radiative phases. Therefore, to illustrate the effect of coordination tailoring, a simple commercial molecule, saccharin (Sacc), was chosen to form stronger coordination to lead ions compared to solvent molecules to tune the phase dimensions of RDPs. The formation of non-radiative low dimensional phases was inhibited due to the system energy of coordinated Pb^{2+} is lower than these low dimensional phases and RDPs with high radiative

phase purity and low defect density are fabricated consequently, as presented in Figure 5.2.

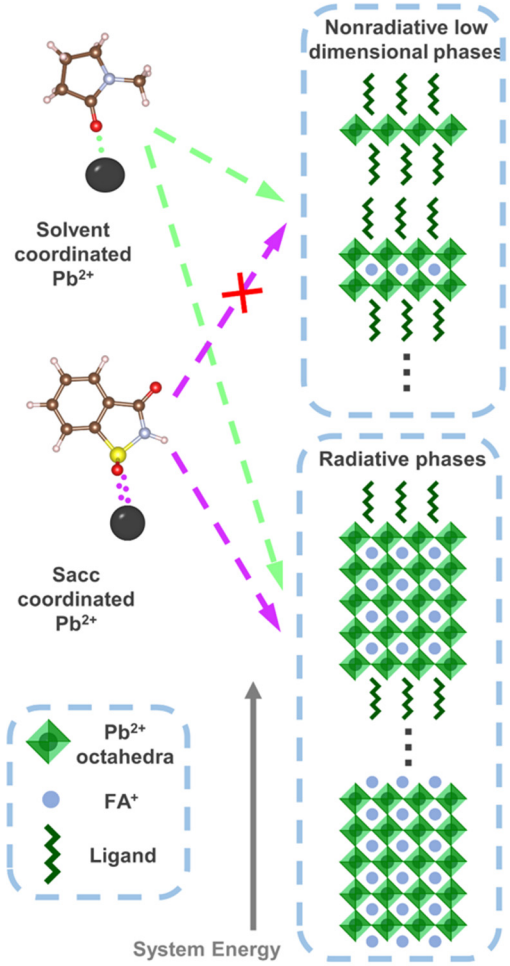

Figure 5.2 | Scheme of tailored phase dimensions. Without tailoring coordination, formation of phases from n=1 to n=∞ occurred spontaneously. With proper coordination, Pb^{2+} system energy is reduced, low dimensional non-radiative phases are no longer stable in the system.

5.2 Coordination between molecules and perovskites

The binding energies of different molecules to perovskites is firstly quantified with *ab initio* simulations. The saccharin molecules can form direct coordination to lead ions due to the strong electron donor affinity of S=O group. Based on the density functional theory [225], the binding energy of saccharin molecules to formamidinium lead bromide ($FAPbBr_3$) perovskite (001) surface is calculated to be 1.82 eV, while the binding energy of NMP is 1.01 eV (Figure 5.3), indicating that stronger coordination of saccharin molecules.

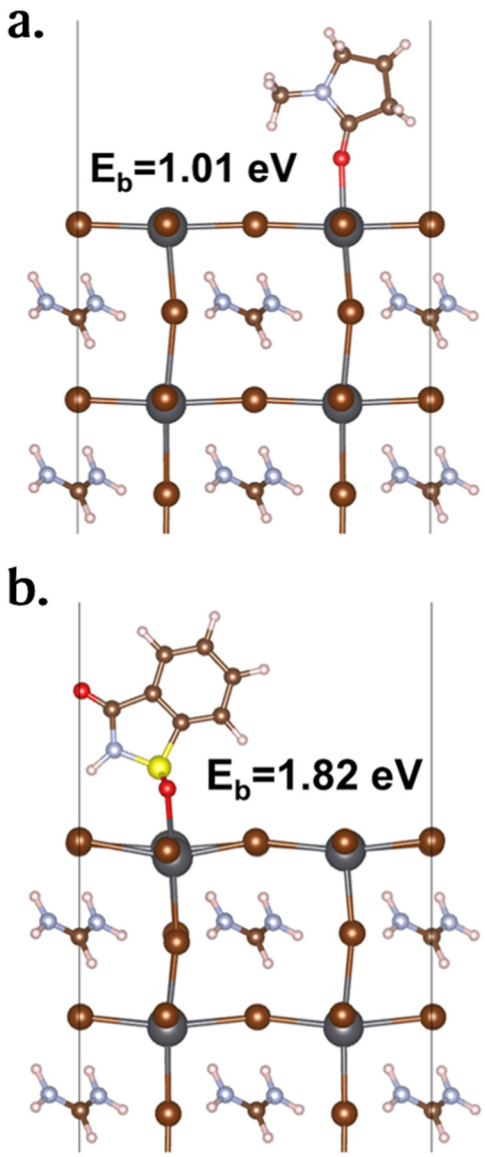

Figure 5.3 | Structures of (a) NMP and (b) saccharin adsorption on $FAPbBr_3$ perovskite (001) surface, respectively.

Fourier transform infrared spectrometer (FTIR) tests are then performed to confirm the stronger coordination between saccharin and lead ions. Herein, saccharin molecules together with lead bromide are dissolved in NMP solvent. Figure 5.4 compares the FTIR results of referred systems. It can be found that

in NMP solvent, the S=O peak of saccharin molecules downshifts from 1,329 cm^{-1} to 1,321 cm^{-1} after mixed with lead ions, suggesting that considerable coordination could form between saccharin and lead ions at the competition of NMP solvent molecules.

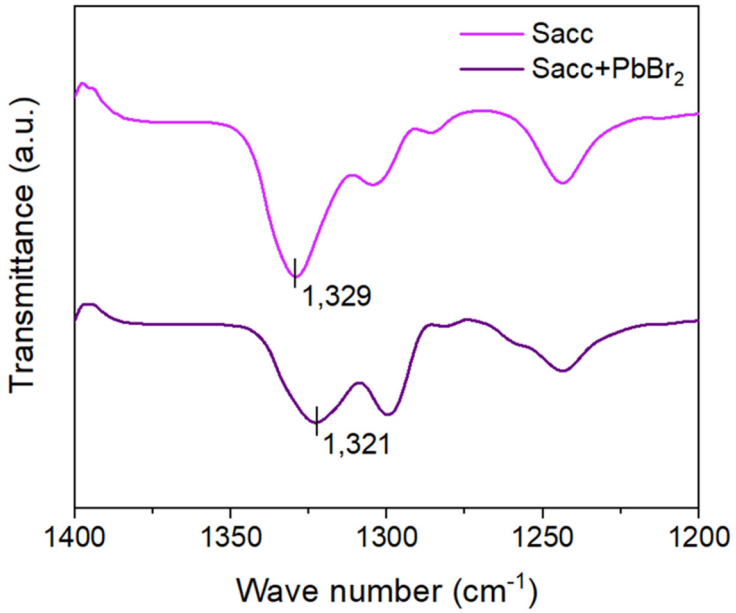

Figure 5.4 | FTIR results of saccharin and mixed systems.

X-ray photoelectron spectroscopy (XPS) tests of RDP films are then performed to unveil if such coordination can be maintained in solids. As shown in Figure 5.5, compared with the pristine RDPs, the binding energy of Pb 4f peaks downshifts with the coordination of saccharin, which demonstrates that lone electron pairs are denoted to the empty 6p orbitals of lead ions, forming coordination bonds. In addition, the S to Pb atomic ratio from the XPS results showed a significant increase from 4.1% (Pristine) to 16.8%

(Sacc), indicating that strong coordination of saccharin is retained in the perovskite films.

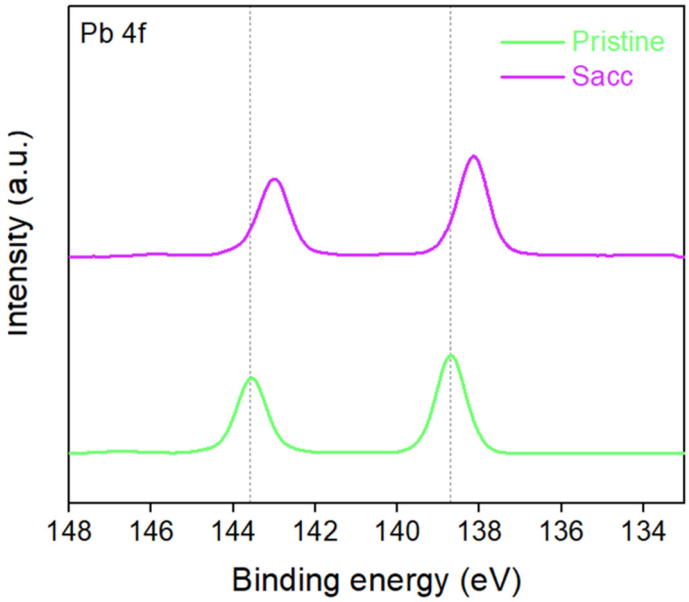

Figure 5.5 | XPS spectra for Pb 4f orbitals of pristine and saccharin incorporated RDPs.

To examine that the saccharin coordination has a system energy between low dimension and high dimension phases, monocrystals of low n phase (n=1 $(PEA)_2PbBr_4$ as the representative) and three-dimension phase (3D $FAPbBr_3$) are synthesized to check their stability and solubility with saccharin molecules [200, 226]. The phase purity of synthesized powder is further confirmed by X-ray diffraction, as shown in Figure 5.6. The monodispersed diffraction patterns of n=1 and 3D phases confirm the high quality and phase purity of synthesized monocrystal powders.

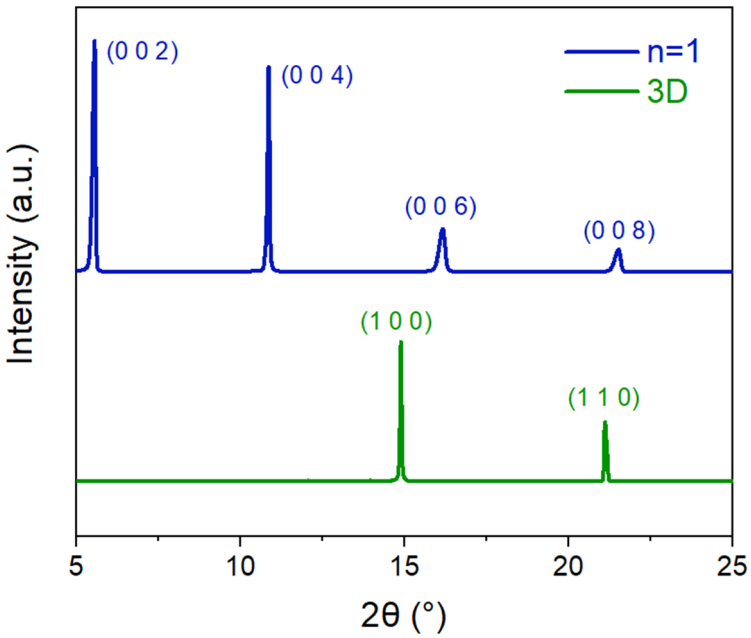

Figure 5.6 | X-ray diffraction pattern of synthesized monocrystal powders.

First, the effect of saccharin molecules on monocrystal powders are evaluated in nitrobenzene (NB) solvent. It can be found that both n=1 phase and 3D phase monocrystals are hardly soluble in pure NB. However, at the presence of saccharin, n=1 phases diminished rapidly while the 3D phase remains (Figure 5.7), showing that low dimensional phases are no longer stable at the presence of saccharin molecules. The added powders and saccharin are both 10 mg/ml. It can also be observed that both 3D and n=1 powders are hardly dissolved in pure NB solvents. However, in the presence of saccharin molecules, low dimensional phases (n=1) are dissolved rapidly, while no significant changes have occurred for 3D phases, indicating that saccharin molecules can selectively inhibit the deposition of low dimensional phases.

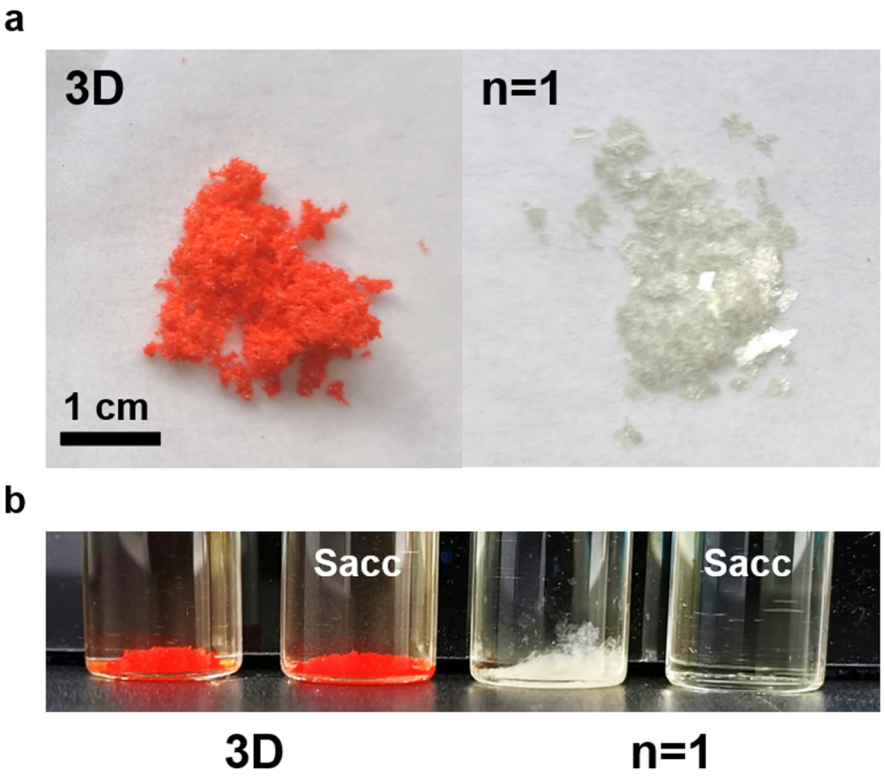

Figure 5.7 | (a) Photographs of 3D and n=1 phase powders and (b) Corresponding solutions in NB solvent.

The solubilities of n=1 phase and 3D phase in NMP are further measured by the dynamic dissolving method. The solubility of the n=1 phase improved significantly with saccharin, as shown in Figure 5.8, while the solubility of 3D phases is only slightly changed. Both results indicate that from the scope of system energy, saccharin coordinated lead ions are more stable than low dimensional phases under the precursor conditions. In pristine precursor system, lead ions can form low dimensional non-radiative phases spontaneously, while for saccharin coordinated lead ions, they can only spontaneously form large dimensional radiative phases rather than low

dimensional non-radiative ones, and thus low n phase dimensions are tailored.

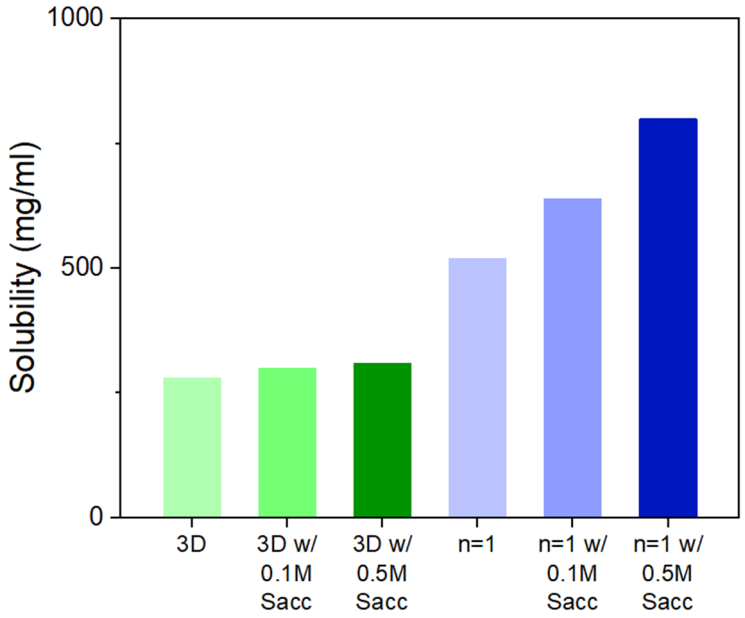

Figure 5.8 | Solubility of n=1 and 3D phase in NMP solvent (16 °C).

5.3 Optimized perovskite formation process with saccharin

Based on the results of the monocrystal solution tests, in-situ UV-Vis absorption measurements are performed to characterise the phase formation processes during spin-coating with saccharin coordination, as shown in Figure 5.9a and Figure 5.9b, respectively. It can be clearly seen that in the pristine sample, solid phase formation occurs immediately after anti-solvent dripping with a significant and rapid increase in absorption intensity, while such formation process is much slower and gentle in saccharin RDPs. Furthermore, the massive solid phase formation process in pristine

perovskites occurs within 1.5 s, which takes about 3 s after saccharin coordination. Thus, the relatively slow nucleation and growth rates in saccharin RDPs allow sufficient particle diffusion and consequently higher film quality. More importantly, the formation processes of divergent phases can be distinguished by intensity changes at different characteristic wavelengths. In the spin deposition process of pristine RDPs, low n phases formed rapidly after anti-solvent dripping, where distinct and discrete low n phase absorption peaks can be clearly observed at about 400 nm for n=1, 430 nm for n=2 and 465 nm for n=3 phases, followed by larger dimensional phases. However, for saccharin RDPs, no significant low n phase formation peaks are observed, instead a smooth and homogeneous film growth process is observed. Therefore, the saccharin coordination strategy not only allows better film growth and higher film quality, but also prevents the formation of non-radiative low n phases.

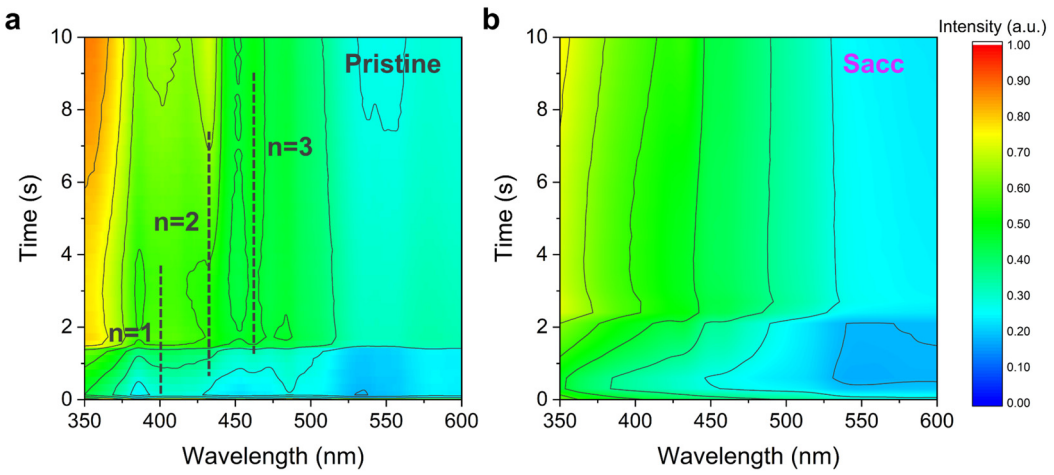

Figure 5.9 | In-situ UV-Vis absorption results in (a) Pristine and (b) Saccharin RDPs formation during spin-coating process (t=0 s represents the dripping of anti-solvent).

Then, more detailed structure information of RDP film is confirmed with grazing incidence wide-angle X-ray scattering (GIWAXS) measurements. Compared with pristine RDPs with considerable n=2 scattering patterns (Figure 5.10a), no low n phases scattering peaks are observed in saccharin RDPs (Figure 5.10b). Meanwhile, saccharin RDPs show much more uniform and narrower scattering patterns, indicating a better crystal growth process and high film quality, which is also consistent with the surface morphology results by SEM (Figure 5.11). It can be observed that the surface of saccharin perovskite film is more homogenous with fewer pinholes, in good accordance with the improved film quality and lower defect density of saccharin perovskite films.

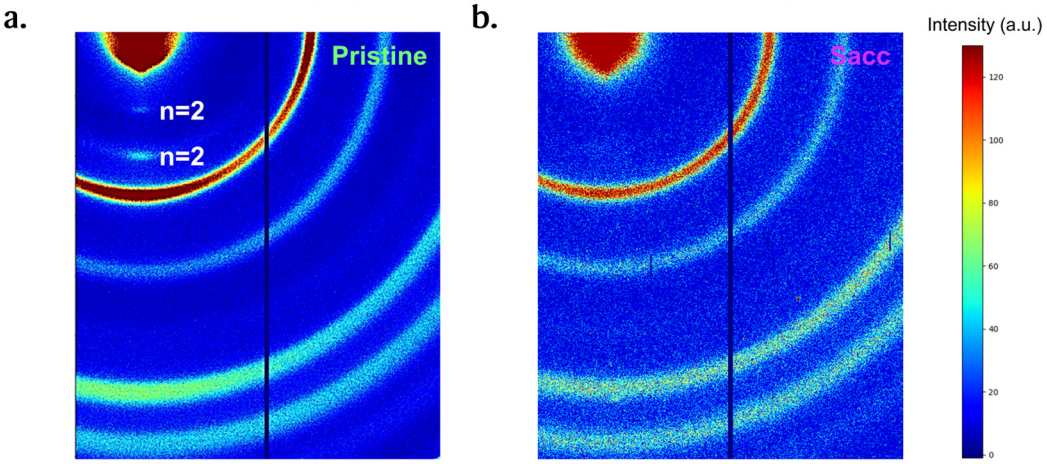

Figure 5.10 | GIWAXS results of (a) pristine and (b) saccharin RDPs, respectively.

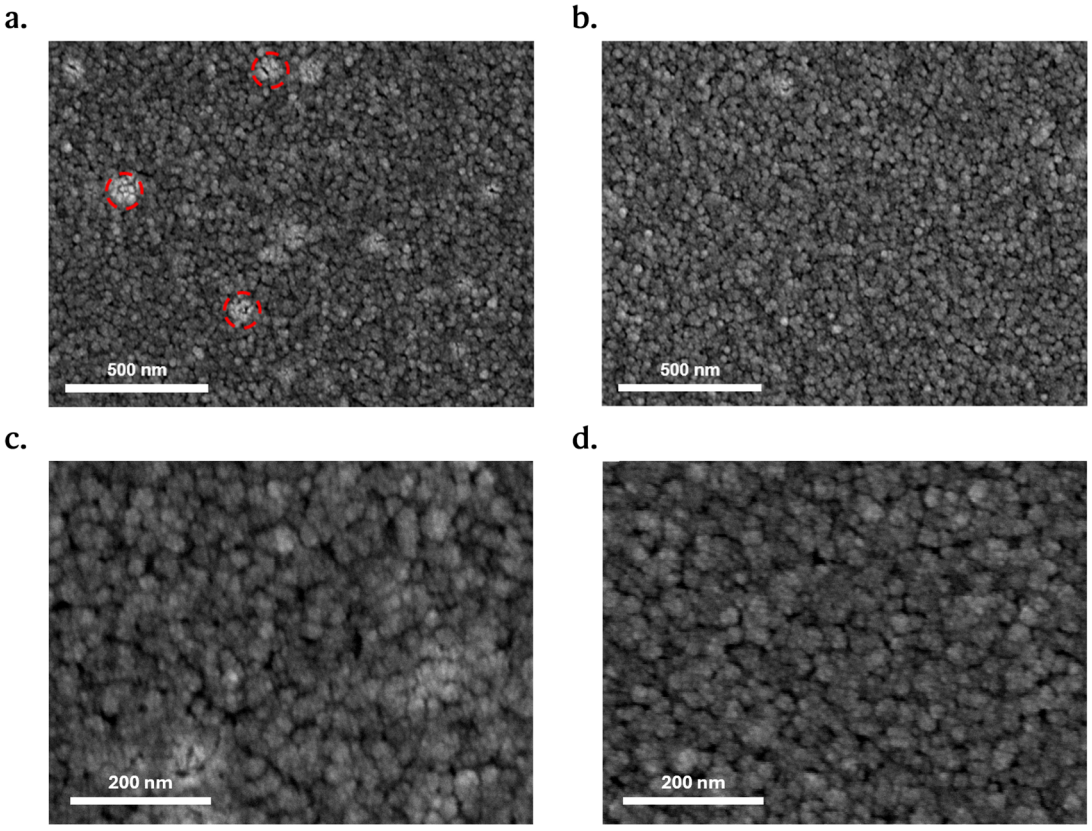

Figure 5.11 | Surface SEM images of pristine (a) and saccharin (b) perovskite films.

5.4 Improved luminescent properties of perovskites

Due to effective removal of non-radiative low n phases, the tailored-phase-dimension RDPs raise excellent optical properties. As shown in Figure 5.12, the photoluminescent quantum efficiency of coordinated RDPs are much higher compared with the pristine samples, indicating an efficient suppression of non-radiative recombination and corresponding decreased trap densities inside perovskite films.

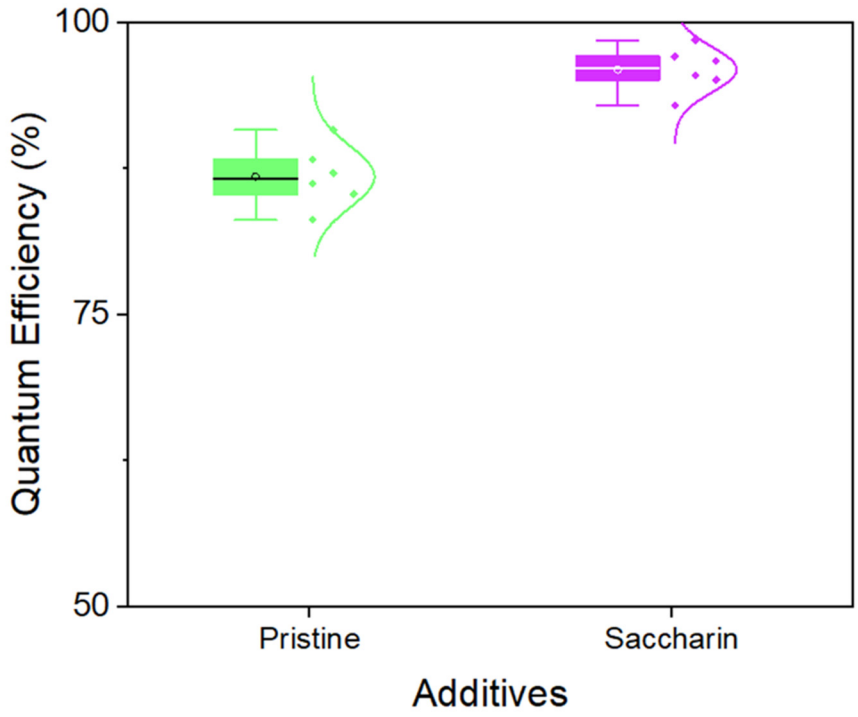

Figure 5.12 | Photoluminescent quantum efficiency statistical data of pristine and saccharin RDPs.

Meanwhile, transient photoluminescence (PL) measurements are conducted to reveal the exciton dynamics inside RDPs. In a typical measurement (Figure

5.13), the PL decay lifetime of saccharin RDPs is nearly one-fold longer than the pristine one, as the result of improved film quality and decreased trap density.

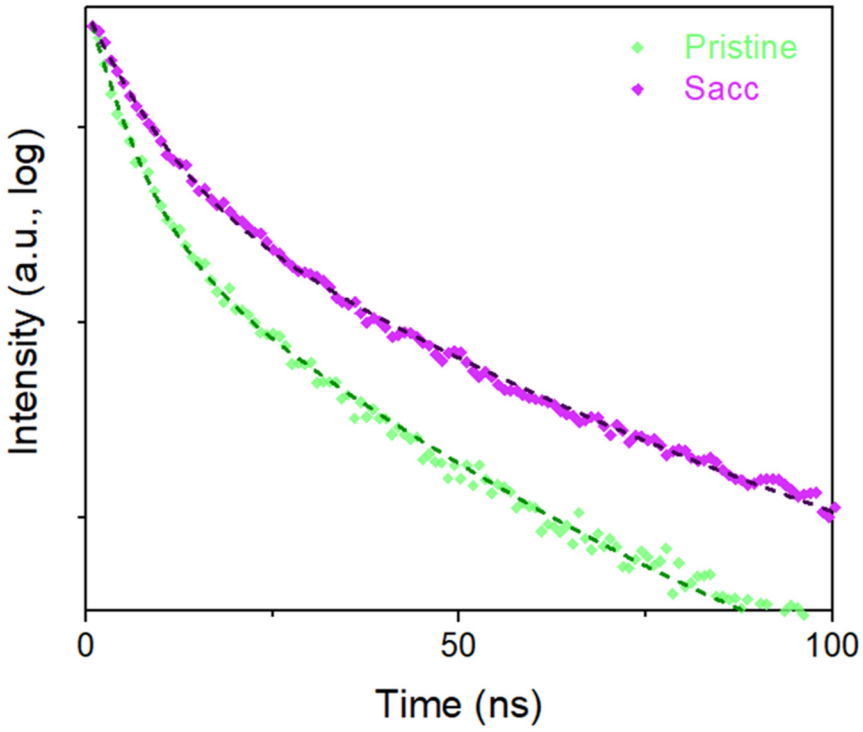

Figure 5.13 | Representative transient PL curves of RDPs.

Space charge limited current (SCLC) test is also used to quantify defect densities within the perovskite films. The structure of hole-only devices is FTO/NiOx/PVP/Perovskite/MoOx (12 nm)/Au (100 nm). The trap densities are calculated with the trap filled limited voltage (V_{TFL}) based on the method reported in literature [209]. Based on the results of the hole-only devices (Figure 5.14), saccharin coordination reduced the trap density by more than half, indicating a significant improvement in film quality.

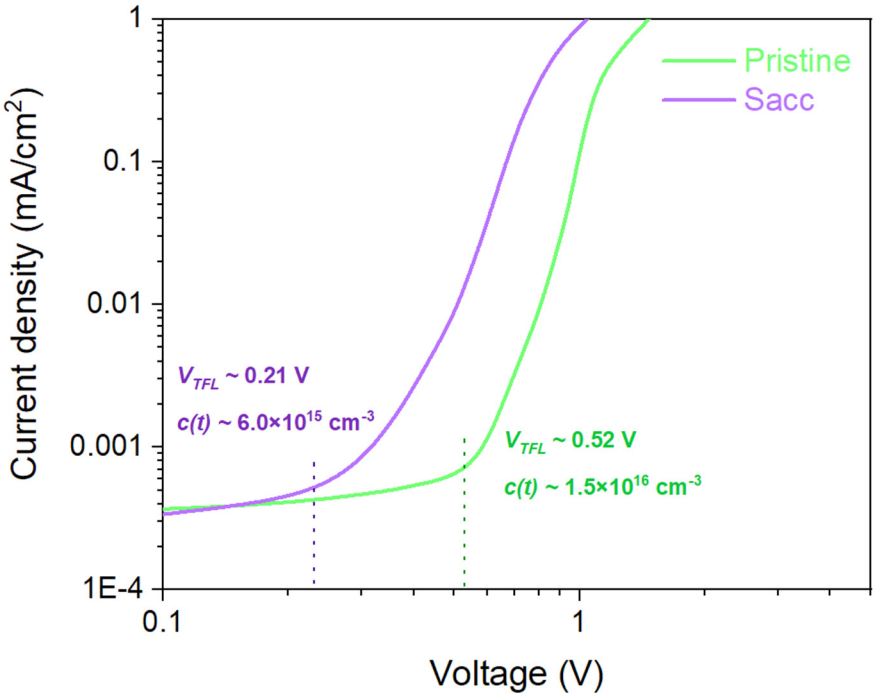

Figure 5.14 | SCLC results of pristine and saccharin perovskites.

Then, time-resolved absorption spectroscopy (TAS) measurements are employed to analyse the energy funnelling process, as shown in Figure 5.15. It can be observed that the pristine RDPs show evident bleaching peaks at the short wavelengths of 435 nm (n=2) and 470 nm (n=3), indicating that considerable low n phases existed in the pristine films. However, the intensity changes of saccharin RDPs for low n phases are negligible compared with the pristine ones, suggesting that saccharin coordination successfully hindered the formation of non-radiative low n phases.

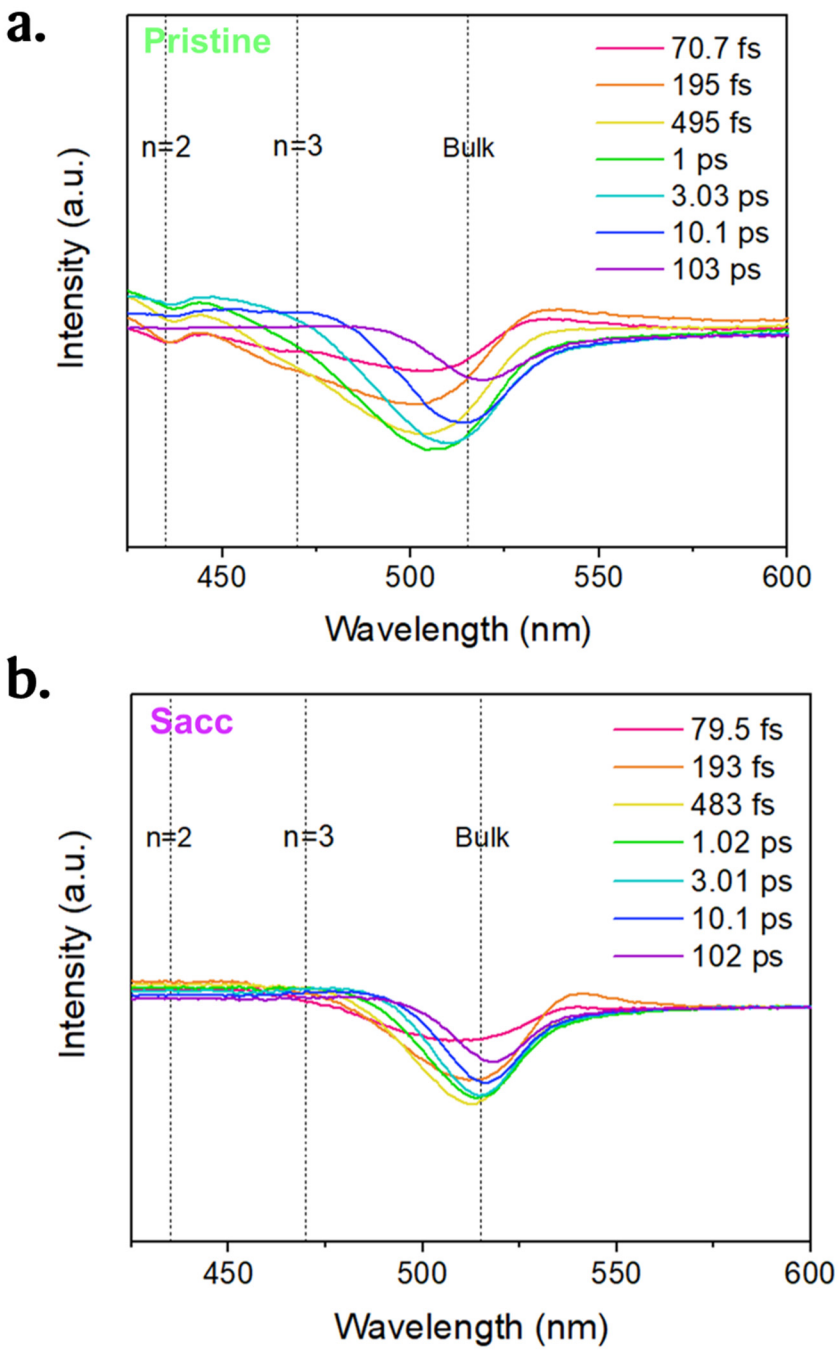

Figure 5.15 | Representative TAS results of (a) pristine and (b) saccharin RDPs, respectively.

Moreover, as for the radiative phases, the absorption intensity change reached maximum in no more than 0.6 ps at the wavelength of 515 nm for

saccharin RDP, while it took almost 3 ps in pristine one to reach the maximum, as shown in Figure 5.16, indicating a much faster and more efficient energy funnelling to radiative bulk phases with saccharin coordination. The improved energy funnelling to luminescent phase will significantly reduce energy losses and improve the luminescent properties of saccharin perovskites, showing enormous potential for high performance PeLED applications.

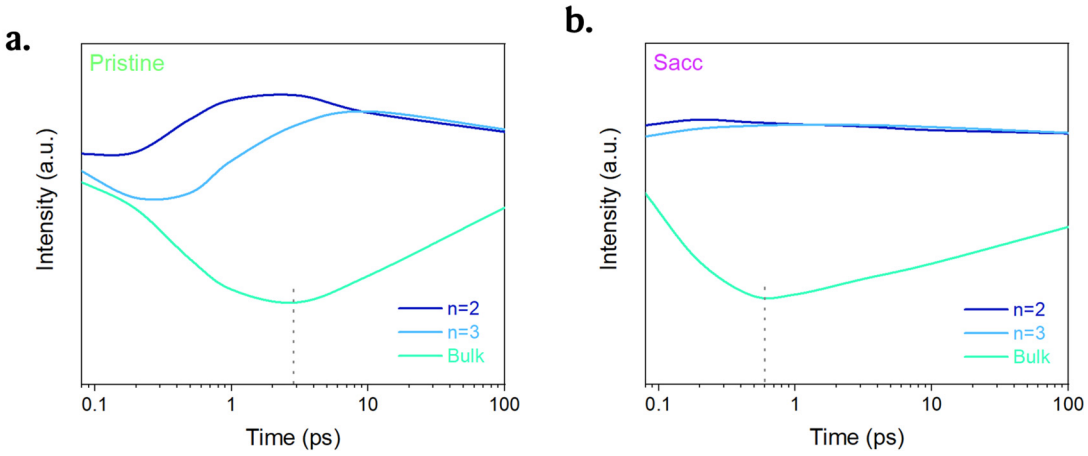

Figure 5.16 | Time-resolved intensity change figures of TAS results for different phases in (a) pristine and (b) Sacc perovskite films.

5.5 High efficiency PeLED devices

With the tailored phase dimensions and improved optical properties of saccharin RDPs, high-performance PeLED devices are then fabricated. The PeLEDs device structure applied in this study is FTO / NiOx / PVP / RDPs / TmPPPyTz / ADN-PBIP / LiF / Al / Ag, and the corresponding energy level

diagrams are shown in Figure 5.17, indicating a proper carrier injection with matched energy levels.

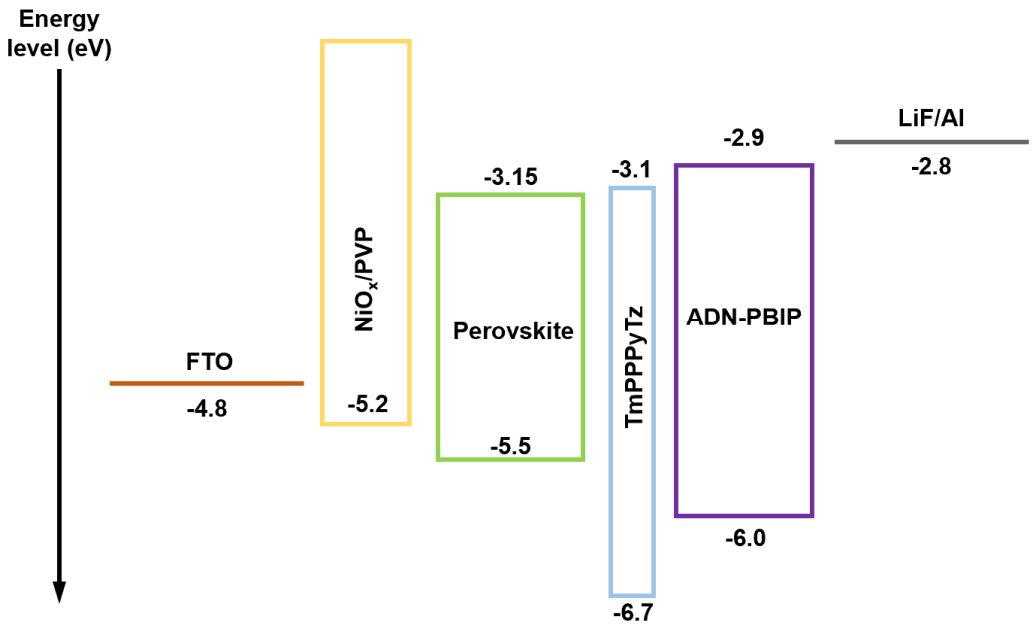

Figure 5.17 | Structure and corresponding energy band diagram of PeLED device.

The FTO substrates chosen here showed substantial high-temperature stability and compatibility with NiO_x processing, with negligible sheet resistance changes even after long period high temperature annealing, as shown in Table 5.1. All substrates are annealed at 550 °C for 1 h in the ambient. 6 substrates per group are measured. The optimization results of saccharin concentration are listed as Table 5.2, and the optimized saccharin concentration is determined as 10 mg/mL with the highest device EQEs.

Table 5.1 | Sheet resistivity of substrates under high-temperature annealing.

Average sheet resistivity (Ω/sq.)	FTO	ITO
Before annealing	13.8	15.2
Annealed	14.7 (+6.5%)	101.8 (+569.7%)

Table 5.2 | Maximum EQE of PeLEDs with different saccharin concentrations.

Saccharin concentration (mg/mL)	EQE_{max} (%)
0	27.5
2	28.9
5	30.7
10	31.3
15	25.9
20	5.2

The electroluminescence (EL) spectra, current density–voltage–luminance (*J-V-L*) and the EQE curves are plotted as Figure 5.18, respectively. The EL peak of saccharin PeLEDs is 529 nm with a FWHM of 20.6 nm (CIE coordination (0.178, 0.774)), different from those of pristine PeLEDs of 525 nm and 22.8 nm (CIE coordination (0.162, 0.776)). The reduction in FWHM indicates an improvement on radiative phase purity and reduced defect density. Meanwhile, The *J-V-L* curve of saccharin PeLED shows enhanced current

density and luminance than the pristine one (Figure 5.18b), in good accordance with the improved energy funnelling and optical properties. The saccharin PeLEDs possess a highest EQE of 31.3% (Table A2-1), with an average EQE of 28.4±1.1% over 40 devices (Figure 5.19), much higher than the pristine EQE_{max} of 27.5%. The maximum current efficiency (CE) of saccharin PeLEDs also reaches impressive 132.1 cd/A (Figure 5.20), and the highest luminance of saccharin PeLEDs reaches about 277,000 cd/m^2, indicating a bright potential on outdoor display and lighting applications.

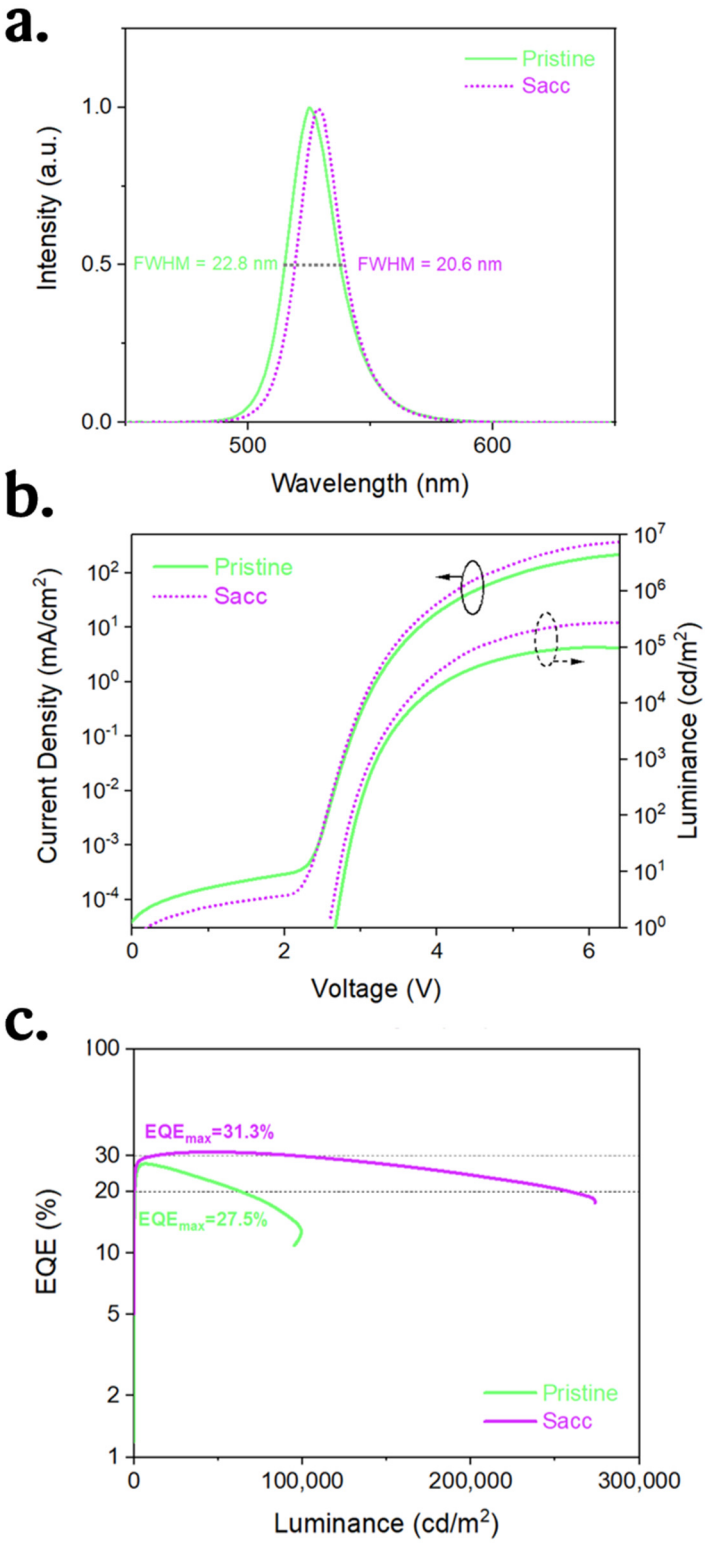

Figure 5.18 | PeLEDs performance. (a) EL Spectra of PeLEDs. (b) Representative *J*–*V*–*L* data of PeLEDs. (c) EQE of the pristine and saccharin devices, respectively.

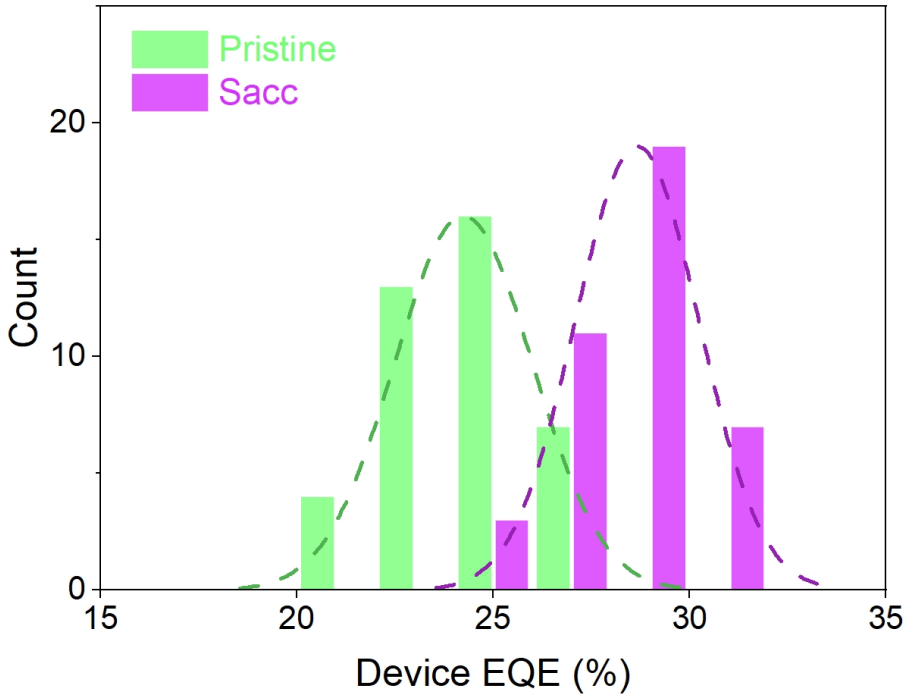

Figure 5.19 | Statistical device EQE_{max} of pristine and Sacc PeLEDs. 40 devices are measured in total, respectively.

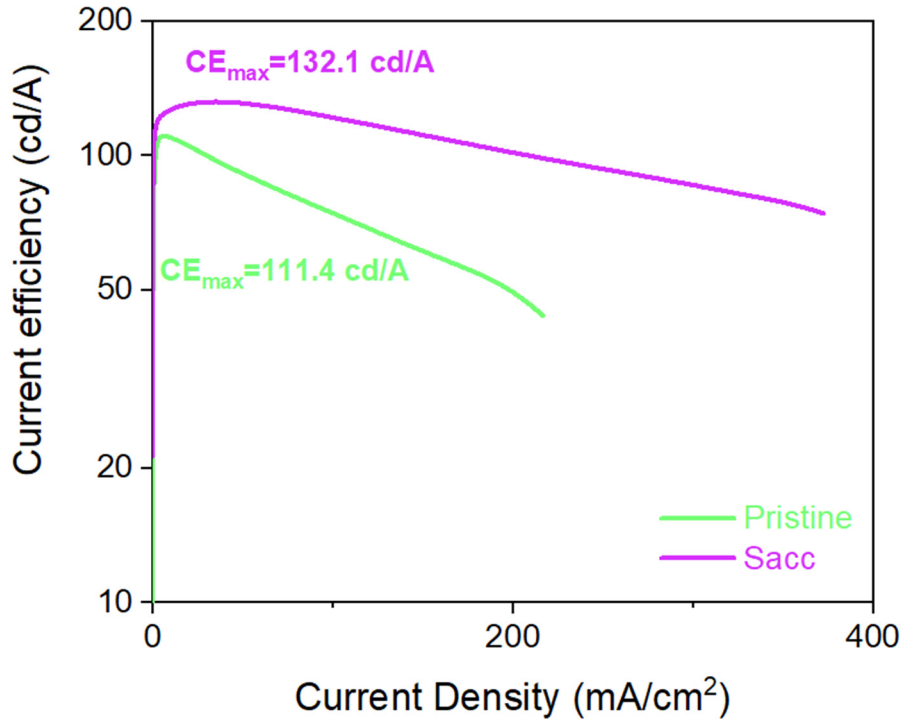

Figure 5.20 | Current efficiency (CE) versus current density for PeLED devices.

Then, optical simulation with reported device structures is performed to confirm the EQE measurements. The maximum EQE of saccharin PeLEDs is close to the theoretical outcoupling efficiency of 35.7% considering the photon recycling effect [206, 207], as shown in Figure 5.21, indicating state-of-art device fabrication and material optimization techniques.

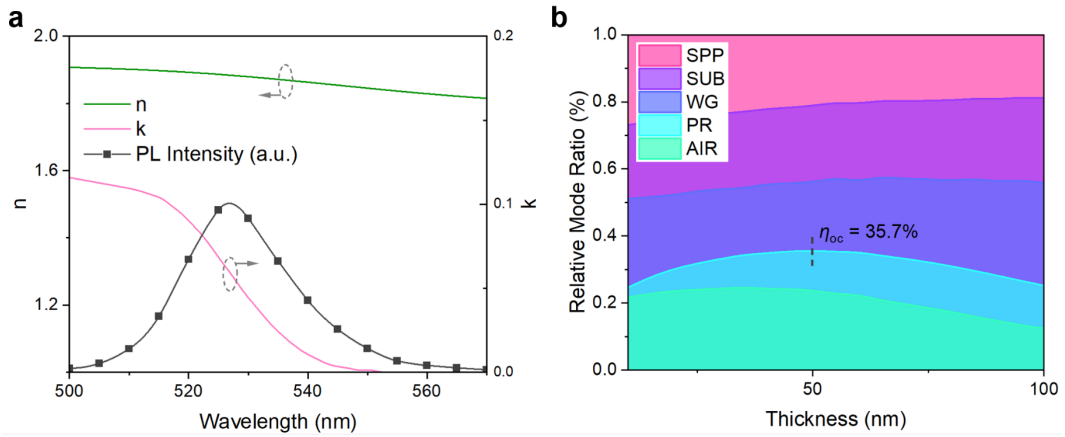

Figure 5.21 | Optical simulations of PeLEDs. (a) Refractive index (n, k) and photoluminescent spectrum of perovskite film employed in the simulation. (b) Calculated outcoupling efficiency considering the effect of photon recycling as a function of perovskite thickness in our device. Background colours represent the fractions of air (AIR), waveguide (WG), substrate (SUB), and surface plasmon polariton (SPP) modes.

Also, the angular intensity distribution of our LEDs followed the Lambertian distribution (Figure 5.22), indicating that the normal structure of our LED devices without extra optical outcoupling strategy. Our device EQEs as well

as the EQE measurement are then cross-checked to ensure the reproducibility of our results, as shown in Figure 5.23. Both crosscheck results have underscored the reliability of our setups and the results with great consistency.

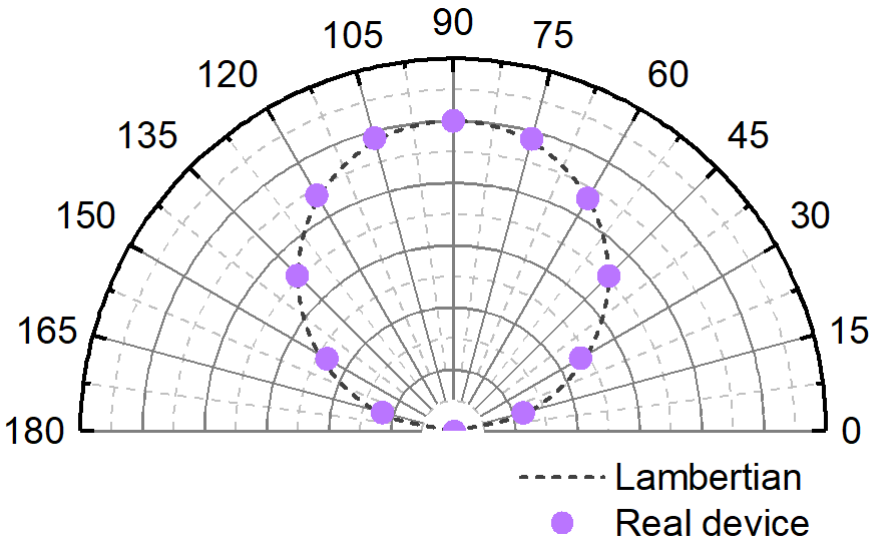

Figure 5.22 | The angular intensity distribution of Sacc PeLED.

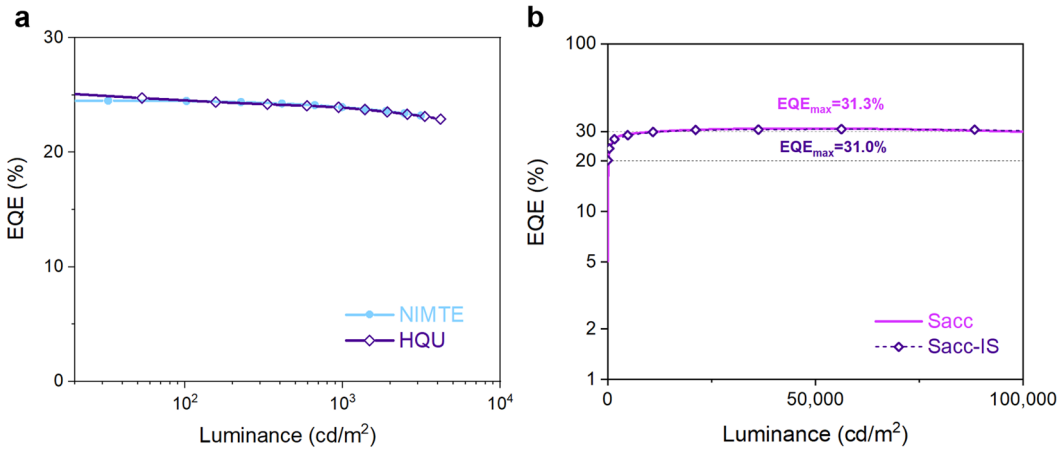

Figure 5.23 | Cross-check results of device EQEs as well as the EQE measurement. (a) Cross-check results of OLED (commercial device from Brilliant Optoelectronics, Zhejiang) measured in our lab at Ningbo Institute of Materials Technology and Engineering, Chinese Academy of Sciences (NIMTE) and at Dr Zhanhua Wei's group, Huaqiao University (HQU). (b) Cross-check results of our PeLEDs measured at our setup (photodiode) and the integrating sphere (IS, XP-EQE-Adv, Guangzhou Xipu Optoelectronics).

The tailored-phase dimensions of RDPs also contribute to extraordinary device operational stability owing to the removal of unstable phases. The operational lifetime of PeLEDs is presented in Figure 5.24. The initial luminance is tuned at 10,000 cd/m² and all the devices are measured at the constant current density mode. The champion T_{50} lifetime (time when the luminance drops to the 50% of initial value) of saccharin PeLEDs reached over 76.9 hours (equivalent over 211,800 hours at the initial luminance of 100 cd/m², Figure 5.25), while the highest T_{50} of pristine devices is only 6.5 h.

Herein, Equivalent operational lifetime T is calculated with the relationship of

$$T/T_0 = (L/L_0)^n \qquad 5.2.$$

Wherein T_0 and L_0 are the referenced lifetime and luminance, respectively. The calculated T_{50} lifetime at 100 cd/m² is about 211,846.1 hours with the slope n of -1.72. The *impressive* stability of saccharin PeLEDs is, to our knowledge, the highest T_{50} estimated so far in PeLEDs.

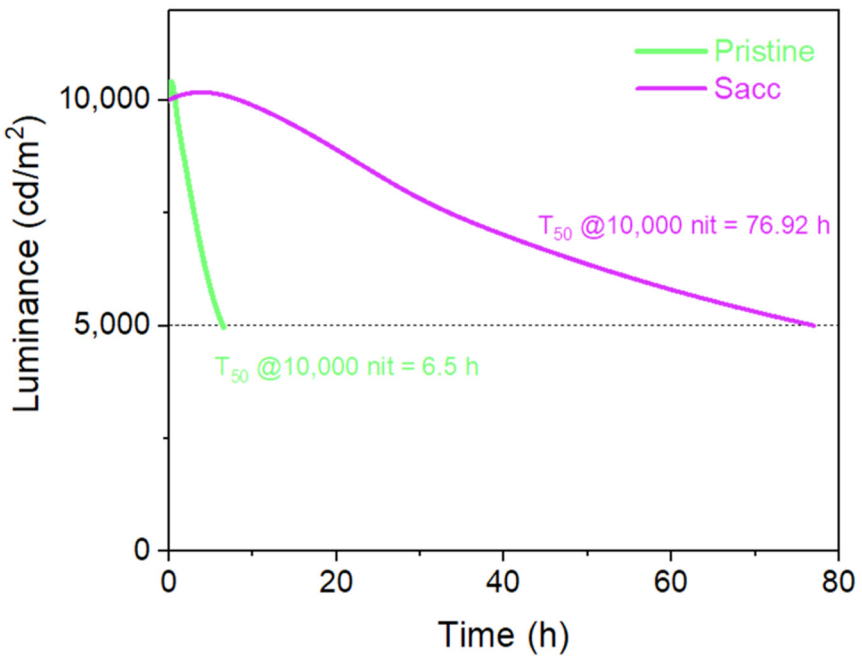

Figure 5.24 | Operational lifetime of PeLEDs.

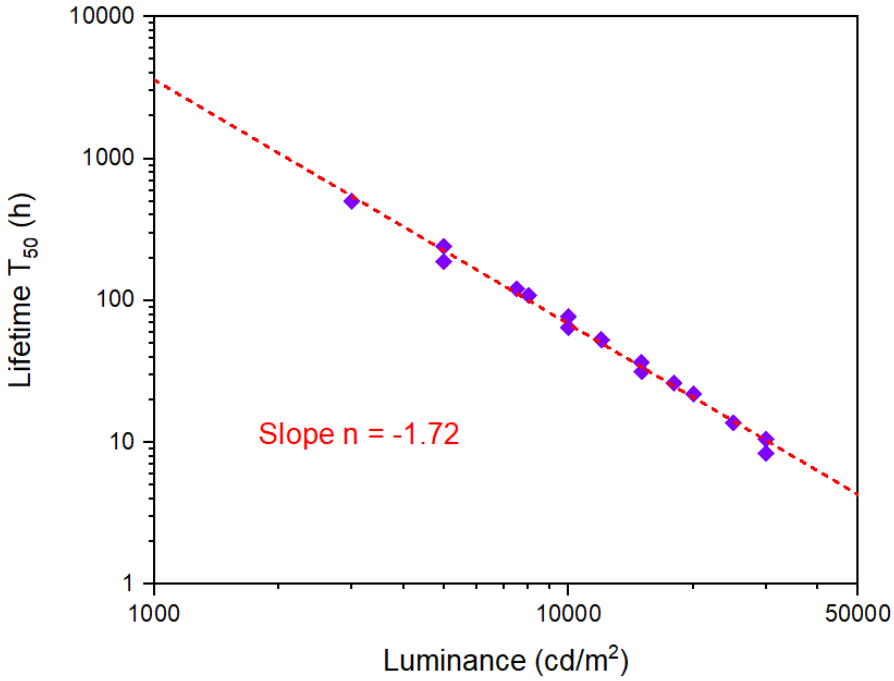

Figure 5.25 | Representative T_{50} lifetime of PeLEDs at different initial luminance.

Moreover, it is noteworthy that additional sweeteners or sweet molecules, such as D-Glu and Cyc Na (Figure 5.26), have also been demonstrated as performance-enhancing additives in PeLEDs. A comprehensive summary of the maximum EQEs achieved with various sweet molecule additives is presented in Table 5.3. Remarkably, every molecule listed contributes to a notable improvement in device efficiency, confirming the generality and robustness of our coordination-based approach.

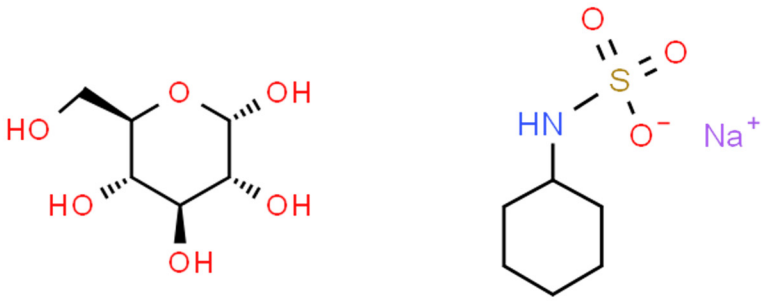

D-glucose (D-Glc) Cyclamate sodium (Cyc Na)

Figure 5.26 | Molecular structure of D-Glu and Cyc Na.

Table 5.3 | Maximum EQE of PeLEDs with different additives.

Additive	EQE_{max} (%)
No additive	27.5
Sacc	31.3
D-Glu	29.5
Cyc Na	30.8

Finally, since the coordination between saccharin molecules and lead ions are independent of the halide types and other ion components within perovskites, underscoring the generality of our coordination strategy with broad applications transcending the perovskite category limitations. Therefore, the universality of this approach is further highlighted by successful extension to other promising PeLED systems, and consistently improvements on device performance are also achieved.

First, anti-solvent-free inorganic PeLEDs are fabricated to confirm the universality. In a typical inorganic RDP (caesium lead bromide, $CsPbBr_3$) green LEDs, even the A-site ions are substituted with Cs^+, a narrow emission spectrum with FWHM only 18.4 nm and maximum EQE of over 23% is still achieved with saccharin coordination, around four-fold higher than the pristine ones, as shown in Figure 5.27, indicating an significant enhancement of device performance with our saccharin coordination strategy independent of A-site ions.

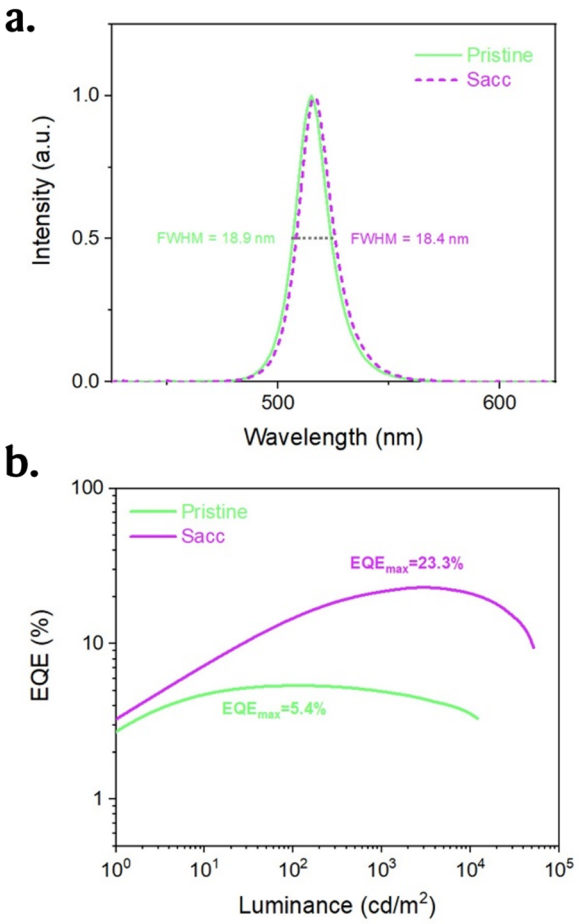

Figure 5.27 | Inorganic Green PeLEDs performance. (a) EL Spectra. (b) EQE of the pristine and saccharin devices, respectively.

Furthermore, the application of this same strategy has been pivotal in achieving pure red PeLEDs based on caesium lead iodide ($CsPbI_3$), yielding EQE surpassing 16% with emission peaks centred around 630 nm (Figure 5.28), highlights one of the highest efficiencies recorded for pure red PeLEDs within the wavelength range of 625 to 635 nm (Table A2-2). Importantly, the results extend to perovskite systems with varied A-site cations and halide compositions, demonstrating its remarkable universality across different material formulations. These results may also shed light on the possibility of future commercial anti-solvent-free PeLEDs.

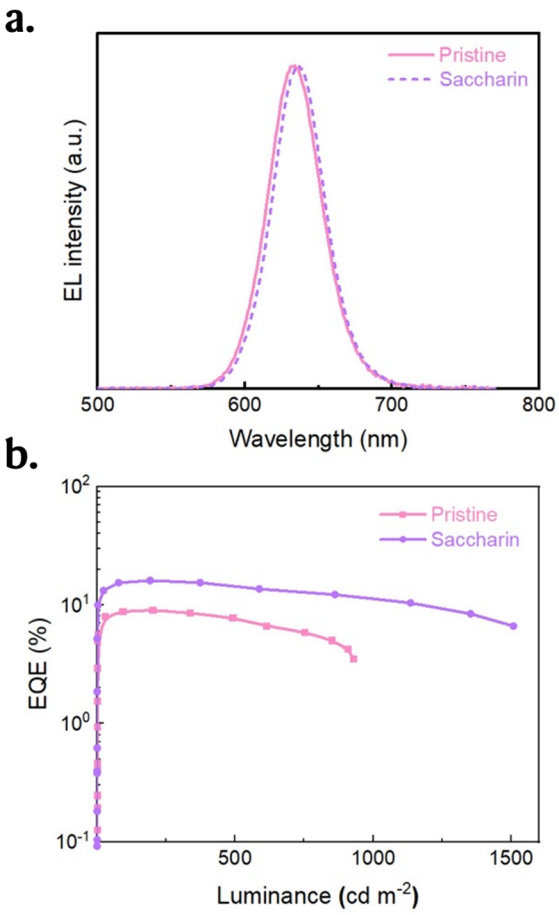

Figure 5.28 | Inorganic Pure Red PeLEDs performance. (a) EL Spectra. (b) EQE of pristine and saccharin devices, respectively.

5.6 Discussion

In this chapter, a novel sweet coordination strategy is introduced to optimize the crystallization process of perovskites and suppress the defects, thereby fabricating high-quality perovskite film and efficient and stable PeLEDs. The idea originated from the sweetness of lead acetate salts, but the comprehensive investigation on the mechanism has brought insights into the formation process of perovskite, supplementing our ideas in Chapter 4 about decelerating the crystallization of perovskites.

The underlying mechanism of the strong coordination of sweet molecules originates from the distinctive sweet functional group, which facilitates binding through coordination bonds and to hydrogen-bond-like interactions with both cationic (Pb^{2+}) and anionic (Br^{-}) species, as depicted in Figure 5.4 and Figure 5.5. The interactions between sweet molecules and ions markedly decelerate the formation process of perovskites, necessitating the disruption of these molecular-ion interactions prior to perovskite formation, thereby enabling a gradual and uniform perovskite crystallization process compared to the pristine samples, as Figure 5.9 shows. Consequently, the resultant perovskite crystallinity was apparently improved compared to pristine sample, as evidenced by the GIWAXS results (Figure 5.10), with greatly improved luminescent efficiency (Figure 5.12). Furthermore, the optimized crystallization process has suppressed the defect formation and

markedly diminishes the defect density in the corresponding perovskite films, as characterized in Figure 5.13 and Figure 5.14, thereby resulting in the enhanced device EQE as well as operational stability.

Moreover, other sweet molecules enhancing the performance of PeLEDs, as listed in Table 5.3, together with the successful applications of sweet molecules to other categories of perovskites (Figure 5.27 and Figure 5.28), has confirmed the generality and robustness of our coordination-based approach. These results have also inspired the additive selection for PeLEDs based on the strong coordination principles between sweet functional groups and lead ions. Further investigation about more sweet molecules screening can be performed to consolidate the scientific foundation of our strategy.

The successful employments of sweet small molecules are impressive, while alternative sweet "molecules" shall not be overlooked. Sweet proteins [227], with much larger molecular weight, are also important sweeteners in food science. Despite the challenges that the enormous size of proteins may hinder the charge transfer inside LEDs, and the threats of thermal instability as well as the degradation triggered by heavy metal ions, those sweet proteins can also offer a compelling comparator to enrich our understanding of the mechanisms of sweet functional groups.

Finally, the sweet coordination strategy proposed in this chapter has brought up the concern about the additive availability for high-performance PeLEDs. To date, in the pursuit of improving PeLEDs performance, employment of additives has become one of the most common strategies, with a key distinction being between ready-made commercial molecules and those specifically synthesized. For example, as a successful sweetener molecule, our saccharin additive has exhibited a good availability throughout the market, with low cost due to the industrialized manufacturing (no more than 0.1 Chinese yuan per gram based on chemical platforms like Merck or CASMart, in stock). Meanwhile, the quick access of commercial molecules supports rapid experimentation without any warehouse management for laboratory research, with usually well refined eco-friendly synthesis and high yield. However, for most specifically synthesized molecules at an early stage, the availability and cost often hinder further investigation. For example, one of the successful custom-designed additive molecules, tris(4-fluorophenyl)phosphine oxide [72] (Figure 5.29), not only shows low yield during the laboratory level synthesis, but also have relatively inferior availability and higher cost (over 300 Chinese yuan per gram based on CASMart, three weeks delivery period; unavailable on Merck).

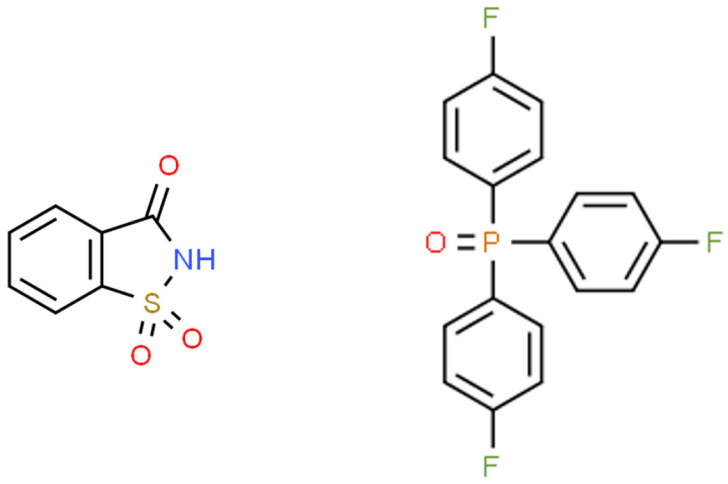

Saccharin Tris(4-fluorophenyl)phosphine oxide

Figure 5.29 | Molecular structure of saccharin and tris(4-fluorophenyl)phosphine oxide.

Therefore, although synthesizing new additive molecules remain critical and innovative for high-performance PeLEDs, and the availability as well as the costs can be gradually improved from time to time, employment of current commercial molecules also provides an accessible path. Their wide availability, lower costs, and straightforward procurement can facilitate the scaling up of PeLED technology towards real-world applications. To date, a large variety of commercial molecules remains hardly investigated as perovskite additive, with a significant opportunity for further development. With commercially available molecules, scientists can speed up the improvements on PeLEDs and MHP-based optoelectronic devices with better availability, striking a balance between performance, cost, and environmental sustainability.

5.7 Summary

In this chapter, the phase dimensions of RDPs could be tailored, and the defects can be suppressed by a simple sweet coordination strategy. By maintaining proper coordination with lead ions using commercial molecule saccharin during film deposition stages, the radiative phases are purified, and the film quality of RDPs are significantly improved. High-performance green PeLED device with highest EQE of 31.3% (28.4±1.1% in average) and champion T_{50} lifetime of 76.9 hours at 10,000 cd/m^2 is fabricated, with the highest luminance of 277,000 cd/m^2.

Moreover, utilizing commercially available sweet molecules, highly efficient green and record efficiency pure-red inorganic PeLEDs are also fabricated following the same strategy without anti-solvent, confirming the universality of our coordination mechanism and strategy. By transcending the specificity of perovskite compositions, our strategy paves the way for a new framework for optimizing PeLED systems. This generalizability of our strategy has signified a critical step forward in the strategy design of PeLEDs, not only fortifying the conceptual understandings of MHP material formation during solution process, but also advancing the frontiers of MHP-based lighting and display technologies.

Chapter 6. Hindering Ion Migration with Ion Pinning Strategy

6.1 Introduction

In this chapter, a formamidinium-based organometal quasi-2D perovskite material system and corresponding PeLED devices are investigated. Different from previous two chapters, the quasi-2D perovskites here are fabricated by spin-coating the precursors with 4-fluoro-phenethylammonium bromide (FPEABr) ligands, and the main chemical reaction is:

$$2FPEABr + (n-1)FABr + nPbBr_2 \rightarrow FPEA_2FA_{n-1}Pb_nBr_{3n+1} \qquad 6.1$$

Wherein n represents the n value. The application of FPEABr here is reported to improve the operational stability of PeLEDs based on the literature [209], in good accordance with the main topic of PeLEDs ion migration and related stability issues.

To solve the PeLEDs stability issues, in this chapter, a simple and effective ion pinning strategy is demonstrated to pin all perovskite ions spontaneously, suppress the ion migration process and significantly improve the operational lifetime of PeLEDs. A highly fluorinated molecule, 1H,1H-perfluorohexylamine (PFHA), could form strong coordination with all perovskite ions spontaneously and significantly suppressed the ion migration process, as Figure 6.1 shows. Therefore, by inducing PFHA into perovskites, ultra-stable and efficient green PeLEDs are fabricated, confirming the stability and future industrialization potential of for display and lighting industries [228].

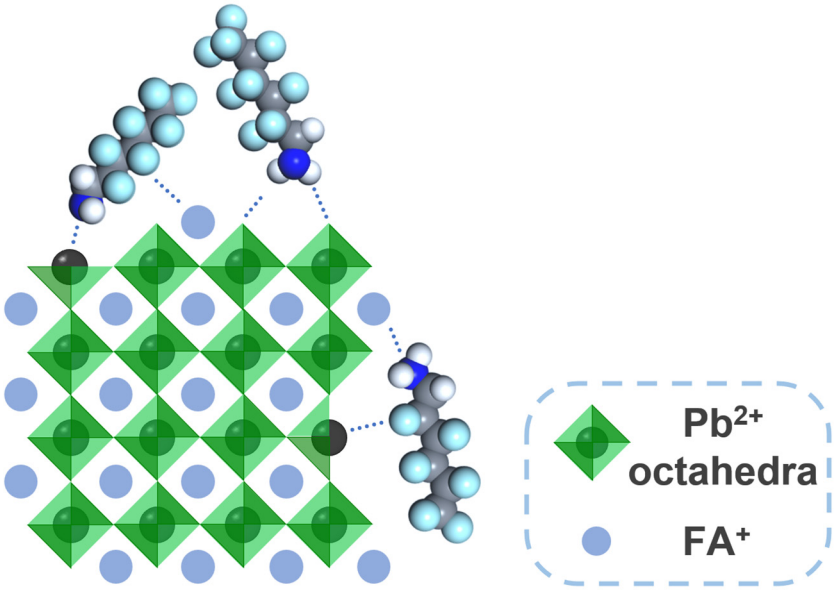

Figure 6.1 | Scheme of ion pinning effect.

6.2 Strong pinning effect of PFHA molecules to perovskites

As shown in Figure 6.2, the degradation of perovskite phase is typically mediated through the phase transition, characterized by the conversion of luminescent perovskite phases into non-luminescent PbX_2 counterparts. These A-site ions, particularly MA^+ and FA^+, tend to decompose upon exposure to external stimuli such as moisture and oxygen, which inevitably trigger the degradation of MHP film [229].

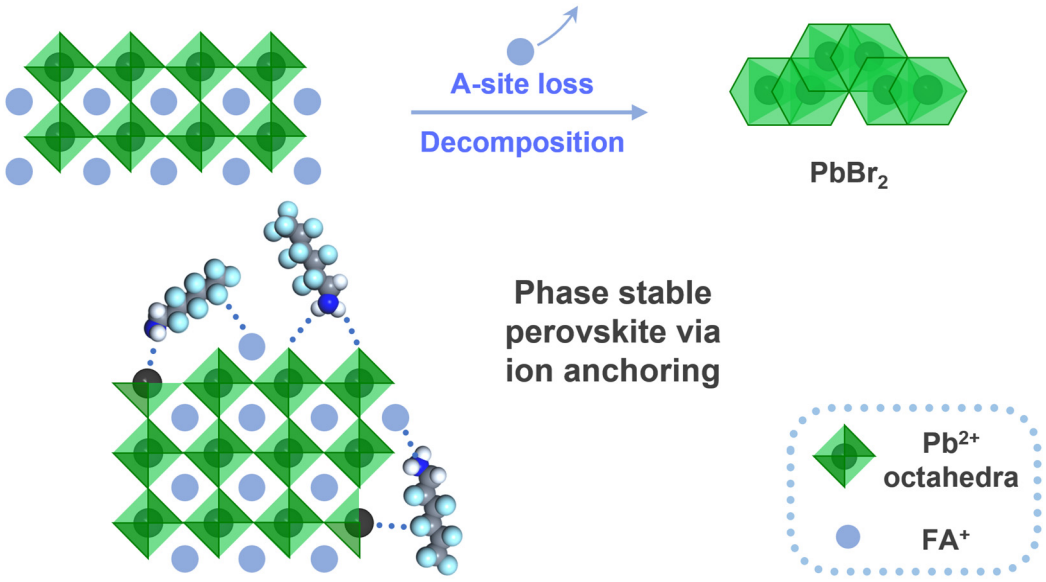

Figure 6.2 | Typical degradation process of organometal halide perovskite and scheme of ion pinning effect.

This transformation is clearly evidenced by X-ray diffraction (XRD) analysis in Figure 6.3. The scattering patterns of as-prepared pristine perovskite film manifested definitive peaks corresponding to the perovskite phase initially, yet upon 28 days of ambient storage (at 20 °C and 50% relative humidity), the XRD spectra indicated a comprehensive shift to the $PbBr_2$ phase, indicating the intrinsic susceptibility of perovskite phase transition.

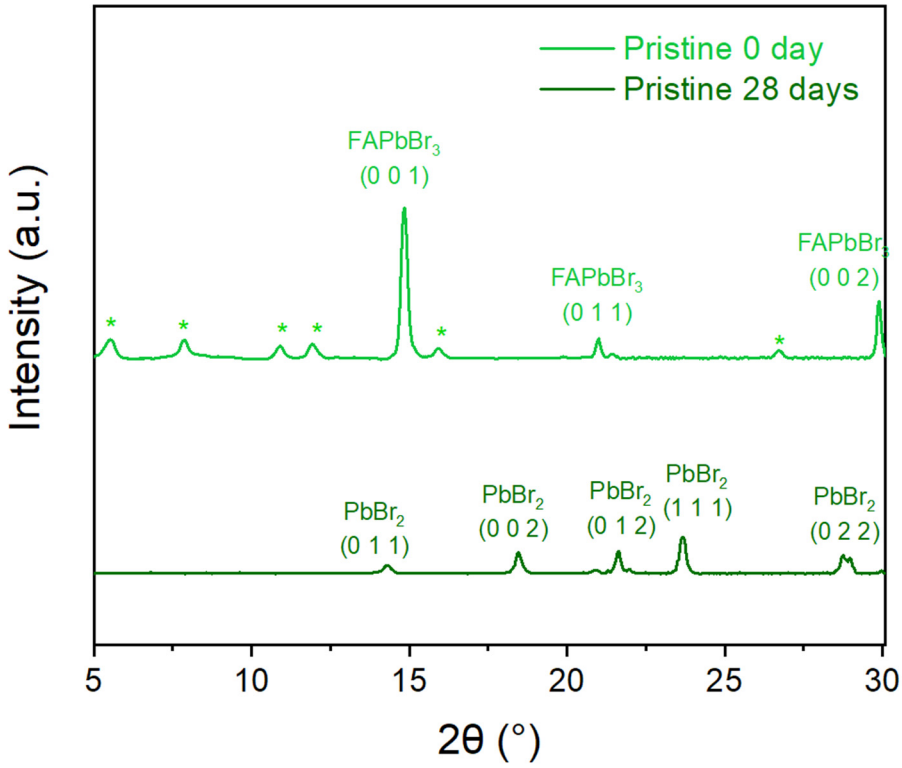

Figure 6.3 | XRD patterns of pristine perovskite film before after ambient storage for 28 days (*: low dimensional phases).

Such process can be further fortified with X-ray photoelectron spectroscopy (XPS) atomic ratio results, as revealed in Figure 6.4. Herein, an absence of nitrogen element of the pristine perovskite film, while a reduction in the Br-to-Pb atomic ratio from approximately 3.09:1 to 2.06:1 upon 28 days of storage, was noted, corroborating the phase transition from a luminescent perovskite to non-luminescent $PbBr_2$. The loss of nitrogen, a key indicator of A-site ions inside organometal halide perovskites, has presented the critical routine to the understanding of perovskite degradation process.

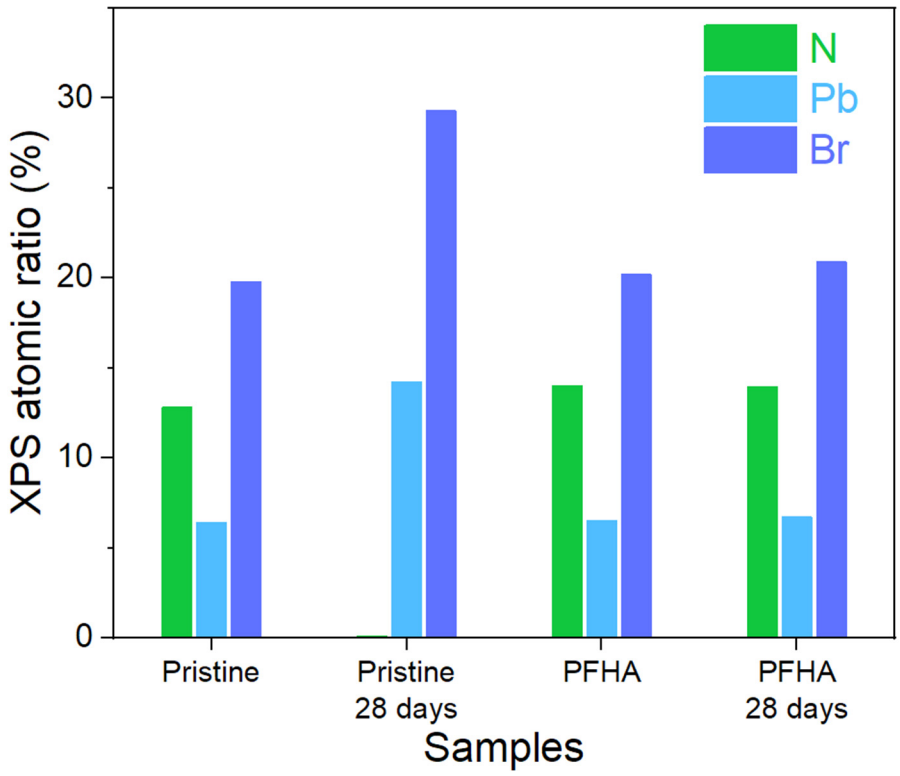

Figure 6.4 | XPS atomic ratio changes for pristine and PFHA perovskite film before after ambient storage for 28 days.

Collectively, these findings have highlighted the centrality of phase stabilization in the pursuit of long-term stable perovskite-based photoelectronic devices. Evidently, maintaining the luminescent phase stability is paramount to the fabrication of ultra-stable PeLEDs, necessitating the development of efficacious methodologies for phase stabilization. The phase transition of perovskite is predominantly rooted in the profound ion mobilities and subsequent severe ion migration [22]. To address this challenge, an effective ion pinning strategy to spontaneously immobilize all perovskite ions have been developed, particularly A-site ions, achieving

significant phase stabilization effect. While critical phase stabilization was achieved with our ion pinning strategy. As evidenced by the XRD measurement, the PFHA pinned perovskite retained their phase structure, exhibiting unaltered XRD patterns even following a 28-day exposure to ambient conditions, as shown in Figure 6.5.

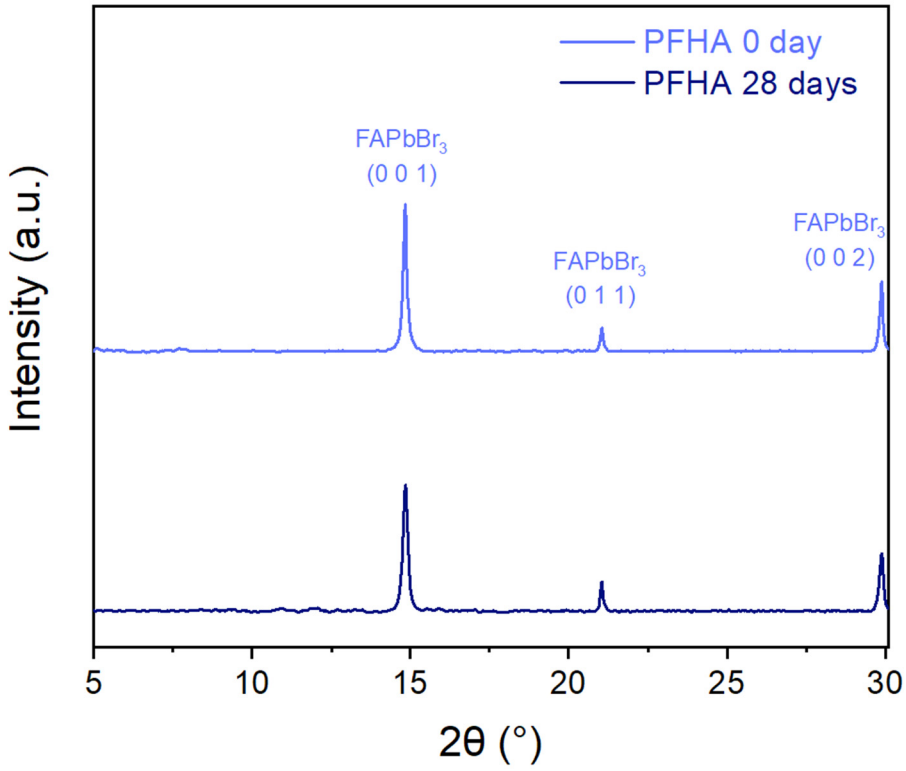

Figure 6.5 | XRD patterns of PFHA pinned perovskite film before after storage in the ambient for 28 days.

Notably, the disappearance of the low dimensional phases is attributed to a process known as "solvent sieve", wherein polar solvents selectively dissolve and remove low dimensional phases, thereby leaving perovskites with higher

dimensional perovskite structures [73]. Such effect can be also confirmed with the UV-Vis spectroscopy, where the peaks for low dimensional phases totally disappeared after PFHA treatment, as presented in Figure 6.6.

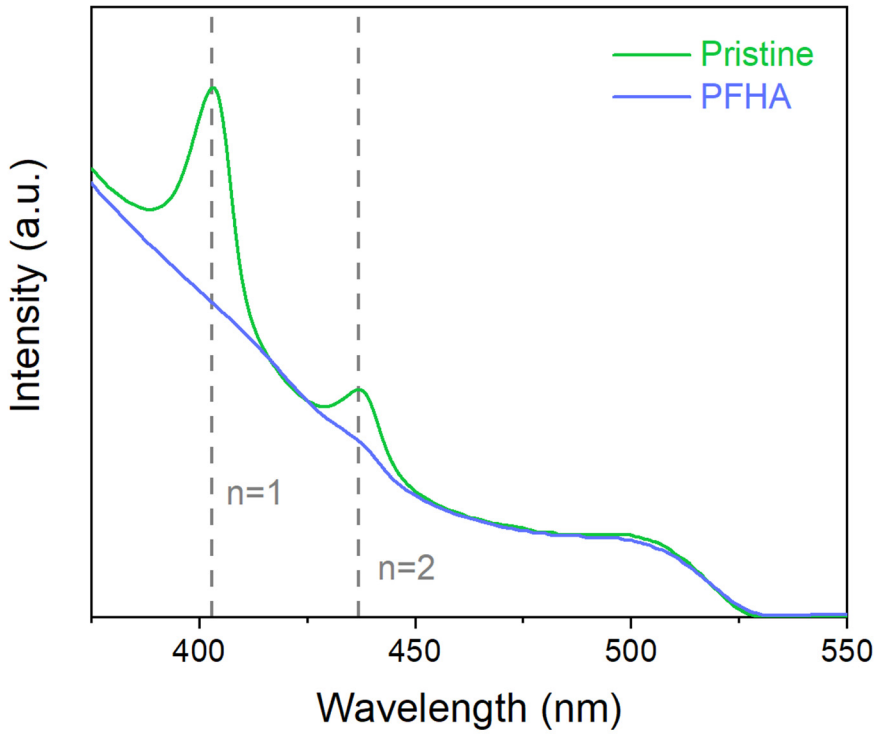

Figure 6.6 | UV-Vis absorption spectra of pristine and PFHA perovskites.

Meanwhile, superior A-site ions stabilization effect as well as enhanced material stability compared to the pristine sample can be validated based on XPS element atomic ratio. For PFHA samples, the N element ratio, as well as the Br-to-Pb atomic ratio, exhibit remarkable stability, without discernible changes over the same 28-day storage duration, as shown in Figure 6.4. This preservation of the A-site ions has signified a marked improvement in phase stability after PFHA pinning.

The ion pinning effect of PFHA molecule is achieved via strong coordination with all the perovskite ions. Specifically, The N atoms in the amine group function as strong electron donors, fostering substantial coordination with cations, such as Pb ions, with the N-H serving as a hydrogen bond donor to anions. Furthermore, the highly fluorinated alkyl appendage of PFHA facilitates additional coordination to both A-site and B-site cations through the formation of robust hydrogen and coordination bonds. Therefore, this ion pinning strategy have coordinate with both anions and cations within the perovskite lattice, markedly inhibited ion migration effects. In addition, the large van der Waals radius of the fluorocarbon functional group [230] exhibited significant steric hindrance, thereby further hindering ion migration and enhancing phase stability of MHPs.

The coordination ability of PFHA to perovskite could be assessed with theoretical simulation based on density functional theory (DFT) [202]. Our investigation initiated with the examination of the interaction between PFHA molecules and single ions such as FA^+. Based on the results, the typical binding energy (E_b) of PFHA coordination with FA^+ reached -1.18 eV, as presented in Figure 6.7, underscoring an exceedingly strong affinity between PFHA molecules and FA^+ ions. Meanwhile, the DFT simulation also validated the pinning effect of PFHA on perovskite structures. For a representative surface binding configuration, the binding energy of the PFHA molecule to

the perovskite (0 0 1) surface was -2.15 eV, suggesting an efficient coordination ability of PFHA to the perovskite surface, as shown in Figure 6.8. All the strong coordination to individual ion and perovskite structures have established a grounded foundation for our efficacious ion pinning strategy.

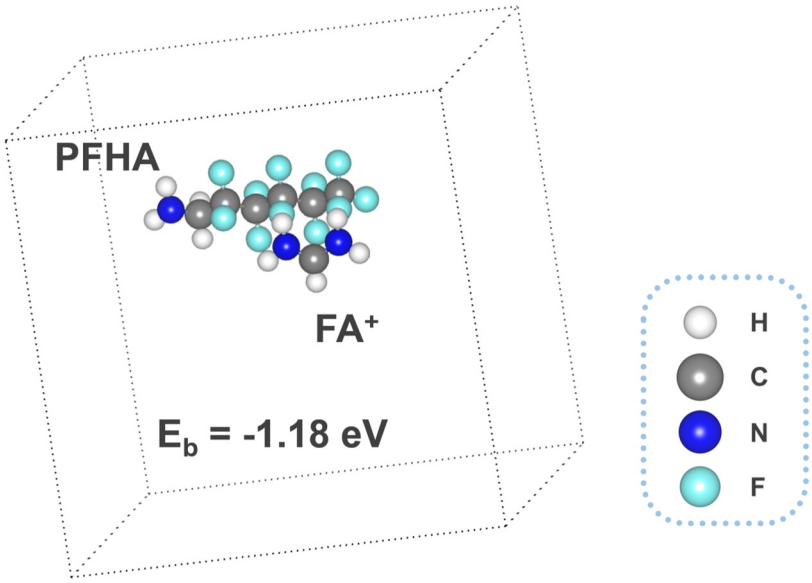

Figure 6.7 | Representative configuration of PFHA coordination with FA^+. The calculated binding energy is -1.18 eV.

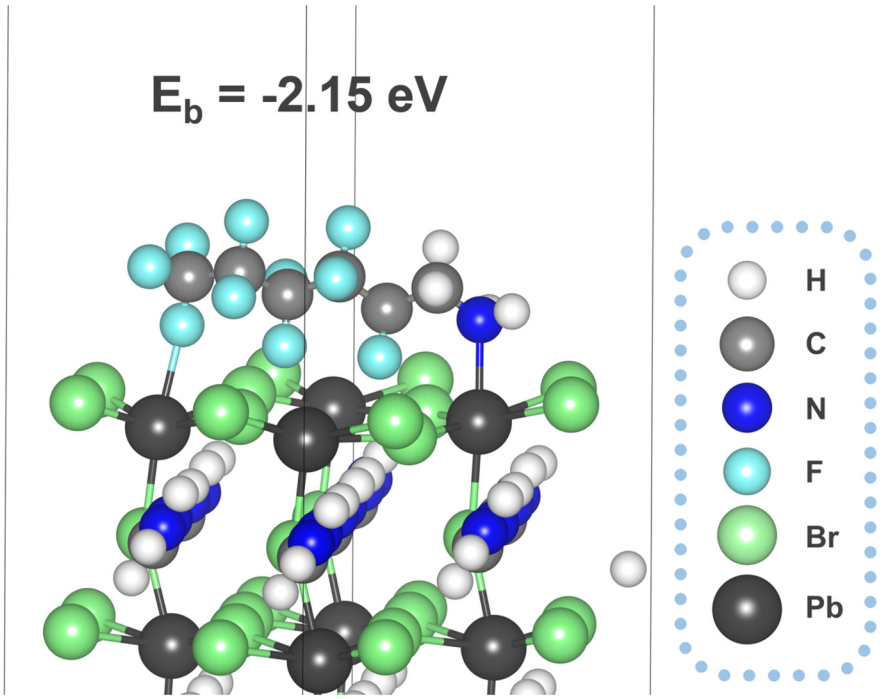

Figure 6.8 | Representative configuration of PFHA coordination on $FAPbBr_3$ perovskite (0 0 1) surface.

Then, Fourier transform infrared spectrometer (FTIR) tests was employed to unveil the interaction between PFHA and different perovskite ions comprehensively. PFHA was dissolved together with perovskite ionic components, formamidine hydrobromide (FABr) and lead bromide ($PbBr_2$), in the carbon tetrachloride (CT) solvent, as shown in Figure 6.9. Here, CT was applied as a background solvent for FTIR evaluates due to its absence of peaks within the wave number range of 1,000 to 4,000 cm^{-1}. The characteristic peaks for C-F stretching can be observed at the wavenumber of 1239.5 cm^{-1} for pure PFHA molecules in CT, while considerable downshifts could be observed with the addition of either FABr or $PbBr_2$, which suggested

that the electron lone pairs of F atoms were denoted to cations. Similarly, downshifts of C-N bond stretching at the wavenumber of 1141.7 cm^{-1} for PFHA samples were also found after FABr and $PbBr_2$ addition, indicating the coordination between N atoms and cations. Meanwhile, significant upshifts of the N-H bending peaks also occurred in the ion-supplemented samples, indicating that hydrogen bonds were formed between anions and amine functional groups. Therefore, all the shifts of the characteristic FTIR peaks had confirmed the strong coordination between PFHA molecules and all kinds of perovskite ionic components in solution form, indicating a superior potential for ion pinning through PFHA.

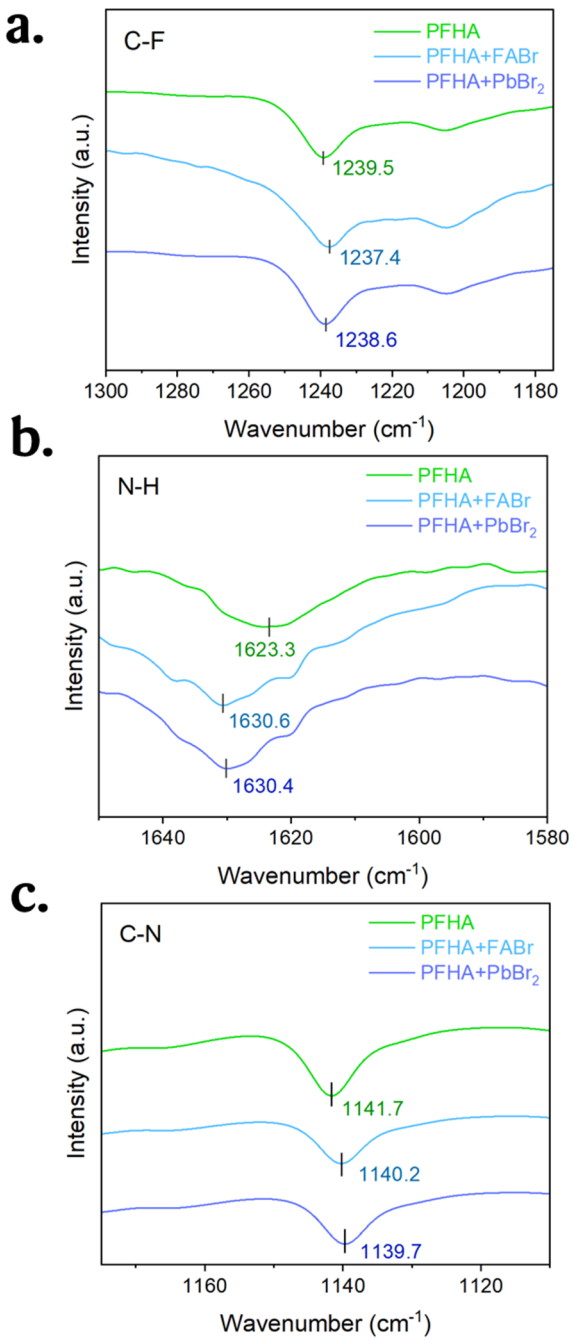

Figure 6.9 | FTIR results of pristine and PFHA-containing mixed systems for (a) C-F stretching (b) N-H bending and (c) C-N stretching.

To comprehensively evaluate the robustness and efficacy of ion pinning within perovskite films, XPS of pristine and PFHA pinned perovskite films was

performed. The observed shifts in XPS spectra are attributed to the distinct chemical environments experienced by atoms in the PFHA-treated perovskite films versus the control samples. As shown in Figure 6.10, the XPS spectra revealed apparent shifts in the binding energies of the critical elements presented in the perovskite films. Specifically, the binding energy of the Pb 4f peak underwent an upward shift post-PFHA pinning compared to the pristine MHPs, attributed to the formation of additional coordination bonds between Pb ions and F atoms introduced by the PFHA molecules. Due to the highest electronegativity of fluorine atoms, the electron density redistribution from Pb to F atoms comparing with the Pb to Br atoms only in the pristine samples, has led to the observed upshift in the Pb 4f peak, confirming the establishment of coordination bonds between PFHA molecules and Pb ions within the perovskite films. Meanwhile, for Br and F atoms, the binding energies of both Br 3d and F 1s were observed to undergo downward shifts. These shifts are indicative of the formation of hydrogen-bond-like interactions between Br atoms and the amine groups of the PFHA, as well as hydrogen bonds between F atoms and formamidinium ions, respectively. Collectively, these findings have demonstrated that PFHA could retain significant coordination to perovskite ions even in solid state films, allowing for significant ion pinning and consequent phase stabilization.

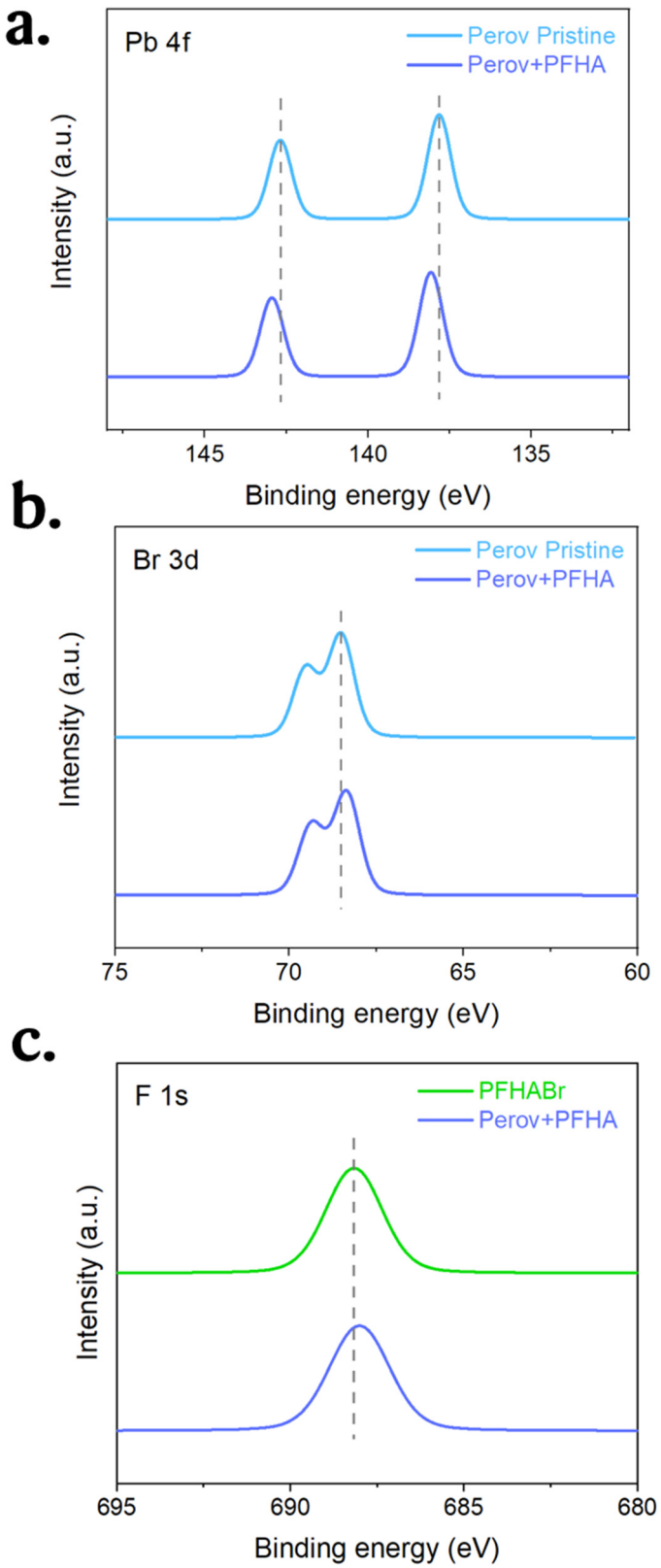

Figure 6.10 | XPS spectra for (a) Pb 4f, (b) Br 3d and (c) F 1s orbitals of pristine and pinned MHPs.

6.3 Effective ion migration inhibition via ion pinning

Although it is renowned that perovskites are extremely sensitive to external stimuli such as ambient air and moisture, after ion pinning, the perovskite films exhibit impressive stability. Figure 6.11 showcases the photoluminescence (PL) spectra of both pristine and PFHA perovskites, stored under ambient conditions over a period of 28 days (approximately 20 °C with 50% relative humidity) without any encapsulation. During the storage, the pristine perovskite sample exhibited a complete loss of photoluminescence, indicating the degradation of perovskite phases. In contrast, the PFHA perovskite retained its photoluminescence properties almost unchanged throughout the same period, underscoring the remarkable stability enhancement via PFHA ion pinning. Meanwhile, the narrowing of PL spectra is also in good consistency with the improved luminescent phase purity with the removal of low dimensional phases [72, 73, 209], and the decreased defect density achieved by PFHA defect passivation.

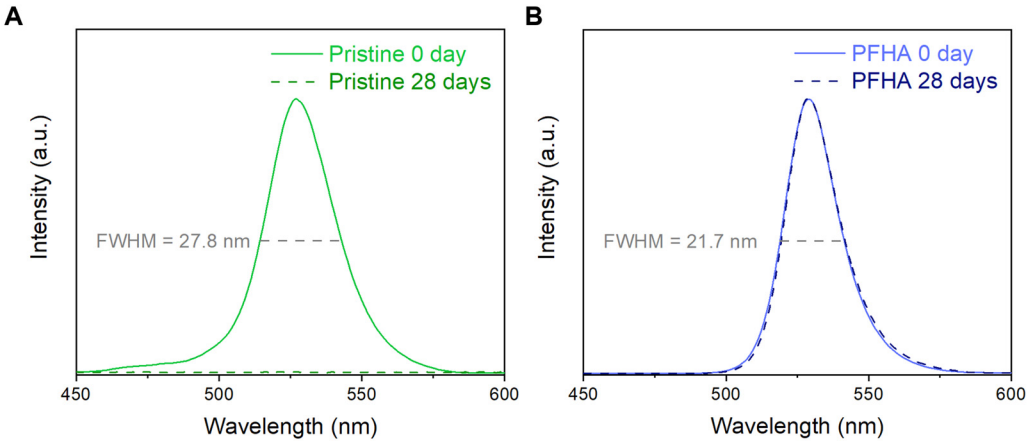

Figure 6.11 | PL spectra of (A) pristine and (B) PFHA perovskite films upon 28 days ambient storage.

Furthermore, the photoluminescence quantum yield (PLQY) of ion pinned sample could maintain over 95% of the initial value over a period of 28 days under the ambient condition, whereas the pristine perovskites lost almost all the PLQY after exposure to ambient air within the first day, as presented in Figure 6.12. Furthermore, to unveil the perovskite stability under the actual device conditions, the PLQY changes of the perovskite samples with ETLs covered was also tracked. Therefore, regardless of the presence of ETLs, the trends in PLQY change remain consistent with that observed in uncovered samples. Specifically, the pristine sample sandwiched between ETLs and HTLs also experiences a drastic loss in PLQY within a single day. In contrast, the PFHA counterparts can maintain the luminescent property for 28 days without any notable changes. Such impressive ambient stability of ion pinned

perovskite will be beneficial to the long-term stability of perovskite devices and simplify the fabrication process.

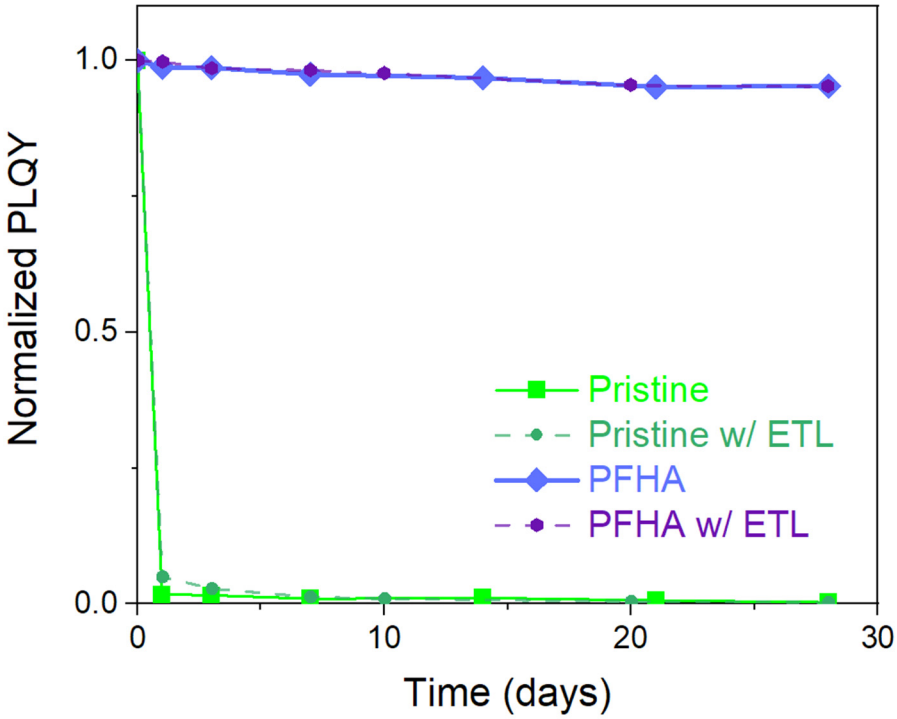

Figure 6.12 | PLQY change with time for pristine and pinned perovskite films in ambient air.

The strong ion pinning effect of PFHA to perovskites enables effective inhibition of ion migration and phase stability. This was further confirmed by impedance spectroscopy analysis. The capacitance-frequency (*C-F*) measurement was performed to quantify the ion migration effect and the resulting charge accumulation effect. Owing to the substantial mass difference between ions and electrons, the significantly heavier ions exhibit a considerably slower response compared to electrons. Therefore, the device

capacitance is dominated by the electronic response at high frequencies, while ion migration and resulting interfacial ion accumulation become more dominant at low frequencies due to the relatively slow response rate of ions [16]. Thus, as shown in Figure 6.13, the capacitance of the PFHA-pinned device was significantly lower than that of the control device, especially at low frequency. Meanwhile, the pristine device exhibited significant increase in capacitance from high frequency to low frequency, indicating strong ion migration effect. However, this difference was almost negligible for the PFHA devices, indicating that ion migration was effectively prevented by PFHA pinning. Furthermore, to further characterize the impact of operational conditions of PeLEDs under current density, the capacitance changes were then measured after constant current density operation (1 mA/cm^2 for 1 h). The capacitance of pristine device become even larger, indicating more severe ion migration effect, while no significant changes occurred for the PFHA device, thereby confirming the outstanding stability of our device under the operation conditions. The suppression of ion migration and the prevention of charge accumulation contributed to the high operational stability of PFHA-pinned PeLEDs.

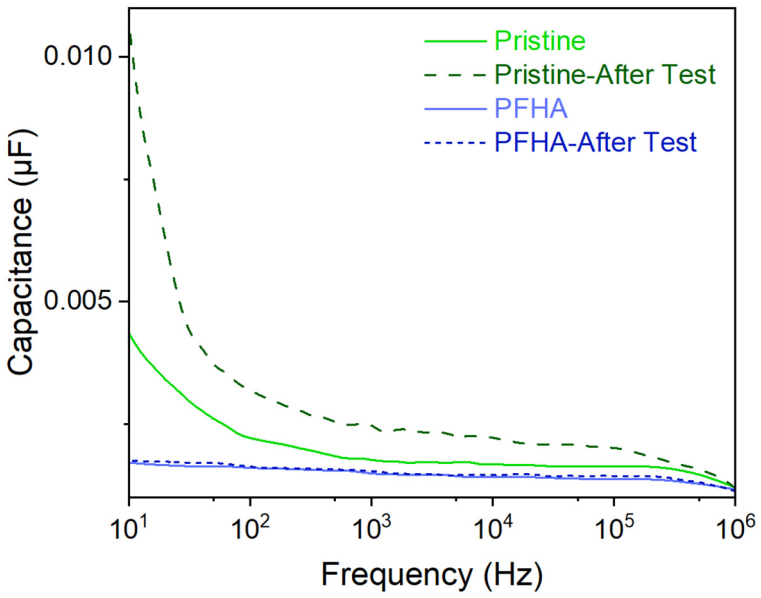

Figure 6.13 | Capacitance to frequency results of pristine and PFHA pinned PeLED devices.

To unveil the phase stabilization effect as well as the hindrance of ion migration effects, direct observation of ion behaviour should be conducted. Therefore, the device for ion migration analysis was fabricated with the structure of ITO / NiOx / PVP / Perovskite / PCBM / Cu. The device was driven at a constant current density of 1 mA/cm^2 for 1 hour (Cu as the cathode), and the Cu electrodes were then peeled off using scotch tapes [231], as shown in Figure 6.14.

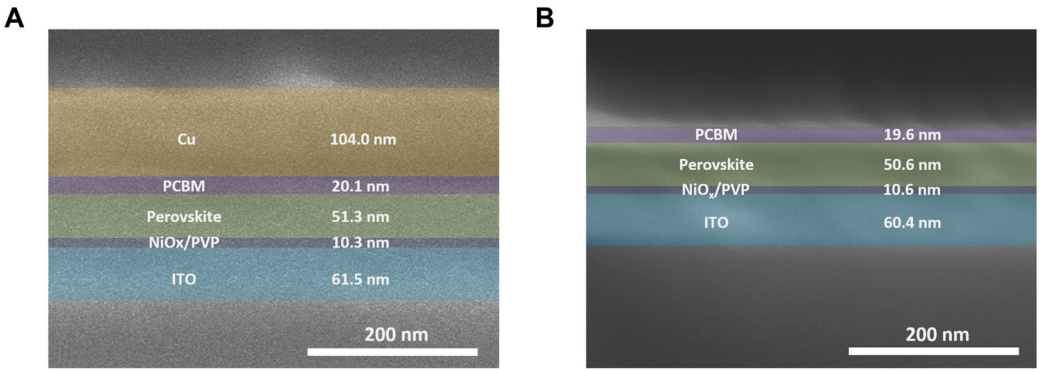

Figure 6.14 | Cross-sectional SEM images for ion migration analysis. The device structure is ITO / NiOx / PVP / Perovskite / PCBM / Cu. (A) The entire device structure. (B) The device after the removal of the surface Cu electrodes using scotch tapes.

Then, surface XPS measurement of PCBM surface of the peeled device was conducted. Our XPS results have revealed a distinct difference in the Br elemental composition between the pristine and PFHA-treated samples, as Figure 6.15 showed. For the pristine sample, an apparent signal corresponding to the Br element was detected on the surface of the PCBM layer, indicating significant ion migration beyond the perovskite layer. Conversely, in the case of PFHA-treated samples, no discernible Br XPS signal could be observed on the PCBM surface, suggesting that PFHA effectively pins ions within the perovskite layer, thereby inhibiting ion migration. Moreover, quantitative analysis via XPS atomic ratio measurements showed that the pristine sample displayed a substantial presence of Br element on its

surface, whereas PFHA-treated counterparts exhibited negligible levels of Br, as Figure 6.16 presented. This quantitative confirmation further solidifies that PFHA exhibits significant ion pinning effect, thereby preventing the ion migration, and contributing to enhanced perovskite stability.

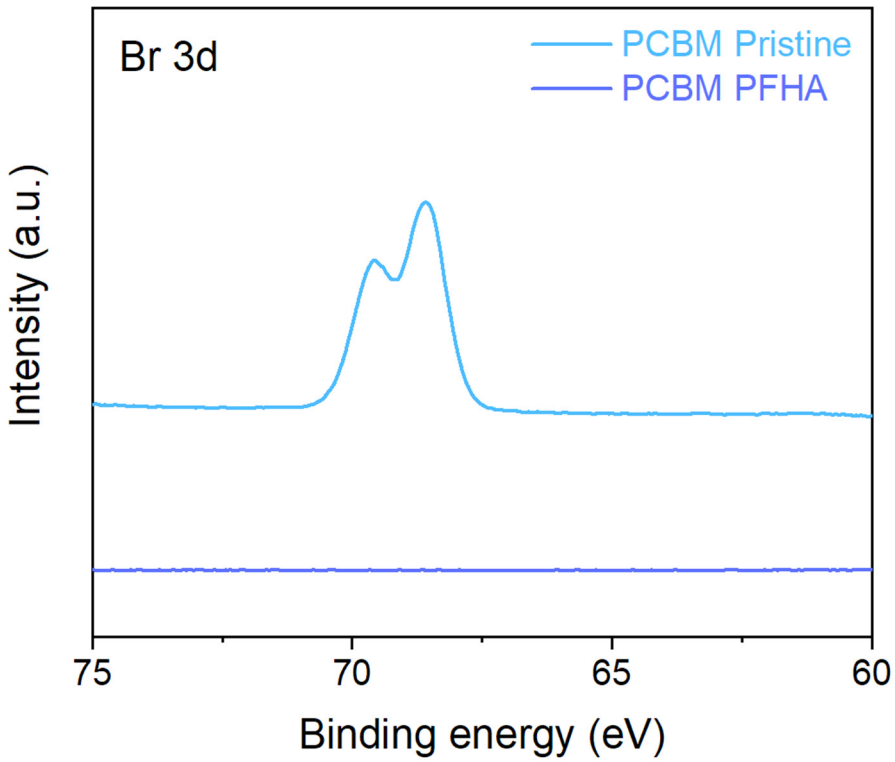

Figure 6.15 | Surface XPS spectra of PCBM surface of pristine and PFHA devices.

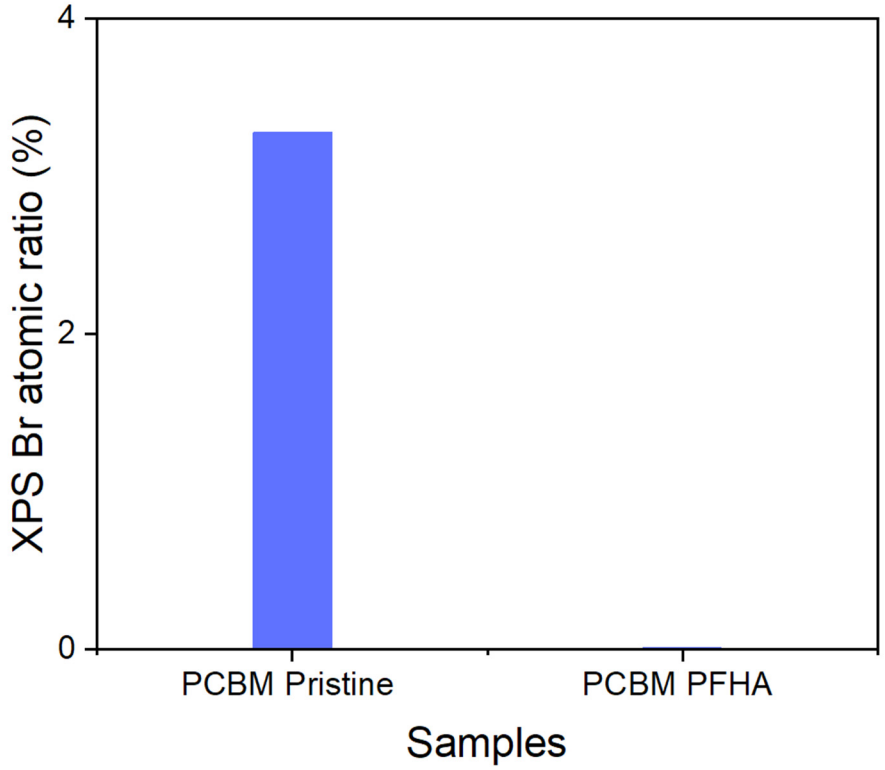

Figure 6.16 | XPS Br atomic ratio of pristine and PFHA devices for ion migration analysis.

Then, direct observation of the surface of PCBM was performed using scanning electron microscopy with energy dispersive X-ray spectroscopy (SEM-EDX). The surface SEM-EDX images of Br element for pristine and PFHA pinned perovskite films were displayed as Figure 6.17. For the pristine perovskites, strong Br signals could be observed, indicating that substantial number of bromide ions were mobile and migrated outside the perovskite films. While for the PFHA pinned perovskites, the signal of Br element was quite close to the background noise (PCBM only sample), indicating a

neglectable bromide ions migration from the PFHA pinned perovskites. Therefore, direct observations of ion behaviours have proved that the PFHA-pinned perovskites can effectively suppress the ion migration.

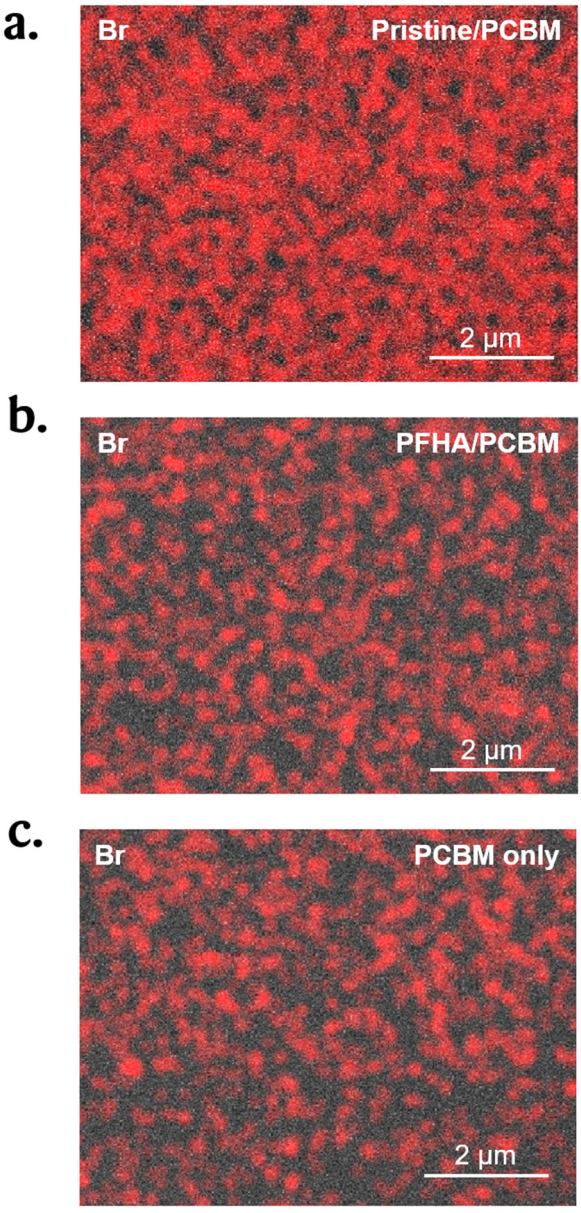

Figure 6.17 | SEM-EDX mapping results of Br element on the PCBM surfaces of (a) pristine, (b) PFHA pinned samples and (c) PCBM only samples.

The PFHA pinning strategy also improved the luminescent properties of perovskites. Since the PFHA molecules can bond to the perovskite ions, significant defect passivation and consequent improvements in PLQY could be achieved after PFHA pinning, as shown in Figure 6.18. The improved PLQYs for pinned perovskites are beneficial to achieving high efficiency PeLED devices due to reduced defect mediated energy losses.

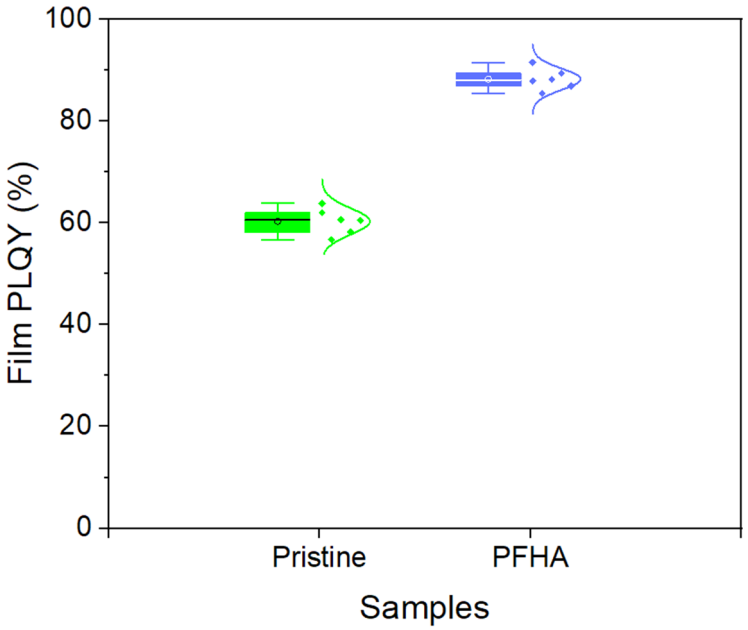

Figure 6.18 | PLQY box plots for pristine and PFHA pinned perovskites. In the box plots, the dots represent the data points, and the curves show the distribution trends; the middle bar represents the median, and the box represents the interquartile range; bars extend to 1.5× the interquartile range.

The trap density inside perovskite films can be evaluated through space charge limited current (SCLC) measurements. Therefore, the hole-only

devices are fabricated with a structure of ITO / NiOx / PVP / perovskite / MoOx / Au [232]. The trap density c(t) calculation is based on the trap filling limited voltage (V_{TFL}) [209]. The PFHA-pinned perovskite exhibited a significantly lower trap density than the pristine film, indicating effective passivation of non-radiative defects, as presented in Figure 6.19. Consequently, pinning through PFHA reduced defect-assisted non-radiative recombination, increasing the radiative recombination ratio, and contributing to higher device EQEs.

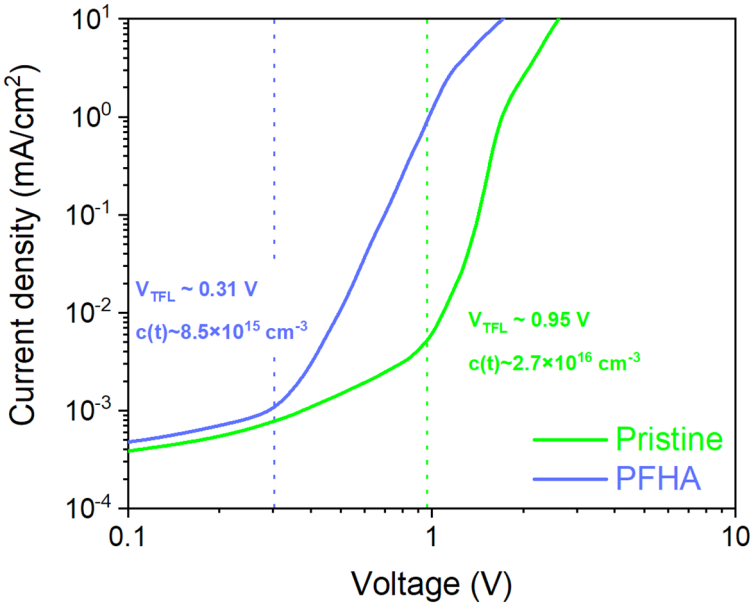

Figure 6.19 | Current density versus voltage curve for hole-only devices.

6.4 Stable PeLEDs after ion pinning

Encouraged by the extraordinary ion migration hindrance and improved luminescent property achieved via PFHA pinning, stable and efficient PeLED

devices are then fabricated. The PeLED structure is ITO / NiOx / PVP / perovskite / TmPPPyTz / ADN-PBIP / LiF / Al / Ag, as shown in Figure 6.20.

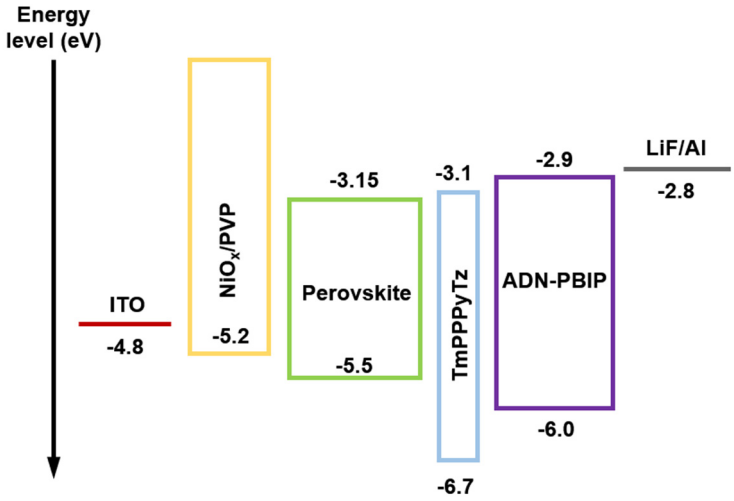

Figure 6.20 | Device structure and corresponding energy levels.

As a result, the electroluminescence (EL) spectra, current density–voltage–luminance (*J-V-L*) and the EQE curves are plotted as Figure 6.21a, Figure 6.21b, and Figure 6.21c, respectively. The EL peak of PFHA pinned PeLEDs is 530 nm with a FWHM of 20.8 nm (CIE coordination (0.185, 0.767)). Compared to the FWHM of 25.3 nm for pristine sample, the narrowing of emission spectra on one hand indicates the improved luminescent phase purity with the removal of low dimensional phases [72, 73, 209], on the other hand show the decreased defect density achieved by PFHA defect passivation. The *J-V-L* curve of pinned PeLED shows improved current density and, in accordance with the improved optical properties after PFHA pinning. Meanwhile, a

highest EQE of 27.1% and, with an average EQE of 25.4±0.9% over 40 devices (Figure 6.21d), much higher than maximum EQE of 12.5% for the pristine devices. The highest device current efficiency (CE) with PFHA pinning also reached 115.8 cd/A, as shown in Figure 6.22.

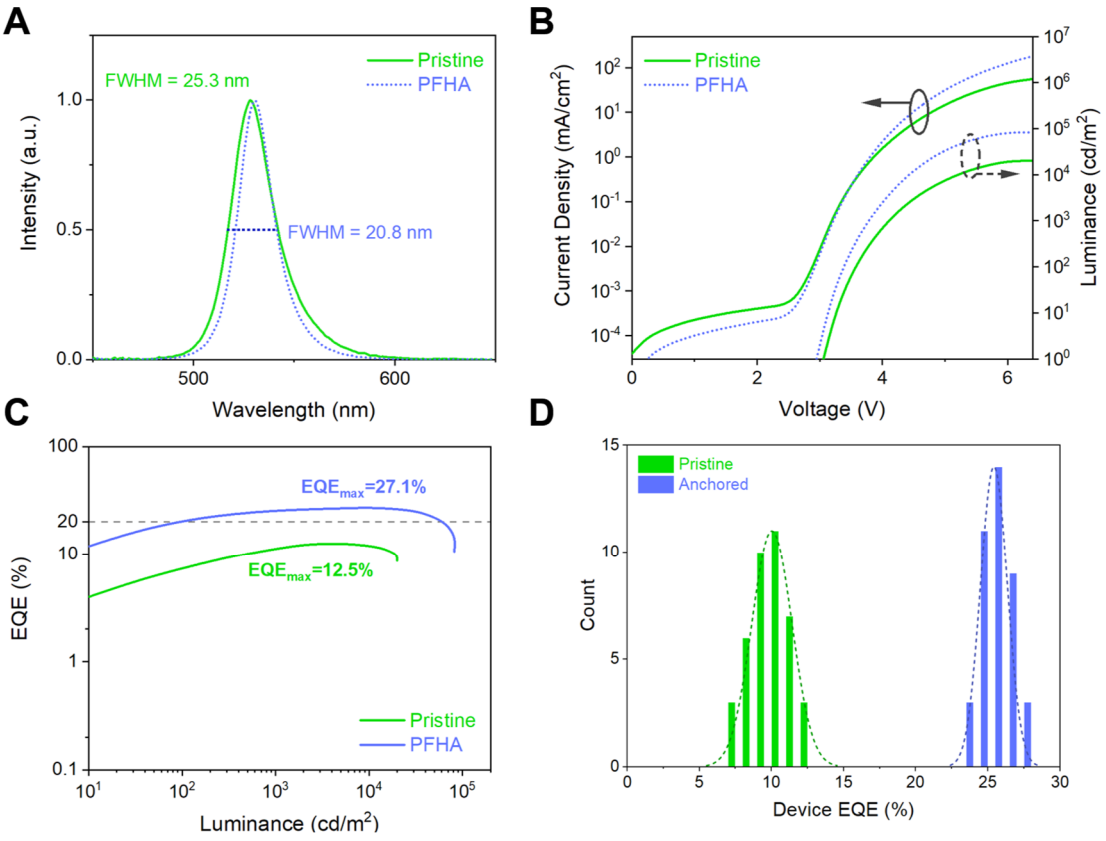

Figure 6.21 | Ultra-stable and efficient PeLEDs. a EL spectra and b. *J-V-L* plots of representative PeLED devices. c. EQE to luminance curve of PeLEDs. d. Statistical device EQE_{max} of pristine and PFHA PeLEDs. 40 devices are measured in total, respectively.

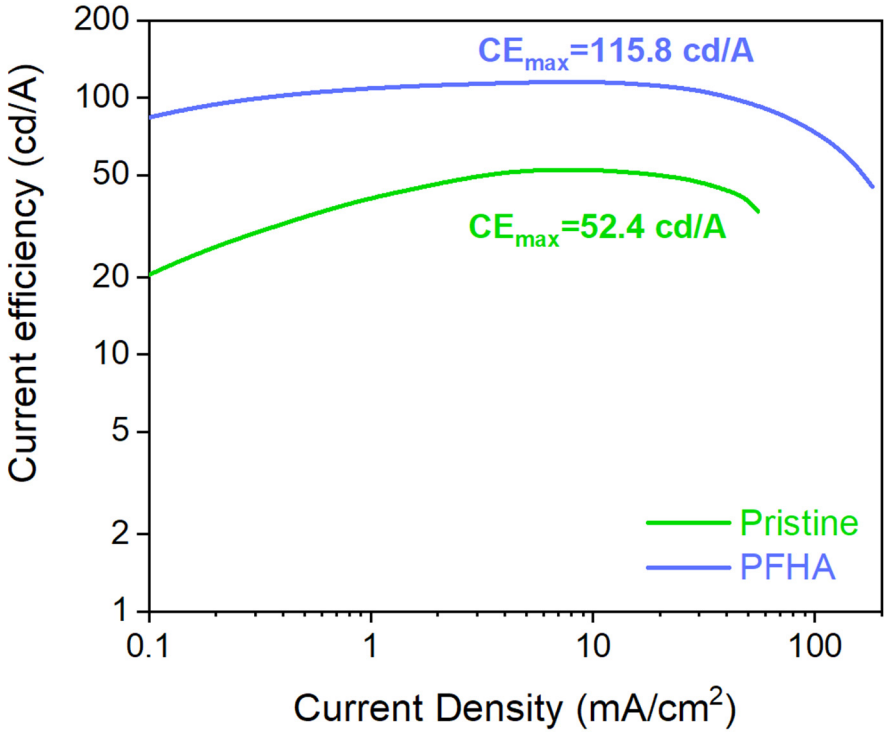

Figure 6.22 | Current efficiency (CE) versus current density for PeLEDs.

More importantly, the operational stability of PeLED devices is also significantly improved after the ion pinning. The operational lifetime of PeLEDs is measured at the constant current density, and the initial luminance is tuned to 10,000 cd/m^2 for both devices. The champion operational lifetime T_{50} of PFHA-pinned PeLEDs reached 103.17 hours (equivalent over 326,252 hours at the initial luminance of 100 cd/m^2 with fitted slope of -1.75, Figure 6.23), while the highest T_{50} of pristine devices is only 0.92 h, as shown in Figure 6.24. Therefore, a dramatic improvement of operational lifetime over two orders of magnitude has been achieved with the ion pinning strategy. Such improvement has emphasized the importance of ion migration inhibition for stable PeLEDs, and the operational stability of pinned PeLEDs is,

to our best knowledge, the highest T_{50} reported so far (Figure 6.25, Table A3-1).

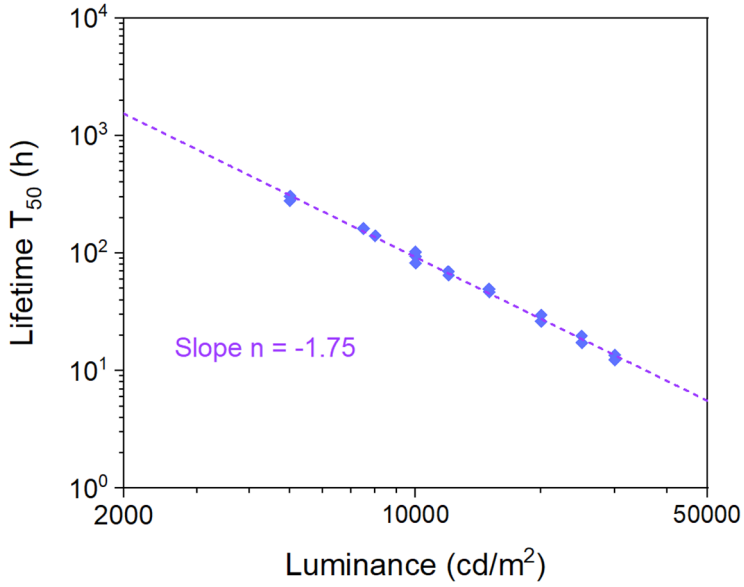

Figure 6.23 | Representative T_{50} lifetime of PFHA PeLEDs at different initial luminance.

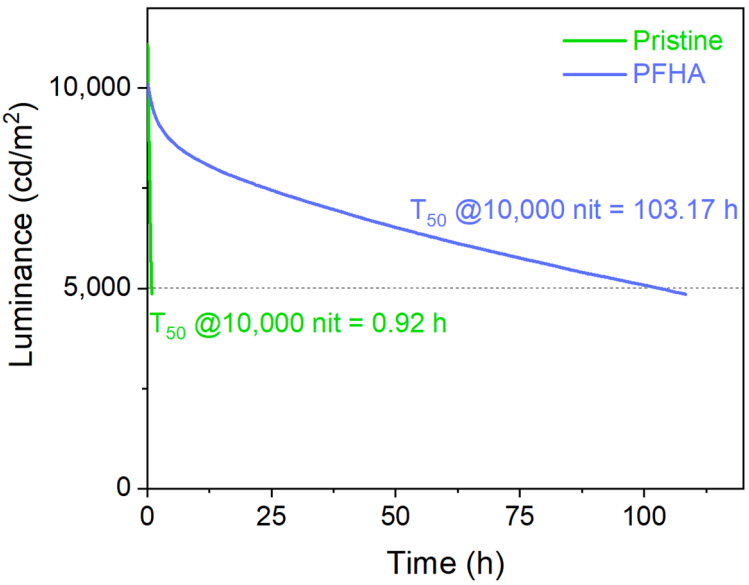

Figure 6.24 | Operational lifetime of pristine and PFHA-pinned PeLED devices, respectively.

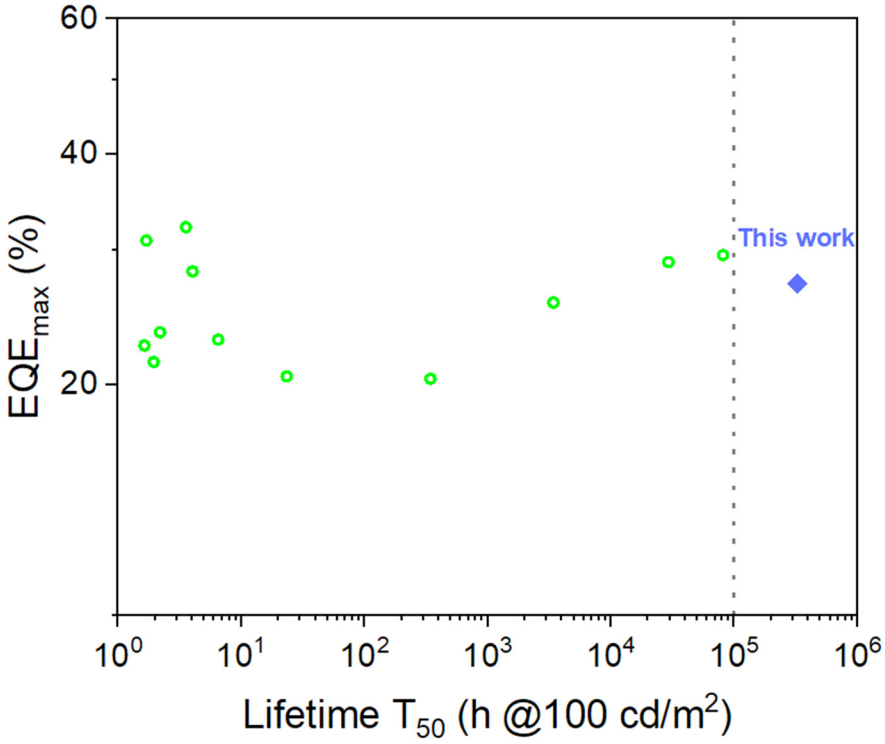

Figure 6.25 | Summary of the reported PeLED performance based on the maximum EQE and estimated or measured T_{50} at 100 cd m^{-2}.

The laser intensity dependent PLQYs reveal the difference of exciton behaviours for both pristine and PFHA perovskite films, as shown in Figure 6.26. Under low excitation powers, the pristine perovskites exhibit a more pronounced enhancement in PLQY with increasing laser intensity, indicating more trap states to be filled. Conversely, under higher excitation power, a more significant decline in PLQY can be found in pristine perovskites, suggesting more significant Auger non-radiative recombination [209] and thereby more severe efficiency roll-off at high luminance for pristine PeLEDs. These results have underscored the critical role of PFHA ion pinning in suppressing non-radiative recombination and enhancing PeLED

performance.

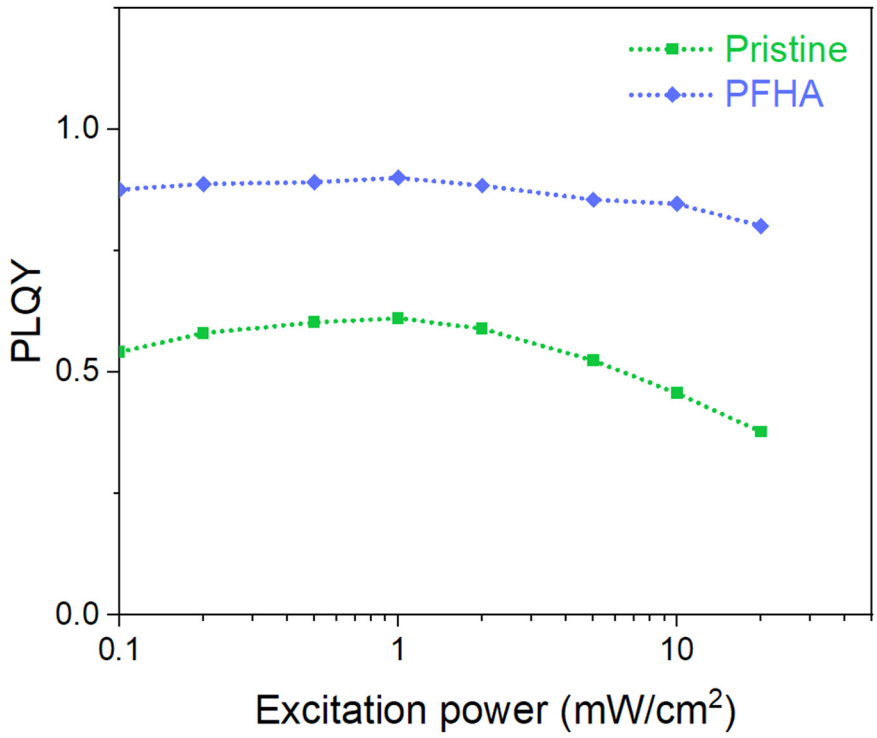

Figure 6.26 | Excitation-dependent PLQY of pristine and PFHA films.

6.5 Discussion

This chapter has concentrated on addressing the crucial stability challenges of PeLEDs. In the pursuit of highly stable and efficient PeLEDs, the pivotal role of ion migration has been identified and the utilization of PFHA pinning has achieved a comprehensive immobilization of ions within perovskite structures, effectively suppressing ion migration and thereby facilitating the fabrication of ultra-stable PeLEDs.

The most critical mechanism for ion pinning strategy is the robust coordination to the mobile ions inside perovskite lattice. In this work, highly fluorinated molecules, PFHA, are employed to achieve the coordination. Our PFHA-based ion pinning strategy has inspired the systematic design principle of potential ion immobilizing additives to enhance perovskite stability. Herein, PFHA acts as a "molecular glue" with robust intermolecular interactions, including coordination and hydrogen bonds, with all perovskite ions, as displayed in Figure 6.9 and Figure 6.10. The significant improvement on perovskite stability can be attributed to its C-F bonds due to fluorine's highest electronegativity, surpassing traditional amine-based coordinating molecules [163]. As a result, the ion immobilization effect was confirmed through both electronic characterization and direct elemental observations, wherein both capacitance-frequency tests unveil the suppressed ion mobility under external electric field (Figure 6.13), and the SEM-EDX measurements show the absence of Br^- ions into ETLs even after constant operation of diode device, as shown in Figure 6.17. Therefore, the excellent ion pinning effect to suppress the ion migration and stabilize perovskite materials has been evidenced, thereby achieving the fabrication of ultra-stable PeLEDs (Figure 6.24).

Meanwhile, a broader question whether any fluorine-containing compound could emulate the PFHA's exceptional ion coordination and immobilization

capabilities in high-performance PeLEDs has been raised. The answer can be much more complicated with comprehensive concerns about material structure and device engineering. For example, polyvinylidene fluoride (PVDF), a fluorine-rich polymer also been reported to suppress ion migration in stable PeLEDs [233], , and the molecular structure of both PFHA and PVDF are listed in Figure 6.27. A crucial distinction between PFHA and PVDF is the molecular size or the chain length. The elongated carbon-fluorine chains inside PVDF polymer, in contrast to PFHA's compact molecular architecture, pose a significant hindrance to charge transport within the perovskite layer, and results in the limited maximum luminance of no more than 6,000 cd/m^2, more than one order of magnitude lower than our results (over 80,000 cd/m^2 as presented in Figure 6.21). Such discrepancy emphasizes the importance of rational molecular design in balancing ion immobilization ability with charge transporting dynamics, necessitating comprehensive considerations on molecular design and selection for high-performance PeLEDs.

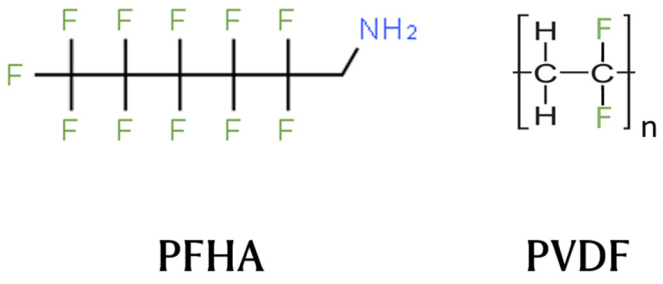

Figure 6.27 | Molecular structure of PFHA and PVDF.

Nonetheless, the exploration of alternative highly fluorinated compounds encounters obstacles imposed by the scarcity of accessible chemicals, a limitation discussed in Chapter 5. Specifically, the PFHA stands as the only linear, highly fluorinated amine commercially available via chemical platforms like CASMart, thereby hindering the examination of structurally analogous molecules. While the comparison between PFHA and PVDF has underscored the pivotal role of molecular size and chain length on charge transportation and corresponding device performance, questions persist regarding the optimality of PFHA concerning carbon chain length. Additionally, the implications of appending side chains on its ion pinning capacity, and the subsequent effects on material stability and the performance of PeLEDs, are urgently demanded to be investigated in the future works.

Furthermore, the decision to employ an amine functional group is inspired by the former solvent sieve method with mixed solvents of HA/CB. The amine functional group's efficacy in enhancing the performance of MHP-based optoelectronic devices is partially attributed to its proficient ionic coordination capabilities [163]. Nevertheless, the potential for developing ion pinning molecules centred around alternative functional groups, such as sulphates [234], also represents an promising avenue for future research beyond our conventional amine groups.

Finally, to conclude this last chapter dedicated to PeLEDs, an overall summary and comparison of our works with the state-of-the-art PeLED research endeavours has been performed, as listed in Table 6.1. The results reveal that even comparing with the most advanced studies across the world, our results still show competitive device efficiency and operational stability.

Meanwhile, a distinctive hallmark of our research lies in the broad spectrum of applicable MHP systems, with two distinct methodologies across all MHPs, underscoring a universality critical for the advancement of PeLEDs. The ion pinning strategy has also emerged as a universal strategy due to the non-sensitivity of PFHA pinning to different perovskite A-site ions and halides, and further examinations of PFHA with other MHP systems will be performed in future endeavours.

Table 6.1 | State-of-the-art PeLED research works and our results.

	D. Ma *et al.* [72]	J. S. Kim *et al.* [67]	**Chapter 4 Solvent sieve method** [73]	**Chapter 5 sweet coordination**	**Chapter 6 ion pinning**
Applicable MHP systems	Quasi-2D $CsPbBr_3$	$FAPbBr_3$	**Multiple MHPs**	**Multiple MHPs**	**Quasi-2D $FAPbBr_3$, other systems to be evaluated.**
EQE (%)	25.6	28.5	**29.5**	**31.3**	**27.1**
Operational lifetime (T_{50}@100 cd/m², h)	2,224	23,228	**>50,000**	**>200,000**	**>320,000**
Material availability	Synthesized	Commercial	**Commercial**	**Commercial**	**Commercial**

Furthermore, with a consistent target towards the prospective industrialization of PeLED technology, our research integrates commercially available molecules throughout to facilitate the development of large-scale fabrication techniques. By high accessibility and practicality alongside excellence of device performance, our work paves the pathway for accelerated innovation in PeLEDs, targeting at bridging the gap between laboratory breakthroughs and mass-produced next-generation PeLEDs.

6.6 Summary

In conclusion, a simple and effective ion pinning strategy has been demonstrated to significantly prevent the ion migration process of MHPs. The strong interaction between PFHA molecules and all perovskite ions enables effective ion pinning, which significantly hinders the ion migration process and contributes to the excellent operational stability of PFHA-pinned PeLEDs. As a result, ultra-stable and efficient green PeLEDs are fabricated with a T_{50} lifetime of 103.17 hours at 10,000 cd/m^2 (equivalent to over 326,252 hours or 37.2 years at 100 cd/m^2) and a champion EQE of 27.1%, establishing the operational lifetime benchmark for all green PeLEDs.

Moreover, this chapter has discussed the comprehensive design strategy for ion pinning molecules, followed by brief comparison of our PeLEDs research outcomes, highlighting critical stability enhancing principles and charting

prospective pathways toward the industrialization of PeLEDs. Our outcomes have fortified the viewpoint that the fabrication of robust, ultra-stable PeLED devices is not only theoretically possible but achievable in practice, and the industrialization of PeLEDs is not a remote aspiration but an impending reality with our own endeavours.

Chapter 7. Optimizing Interface with Interfacial Modification Method

7.1 Introduction

In this chapter, formamidinium-based organometal quasi-2D perovskites and corresponding PePV devices are studied. For photovoltaic applications, the quasi-2D perovskites here are much thicker comparing to former chapters (typically over 500 nm vs. 50 nm for LEDs), and the main chemical reaction is:

$$2PEAI + (n-1)FAI + nPbI_2 \rightarrow PEA_2FA_{n-1}Pb_nI_{3n+1} \quad 7.1$$

Wherein n represents the n value for quasi-2D perovskites.

The device structure of optimized PePVs here is ITO / SnO_2 / NH_4SCN / perovskite / Spiro-OMeTAD / Au, as Figure 7.1 shows. Herein, SnO_2 is a widely applied ETL in PePVs, renowned for its outstanding optical characteristics: a wide bandgap minimizing light loss, high carrier mobility, and exceptional chemical stability. Nevertheless, to achieve high efficiency and stability PePVs, addressing surface defects and enhancing the SnO_2-perovskite interface compatibility have become imperative.

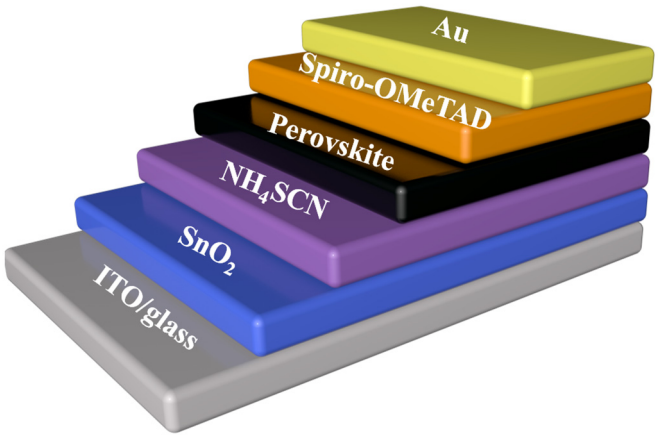

Figure 7.1 | Schematic diagram of the device structure.

Herein, an interfacial modification strategy of SnO_2 with NH_4SCN is introduced. The schematic diagram depicting the formation of the passivation layer between the SnO_2 ETL and the perovskite layer is illustrated as Figure 7.2. The thiocyanate anion, characterized by strong electronegativity, effectively interacts with unbound Sn at the tin dioxide surface, passivating surface defects. Concurrently, ammonium ions promote perovskite surface wettability, enhancing the crystalline quality of the perovskite layer. Diverging from conventional practices that incorporate NH_4SCN directly into the perovskite precursor [199, 235–239], our interfacial passivation approach achieves better energy level matching, yielding increased PCEs. This modification strategy not only tackles the existing interfacial challenges but also enhances our understanding of interface engineering for advancing PePVs.

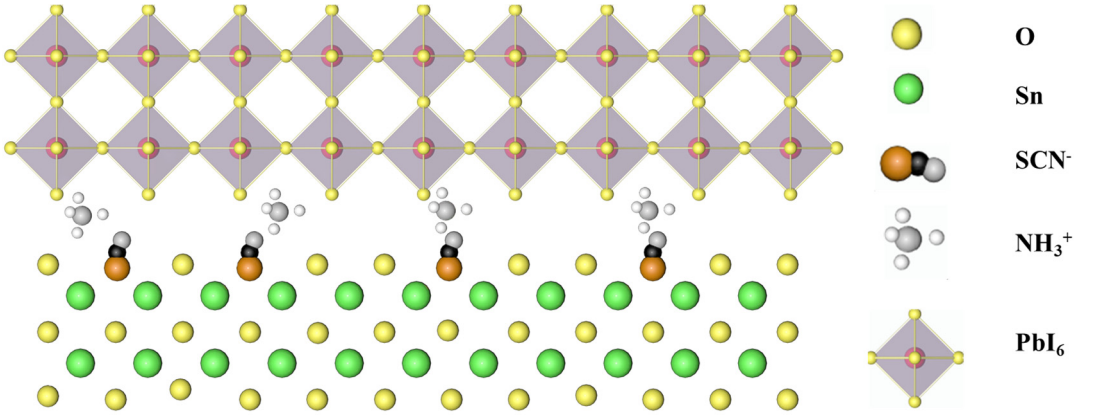

Figure 7.2 | Schematic diagram of the passivation layer formed between the SnO_2 ETL and perovskite layer.

7.2 Surface bonding and passivation of NH_4SCN

To illustrate the passivation effect of NH_4SCN on the SnO_2 interface, quasi-2D PSCs are fabricated using a two-step method. From the results of XRD, as shown in Figure 7.3, clear quasi-2D peaks of low dimensional phases (n=1 (0 0 1) and n=2 (0 0 2)) can be observed, indicating that quasi-2D perovskites instead of conventional 3D perovskites are fabricated.

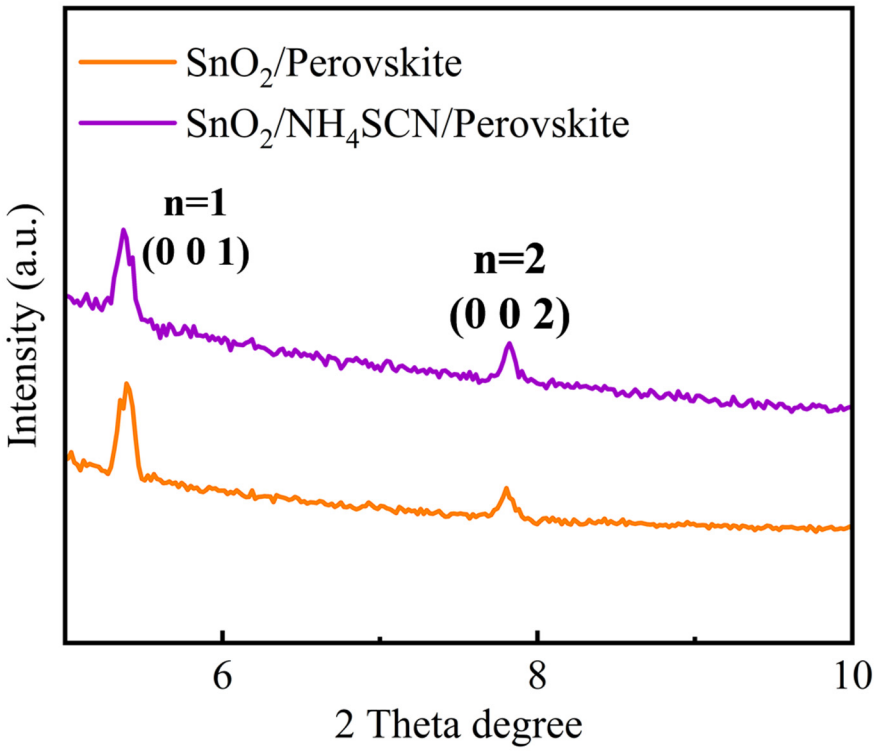

Figure 7.3 | XRD patterns of perovskite films deposited on SnO_2 and SnO_2/NH_4SCN substrates.

Multiple characterizations have been performed to demonstrate the mechanism of NH_4SCN passivation. First, the interaction of NH_4SCN and SnO_2 is investigated by XPS. As Figure 7.4 and Figure 7.5a show, the SnO_2/NH_4SCN sample has an additional S 2p peak at 167.66 eV compared to SnO_2, showing existence of NH_4SCN the surface of SnO_2 film. From the high-resolution XPS spectra in Figure 7.5b, NH_4SCN passivated SnO_2 of signal peaks of Sn $3d_3/2$ and Sn $3d_5/2$ binding energy reduced to 0.2 eV relative to SnO_2, which indicates that the uncoordinated Sn^+ ions are electrostatically coupled to the highly electronegative thiocyanates. Furthermore, by analysing the O 1s peaks in the

XPS high-resolution spectra (Figure 7.5c), for untreated SnO_2 sample, peaks at 528.87 eV and 529.9 eV can be attributed to the Sn-O bond in SnO_2 and the oxygen vacancy (V_O) on the surface of SnO_2 respectively [240]. After passivation with NH_4SCN, the two peaks increased to 529.12 eV and 530.56 eV, respectively, which implies that the oxygen vacancies on the interface of SnO_2 films are effectively passivated. The additional negative charge provided by the strongly electronegative thiocyanates fill part of the oxygen vacancies present on the surface of SnO_2 due to the insufficient Sn coordination.

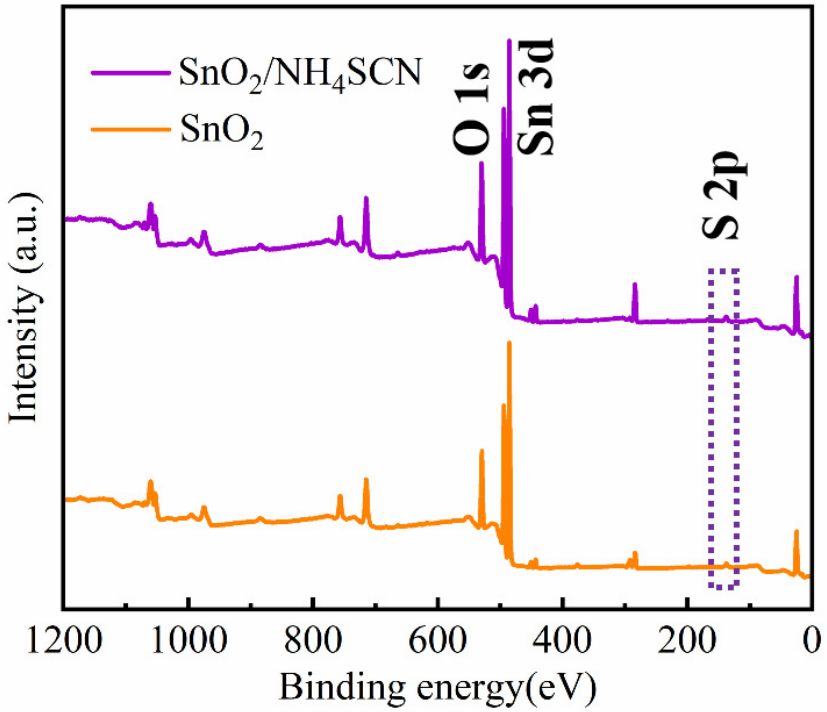

Figure 7.4 | XPS full spectra of SnO_2 and SnO_2/NH_4SCN.

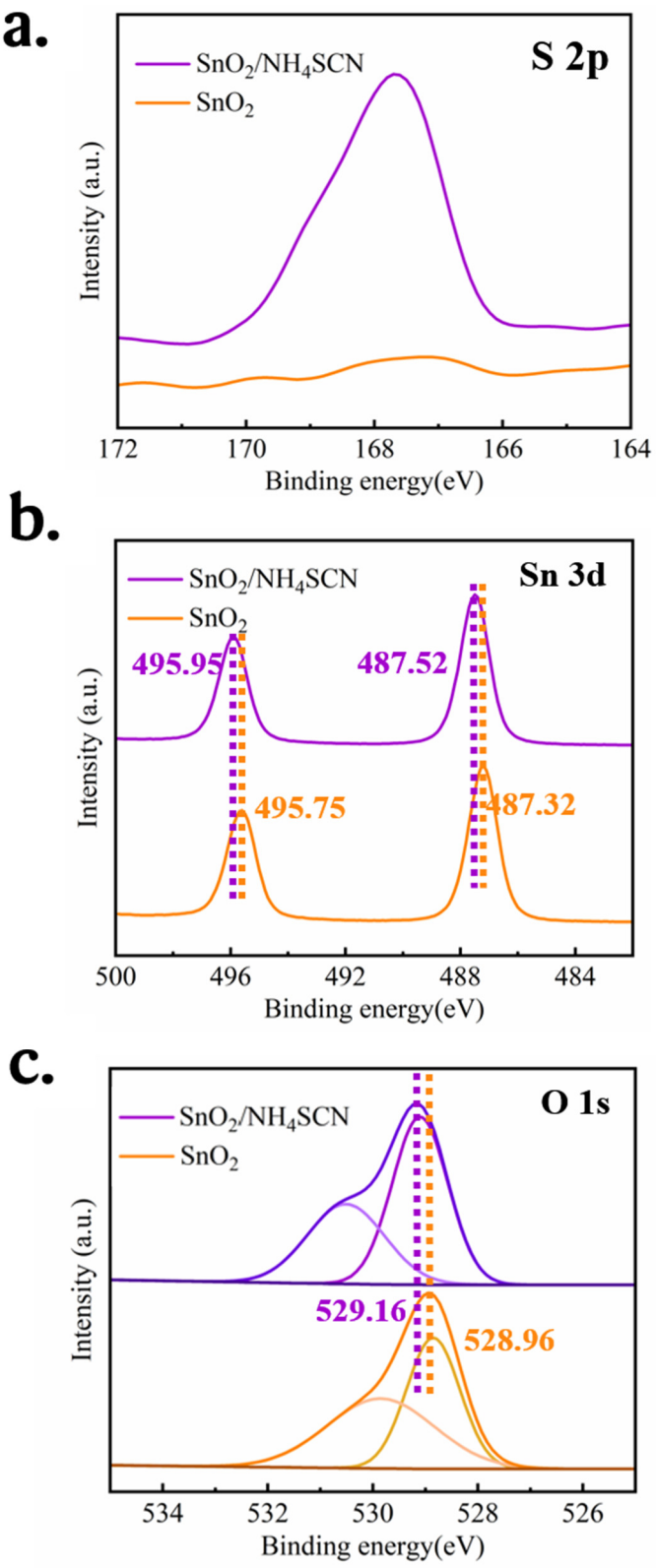

Figure 7.5 | XPS high-resolution spectra of SnO_2 and SnO_2/NH_4SCN for (a) S 2p, (b) Sn 3d, and (c) O 1s.

Also, FTIR results confirmed the presence of both ammonium and thiocyanate ions in the NH_4SCN modified SnO_2 films, as shown in Figure 7.6. From the results, the N-H stretching peak around 3130 cm^{-1} for ammonium ions and S-C≡N stretching around 2050 cm^{-1} for thiocyanate ions indicating the presence of both ammonium and thiocyanate ions in the NH_4SCN modified SnO_2 films.

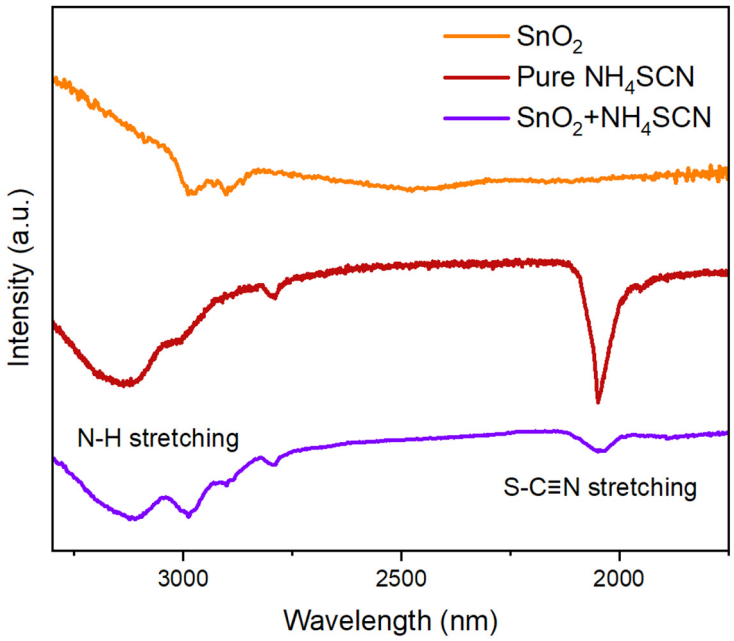

Figure 7.6 | FTIR results of SnO_2 film, pure NH_4SCN film and NH_4SCN modified SnO_2 film.

7.3 Improved charge transport and perovskite film quality

Calculated from the UV photoelectron spectrometer (UPS) test results (Figure 7.7), the conduction band minimum (CBM) is -4.45 eV and -4.27 eV, respectively. The rise in CBM leads to a reduction in the energy offset

between perovskite and SnO_2 layer, thereby enhancing electronic extraction [241, 242]. Better matched surface energy levels will affect the dynamic transport of interfacial carriers [243, 244]. UPS results also disclose the difference between our interfacial passivation strategy and conventional treatments of adding NH_4SCN as additive in perovskite precursor [199, 235–239], where the NH_4SCN interfacial passivation does not change the energy level of perovskite, while the NH_4SCN additive method shifts the perovskite energy level upwards and hinders the electron transport, leading to a decrease in PCE compared to our interfacial passivation strategy, as presented in Figure 7.8.

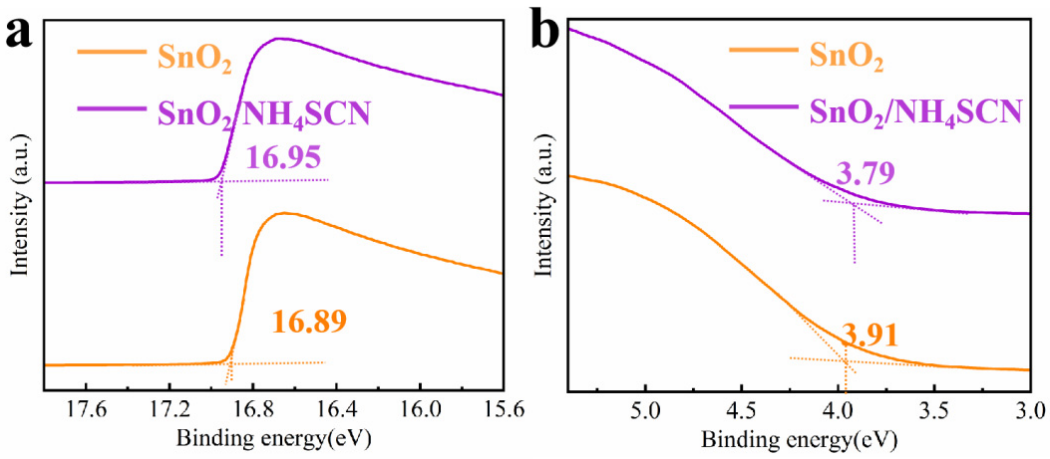

Figure 7.7 | UPS of (a) SnO_2 and (b) SnO_2/NH_4SCN films.

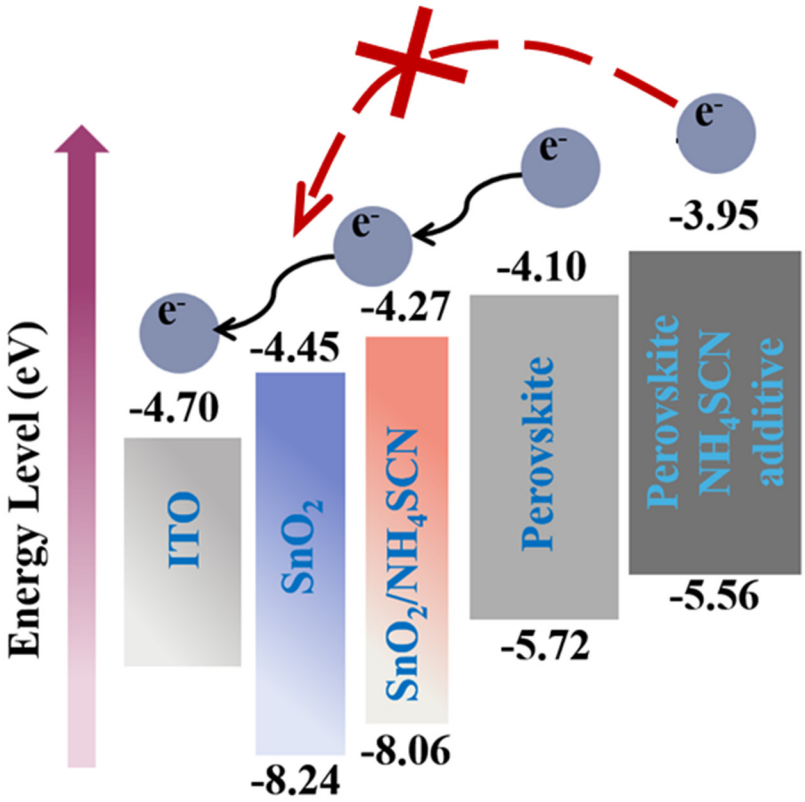

Figure 7.8 | Energy level diagram of the device.

Also, as shown in the steady-state photoluminescence (PL) curves in Figure 7.9, a significant PL quench is noted for the SnO_2/NH_4SCN-based perovskite films compared with the SnO_2 based perovskite films, which indicates that the excitons generated in perovskite can be quickly transported to SnO_2 layer and quenched, demonstrating the improved carrier transporting ability at the interface [245, 246].

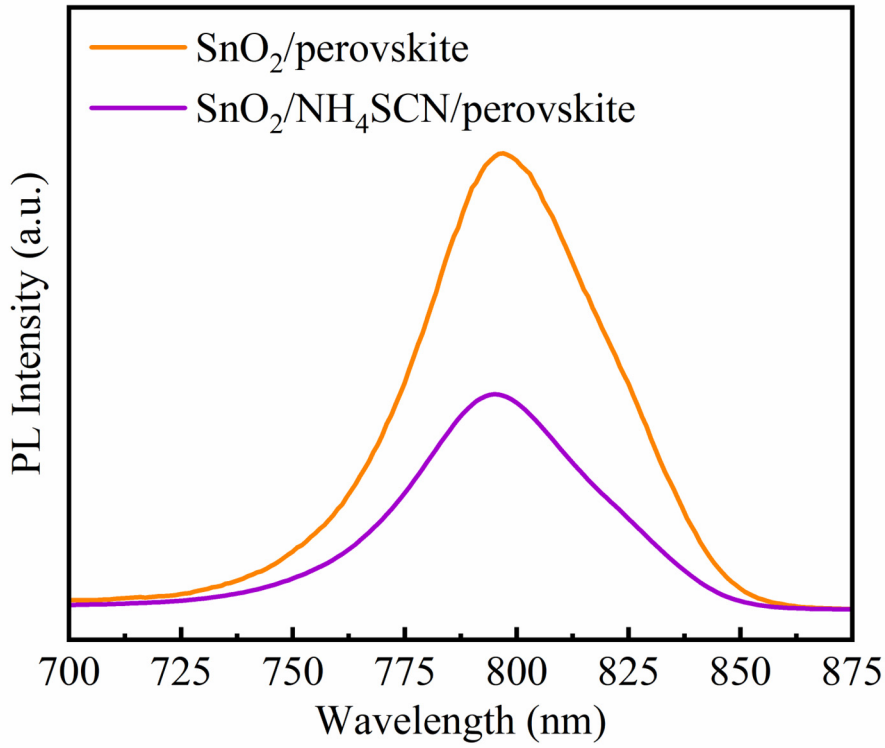

Figure 7.9 | PL spectra of perovskite films deposited on SnO_2 with and without NH_4SCN.

Good wettability of the perovskite precursor solution on the SnO_2 interface could improve the crystalline quality of the perovskite crystals and film coverage level , which is crucial for achieving high-performance PSCs [247]. The contact angle test results are presented in Figure 7.10, indicating that on SnO_2/NH_4SCN, the contact angle of the perovskite solution decreased to 13.2° compared to the 21.3° observed on the SnO_2 substrate. With reduced contact angle, precursor solution of perovskite can be better dispersed during the spin-coating process, with consequent better film quality.

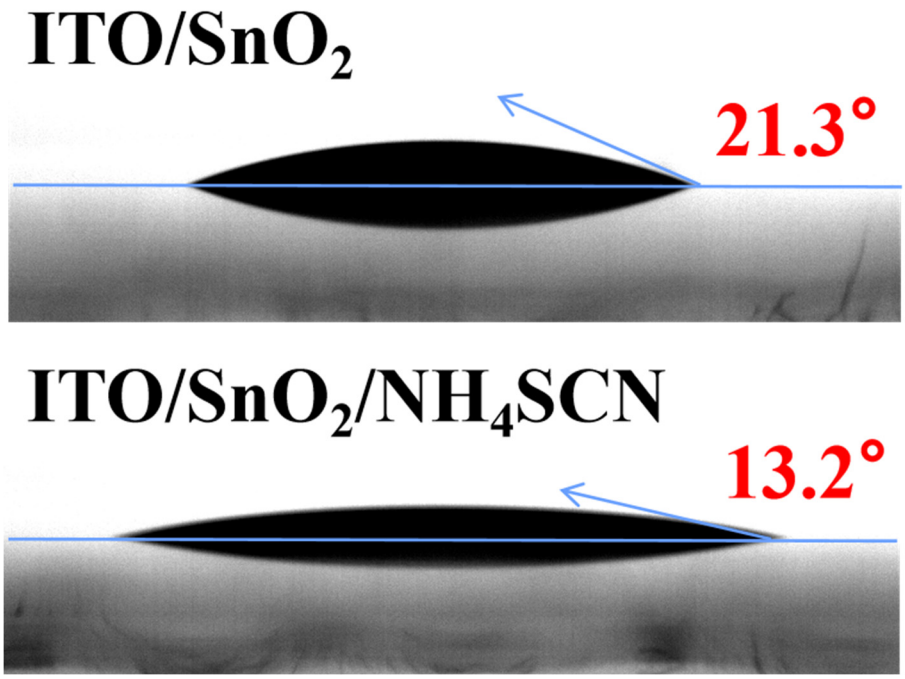

Figure 7.10 | The contact angles of perovskite precursor solution on ITO/SnO_2 and ITO/SnO_2/NH_4SCN.

As scanning electron microscopy (SEM) images shown in Figure 7.11a and Figure 7.11b, Gibbs free energy of perovskite nucleation is repressed for a smaller contact angle, leading to a larger grain size during perovskite growth and consequent better film quality [248]. Atomic force microscopy (AFM) measurements indicated minimal impact on the surface roughness of perovskite films after NH_4SCN modification (Figure 7.11c, Figure 7.11d).

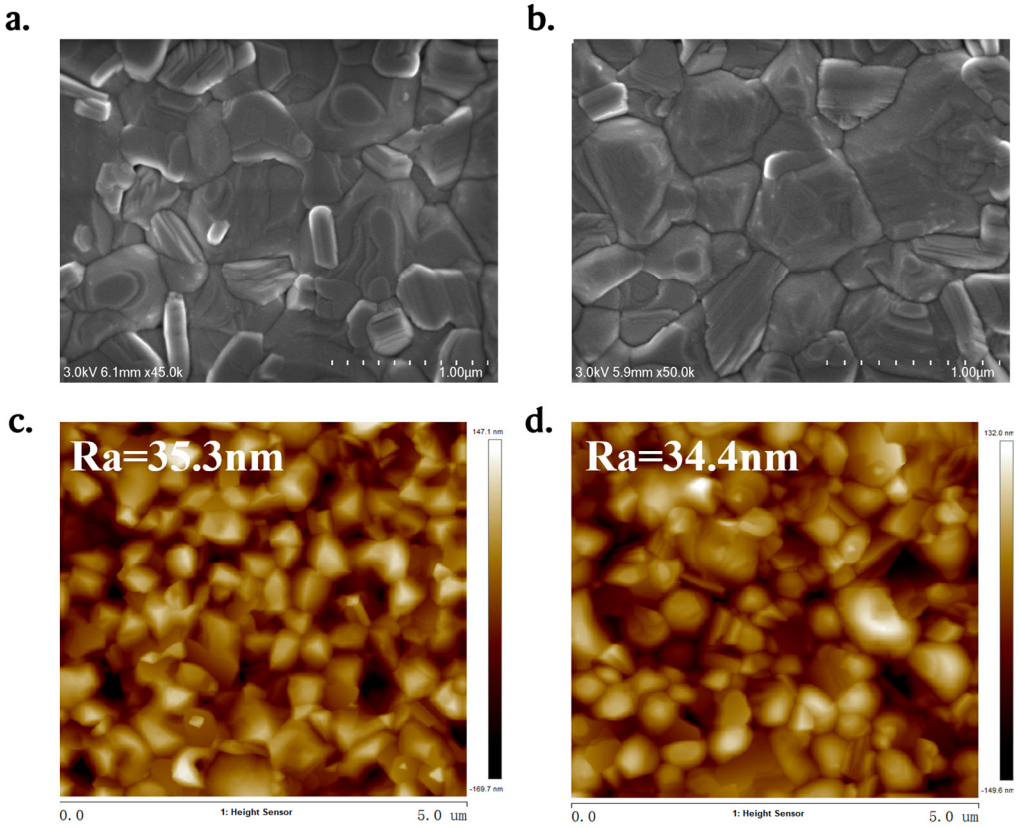

Figure 7.11 | (a) (b) SEM results of perovskite films on SnO_2 and SnO_2/NH_4SCN substrates. (c) (d) AFM images of perovskite films on SnO_2 and SnO_2/NH_4SCN substrates.

To investigate the effect of NH_4SCN passivation on the crystalline characteristics of perovskite, XRD tests are then performed. As in Figure 7.12 (full spectra) and Figure 7.13 (fine spectra), the presence of NH_4SCN decreased the peak intensity of PbI_2 at 12.6°, indicating a significant removal of residual PbI_2 content from perovskites. Also, the FWHM of perovskite decreased while the peak intensity increased, showing a decrease in the residual level of PbI_2 and an enhancement in the crystallinity of the perovskite

following the treatment. In the common two-step manufacturing process, the remaining amount of PbI_2 present in the crystals of the perovskite contribute to defects formation [249, 250], and the reduced PbI_2 indicates fewer defects in perovskite crystals. Furthermore, diffraction peak positions remained consistent across all perovskite films, indicating that NH_4SCN inclusion did not change perovskite lattice parameters but as an interfacial passivator.

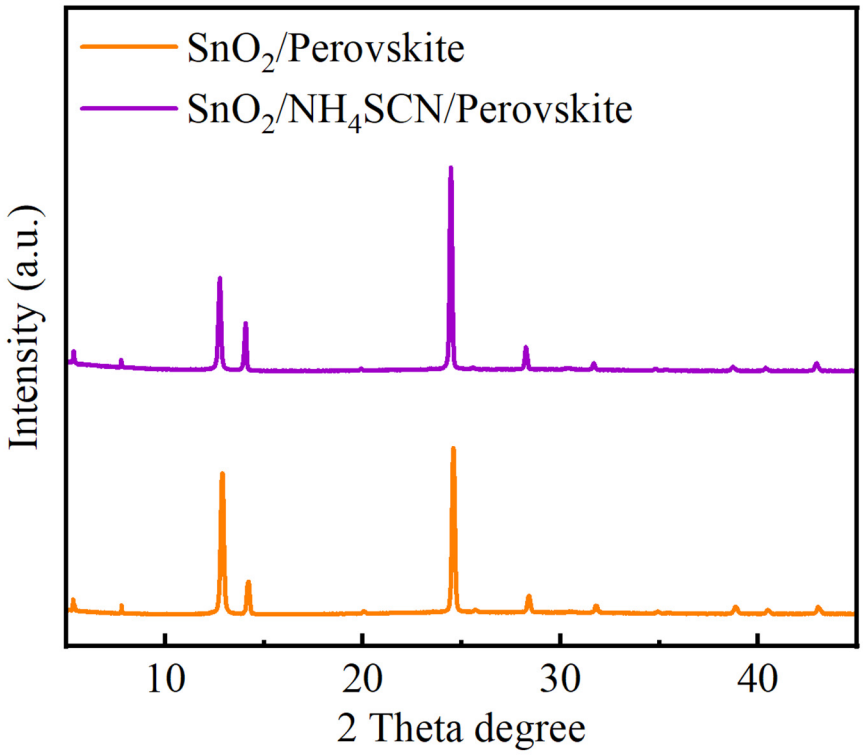

Figure 7.12 | a) c) f) XRD full spectra of perovskite films on SnO_2 and SnO_2/NH_4SCN substrates.

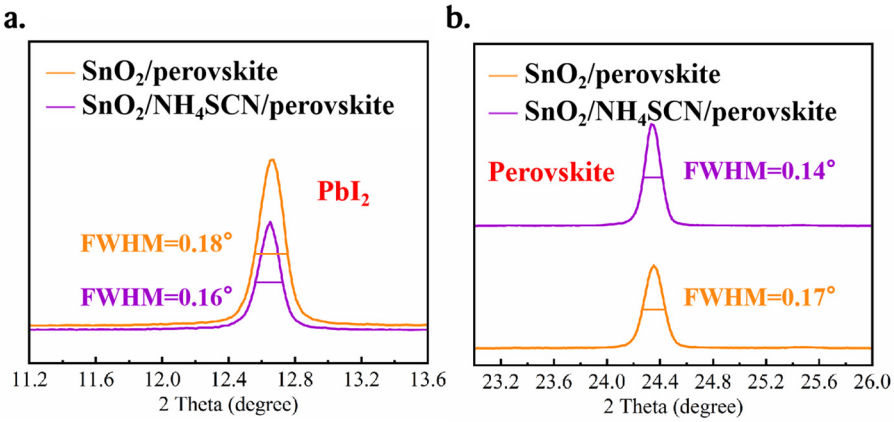

Figure 7.13 | XRD fine patterns of (a) PbI_2 peaks and (b) perovskite peaks for films deposited on ITO/SnO_2 and ITO/SnO_2/NH_4SCN.

The NH_4SCN interfacial passivation strategy can also passivate the defects in perovskite film since both ammonium and thiocyanate ions are mainly located near the SnO_2/perovskite surface but can also diffuse throughout the bulk of the perovskite layers, as shown in TOF-SIMS results (Figure 7.14). From the results, both intensities of N and S elements increase gradually with the sputter time, indicating the existence of both ammonium and thiocyanate ions, and this can be attributed to the addition of NH_4SCN at the SnO_2/perovskite surface. Also, after the sputter time of 300 s, Sn element intensity increases rapidly while Pb element intensity drops, indicating the sputtering process is close to SnO_2/perovskite surface. The highest intensities of both N and S elements appear near 350 s, showing that NH_4SCN is mainly located near the SnO_2/perovskite surface but can also diffuse throughout the bulk of the perovskite layers.

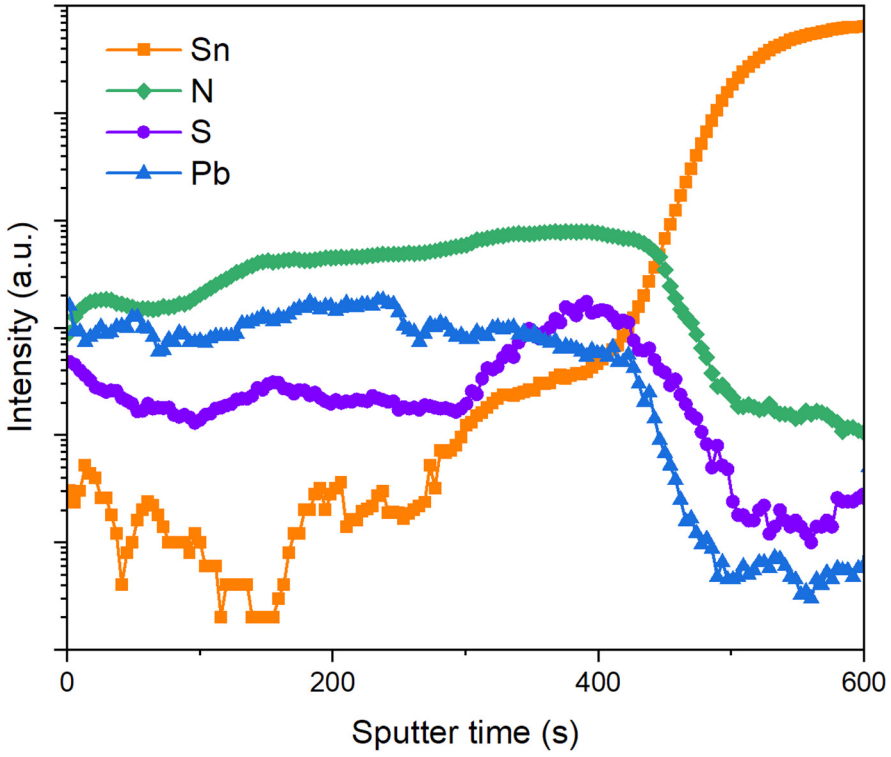

Figure 7.14 | TOF-SIMS results of SnO_2/NH_4SCN perovskite film.

Steady-state PL is employed to analyse perovskite films fabricated by deposition on glass substrates whether or not with NH_4SCN treatment (as shown in Figure 7.15) [251]. With NH_4SCN, the photoluminescence (PL) intensity of the perovskite films is enhanced by about 0.8 times, meaning that nonradiative recombination is suppressed.

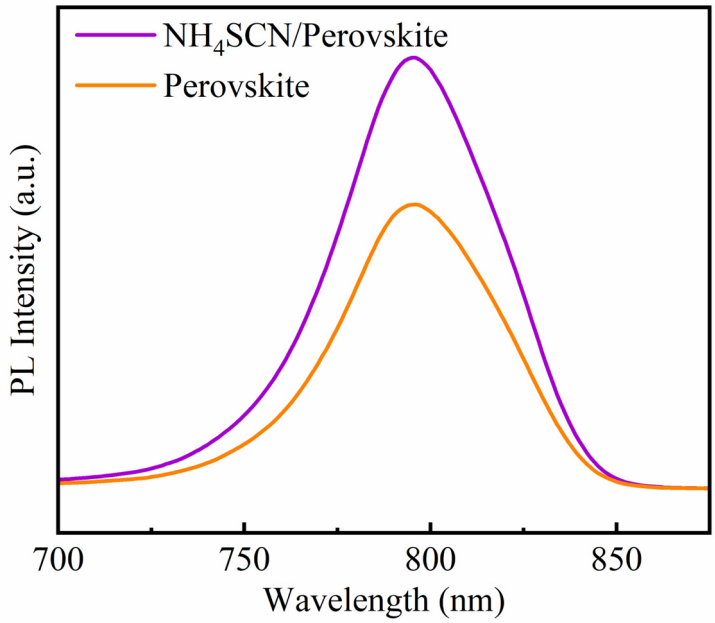

Figure 7.15 | PL spectra of different perovskite films with NH_4SCN and without NH_4SCN.

Space Charge Limited Current (SCLC) technology is then used to quantify trap state concentration in perovskite films on the devices with structure of ITO / ETLs / Perovskite / PCBM / Au (Figure 7.16). Herein, the passivated film exhibited a lower voltage limited by trap filling (V_{TFL}) and a corresponding lower defect density [63], indicating efficient defect passivation and suppression effect via NH_4SCN.

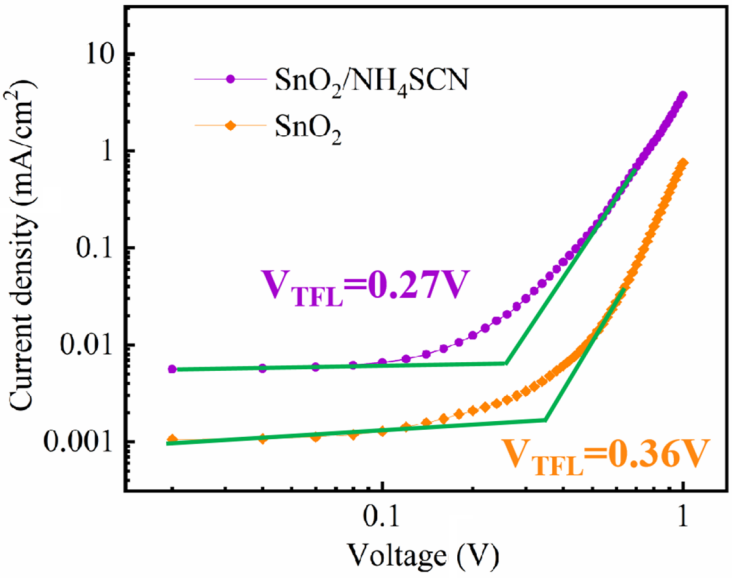

Figure 7.16 | SCLC test of electron-only devices with and without adding NH_4SCN.

7.4 High efficiency and stability quasi-2D PePVs

Inspired by the improved interfacial matching and perovskite film quality, quasi-2D PePVs are then fabricated. The NH_4SCN based devices have the best performance with PCE of 21.96%, higher than the control device with PCE of 20.32% (Figure 7.17a). The enhanced device performance is primarily attributed to the increase of V_{OC} and *FF*, reflecting better interfacial contact via the utilization of NH_4SCN. The EQE spectra of the respective devices are shown in Figure 7.17b. The total current densities obtained from the EQE spectra for the control and target devices are 24.93 mA/cm^2 and 24.96 mA/cm^2, respectively. These values are in good consistency with the J_{sc} values derived from the current density-voltage (I-V) test.

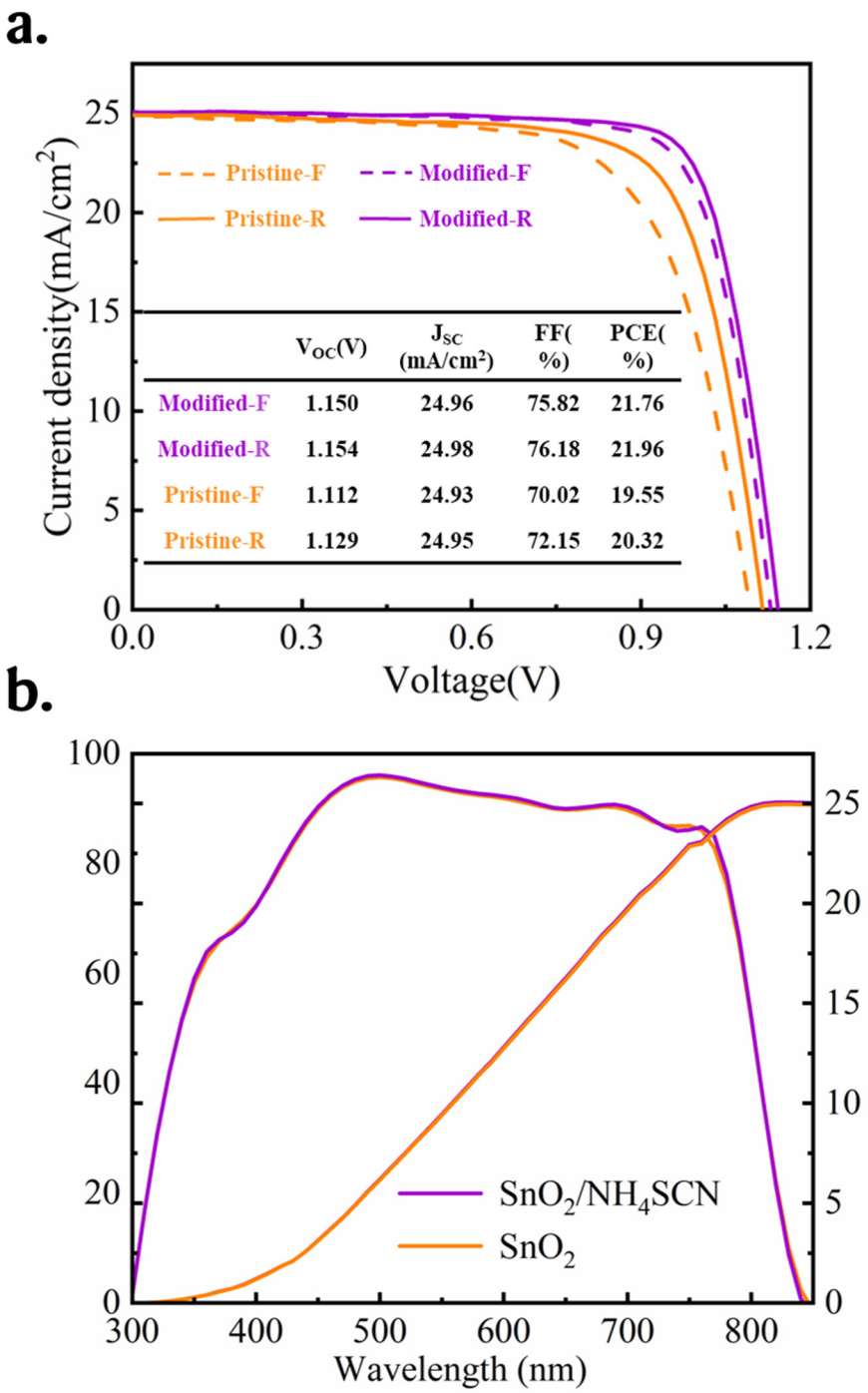

	V_{OC}(V)	J_{SC} (mA/cm²)	FF(%)	PCE(%)
Modified-F	1.150	24.96	75.82	21.76
Modified-R	1.154	24.98	76.18	21.96
Pristine-F	1.112	24.93	70.02	19.55
Pristine-R	1.129	24.95	72.15	20.32

Figure 7.17 | (a) *J-V* curves of SnO_2 and SnO_2/NH_4SCN ETL devices. (b) EQE of SnO_2 and SnO_2/NH_4SCN ETL devices.

Meanwhile, as the comparison, the NH_4SCN interfacial passivation devices show even higher PCE than the conventional devices using NH_4SCN as

additive (Figure 7.18), indicating the efficacy of the interfacial passivation strategy comparing to conventional NH_4SCN additive method, in good consistence with the better energy level matching (Figure 7.8).

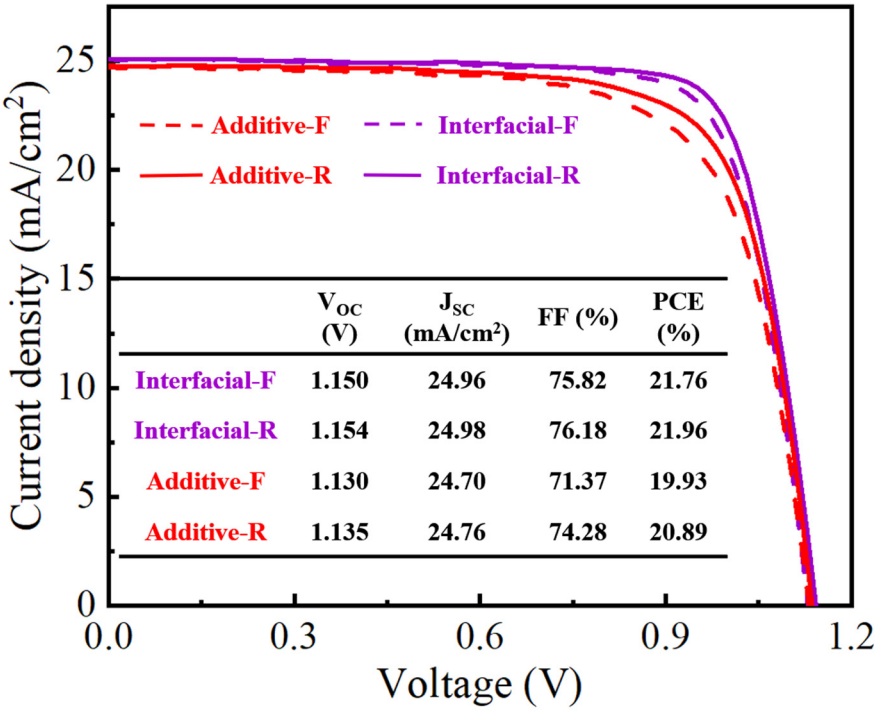

	V_{OC} (V)	J_{SC} (mA/cm²)	FF (%)	PCE (%)
Interfacial-F	1.150	24.96	75.82	21.76
Interfacial-R	1.154	24.98	76.18	21.96
Additive-F	1.130	24.70	71.37	19.93
Additive-R	1.135	24.76	74.28	20.89

Figure 7.18 | *J-V* curves of devices based on NH_4SCN interfacial passivation and NH_4SCN as additive.

The repeatability of the devices is assessed, both pre- and post-passivation. 30 identical devices are subsequently prepared to assess consistency and consistency in device performance (Figure 7.19 and Figure 7.20). In contrast to PCE variability of 18.2% to 20.2% in devices with SnO_2 ETL, those using SnO_2/NH_4SCN ETL exhibited a PCE range of 19.8 to 22.0%, indicating no harm in fabrication reproducibility.

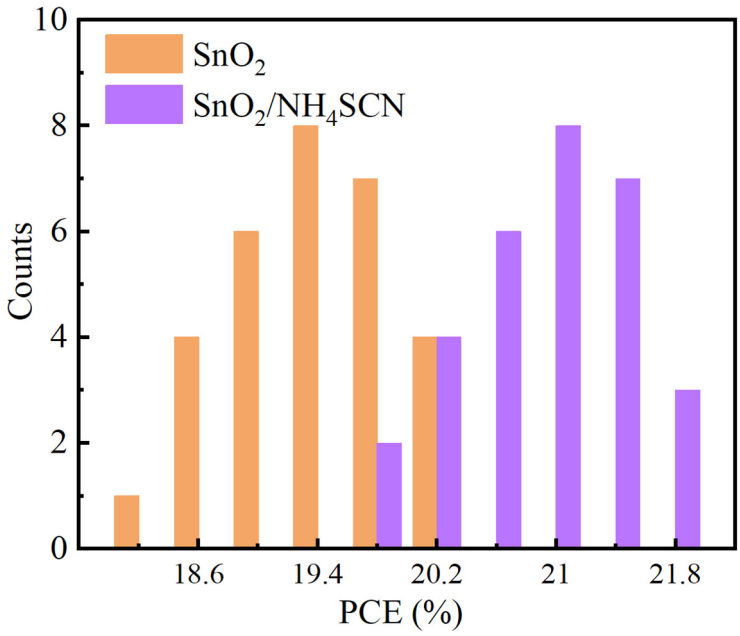

Figure 7.19 | The PCE distribution of 30 devices with or without NH_4SCN.

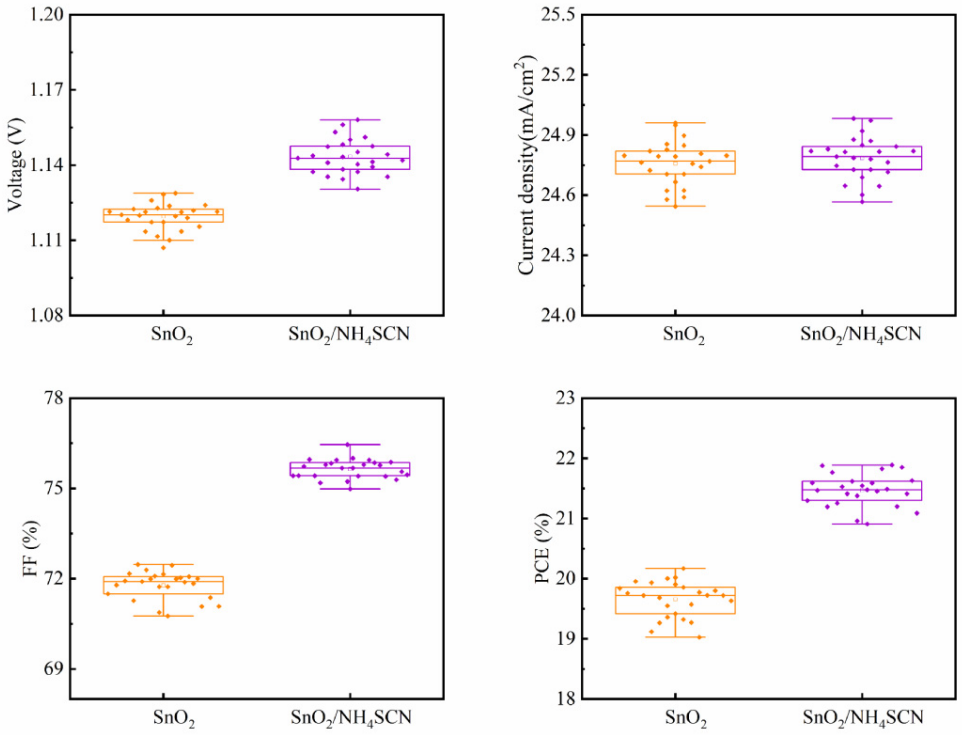

Figure 7.20 | Statistics of PCE distribution of 30 devices with or without NH_4SCN passivation.

The correlation between V_{OC} and the light intensity is revealed in Figure 7.21. The slope deviation from unity in solar cells suggests trap-assisted recombination, where K_B represents the Boltzmann constant, T for absolute temperature, and q for elementary charge. The slope of the device using SnO_2/NH_4SCN ETL is 1.57 K_BT/q, smaller than that of the device based on SnO_2 ETL (1.81 K_BT/q), suggesting a substantial decrease in defect-assisted charge recombination [252, 253].

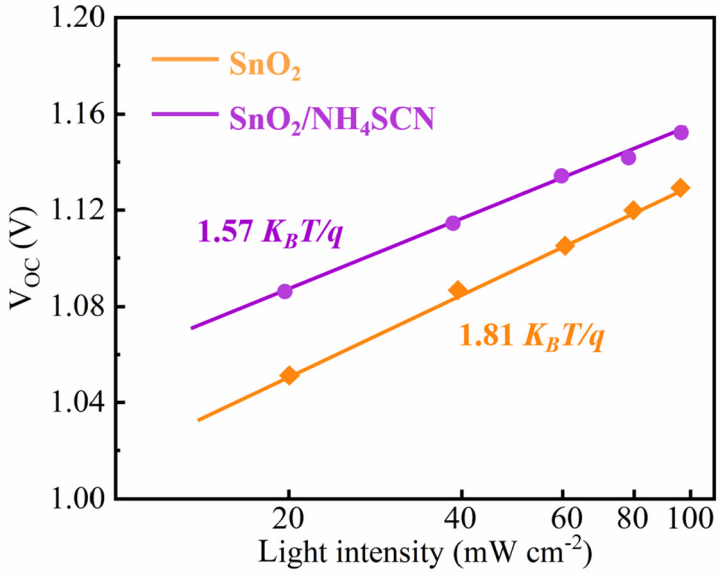

Figure 7.21 | The correlation between V_{oc} and light intensity with and without adding NH_4SCN.

Then, Figure 7.22 illustrates the Nyquist plots and the corresponding equivalent circuit representing the carrier recombination process, with Rs denoting the devices' series resistance. Rrec and CPE are terms used to describe the resistance to recombination at the ETL-perovskite interface,

along with chemical capacitance [254]. The fitted Rs for SnO_2/NH_4SCN is smaller comparing to the pristine device, indicating reduced series resistance after NH_4SCN modification. While the Rrec of SnO_2/NH_4SCN based device is larger, suggesting suppressed defect-assisted recombination within the device.

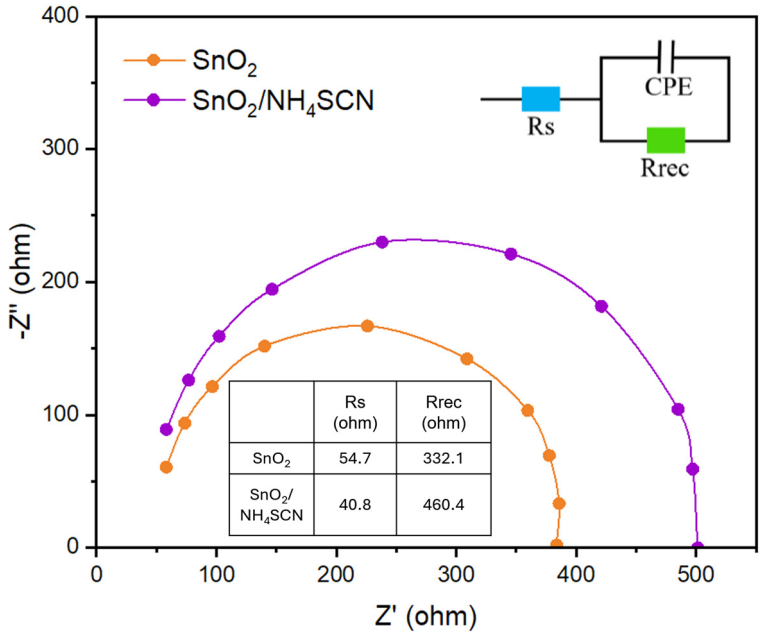

Figure 7.22 | Nyquist plots for both devices.

The stability results of non-encapsulated devices aged in dry air at ambient temperature are illustrated in Figure 7.23 and Figure S7-9. The PSC that uses SnO_2/NH_4SCN ETL sustains 90% of the initial PCE after 3,000 hours, showing an impressive stability consistent with the improvement on film crystallinity, while the PCE of the PSC with SnO_2 ETL decreases by approximately 30% after 3,000 hours. The significant enhancements on device stability without

encapsulation have presented a bright future for industrial scale applications.

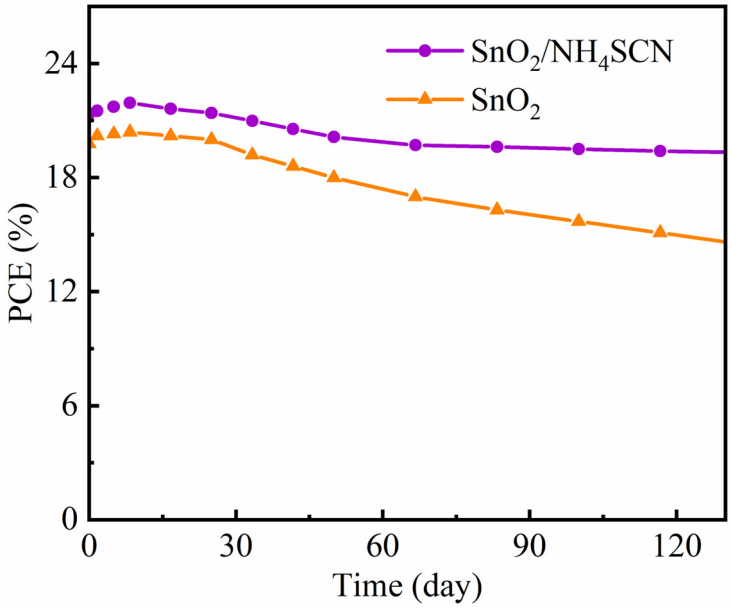

Figure 7.23 | Storage stability (O_2, 25 °C) of SnO_2 and SnO_2/NH_4SCN ETL perovskite photovoltaic devices.

What's more, the MPP tracking results also confirmed that the SnO_2/NH_4SCN interfacial passivation can improve the operational stability, as shown in Figure 7.24 and Figure 7.25. At room temperature (25 °C), the pristine device retains only 78.5% of the original PCE after 400 h operation, while the device with NH_4SCN interfacial passivation can maintain over 94.0% of the initial PCE. All the results have confirmed that the SnO_2/NH_4SCN interfacial passivation strategy can improve both the storage and operational stability of PSCS, in good accordance with the improved film quality and crystallinity as well as lowered defect density.

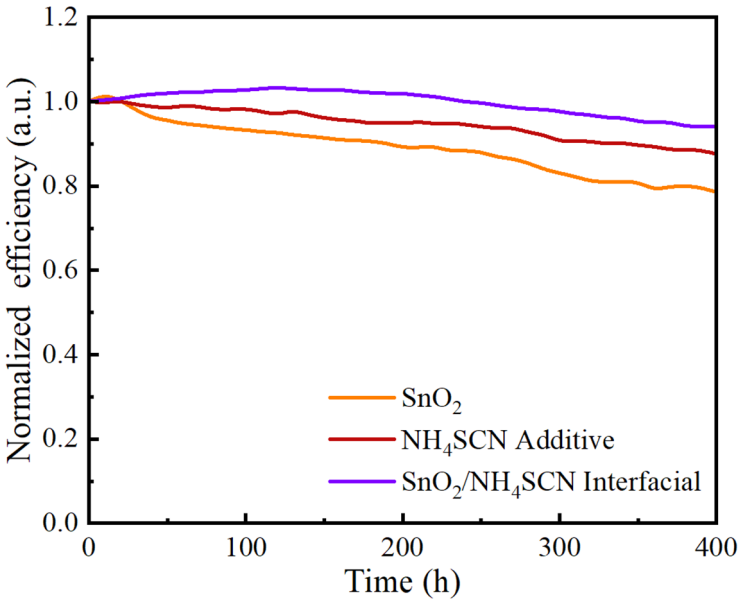

Figure 7.24 | MPP tracking results of different devices under 1 sun illumination at room temperature (25 °C).

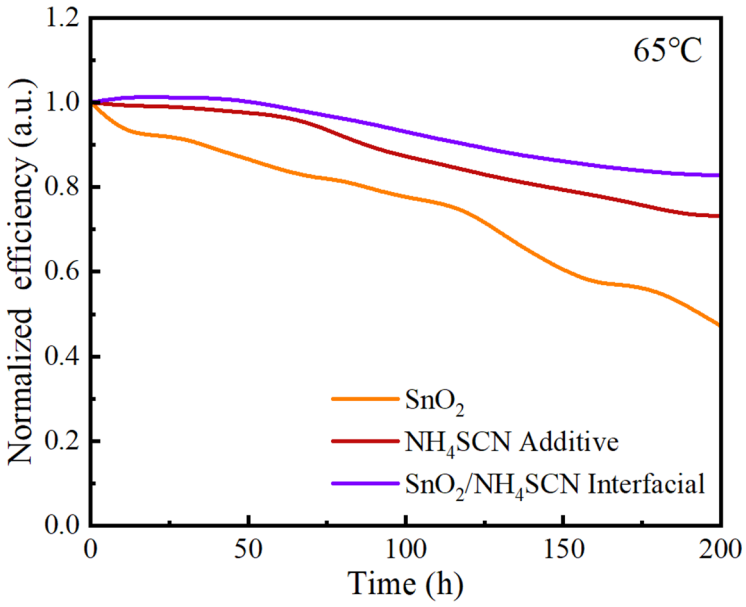

Figure 7.25 | MPP tracking results of different devices under 1 sun illumination at 65 °C.

Finally, the solvent sieve method has been employed to further improve the

efficiency of PePVs, as summarized in Table 7.1. The treated PCE is improved to 22.35%, one of the highest PCEs for all reported quasi-2D PePVs, with further improvement in operational stability, further affirming the versatility of our solvent sieve method.

Table 7.1 | Performance of pristine and solvent sieved PePVs.

	Pristine	Solvent sieved
Maximum PCE (%)	21.96	22.35
PCE maintained after 1,000 h MPP tracking (%)	86.2	91.4

7.5 Discussion

This chapter introduces a novel interfacial modification approach utilizing NH_4SCN to attain highly efficient and stable quasi-2D PePVs. Departing from conventional NH_4SCN additive strategies [199, 235–239], which incorporate NH_4SCN within the perovskite layer and elevate the energy levels and thereby impede electron transport, the proposed NH_4SCN interfacial passivation mechanism prevents altering the energy levels of the bulk perovskites and maintains unhindered electron extraction, as illustrated in Figure 7.8. Meanwhile, the interfacial modification strategy can further improve the wetting of perovskite precursors on SnO_2 layer (Figure 7.10), leading to higher perovskite film quality as well as higher device PCEs compared to pristine and conventional NH_4SCN additives, as compared in Figure 7.17 and Figure 7.18.

This interfacial modification strategy rather than conventional additives has underscored the importance of rationally and precisely applying chemicals, such as additives or for interfacial modifications, grounded in deeper understandings of their specific mechanisms and the resultant material properties.

To date, the interfacial modifications of SnO_2 ETL have been substantially studied, with recent focus on the interface defects passivation. Inorganic ionic compounds, such as potassium chloride (KCl) and potassium iodide (KI), employ both anionic and cationic components to coordinate with both negative and positive defects at the SnO_2-perovskite interface [252, 255, 256]. Meanwhile, some organic molecules with functional groups such as amines (-NH_2), carboxylic acids (-COOH), and halides (F, Cl), have also demonstrated efficacy in coordinating with defect sites at interfaces, and significantly tune the surface energy level of SnO_2 and suppress surface defects [255, 257–259]. To enhance the quality of perovskite films and address SnO_2 interfacial defects issues, ionic compounds NH_4SCN with large electronegative anions and cations are strategically selected. Therefore, the NH_4SCN interfacial modification significantly enhances the interface quality of high-performance PePVs, with optimized interfacial defect passivation (Figure 7.5) as well as improved perovskite precursor wetting (Figure 7.10). Therefore, the perovskite crystallinity is significantly improved, as evidenced by the XRD

patterns (Figure 7.12 and Figure 7.13), and the defects are reduced (Figure 7.16). Thus, with comprehensive considerations of efficient interfacial defect passivation, improved interfacial energy level matching, and optimized perovskite precursors wettability, high efficiency, and operational stability quasi-2D PePVs are finally achieved with our strategy.

The concern regarding the perovskite material system is crucial. In this chapter, quasi-2D perovskite solar cells are fabricated. Theoretically, compared to 3D ones, quasi-2D perovskite solar cells can exhibit potentially high stability due to the stabilization effect of incorporated ligands [37, 260]. However, to date, no significant advantages on device stability have been achieved for quasi-2D PePVs compared to the 3D counterparts, wherein both PePVs can maintain over 90% PCEs after more than 1,000 h MPP tracking [261, 262]. On the other hand, the PCEs of quasi-2D PePVs have fallen behind, with highest PCEs slightly higher than 22% [37, 261, 263, 264] compared to over 26% of 3D PePVs [265]. Therefore, underlying factors contributing to this discrepancy can be analysed from both material and device levels.

As reviewed in Chapter 2, quasi-2D perovskites possess a distinctive mixed-quantum-well architecture integrating bulky organic ligand layers between the perovskite slabs. This structure, while tending to enhance material stability by suppressing ion migration, inadvertently introduces barrier

layers to charge carrier transportation, as shown in Figure 7.26 [266]. These barriers thereby impede exciton dissociation and subsequent electricity conversion of PePVs. Conversely, 3D perovskites exhibit continuous and extensive crystal structure that facilitate efficient charge transportation, resulting in enhanced exciton dissociation and higher PCEs. Hence, the quantum confinement effect with multi-quantum-well structure might not be a prerequisite for attaining substantially high PCEs.

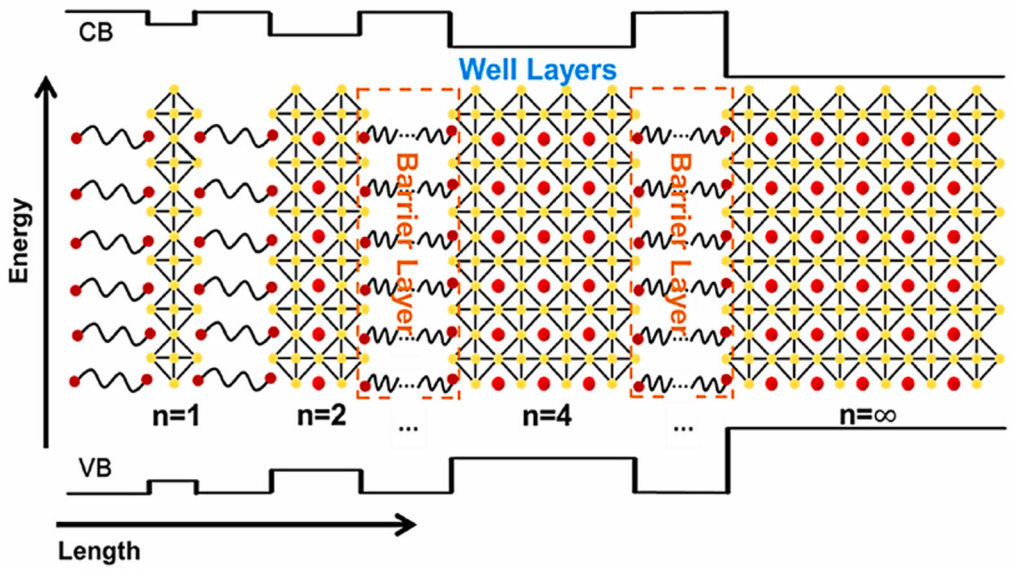

Figure 7.26 | Scheme of charrier transportation across quasi-2D perovskites [266].

Extending this concern, perovskite quantum dots PVs (PeQDPVs) with even stronger quantum confinement alongside bulky organic ligands introduction have encountered severe challenges on PCEs. To date, the

maximum PCEs of PeQDPVs have not exceeded 18% [267–269]. Consequently, there arises a demand to critically re-evaluate the essentiality of quantum confinement in architectural design for high efficiency PePVs, while innovative strategies that can facilitate efficient charge transfer and exciton dissociation within locally quantum confined material systems shall be developed to transcend current PCE limitations.

Regarding the stability concerns, the failure of quasi-2D PePVs to exhibit much longer lifetime can partly attribute to the increased chemical complexity after large cations introduction, necessitating even finer tuning for quasi-2D systems. However, one critical factor that received inadequate attention is that all the state-of-the-art quasi-2D PePVs still contain low n phases [37, 261, 263, 264, 270]. As thoroughly deliberated in Chapter 4, the low n phases inside quasi-2D perovskite are the origin of instability, potentially preventing the manifestation of the stability advantages of quasi-2D perovskites. Therefore, the removal of low n phases from quasi-2D PePVs might be another decisive advance for exceptionally stable PePVs.

Finally, as the employment of solvent sieve method to our quasi-2D PePVs (Table 7.1), although the sieved quasi-2D PePVs still show the highest PCEs for all reported quasi-2D PePVs, the enhancements of device performance is not as critical as PeLEDs counterparts. The discrepancy might lie in the different

film thicknesses, where PeLEDs typically have a perovskite layer thickness of approximately 50 nm, a dimension that permits solvent penetration and thorough removal of low-n phases. However, PePVs possess much greater thickness, exceeding 500 nm in our experiments, which impedes the solvent's capacity to fully dissolve all low n phases. Thus, the development of thick film applicable solvent sieve method to overcome the phase dimensions challenges will be performed following the confirmation of advantages for quasi-2D PePVs.

7.6 Summary

In conclusion, ammonium thiocyanate can effectively passivate the buried interface defects of quasi-2D perovskite devices. Detailed characterization shows that the NH_4SCN passivation plays multiple roles in improving the PSC performance. The interaction between NH_4SCN and SnO_2 ETL can effectively reduce the defect density of the SnO_2 interface and improve the energy level matching between SnO_2 and perovskite films, ultimately leading to an improvement in device efficiency. Then, preparing perovskite films with smaller contact angles on the SnO_2/NH_4SCN ETL substrate results in larger grains and lower defect density, leading to significant increase in V_{OC} and *FF*. The SnO_2/NH_4SCN-based PSCs achieved improved performance with an optimum PCE of 21.96%. Additionally, the devices retained 90% of their initial PCE after 3,000 hours in dry air without encapsulation, underscoring the

critical role of improving the interface quality in the fabrication of efficient and stable PePVs.

Moreover, the intrinsic concerns about interfacial modification molecule selection and quantum confinement in PePVs have been discussed. Although theoretically quantum confinement with ligands can stabilize perovskite structures, the hindrance to charge extraction shall not be neglected. Meanwhile, optimized solvent sieve method might be of great enhancement to quasi-2D PePVs, while critical challenges on treatment depth should be overcome in the future.

Chapter 8. Conclusions and Perspective

To summarize, this thesis begins with a comprehensive overview of MHP materials and their applications in optoelectronic devices. Owing to their unique electronic and optical characteristics, MHPs have emerged as a leading candidate for next generation optoelectronic materials, finding widespread applications in diverse areas, including PeLEDs and PePVs. However, to meet the rigorous industrial standards, there is an urgent need to enhance the stability and efficiency of MHP-based devices. However, the incomplete understanding of the complex origins behind their instability and inefficiency still hinders the improvements on device performance. Consequently, this thesis aims to delve into the fundamental mechanisms governing these issues and proposes efficacious solutions to improve the performance of MHP-based optoelectronic devices, particularly focusing on PeLEDs and PePVs.

Through a thorough literature review of the fundamental structures and key properties of MHP materials, this thesis has identified the principal challenges affecting the performance of PeLEDs and PePVs. For PeLEDs, the resolving of phase dimensions, suppression of defects, and hindrance of ion migration are predominant concerns impacting device efficiency and stability. Conversely, for PePVs, interface optimization is vital for enhancing device performance.

- Phase Dimensions Resolving: Quasi-2D perovskites exhibit a unique multi-quantum-well structure characterized by mixed phase dimensions, where the thickness of a single quantum well is defined by the n value (representing the number of lead-centred octahedra along the thickness direction). Therefore, excitons can funnel from high-bandgap low n phases to low-bandgap high n ones. To effectively resolve these phase dimensions, meticulous characterizations are conducted revealing that low n phases are responsible for perovskite instability and performance deficiencies. A simple and innovative solvent sieve post-treatment method is developed to selectively remove low n phases, thereby promoting efficient inter-phase energy funnelling. This leads to the fabrication of highly stable and efficient PeLEDs, displaying peak EQE of 29.5% and half-lifetime T_{50} of 18.67 hours at 12,000 cd/m² (corresponding to over 50,317 hours or 5.7 years at 100 cd/m²). These PeLEDs also show exceptional resistance to environmental degradation, retaining over 75% of their film photoluminescence quantum yield and 80% of device EQE even after 100 days in ambient conditions. This solvent sieve method underscores the feasibility of MHPs for advanced luminescence applications and unlocks their potential for industrial grade efficiency and stability in PeLEDs.
- Defect Suppression: Defects within MHPs induce non-radiative recombination of excitons and severe ion mobility, degrading the

efficiency and stability of PeLEDs. To counteract this, a sweet coordination strategy is proposed to optimize the perovskite growth process, effectively suppressing defect formation. Application of this strategy results in the fabrication of PeLEDs with outstanding efficiency (maximum EQE of 31.3%) and operational stability (half-life T_{50} exceeding 76.9 hours at an initial luminance of 10,000 cd/m^2, equivalent to over 211,800 hours or 24.2 years at 100 cd/m^2). This breakthrough paves the way for future PeLED applications in the display and lighting sectors.

- Ion Migration Hindrance: Ion migration, a phenomenon stemming from the soft and deformable lattice of MHPs, has contributed significantly to the limited operational lifetime of PeLEDs. To address this challenge, a highly fluorinated molecule, PFHA, is employed to spontaneously form strong coordinative bonds with all perovskite ions, effectively hindering ion migration. This enables ultra-stable and efficient green PeLEDs with a peak EQE of 27.1% and an unprecedented T_{50} lifetime of 103.17 hours at 10,000 cd/m^2 (corresponding to over 326,252 hours or 37.2 years at 100 cd/m^2), setting a benchmark for PeLED operational stability. This work confirms the prospects of PeLEDs for the industrialization in future display and lighting technologies.
- Interface Optimization in PePVs: In quasi-2D PePVs, the organic ligands stabilize the perovskite structure and improve device stability. However, unresolved interfacial issues between the perovskite and charge

transporting layers hinders further progress. To overcome this, interface modification is undertaken with NH_4SCN as a multifunctional passivator at the SnO_2/perovskite interface in quasi-2D PePVs. This effectively passivates interfacial defects, regulates energy levels, and significantly improves precursor wetting and consequent perovskite film quality. This NH_4SCN interfacial modification strategy yields highly efficient and stable quasi-2D PePVs, with a maximum PCE of 21.96% and an impressive stability retaining 90% of the initial PCE after 3,000 hours in ambient conditions.

In conclusion, this thesis has summarized four critical issues of both PeLEDs and PePVs and presented four corresponding solutions to overcome these challenges. As a result, highly stable and efficient PeLEDs and PePVs have been successfully developed. Collectively, these solutions have shown the promising future for the industrialization of perovskite optoelectronic devices.

Chapter 9. Future Work

Overall, although impressive milestones have been achieved with the endeavours of researchers in the field of perovskite optoelectronic devices, future works are still demanded to fulfil the requisites of sustainable, efficient, and scalable technologies. Looking forward, the future trajectory of perovskite optoelectronic devices is underscored by three key areas: further enhancing long term operational stability and manufacturability, advancing towards industry-scale fabrication techniques such as large area and pixelated fabrication, and developing environmentally friendly lead-free perovskites.

Firstly, addressing the Achilles heel of perovskite devices, the operational stability and fabrication reproducibility, remains a pivotal task. The intrinsic instabilities of fabricated perovskite materials, as well as outside stimuli, such as humidity, heat, and UV radiation, have hindered their application from laboratory prototypes to industry-grade products. Future research should concentrate on the underlying mechanisms of degradation from both materials and device levels, including ion migration, phase segregation, and interfacial reactions. Furthermore, advanced encapsulation strategies to protect the active perovskite layer from environmental stresses are also crucial to promoting the industrialization of MHP base optoelectronic devices. Finally, the manufacturability and fabrication repeatability of MHP based optoelectronic devices should be improved with optimizing precursor

compositions, the synthesis procedures, deposition techniques, annealing conditions, and other processing parameters from batches to batches.

Secondly, the transition from laboratory scale prototypes to industry level mass production necessitates the exploration and implementation of scalable fabrication methods. The industrially compatible processes such as roll-to-roll process, inkjet printing, slot-die coating, and spray-coating techniques that can maintain homogeneity and film quality over large areas should be further developed for MHP based devices. Additionally, the integration of MHP materials into pixelated architectures for displays and sensors requires the design and development of patterning methods that preserve the high performance of individual pixels while ensuring good connectivity across the entire pixel array, with novel nano-scale fabrication methods such as lithography, mass transfer and etching.

Finally, the development of environmentally friendly alternatives to conventional lead-based perovskites is also critical in the field. Despite the exceptional optoelectronic properties of lead-halide perovskites, the toxicity and environmental concerns related to lead have prompted intensive research into lead-free candidates. This includes alternative metal cations like tin, germanium, or bismuth, which can potentially maintain the favourable optoelectronic properties of lead while reducing toxicity. Future

studies should focus on synthesizing and optimizing these lead-free perovskites, aiming to achieve comparable or even better performance than the lead-containing counterparts. Additionally, the control and management of lead leakage for current lead containing MHP devices are also instrumental in the realization of environmentally friendly perovskite optoelectronic devices.

In conclusion, the outlooks for perovskite optoelectronic devices have envisioned multiple directions including the improvement of long-term stability and manufacturability, the study of scalable and industry compatible fabrication methodologies, and the development of lead-free alternatives. These efforts are promising to propel MHP based technologies towards a critical and sustainable presence into the global renewable energy and optoelectronic markets, transcending the boundaries of current state-of-the-art devices and pave the roads towards a new era of green, efficient, and cost-effective optoelectronics.

References

[1] R. Wang, H. Liu, Y. Zhang, K. Sun, W. Bao, Integrated Photovoltaic Charging and Energy Storage Systems: Mechanism, Optimization, and Future, Small 18 (2022). https://doi.org/10.1002/smll.202203014.

[2] P. Du, J. Li, L. Wang, L. Sun, X. Wang, X. Xu, L. Yang, J. Pang, W. Liang, J. Luo, Y. Ma, J. Tang, Efficient and large-area all vacuum-deposited perovskite light-emitting diodes via spatial confinement, Nat. Commun. 12 (2021) 4751. https://doi.org/10.1038/s41467-021-25093-6.

[3] K. Sakhatskyi, B. Turedi, G.J. Matt, E. Wu, A. Sakhatska, V. Bartosh, M.N. Lintangpradipto, R. Naphade, I. Shorubalko, O.F. Mohammed, S. Yakunin, O.M. Bakr, M. V. Kovalenko, Stable perovskite single-crystal X-ray imaging detectors with single-photon sensitivity, Nat. Photonics 17 (2023) 510–517. https://doi.org/10.1038/s41566-023-01207-y.

[4] A. Goetzberger, C. Hebling, H.-W. Schock, Photovoltaic materials, history, status and outlook, Mater. Sci. Eng. R Reports 40 (2003) 1–46. https://doi.org/10.1016/S0927-796X(02)00092-X.

[5] N. Zheludev, The life and times of the LED — a 100-year history, Nat. Photonics 1 (2007) 189–192. https://doi.org/10.1038/nphoton.2007.34.

[6] Q. (Frank) Yan, Emissive Displays Rise and Fall – and Rise Again, (n.d.). http://archive.informationdisplay.org/id-archive/2016/november-

december/guest-editorial.

[7] W. Jin, Y. Deng, B. Guo, Y. Lian, B. Zhao, D. Di, X. Sun, K. Wang, S. Chen, Y. Yang, W. Cao, S. Chen, W. Ji, X. Yang, Y. Gao, S. Wang, H. Shen, J. Zhao, L. Qian, F. Li, Y. Jin, On the accurate characterization of quantum-dot light-emitting diodes for display applications, Npj Flex. Electron. 6 (2022) 35. https://doi.org/10.1038/s41528-022-00169-5.

[8] J. Xiong, E.-L. Hsiang, Z. He, T. Zhan, S.-T. Wu, Augmented reality and virtual reality displays: emerging technologies and future perspectives, Light Sci. Appl. 10 (2021) 216. https://doi.org/10.1038/s41377-021-00658-8.

[9] X. Yang, L. Ma, L. Li, M. Luo, X. Wang, Q. Gong, C. Lu, R. Zhu, Towards micro-PeLED displays, Nat. Rev. Mater. 8 (2023) 341–353. https://doi.org/10.1038/s41578-022-00522-0.

[10] X. Wu, H. Ji, X. Yan, H. Zhong, Industry outlook of perovskite quantum dots for display applications, Nat. Nanotechnol. 17 (2022) 813–816. https://doi.org/10.1038/s41565-022-01163-8.

[11] L. Zhang, L. Mei, K. Wang, Y. Lv, S. Zhang, Y. Lian, X. Liu, Z. Ma, G. Xiao, Q. Liu, S. Zhai, S. Zhang, G. Liu, L. Yuan, B. Guo, Z. Chen, K. Wei, A. Liu, S. Yue, G. Niu, X. Pan, J. Sun, Y. Hua, W.-Q. Wu, D. Di, B. Zhao, J. Tian, Z. Wang, Y. Yang, L. Chu, M. Yuan, H. Zeng, H.-L. Yip, K. Yan, W. Xu, L. Zhu, W. Zhang, G. Xing, F. Gao, L. Ding, Advances in the Application of Perovskite Materials, Nano-Micro Lett. 15 (2023) 177.

https://doi.org/10.1007/s40820-023-01140-3.

[12] J. Yan, H. Li, M.H. Aldamasy, C. Frasca, A. Abate, K. Zhao, Y. Hu, Advances in the Synthesis of Halide Perovskite Single Crystals for Optoelectronic Applications, Chem. Mater. 35 (2023) 2683–2712. https://doi.org/10.1021/acs.chemmater.2c03505.

[13] Z. Li, Z. Chen, Y. Yang, Q. Xue, H.-L. Yip, Y. Cao, Modulation of recombination zone position for quasi-two-dimensional blue perovskite light-emitting diodes with efficiency exceeding 5%, Nat. Commun. 10 (2019) 1027. https://doi.org/10.1038/s41467-019-09011-5.

[14] A. Rajagopal, K. Yao, A.K. Jen, Toward Perovskite Solar Cell Commercialization: A Perspective and Research Roadmap Based on Interfacial Engineering, Adv. Mater. 30 (2018) e1800455. https://doi.org/10.1002/adma.201800455.

[15] S.-H. Jeong, J. Park, T.-H. Han, F. Zhang, K. Zhu, J.S. Kim, M.-H. Park, M.O. Reese, S. Yoo, T.-W. Lee, Characterizing the Efficiency of Perovskite Solar Cells and Light-Emitting Diodes, Joule 4 (2020) 1206–1235. https://doi.org/10.1016/j.joule.2020.04.007.

[16] Q. Wang, S. Ding, S. He, T. Zhang, L. Qian, P. Xiao, T. Chen, C. Xiang, Improving the Operational Stability of Near-Infrared Quasi-2D Perovskite Light-Emitting Diodes by Cation Engineering, Adv. Opt. Mater. 11 (2023) 2201778. https://doi.org/10.1002/adom.202201778.

[17] H. Lu, Y. Liu, P. Ahlawat, A. Mishra, W.R. Tress, F.T. Eickemeyer, Y. Yang, F. Fu, Z. Wang, C.E. Avalos, B.I. Carlsen, A. Agarwalla, X. Zhang, X. Li, Y. Zhan, S.M. Zakeeruddin, L. Emsley, U. Rothlisberger, L. Zheng, A. Hagfeldt, M. Grätzel, Vapor-assisted deposition of highly efficient, stable black-phase FAPbI 3 perovskite solar cells, Science (80-.). 370 (2020). https://doi.org/10.1126/science.abb8985.

[18] H. Su, Z. Xu, X. He, Y. Yao, X. Zheng, Y. She, Y. Zhu, J. Zhang, S. (Frank) Liu, Surface Energy Engineering of Buried Interface for Highly Stable Perovskite Solar Cells with Efficiency Over 25%, Adv. Mater. (2023). https://doi.org/10.1002/adma.202306724.

[19] Z.-K. Tan, R.S. Moghaddam, M.L. Lai, P. Docampo, R. Higler, F. Deschler, M. Price, A. Sadhanala, L.M. Pazos, D. Credgington, F. Hanusch, T. Bein, H.J. Snaith, R.H. Friend, Bright light-emitting diodes based on organometal halide perovskite, Nat. Nanotechnol. 9 (2014) 687–692. https://doi.org/10.1038/nnano.2014.149.

[20] W. Bai, T. Xuan, H. Zhao, H. Dong, X. Cheng, L. Wang, R. Xie, Perovskite Light-Emitting Diodes with an External Quantum Efficiency Exceeding 30%, Adv. Mater. 35 (2023). https://doi.org/10.1002/adma.202302283.

[21] X. Xiao, J. Dai, Y. Fang, J. Zhao, X. Zheng, S. Tang, P.N. Rudd, X.C. Zeng, J. Huang, Suppressed Ion Migration along the In-Plane Direction in Layered Perovskites, ACS Energy Lett. 3 (2018) 684–688.

https://doi.org/10.1021/acsenergylett.8b00047.

[22] Q. Dong, J. Mendes, L. Lei, D. Seyitliyev, L. Zhu, S. He, K. Gundogdu, F. So, Understanding the Role of Ion Migration in the Operation of Perovskite Light-Emitting Diodes by Transient Measurements, ACS Appl. Mater. Interfaces 12 (2020) 48845–48853. https://doi.org/10.1021/acsami.0c14269.

[23] Z. Wang, Z. Luo, C. Zhao, Q. Guo, Y. Wang, F. Wang, X. Bian, A. Alsaedi, T. Hayat, Z. Tan, Efficient and Stable Pure Green All-Inorganic Perovskite CsPbBr3 Light-Emitting Diodes with a Solution-Processed NiOx Interlayer, J. Phys. Chem. C 121 (2017) 28132–28138. https://doi.org/10.1021/acs.jpcc.7b11518.

[24] Y. Wei, Z. Cheng, J. Lin, An overview on enhancing the stability of lead halide perovskite quantum dots and their applications in phosphor-converted LEDs, Chem. Soc. Rev. 48 (2019) 310–350. https://doi.org/10.1039/C8CS00740C.

[25] A. Morteza Najarian, F. Dinic, H. Chen, R. Sabatini, C. Zheng, A. Lough, T. Maris, M.I. Saidaminov, F.P. García de Arquer, O. Voznyy, S. Hoogland, E.H. Sargent, Homomeric chains of intermolecular bonds scaffold octahedral germanium perovskites, Nature 620 (2023) 328–335. https://doi.org/10.1038/s41586-023-06209-y.

[26] C. Xiang, L. Wu, Z. Lu, M. Li, Y. Wen, Y. Yang, W. Liu, T. Zhang, W. Cao, S.-W. Tsang, B. Shan, X. Yan, L. Qian, High efficiency and stability of

ink-jet printed quantum dot light emitting diodes, Nat. Commun. 11 (2020) 1646. https://doi.org/10.1038/s41467-020-15481-9.

[27] NREL, Best Research-Cell Efficiency Chart, (n.d.). https://www.nrel.gov/pv/cell-efficiency.html.

[28] R. Azmi, D.S. Utomo, B. Vishal, S. Zhumagali, P. Dally, A.M. Risqi, A. Prasetio, E. Ugur, F. Cao, I.F. Imran, A.A. Said, A.R. Pininti, A.S. Subbiah, E. Aydin, C. Xiao, S. Il Seok, S. De Wolf, Double-side 2-dimensional/3-dimensional heterojunctions for inverted perovskite solar cells, Nature (2024). https://doi.org/10.1038/s41586-024-07189-3.

[29] H. Li, C. Zhang, C. Gong, D. Zhang, H. Zhang, Q. Zhuang, X. Yu, S. Gong, X. Chen, J. Yang, X. Li, R. Li, J. Li, J. Zhou, H. Yang, Q. Lin, J. Chu, M. Grätzel, J. Chen, Z. Zang, 2D/3D heterojunction engineering at the buried interface towards high-performance inverted methylammonium-free perovskite solar cells, Nat. Energy 8 (2023) 946–955. https://doi.org/10.1038/s41560-023-01295-8.

[30] Z. Ren, K. Liu, H. Hu, X. Guo, Y. Gao, P.W.K. Fong, Q. Liang, H. Tang, J. Huang, H. Zhang, M. Qin, L. Cui, H.T. Chandran, D. Shen, M.-F. Lo, A. Ng, C. Surya, M. Shao, C.-S. Lee, X. Lu, F. Laquai, Y. Zhu, G. Li, Room-temperature multiple ligands-tailored SnO2 quantum dots endow in situ dual-interface binding for upscaling efficient perovskite photovoltaics with high VOC, Light Sci. Appl. 10 (2021) 239. https://doi.org/10.1038/s41377-021-00676-6.

[31] P.W.K. Fong, G. Li, The Challenge of Ambient Air–Processed Organometallic Halide Perovskite: Technology Transfer From Spin Coating to Meniscus Blade Coating of Perovskite Thin Films, Front. Mater. 8 (2021) 18. https://doi.org/10.3389/FMATS.2021.635224/BIBTEX.

[32] S.K. Karunakaran, G.M. Arumugam, W. Yang, S. Ge, S.N. Khan, X. Lin, G. Yang, Recent progress in inkjet-printed solar cells, J. Mater. Chem. A 7 (2019) 13873–13902. https://doi.org/10.1039/C9TA03155C.

[33] F. Schackmar, H. Eggers, M. Frericks, B.S. Richards, U. Lemmer, G. Hernandez-Sosa, U.W. Paetzold, Perovskite Solar Cells with All-Inkjet-Printed Absorber and Charge Transport Layers, Adv. Mater. Technol. 6 (2021). https://doi.org/10.1002/admt.202000271.

[34] Z. Tang, S. Ding, K. Kang, T. Zhang, C. Xiang, L. Qian, Application of inkjet printing in the large area display of organic light-emitting diode, Chinese Sci. Bull. 66 (2021) 2117–2128. https://doi.org/10.1360/TB-2020-1350.

[35] Y.Y. Kim, T.-Y. Yang, R. Suhonen, A. Kemppainen, K. Hwang, N.J. Jeon, J. Seo, Roll-to-roll gravure-printed flexible perovskite solar cells using eco-friendly antisolvent bathing with wide processing window, Nat. Commun. 11 (2020) 5146. https://doi.org/10.1038/s41467-020-18940-5.

[36] B. Dou, J.B. Whitaker, K. Bruening, D.T. Moore, L.M. Wheeler, J. Ryter,

N.J. Breslin, J.J. Berry, S.M. Garner, F.S. Barnes, S.E. Shaheen, C.J. Tassone, K. Zhu, M.F.A.M. van Hest, Roll-to-Roll Printing of Perovskite Solar Cells, ACS Energy Lett. 3 (2018) 2558–2565. https://doi.org/10.1021/acsenergylett.8b01556.

[37] Y. Zhang, N.-G. Park, Quasi-Two-Dimensional Perovskite Solar Cells with Efficiency Exceeding 22%, ACS Energy Lett. 7 (2022) 757–765. https://doi.org/10.1021/acsenergylett.1c02645.

[38] A. Kojima, K. Teshima, Y. Shirai, T. Miyasaka, Organometal Halide Perovskites as Visible-Light Sensitizers for Photovoltaic Cells, J. Am. Chem. Soc. 131 (2009) 6050–6051. https://doi.org/10.1021/ja809598r.

[39] K. Lin, J. Xing, L.N. Quan, F.P.G. de Arquer, X. Gong, J. Lu, L. Xie, W. Zhao, D. Zhang, C. Yan, W. Li, X. Liu, Y. Lu, J. Kirman, E.H. Sargent, Q. Xiong, Z. Wei, Perovskite light-emitting diodes with external quantum efficiency exceeding 20 per cent, Nature 562 (2018) 245–248. https://doi.org/10.1038/s41586-018-0575-3.

[40] Y.-H. Kim, S. Kim, A. Kakekhani, J. Park, J. Park, Y.-H. Lee, H. Xu, S. Nagane, R.B. Wexler, D.-H. Kim, S.H. Jo, L. Martínez-Sarti, P. Tan, A. Sadhanala, G.-S. Park, Y.-W. Kim, B. Hu, H.J. Bolink, S. Yoo, R.H. Friend, A.M. Rappe, T.-W. Lee, Comprehensive defect suppression in perovskite nanocrystals for high-efficiency light-emitting diodes, Nat. Photonics 15 (2021) 148–155. https://doi.org/10.1038/s41566-020-00732-4.

[41] X.-K. Liu, W. Xu, S. Bai, Y. Jin, J. Wang, R.H. Friend, F. Gao, Metal halide perovskites for light-emitting diodes, Nat. Mater. 20 (2021) 10–21. https://doi.org/10.1038/s41563-020-0784-7.

[42] C. Sun, Y. Jiang, M. Cui, L. Qiao, J. Wei, Y. Huang, L. Zhang, T. He, S. Li, H.-Y. Hsu, C. Qin, R. Long, M. Yuan, High-performance large-area quasi-2D perovskite light-emitting diodes, Nat. Commun. 12 (2021) 2207. https://doi.org/10.1038/s41467-021-22529-x.

[43] F. Li, J. Yuan, X. Ling, Y. Zhang, Y. Yang, S.H. Cheung, C.H.Y. Ho, X. Gao, W. Ma, A Universal Strategy to Utilize Polymeric Semiconductors for Perovskite Solar Cells with Enhanced Efficiency and Longevity, Adv. Funct. Mater. 28 (2018). https://doi.org/10.1002/adfm.201706377.

[44] Q. Shan, J. Song, Y. Zou, J. Li, L. Xu, J. Xue, Y. Dong, B. Han, J. Chen, H. Zeng, High Performance Metal Halide Perovskite Light-Emitting Diode: From Material Design to Device Optimization, Small 13 (2017) 1701770. https://doi.org/10.1002/smll.201701770.

[45] W. Zhan, L. Meng, C. Shao, X. Wu, K. Shi, H. Zhong, In Situ Patterning Perovskite Quantum Dots by Direct Laser Writing Fabrication, ACS Photonics 8 (2021) 765–770. https://doi.org/10.1021/acsphotonics.1c00118.

[46] F. Li, J. Yuan, X. Ling, Y. Zhang, Y. Yang, S.H. Cheung, C.H.Y. Ho, X. Gao, W. Ma, A Universal Strategy to Utilize Polymeric Semiconductors for Perovskite Solar Cells with Enhanced Efficiency and Longevity, Adv.

Funct. Mater. 28 (2018) 1706377. https://doi.org/10.1002/adfm.201706377.

[47] X. Xu, Y. Zhong, Z. Shao, Double Perovskites in Catalysis, Electrocatalysis, and Photo(electro)catalysis, Trends Chem. 1 (2019) 410–424. https://doi.org/10.1016/j.trechm.2019.05.006.

[48] L.A. Muscarella, E.M. Hutter, Halide Double-Perovskite Semiconductors beyond Photovoltaics, ACS Energy Lett. 7 (2022) 2128–2135. https://doi.org/10.1021/acsenergylett.2c00811.

[49] S. Vasala, M. Karppinen, A2B′B″O6 perovskites: A review, Prog. Solid State Chem. 43 (2015) 1–36. https://doi.org/10.1016/j.progsolidstchem.2014.08.001.

[50] G. Volonakis, M.R. Filip, A.A. Haghighirad, N. Sakai, B. Wenger, H.J. Snaith, F. Giustino, Lead-Free Halide Double Perovskites via Heterovalent Substitution of Noble Metals, J. Phys. Chem. Lett. 7 (2016) 1254–1259. https://doi.org/10.1021/acs.jpclett.6b00376.

[51] X. Gong, O. Voznyy, A. Jain, W. Liu, R. Sabatini, Z. Piontkowski, G. Walters, G. Bappi, S. Nokhrin, O. Bushuyev, M. Yuan, R. Comin, D. McCamant, S.O. Kelley, E.H. Sargent, Electron–phonon interaction in efficient perovskite blue emitters, Nat. Mater. 17 (2018) 550–556. https://doi.org/10.1038/s41563-018-0081-x.

[52] W. Kyung, C.H. Kim, Y.K. Kim, B. Kim, C. Kim, W. Jung, J. Kwon, M. Kim, A. Bostwick, J.D. Denlinger, Y. Yoshida, C. Kim, Electric-field-driven

octahedral rotation in perovskite, Npj Quantum Mater. 6 (2021) 5. https://doi.org/10.1038/s41535-020-00306-1.

[53] Q.A. Akkerman, L. Manna, What Defines a Halide Perovskite?, ACS Energy Lett. 5 (2020) 604–610. https://doi.org/10.1021/acsenergylett.0c00039.

[54] T. Masuda, Y. Zhang, C. Ding, F. Liu, K. Sasaki, Q. Shen, M. Endo, All-inorganic cesium lead halide perovskite nanocrystals for solar-pumped laser application, J. Appl. Phys. 127 (2020) 243104. https://doi.org/10.1063/5.0011945.

[55] L. Zhang, C. Sun, T. He, Y. Jiang, J. Wei, Y. Huang, M. Yuan, High-performance quasi-2D perovskite light-emitting diodes: from materials to devices, Light Sci. Appl. 10 (2021) 61. https://doi.org/10.1038/s41377-021-00501-0.

[56] C. Katan, N. Mercier, J. Even, Quantum and Dielectric Confinement Effects in Lower-Dimensional Hybrid Perovskite Semiconductors, Chem. Rev. 119 (2019) 3140–3192. https://doi.org/10.1021/acs.chemrev.8b00417.

[57] B. Traore, L. Pedesseau, L. Assam, X. Che, J.-C. Blancon, H. Tsai, W. Nie, C.C. Stoumpos, M.G. Kanatzidis, S. Tretiak, A.D. Mohite, J. Even, M. Kepenekian, C. Katan, Composite Nature of Layered Hybrid Perovskites: Assessment on Quantum and Dielectric Confinements and Band Alignment, ACS Nano 12 (2018) 3321–3332.

https://doi.org/10.1021/acsnano.7b08202.

[58] Z. He, Y. Liu, Z. Yang, J. Li, J. Cui, D. Chen, Z. Fang, H. He, Z. Ye, H. Zhu, N. Wang, J. Wang, Y. Jin, High-Efficiency Red Light-Emitting Diodes Based on Multiple Quantum Wells of Phenylbutylammonium-Cesium Lead Iodide Perovskites, ACS Photonics 6 (2019) 587–594. https://doi.org/10.1021/acsphotonics.8b01435.

[59] C. Wu, T. Wu, Y. Yang, J.A. McLeod, Y. Wang, Y. Zou, T. Zhai, J. Li, M. Ban, T. Song, X. Gao, S. Duhm, H. Sirringhaus, B. Sun, Alternative Type Two-Dimensional–Three-Dimensional Lead Halide Perovskite with Inorganic Sodium Ions as a Spacer for High-Performance Light-Emitting Diodes, ACS Nano (2019) acsnano.8b07632. https://doi.org/10.1021/acsnano.8b07632.

[60] Y. Miao, L. Cheng, W. Zou, L. Gu, J. Zhang, Q. Guo, Q. Peng, M. Xu, Y. He, S. Zhang, Y. Cao, R. Li, N. Wang, W. Huang, J. Wang, Microcavity top-emission perovskite light-emitting diodes, Light Sci. Appl. 9 (2020) 89. https://doi.org/10.1038/s41377-020-0328-6.

[61] M. Kumagai, T. Takagahara, Excitonic and nonlinear-optical properties of dielectric quantum-well structures, Phys. Rev. B 40 (1989) 12359–12381. https://doi.org/10.1103/PhysRevB.40.12359.

[62] C. Gao, Y. Jiang, C. Sun, J. Han, T. He, Y. Huang, K. Yao, M. Han, X. Wang, Y. Wang, Y. Gao, Y. Liu, M. Yuan, H. Liang, Multifunctional Naphthol Sulfonic Salt Incorporated in Lead-Free 2D Tin Halide

Perovskite for Red Light-Emitting Diodes, ACS Photonics 7 (2020) 1915–1922. https://doi.org/10.1021/acsphotonics.0c00497.

[63] W. Li, S. Ding, C. Wu, L. Qian, C. Xiang, Potassium Acetate Passivated SnO 2 Interface for High-Efficiency Two-Step Deposited Perovskite Solar Cells, Adv. Sustain. Syst. 7 (2023). https://doi.org/10.1002/adsu.202300124.

[64] S. Chu, W. Chen, Z. Fang, X. Xiao, Y. Liu, J. Chen, J. Huang, Z. Xiao, Large-area and efficient perovskite light-emitting diodes via low-temperature blade-coating, Nat. Commun. 12 (2021). https://doi.org/10.1038/s41467-020-20433-4.

[65] J.S. Manser, P. V. Kamat, Band filling with free charge carriers in organometal halide perovskites, Nat. Photonics 8 (2014) 737–743. https://doi.org/10.1038/nphoton.2014.171.

[66] A. Miyata, A. Mitioglu, P. Plochocka, O. Portugall, J.T.-W. Wang, S.D. Stranks, H.J. Snaith, R.J. Nicholas, Direct measurement of the exciton binding energy and effective masses for charge carriers in organic–inorganic tri-halide perovskites, Nat. Phys. 11 (2015) 582–587. https://doi.org/10.1038/nphys3357.

[67] J.S. Kim, J.-M. Heo, G.-S. Park, S.-J. Woo, C. Cho, H.J. Yun, D.-H. Kim, J. Park, S.-C. Lee, S.-H. Park, E. Yoon, N.C. Greenham, T.-W. Lee, Ultra-bright, efficient and stable perovskite light-emitting diodes, Nature 611 (2022) 688–694. https://doi.org/10.1038/s41586-022-05304-w.

[68] M. Yuan, L.N. Quan, R. Comin, G. Walters, R. Sabatini, O. Voznyy, S. Hoogland, Y. Zhao, E.M. Beauregard, P. Kanjanaboos, Z. Lu, D.H. Kim, E.H. Sargent, Perovskite energy funnels for efficient light-emitting diodes, Nat. Nanotechnol. 11 (2016) 872–877. https://doi.org/10.1038/nnano.2016.110.

[69] Y. Cao, N. Wang, H. Tian, J. Guo, Y. Wei, H. Chen, Y. Miao, W. Zou, K. Pan, Y. He, H. Cao, Y. Ke, M. Xu, Y. Wang, M. Yang, K. Du, Z. Fu, D. Kong, D. Dai, Y. Jin, G. Li, H. Li, Q. Peng, J. Wang, W. Huang, Perovskite light-emitting diodes based on spontaneously formed submicrometre-scale structures, Nature 562 (2018) 249–253. https://doi.org/10.1038/s41586-018-0576-2.

[70] L.C. Schmidt, A. Pertegás, S. González-Carrero, O. Malinkiewicz, S. Agouram, G. Mínguez Espallargas, H.J. Bolink, R.E. Galian, J. Pérez-Prieto, Nontemplate Synthesis of CH 3 NH 3 PbBr 3 Perovskite Nanoparticles, J. Am. Chem. Soc. 136 (2014) 850–853. https://doi.org/10.1021/ja4109209.

[71] X. Zhang, Q. Wang, Z. Yao, M. Deng, J. Wang, L. Qian, Y. Ren, Y. Yan, C. Xiang, Stable Perovskite Quantum Dots Light-Emitting Diodes with Efficiency Exceeding 24%, Adv. Sci. 10 (2023). https://doi.org/10.1002/advs.202304696.

[72] D. Ma, K. Lin, Y. Dong, H. Choubisa, A.H. Proppe, D. Wu, Y.-K. Wang, B. Chen, P. Li, J.Z. Fan, F. Yuan, A. Johnston, Y. Liu, Y. Kang, Z.-H. Lu, Z.

Wei, E.H. Sargent, Distribution control enables efficient reduced-dimensional perovskite LEDs, Nature 599 (2021) 594–598. https://doi.org/10.1038/s41586-021-03997-z.

[73] S. Ding, Q. Wang, W. Gu, Z. Tang, B. Zhang, C. Wu, X. Zhang, H. Chen, X. Zhang, R. Cao, T. Chen, L. Qian, C. Xiang, Phase dimensions resolving of efficient and stable perovskite light-emitting diodes at high brightness, Nat. Photonics 18 (2024) 363–370. https://doi.org/10.1038/s41566-023-01372-0.

[74] G. Long, R. Sabatini, M.I. Saidaminov, G. Lakhwani, A. Rasmita, X. Liu, E.H. Sargent, W. Gao, Chiral-perovskite optoelectronics, Nat. Rev. Mater. 5 (2020) 423–439. https://doi.org/10.1038/s41578-020-0181-5.

[75] Y.-H. Kim, Y. Zhai, H. Lu, X. Pan, C. Xiao, E.A. Gaulding, S.P. Harvey, J.J. Berry, Z.V. Vardeny, J.M. Luther, M.C. Beard, Chiral-induced spin selectivity enables a room-temperature spin light-emitting diode, Science (80-.). 371 (2021) 1129–1133. https://doi.org/10.1126/science.abf5291.

[76] G. Long, C. Jiang, R. Sabatini, Z. Yang, M. Wei, L.N. Quan, Q. Liang, A. Rasmita, M. Askerka, G. Walters, X. Gong, J. Xing, X. Wen, R. Quintero-Bermudez, H. Yuan, G. Xing, X.R. Wang, D. Song, O. Voznyy, M. Zhang, S. Hoogland, W. Gao, Q. Xiong, E.H. Sargent, Spin control in reduced-dimensional chiral perovskites, Nat. Photonics 12 (2018) 528–533. https://doi.org/10.1038/s41566-018-0220-6.

[77] H. Liang, F. Yuan, A. Johnston, C. Gao, H. Choubisa, Y. Gao, Y. Wang, L.K. Sagar, B. Sun, P. Li, G. Bappi, B. Chen, J. Li, Y. Wang, Y. Dong, D. Ma, Y. Gao, Y. Liu, M. Yuan, M.I. Saidaminov, S. Hoogland, Z. Lu, E.H. Sargent, High Color Purity Lead-Free Perovskite Light-Emitting Diodes via Sn Stabilization, Adv. Sci. 7 (2020). https://doi.org/10.1002/advs.201903213.

[78] J.A. Sichert, Y. Tong, N. Mutz, M. Vollmer, S. Fischer, K.Z. Milowska, R. García Cortadella, B. Nickel, C. Cardenas-Daw, J.K. Stolarczyk, A.S. Urban, J. Feldmann, Quantum Size Effect in Organometal Halide Perovskite Nanoplatelets, Nano Lett. 15 (2015) 6521–6527. https://doi.org/10.1021/acs.nanolett.5b02985.

[79] N. Wang, L. Cheng, R. Ge, S. Zhang, Y. Miao, W. Zou, C. Yi, Y. Sun, Y. Cao, R. Yang, Y. Wei, Q. Guo, Y. Ke, M. Yu, Y. Jin, Y. Liu, Q. Ding, D. Di, L. Yang, G. Xing, H. Tian, C. Jin, F. Gao, R.H. Friend, J. Wang, W. Huang, Perovskite light-emitting diodes based on solution-processed self-organized multiple quantum wells, Nat. Photonics 10 (2016) 699–704. https://doi.org/10.1038/nphoton.2016.185.

[80] C. Ortiz-Cervantes, P. Carmona-Monroy, D. Solis-Ibarra, Two-Dimensional Halide Perovskites in Solar Cells: 2D or not 2D?, ChemSusChem 12 (2019) 1560–1575. https://doi.org/10.1002/cssc.201802992.

[81] L. Cheng, T. Jiang, Y. Cao, C. Yi, N. Wang, W. Huang, J. Wang, Multiple-

Quantum-Well Perovskites for High-Performance Light-Emitting Diodes, Adv. Mater. 32 (2020). https://doi.org/10.1002/adma.201904163.

[82] Z. Fang, W. Chen, Y. Shi, J. Zhao, S. Chu, J. Zhang, Z. Xiao, Dual Passivation of Perovskite Defects for Light-Emitting Diodes with External Quantum Efficiency Exceeding 20%, Adv. Funct. Mater. 30 (2020) 1909754. https://doi.org/10.1002/adfm.201909754.

[83] X. Lao, X. Li, H. Ågren, G. Chen, Highly Controllable Synthesis and DFT Calculations of Double/Triple-Halide CsPbX3 (X = Cl, Br, I) Perovskite Quantum Dots: Application to Light-Emitting Diodes, Nanomaterials 9 (2019) 172. https://doi.org/10.3390/nano9020172.

[84] Y. Jiang, J. Wei, M. Yuan, Energy-Funneling Process in Quasi-2D Perovskite Light-Emitting Diodes, J. Phys. Chem. Lett. 12 (2021) 2593–2606. https://doi.org/10.1021/acs.jpclett.1c00072.

[85] X. Zhang, H. Liu, W. Wang, J. Zhang, B. Xu, K.L. Karen, Y. Zheng, S. Liu, S. Chen, K. Wang, X.W. Sun, Hybrid Perovskite Light-Emitting Diodes Based on Perovskite Nanocrystals with Organic-Inorganic Mixed Cations, Adv. Mater. 29 (2017) 1606405. https://doi.org/10.1002/adma.201606405.

[86] D. Meggiolaro, S.G. Motti, E. Mosconi, A.J. Barker, J. Ball, C. Andrea Riccardo Perini, F. Deschler, A. Petrozza, F. De Angelis, Iodine chemistry determines the defect tolerance of lead-halide perovskites,

Energy Environ. Sci. 11 (2018) 702–713.
https://doi.org/10.1039/C8EE00124C.

[87] Y.-H. Kim, H. Cho, J.H. Heo, T.-S. Kim, N. Myoung, C.-L. Lee, S.H. Im, T.-W. Lee, Multicolored Organic/Inorganic Hybrid Perovskite Light-Emitting Diodes, Adv. Mater. 27 (2015) 1248–1254.
https://doi.org/10.1002/adma.201403751.

[88] X. Wang, Y. Ling, X. Lian, Y. Xin, K.B. Dhungana, F. Perez-Orive, J. Knox, Z. Chen, Y. Zhou, D. Beery, K. Hanson, J. Shi, S. Lin, H. Gao, Suppressed phase separation of mixed-halide perovskites confined in endotaxial matrices, Nat. Commun. 10 (2019) 695.
https://doi.org/10.1038/s41467-019-08610-6.

[89] Y. Fang, Q. Dong, Y. Shao, Y. Yuan, J. Huang, Highly narrowband perovskite single-crystal photodetectors enabled by surface-charge recombination, Nat. Photonics 9 (2015) 679–686.
https://doi.org/10.1038/nphoton.2015.156.

[90] N. Yantara, N.F. Jamaludin, B. Febriansyah, D. Giovanni, A. Bruno, C. Soci, T.C. Sum, S. Mhaisalkar, N. Mathews, Designing the Perovskite Structural Landscape for Efficient Blue Emission, ACS Energy Lett. 5 (2020) 1593–1600. https://doi.org/10.1021/acsenergylett.0c00559.

[91] J. Kang, L.-W. Wang, High Defect Tolerance in Lead Halide Perovskite CsPbBr 3, J. Phys. Chem. Lett. 8 (2017) 489–493.
https://doi.org/10.1021/acs.jpclett.6b02800.

[92] K.X. Steirer, P. Schulz, G. Teeter, V. Stevanovic, M. Yang, K. Zhu, J.J. Berry, Defect Tolerance in Methylammonium Lead Triiodide Perovskite, ACS Energy Lett. 1 (2016) 360–366. https://doi.org/10.1021/acsenergylett.6b00196.

[93] N. Wang, L. Cheng, R. Ge, S. Zhang, Y. Miao, W. Zou, C. Yi, Y. Sun, Y. Cao, R. Yang, Y. Wei, Q. Guo, Y. Ke, M. Yu, Y. Jin, Y. Liu, Q. Ding, D. Di, L. Yang, G. Xing, H. Tian, C. Jin, F. Gao, R.H. Friend, J. Wang, W. Huang, Perovskite light-emitting diodes based on solution-processed self-organized multiple quantum wells, Nat. Photonics 10 (2016) 699–704. https://doi.org/10.1038/nphoton.2016.185.

[94] L.N. Quan, Y. Zhao, F.P. García De Arquer, R. Sabatini, G. Walters, O. Voznyy, R. Comin, Y. Li, J.Z. Fan, H. Tan, J. Pan, M. Yuan, O.M. Bakr, Z. Lu, D.H. Kim, E.H. Sargent, Tailoring the Energy Landscape in Quasi-2D Halide Perovskites Enables Efficient Green-Light Emission, Nano Lett. 17 (2017) 3701–3709. https://doi.org/10.1021/acs.nanolett.7b00976.

[95] D. Zhang, Y. Fu, C. Liu, C. Zhao, X. Gao, J. Zhang, W. Guo, J. Liu, C. Qin, L. Wang, Domain Controlling by Compound Additive toward Highly Efficient Quasi-2D Perovskite Light-Emitting Diodes, Adv. Funct. Mater. 31 (2021). https://doi.org/10.1002/adfm.202103890.

[96] S. Kumar, J. Jagielski, S. Yakunin, P. Rice, Y.-C. Chiu, M. Wang, G. Nedelcu, Y. Kim, S. Lin, E.J.G. Santos, M. V. Kovalenko, C.-J. Shih, Efficient Blue Electroluminescence Using Quantum-Confined Two-

Dimensional Perovskites, ACS Nano 10 (2016) 9720–9729. https://doi.org/10.1021/acsnano.6b05775.

[97] T. Cheng, C. Qin, S. Watanabe, T. Matsushima, C. Adachi, Stoichiometry Control for the Tuning of Grain Passivation and Domain Distribution in Green Quasi-2D Metal Halide Perovskite Films and Light-Emitting Diodes, Adv. Funct. Mater. 30 (2020). https://doi.org/10.1002/adfm.202001816.

[98] J. Xing, Y. Zhao, M. Askerka, L.N. Quan, X. Gong, W. Zhao, J. Zhao, H. Tan, G. Long, L. Gao, Z. Yang, O. Voznyy, J. Tang, Z.-H. Lu, Q. Xiong, E.H. Sargent, Color-stable highly luminescent sky-blue perovskite light-emitting diodes, Nat. Commun. 9 (2018) 3541. https://doi.org/10.1038/s41467-018-05909-8.

[99] K. Gauthron, J.-S. Lauret, L. Doyennette, G. Lanty, A. Al Choueiry, S.J. Zhang, A. Brehier, L. Largeau, O. Mauguin, J. Bloch, E. Deleporte, Optical spectroscopy of two-dimensional layered (C_6H_5C_2H_4-NH_3)_2-PbI_4 perovskite, Opt. Express 18 (2010) 5912. https://doi.org/10.1364/OE.18.005912.

[100] S. Yuan, Z. Wang, L. Xiao, C. Zhang, S. Yang, B. Chen, H. Ge, Q. Tian, Y. Jin, L. Liao, Optimization of Low-Dimensional Components of Quasi-2D Perovskite Films for Deep-Blue Light-Emitting Diodes, Adv. Mater. 31 (2019). https://doi.org/10.1002/adma.201904319.

[101] L. Na Quan, D. Ma, Y. Zhao, O. Voznyy, H. Yuan, E. Bladt, J. Pan, F.P.

Garcia de Arquer, R. Sabatini, Z. Piontkowski, A.H. Emwas, P. Todorovic, R. Quintero-Bermudez, G. Walters, J.Z. Fan, M. Liu, H. Tan, M.I. Saidaminov, L. Gao, Y. Li, D.H. Anjum, N. Wei, J. Tang, D.W. McCamant, M.B.J. Roeffaers, S. Bals, J. Hofkens, O.M. Bakr, Z.H. Lu, E.H. Sargent, Edge stabilization in reduced-dimensional perovskites, Nat Commun 11 (2020) 170. https://doi.org/10.1038/s41467-019-13944-2.

[102] L.N. Quan, M. Yuan, R. Comin, O. Voznyy, E.M. Beauregard, S. Hoogland, A. Buin, A.R. Kirmani, K. Zhao, A. Amassian, D.H. Kim, E.H. Sargent, Ligand-Stabilized Reduced-Dimensionality Perovskites, J. Am. Chem. Soc. 138 (2016) 2649–2655. https://doi.org/10.1021/jacs.5b11740.

[103] L.K. Ono, S. (Frank) Liu, Y. Qi, Reducing Detrimental Defects for High-Performance Metal Halide Perovskite Solar Cells, Angew. Chemie Int. Ed. 59 (2020) 6676–6698. https://doi.org/10.1002/anie.201905521.

[104] Y. Zhou, M. Yang, A.L. Vasiliev, H.F. Garces, Y. Zhao, D. Wang, S. Pang, K. Zhu, N.P. Padture, Growth control of compact CH 3 NH 3 PbI 3 thin films via enhanced solid-state precursor reaction for efficient planar perovskite solar cells, J. Mater. Chem. A 3 (2015) 9249–9256. https://doi.org/10.1039/C4TA07036D.

[105] D. Meggiolaro, E. Mosconi, F. De Angelis, Formation of Surface Defects Dominates Ion Migration in Lead-Halide Perovskites, ACS

Energy Lett. 4 (2019) 779–785.
https://doi.org/10.1021/acsenergylett.9b00247.

[106] C. Ran, J. Xu, W. Gao, C. Huang, S. Dou, Defects in metal triiodide perovskite materials towards high-performance solar cells: origin, impact, characterization, and engineering, Chem. Soc. Rev. 47 (2018) 4581–4610. https://doi.org/10.1039/C7CS00868F.

[107] Q.A. Akkerman, G. Rainò, M. V Kovalenko, L. Manna, Genesis, challenges and opportunities for colloidal lead halide perovskite nanocrystals, Nat. Mater. 17 (2018) 394–405. https://doi.org/10.1038/s41563-018-0018-4.

[108] J.M. Ball, A. Petrozza, Defects in perovskite-halides and their effects in solar cells, Nat. Energy 1 (2016) 16149. https://doi.org/10.1038/nenergy.2016.149.

[109] B. Chen, P.N. Rudd, S. Yang, Y. Yuan, J. Huang, Imperfections and their passivation in halide perovskite solar cells, Chem. Soc. Rev. 48 (2019) 3842–3867. https://doi.org/10.1039/C8CS00853A.

[110] W.-J. Yin, T. Shi, Y. Yan, Unusual defect physics in CH3NH3PbI3 perovskite solar cell absorber, Appl. Phys. Lett. 104 (2014). https://doi.org/10.1063/1.4864778.

[111] W. Yin, T. Shi, Y. Yan, Unique Properties of Halide Perovskites as Possible Origins of the Superior Solar Cell Performance, Adv. Mater. 26 (2014) 4653–4658. https://doi.org/10.1002/adma.201306281.

[112] J. Kim, S.-H. Lee, J.H. Lee, K.-H. Hong, The Role of Intrinsic Defects in Methylammonium Lead Iodide Perovskite, J. Phys. Chem. Lett. 5 (2014) 1312–1317. https://doi.org/10.1021/jz500370k.

[113] Y. Hassan, J.H. Park, M.L. Crawford, A. Sadhanala, J. Lee, J.C. Sadighian, E. Mosconi, R. Shivanna, E. Radicchi, M. Jeong, C. Yang, H. Choi, S.H. Park, M.H. Song, F. De Angelis, C.Y. Wong, R.H. Friend, B.R. Lee, H.J. Snaith, Ligand-engineered bandgap stability in mixed-halide perovskite LEDs, Nature 591 (2021) 72–77. https://doi.org/10.1038/s41586-021-03217-8.

[114] T.A.S. Doherty, A.J. Winchester, S. Macpherson, D.N. Johnstone, V. Pareek, E.M. Tennyson, S. Kosar, F.U. Kosasih, M. Anaya, M. Abdi-Jalebi, Z. Andaji-Garmaroudi, E.L. Wong, J. Madéo, Y.-H. Chiang, J.-S. Park, Y.-K. Jung, C.E. Petoukhoff, G. Divitini, M.K.L. Man, C. Ducati, A. Walsh, P.A. Midgley, K.M. Dani, S.D. Stranks, Performance-limiting nanoscale trap clusters at grain junctions in halide perovskites, Nature 580 (2020) 360–366. https://doi.org/10.1038/s41586-020-2184-1.

[115] E. Mosconi, D. Meggiolaro, H.J. Snaith, S.D. Stranks, F. De Angelis, Light-induced annihilation of Frenkel defects in organo-lead halide perovskites, Energy Environ. Sci. 9 (2016) 3180–3187. https://doi.org/10.1039/C6EE01504B.

[116] M. Worku, A. Ben-Akacha, T. Blessed Shonde, H. Liu, B. Ma, The Past, Present, and Future of Metal Halide Perovskite Light-Emitting Diodes,

Small Sci. 1 (2021). https://doi.org/10.1002/smsc.202000072.

[117] M. Kepenekian, B. Traore, J.-C. Blancon, L. Pedesseau, H. Tsai, W. Nie, C.C. Stoumpos, M.G. Kanatzidis, J. Even, A.D. Mohite, S. Tretiak, C. Katan, Concept of Lattice Mismatch and Emergence of Surface States in Two-dimensional Hybrid Perovskite Quantum Wells, Nano Lett. 18 (2018) 5603–5609. https://doi.org/10.1021/acs.nanolett.8b02078.

[118] Y. Guo, Q. Wang, W.A. Saidi, Structural Stabilities and Electronic Properties of High-Angle Grain Boundaries in Perovskite Cesium Lead Halides, J. Phys. Chem. C 121 (2017) 1715–1722. https://doi.org/10.1021/acs.jpcc.6b11434.

[119] R. Long, J. Liu, O. V. Prezhdo, Unravelling the Effects of Grain Boundary and Chemical Doping on Electron–Hole Recombination in CH 3 NH 3 PbI 3 Perovskite by Time-Domain Atomistic Simulation, J. Am. Chem. Soc. 138 (2016) 3884–3890. https://doi.org/10.1021/jacs.6b00645.

[120] W. Li, M.U. Rothmann, Y. Zhu, W. Chen, C. Yang, Y. Yuan, Y.Y. Choo, X. Wen, Y.-B. Cheng, U. Bach, J. Etheridge, The critical role of composition-dependent intragrain planar defects in the performance of MA1−xFAxPbI3 perovskite solar cells, Nat. Energy 6 (2021) 624–632. https://doi.org/10.1038/s41560-021-00830-9.

[121] Y. Zhou, O.S. Game, S. Pang, N.P. Padture, Microstructures of Organometal Trihalide Perovskites for Solar Cells: Their Evolution

from Solutions and Characterization, J. Phys. Chem. Lett. 6 (2015) 4827–4839. https://doi.org/10.1021/acs.jpclett.5b01843.

[122] Y. Zhang, Y. Liu, Z. Xu, H. Ye, Z. Yang, J. You, M. Liu, Y. He, M.G. Kanatzidis, S. Liu, Nucleation-controlled growth of superior lead-free perovskite Cs3Bi2I9 single-crystals for high-performance X-ray detection, Nat. Commun. 11 (2020) 2304. https://doi.org/10.1038/s41467-020-16034-w.

[123] G. Niu, W. Li, J. Li, X. Liang, L. Wang, Enhancement of thermal stability for perovskite solar cells through cesium doping, RSC Adv. 7 (2017) 17473–17479. https://doi.org/10.1039/C6RA28501E.

[124] L. Zhang, X. Yang, Q. Jiang, P. Wang, Z. Yin, X. Zhang, H. Tan, Y. Yang, M. Wei, B.R. Sutherland, E.H. Sargent, J. You, Ultra-bright and highly efficient inorganic based perovskite light-emitting diodes, Nat. Commun. 8 (2017) 15640. https://doi.org/10.1038/ncomms15640.

[125] Q. Dong, L. Lei, J. Mendes, F. So, Operational stability of perovskite light emitting diodes, J. Phys. Mater. 3 (2020) 012002. https://doi.org/10.1088/2515-7639/ab60c4.

[126] N. Li, Y. Jia, Y. Guo, N. Zhao, Ion Migration in Perovskite Light-Emitting Diodes: Mechanism, Characterizations, and Material and Device Engineering, Adv. Mater. 34 (2022). https://doi.org/10.1002/adma.202108102.

[127] Y. Yamada, Y. Kanemitsu, Electron-phonon interactions in halide

perovskites, NPG Asia Mater. 14 (2022). https://doi.org/10.1038/s41427-022-00394-4.

[128] A.G. Ricciardulli, S. Yang, J.H. Smet, M. Saliba, Emerging perovskite monolayers, Nat. Mater. 20 (2021) 1325–1336. https://doi.org/10.1038/s41563-021-01029-9.

[129] C. Eames, J.M. Frost, P.R.F. Barnes, B.C. O'Regan, A. Walsh, M.S. Islam, Ionic transport in hybrid lead iodide perovskite solar cells, Nat. Commun. 6 (2015) 2–9. https://doi.org/10.1038/ncomms8497.

[130] R. Gottesman, L. Gouda, B.S. Kalanoor, E. Haltzi, S. Tirosh, E. Rosh-Hodesh, Y. Tischler, A. Zaban, C. Quarti, E. Mosconi, F. De Angelis, Photoinduced reversible structural transformations in free-standing CH3NH3PbI3 perovskite films, J. Phys. Chem. Lett. 6 (2015) 2332–2338. https://doi.org/10.1021/acs.jpclett.5b00994.

[131] Y.C. Zhao, W.K. Zhou, X. Zhou, K.H. Liu, D.P. Yu, Q. Zhao, Quantification of light-enhanced ionic transport in lead iodide perovskite thin films and its solar cell applications, Light Sci. Appl. 6 (2017) e16243--8. https://doi.org/10.1038/lsa.2016.243.

[132] G.Y. Kim, A. Senocrate, Y. Wang, D. Moia, J. Maier, Photo-Effect on Ion Transport in Mixed Cation and Halide Perovskites and Implications for Photo-Demixing**, Angew. Chemie Int. Ed. 60 (2021) 820–826. https://doi.org/10.1002/anie.202005853.

[133] J.M. Azpiroz, E. Mosconi, J. Bisquert, F. De Angelis, Defect migration in

methylammonium lead iodide and its role in perovskite solar cell operation, Energy Environ. Sci. 8 (2015) 2118–2127. https://doi.org/10.1039/c5ee01265a.

[134] C. Li, A. Guerrero, Y. Zhong, A. Gräser, C.A.M. Luna, J. Köhler, J. Bisquert, R. Hildner, S. Huettner, Real-Time Observation of Iodide Ion Migration in Methylammonium Lead Halide Perovskites, Small 13 (2017). https://doi.org/10.1002/smll.201701711.

[135] S. Chen, X. Wen, R. Sheng, S. Huang, X. Deng, M.A. Green, A. Ho-Baillie, Mobile Ion Induced Slow Carrier Dynamics in Organic–Inorganic Perovskite CH 3 NH 3 PbBr 3, ACS Appl. Mater. Interfaces 8 (2016) 5351–5357. https://doi.org/10.1021/acsami.5b12376.

[136] X. Deng, X. Wen, C.F.J. Lau, T. Young, J. Yun, M.A. Green, S. Huang, A.W.Y. Ho-Baillie, Electric field induced reversible and irreversible photoluminescence responses in methylammonium lead iodide perovskite, J. Mater. Chem. C 4 (2016) 9060–9068. https://doi.org/10.1039/C6TC03206K.

[137] C. Li, A. Guerrero, S. Huettner, J. Bisquert, Unravelling the role of vacancies in lead halide perovskite through electrical switching of photoluminescence, Nat. Commun. 9 (2018) 5113. https://doi.org/10.1038/s41467-018-07571-6.

[138] D.W. deQuilettes, W. Zhang, V.M. Burlakov, D.J. Graham, T. Leijtens, A. Osherov, V. Bulović, H.J. Snaith, D.S. Ginger, S.D. Stranks, Photo-

induced halide redistribution in organic–inorganic perovskite films, Nat. Commun. 7 (2016) 11683. https://doi.org/10.1038/ncomms11683.

[139] L. Zhao, J. Gao, Y.L. Lin, Y. Yeh, K.M. Lee, N. Yao, Y. Loo, B.P. Rand, Electrical Stress Influences the Efficiency of CH 3 NH 3 PbI 3 Perovskite Light Emitting Devices, Adv. Mater. 29 (2017). https://doi.org/10.1002/adma.201605317.

[140] S.G. Motti, D. Meggiolaro, A.J. Barker, E. Mosconi, C.A.R. Perini, J.M. Ball, M. Gandini, M. Kim, F. De Angelis, A. Petrozza, Controlling competing photochemical reactions stabilizes perovskite solar cells, Nat. Photonics 13 (2019) 532–539. https://doi.org/10.1038/s41566-019-0435-1.

[141] Z. Xu, T. De Rosia, K. Weeks, Photoluminescence–Voltage (PL– V) Hysteresis of Perovskite Solar Cells, J. Phys. Chem. C 121 (2017) 24389–24396. https://doi.org/10.1021/acs.jpcc.7b06711.

[142] B. Xu, W. Wang, X. Zhang, H. Liu, Y. Zhang, G. Mei, S. Chen, K. Wang, L. Wang, X.W. Sun, Electric Bias Induced Degradation in Organic-Inorganic Hybrid Perovskite Light-Emitting Diodes, Sci. Rep. 8 (2018) 15799. https://doi.org/10.1038/s41598-018-34034-1.

[143] V. Prakasam, D. Tordera, H.J. Bolink, G. Gelinck, Degradation Mechanisms in Organic Lead Halide Perovskite Light-Emitting Diodes, Adv. Opt. Mater. 7 (2019). https://doi.org/10.1002/adom.201900902.

[144] H. Zhang, H. Lin, C. Liang, H. Liu, J. Liang, Y. Zhao, W. Zhang, M. Sun, W.

Xiao, H. Li, S. Polizzi, D. Li, F. Zhang, Z. He, W.C.H. Choy, Organic–Inorganic Perovskite Light-Emitting Electrochemical Cells with a Large Capacitance, Adv. Funct. Mater. 25 (2015) 7226–7232. https://doi.org/10.1002/adfm.201502962.

[145] E. Bandiello, J. Ávila, L. Gil-Escrig, E. Tekelenburg, M. Sessolo, H.J. Bolink, Influence of mobile ions on the electroluminescence characteristics of methylammonium lead iodide perovskite diodes, J. Mater. Chem. A 4 (2016) 18614–18620. https://doi.org/10.1039/C6TA06854E.

[146] P. Andričević, X. Mettan, M. Kollár, B. Náfrádi, A. Sienkiewicz, T. Garma, L. Rossi, L. Forró, E. Horváth, Light-Emitting Electrochemical Cells of Single Crystal Hybrid Halide Perovskite with Vertically Aligned Carbon Nanotubes Contacts, ACS Photonics 6 (2019) 967–975. https://doi.org/10.1021/acsphotonics.8b01653.

[147] J. Li, X. Shan, S.G.R. Bade, T. Geske, Q. Jiang, X. Yang, Z. Yu, Single-Layer Halide Perovskite Light-Emitting Diodes with Sub-Band Gap Turn-On Voltage and High Brightness, J. Phys. Chem. Lett. 7 (2016) 4059–4066. https://doi.org/10.1021/acs.jpclett.6b01942.

[148] M. Chen, X. Shan, T. Geske, J. Li, Z. Yu, Manipulating Ion Migration for Highly Stable Light-Emitting Diodes with Single-Crystalline Organometal Halide Perovskite Microplatelets, ACS Nano 11 (2017) 6312–6318. https://doi.org/10.1021/acsnano.7b02629.

[149] H. Lee, D. Ko, C. Lee, Direct Evidence of Ion-Migration-Induced Degradation of Ultrabright Perovskite Light-Emitting Diodes, ACS Appl. Mater. Interfaces 11 (2019) 11667–11673. https://doi.org/10.1021/acsami.8b22217.

[150] E. Bi, H. Chen, F. Xie, Y. Wu, W. Chen, Y. Su, A. Islam, M. Grätzel, X. Yang, L. Han, Diffusion engineering of ions and charge carriers for stable efficient perovskite solar cells, Nat. Commun. 8 (2017) 15330. https://doi.org/10.1038/ncomms15330.

[151] H. Back, G. Kim, J. Kim, J. Kong, T.K. Kim, H. Kang, H. Kim, J. Lee, S. Lee, K. Lee, Achieving long-term stable perovskite solar cells via ion neutralization, Energy Environ. Sci. 9 (2016) 1258–1263. https://doi.org/10.1039/C6EE00612D.

[152] C. Besleaga, L.E. Abramiuc, V. Stancu, A.G. Tomulescu, M. Sima, L. Trinca, N. Plugaru, L. Pintilie, G.A. Nemnes, M. Iliescu, H.G. Svavarsson, A. Manolescu, I. Pintilie, Iodine Migration and Degradation of Perovskite Solar Cells Enhanced by Metallic Electrodes, J. Phys. Chem. Lett. 7 (2016) 5168–5175. https://doi.org/10.1021/acs.jpclett.6b02375.

[153] J. Li, Q. Dong, N. Li, L. Wang, Direct Evidence of Ion Diffusion for the Silver-Electrode-Induced Thermal Degradation of Inverted Perovskite Solar Cells, Adv. Energy Mater. 7 (2017). https://doi.org/10.1002/aenm.201602922.

[154] B. Rivkin, P. Fassl, Q. Sun, A.D. Taylor, Z. Chen, Y. Vaynzof, Effect of Ion Migration-Induced Electrode Degradation on the Operational Stability of Perovskite Solar Cells, ACS Omega 3 (2018) 10042–10047. https://doi.org/10.1021/acsomega.8b01626.

[155] P.F. Sowmeeh, E. Yazdani, Role of cation-mediated recombination on the hysteresis behavior of perovskite light-emitting diodes, J. Phys. Chem. Solids 185 (2024) 111777. https://doi.org/10.1016/j.jpcs.2023.111777.

[156] B. Chen, M. Yang, X. Zheng, C. Wu, W. Li, Y. Yan, J. Bisquert, G. Garcia-Belmonte, K. Zhu, S. Priya, Impact of Capacitive Effect and Ion Migration on the Hysteretic Behavior of Perovskite Solar Cells, J. Phys. Chem. Lett. 6 (2015) 4693–4700. https://doi.org/10.1021/acs.jpclett.5b02229.

[157] Z. Xiao, Y. Yuan, Y. Shao, Q. Wang, Q. Dong, C. Bi, P. Sharma, A. Gruverman, J. Huang, Giant switchable photovoltaic effect in organometal trihalide perovskite devices, Nat. Mater. 14 (2015) 193–198. https://doi.org/10.1038/nmat4150.

[158] X. Wen, A. Ho-Baillie, S. Huang, R. Sheng, S. Chen, H. Ko, M.A. Green, Mobile Charge-Induced Fluorescence Intermittency in Methylammonium Lead Bromide Perovskite, Nano Lett. 15 (2015) 4644–4649. https://doi.org/10.1021/acs.nanolett.5b01405.

[159] H. Zhang, X. Fu, Y. Tang, H. Wang, C. Zhang, W.W. Yu, X. Wang, Y.

Zhang, M. Xiao, Phase segregation due to ion migration in all-inorganic mixed-halide perovskite nanocrystals, Nat. Commun. 10 (2019) 1088. https://doi.org/10.1038/s41467-019-09047-7.

[160] P. Vashishtha, J.E. Halpert, Field-Driven Ion Migration and Color Instability in Red-Emitting Mixed Halide Perovskite Nanocrystal Light-Emitting Diodes, Chem. Mater. 29 (2017) 5965–5973. https://doi.org/10.1021/acs.chemmater.7b01609.

[161] Q. Wang, X. Wang, Z. Yang, N. Zhou, Y. Deng, J. Zhao, X. Xiao, P. Rudd, A. Moran, Y. Yan, J. Huang, Efficient sky-blue perovskite light-emitting diodes via photoluminescence enhancement, Nat. Commun. 10 (2019) 5633. https://doi.org/10.1038/s41467-019-13580-w.

[162] D. Ma, P. Todorović, S. Meshkat, M.I. Saidaminov, Y.-K. Wang, B. Chen, P. Li, B. Scheffel, R. Quintero-Bermudez, J.Z. Fan, Y. Dong, B. Sun, C. Xu, C. Zhou, Y. Hou, X. Li, Y. Kang, O. Voznyy, Z.-H. Lu, D. Ban, E.H. Sargent, Chloride Insertion–Immobilization Enables Bright, Narrowband, and Stable Blue-Emitting Perovskite Diodes, J. Am. Chem. Soc. 142 (2020) 5126–5134. https://doi.org/10.1021/jacs.9b12323.

[163] S. Lee, J.H. Park, B.R. Lee, E.D. Jung, J.C. Yu, D. Di Nuzzo, R.H. Friend, M.H. Song, Amine-Based Passivating Materials for Enhanced Optical Properties and Performance of Organic–Inorganic Perovskites in Light-Emitting Diodes, J. Phys. Chem. Lett. 8 (2017) 1784–1792.

https://doi.org/10.1021/acs.jpclett.7b00372.

[164] G. Szabó, N.-G. Park, F. De Angelis, P. V. Kamat, Are Perovskite Solar Cells Reaching the Efficiency and Voltage Limits?, ACS Energy Lett. 8 (2023) 3829–3831. https://doi.org/10.1021/acsenergylett.3c01649.

[165] S. Yu, Z. Xiong, H. Zhou, Q. Zhang, Z. Wang, F. Ma, Z. Qu, Y. Zhao, X. Chu, X. Zhang, J. You, Homogenized NiO x nanoparticles for improved hole transport in inverted perovskite solar cells, Science (80-.). 382 (2023) 1399–1404. https://doi.org/10.1126/science.adj8858.

[166] C. Liu, Y. Yang, H. Chen, J. Xu, A. Liu, A.S.R. Bati, H. Zhu, L. Grater, S.S. Hadke, C. Huang, V.K. Sangwan, T. Cai, D. Shin, L.X. Chen, M.C. Hersam, C.A. Mirkin, B. Chen, M.G. Kanatzidis, E.H. Sargent, Bimolecularly passivated interface enables efficient and stable inverted perovskite solar cells, Science (80-.). 382 (2023) 810–815. https://doi.org/10.1126/science.adk1633.

[167] Z. Li, X. Sun, X. Zheng, B. Li, D. Gao, S. Zhang, X. Wu, S. Li, J. Gong, J.M. Luther, Z. Li, Z. Zhu, Stabilized hole-selective layer for high-performance inverted p-i-n perovskite solar cells, Science (80-.). 382 (2023) 284–289. https://doi.org/10.1126/science.ade9637.

[168] S.M. Park, M. Wei, J. Xu, H.R. Atapattu, F.T. Eickemeyer, K. Darabi, L. Grater, Y. Yang, C. Liu, S. Teale, B. Chen, H. Chen, T. Wang, L. Zeng, A. Maxwell, Z. Wang, K.R. Rao, Z. Cai, S.M. Zakeeruddin, J.T. Pham, C.M. Risko, A. Amassian, M.G. Kanatzidis, K.R. Graham, M. Grätzel, E.H.

Sargent, Engineering ligand reactivity enables high-temperature operation of stable perovskite solar cells, Science (80-.). 381 (2023) 209–215. https://doi.org/10.1126/science.adi4107.

[169] Z. Liang, Y. Zhang, H. Xu, W. Chen, B. Liu, J. Zhang, H. Zhang, Z. Wang, D.-H. Kang, J. Zeng, X. Gao, Q. Wang, H. Hu, H. Zhou, X. Cai, X. Tian, P. Reiss, B. Xu, T. Kirchartz, Z. Xiao, S. Dai, N.-G. Park, J. Ye, X. Pan, Homogenizing out-of-plane cation composition in perovskite solar cells, Nature 624 (2023) 557–563. https://doi.org/10.1038/s41586-023-06784-0.

[170] S.M. Park, M. Wei, N. Lempesis, W. Yu, T. Hossain, L. Agosta, V. Carnevali, H.R. Atapattu, P. Serles, F.T. Eickemeyer, H. Shin, M. Vafaie, D. Choi, K. Darabi, E.D. Jung, Y. Yang, D. Bin Kim, S.M. Zakeeruddin, B. Chen, A. Amassian, T. Filleter, M.G. Kanatzidis, K.R. Graham, L. Xiao, U. Rothlisberger, M. Grätzel, E.H. Sargent, Low-loss contacts on textured substrates for inverted perovskite solar cells, Nature 624 (2023) 289–294. https://doi.org/10.1038/s41586-023-06745-7.

[171] H.-B. Kim, Y.J. Yoon, J. Jeong, J. Heo, H. Jang, J.H. Seo, B. Walker, J.Y. Kim, Peroptronic devices: perovskite-based light-emitting solar cells, Energy Environ. Sci. 10 (2017) 1950–1957. https://doi.org/10.1039/C7EE01666B.

[172] Y. Lin, Y. Fang, J. Zhao, Y. Shao, S.J. Stuard, M.M. Nahid, H. Ade, Q. Wang, J.E. Shield, N. Zhou, A.M. Moran, J. Huang, Unveiling the

operation mechanism of layered perovskite solar cells, Nat. Commun. 10 (2019) 1008. https://doi.org/10.1038/s41467-019-08958-9.

[173] S. Ravishankar, S. Gharibzadeh, C. Roldán-Carmona, G. Grancini, Y. Lee, M. Ralaiarisoa, A.M. Asiri, N. Koch, J. Bisquert, M.K. Nazeeruddin, Influence of Charge Transport Layers on Open-Circuit Voltage and Hysteresis in Perovskite Solar Cells, Joule 2 (2018) 788–798. https://doi.org/10.1016/j.joule.2018.02.013.

[174] Y. Han, H. Xie, E.L. Lim, D. Bi, Review of Two-Step Method for Lead Halide Perovskite Solar Cells, Sol. RRL 6 (2022). https://doi.org/10.1002/solr.202101007.

[175] Z. Liu, J. Chang, Z. Lin, L. Zhou, Z. Yang, D. Chen, C. Zhang, S. (Frank) Liu, Y. Hao, High-Performance Planar Perovskite Solar Cells Using Low Temperature, Solution–Combustion-Based Nickel Oxide Hole Transporting Layer with Efficiency Exceeding 20%, Adv. Energy Mater. 8 (2018). https://doi.org/10.1002/aenm.201703432.

[176] K. Liang, D.B. Mitzi, M.T. Prikas, Synthesis and Characterization of Organic–Inorganic Perovskite Thin Films Prepared Using a Versatile Two-Step Dipping Technique, Chem. Mater. 10 (1998) 403–411. https://doi.org/10.1021/cm970568f.

[177] F. Huang, M. Li, P. Siffalovic, G. Cao, J. Tian, From scalable solution fabrication of perovskite films towards commercialization of solar cells, Energy Environ. Sci. 12 (2019) 518–549.

https://doi.org/10.1039/C8EE03025A.

[178] Y. Chen, S. Tan, N. Li, B. Huang, X. Niu, L. Li, M. Sun, Y. Zhang, X. Zhang, C. Zhu, N. Yang, H. Zai, Y. Wu, S. Ma, Y. Bai, Q. Chen, F. Xiao, K. Sun, H. Zhou, Self-Elimination of Intrinsic Defects Improves the Low-Temperature Performance of Perovskite Photovoltaics, Joule 4 (2020) 1961–1976. https://doi.org/10.1016/j.joule.2020.07.006.

[179] H. Ling, J. Wu, F. Su, Y. Tian, Y.J. Liu, Automatic light-adjusting electrochromic device powered by perovskite solar cell, Nat. Commun. 12 (2021) 1010. https://doi.org/10.1038/s41467-021-21086-7.

[180] Q. Dong, C. Zhu, M. Chen, C. Jiang, J. Guo, Y. Feng, Z. Dai, S.K. Yadavalli, M. Hu, X. Cao, Y. Li, Y. Huang, Z. Liu, Y. Shi, L. Wang, N.P. Padture, Y. Zhou, Interpenetrating interfaces for efficient perovskite solar cells with high operational stability and mechanical robustness, Nat. Commun. 12 (2021) 973. https://doi.org/10.1038/s41467-021-21292-3.

[181] W. Yu, X. Sun, M. Xiao, T. Hou, X. Liu, B. Zheng, H. Yu, M. Zhang, Y. Huang, X. Hao, Recent advances on interface engineering of perovskite solar cells, Nano Res. 15 (2022) 85–103. https://doi.org/10.1007/s12274-021-3488-7.

[182] A.H. Proppe, A. Johnston, S. Teale, A. Mahata, R. Quintero-Bermudez, E.H. Jung, L. Grater, T. Cui, T. Filleter, C.-Y. Kim, S.O. Kelley, F. De

Angelis, E.H. Sargent, Multication perovskite 2D/3D interfaces form via progressive dimensional reduction, Nat. Commun. 12 (2021) 3472. https://doi.org/10.1038/s41467-021-23616-9.

[183] G. Liu, N. Zhou, S. Tan, J. Zhang, Q. Chen, H. Zhou, Interface charge accumulation dynamics in 3D and quasi-2D perovskite solar cells, J. Phys. D. Appl. Phys. 54 (2021) 014004. https://doi.org/10.1088/1361-6463/abb049.

[184] J. Shi, Y. Li, Y. Li, D. Li, Y. Luo, H. Wu, Q. Meng, From Ultrafast to Ultraslow: Charge-Carrier Dynamics of Perovskite Solar Cells, Joule 2 (2018) 879–901. https://doi.org/10.1016/j.joule.2018.04.010.

[185] S. Zhang, F. Ye, X. Wang, R. Chen, H. Zhang, L. Zhan, X. Jiang, Y. Li, X. Ji, S. Liu, M. Yu, F. Yu, Y. Zhang, R. Wu, Z. Liu, Z. Ning, D. Neher, L. Han, Y. Lin, H. Tian, W. Chen, M. Stolterfoht, L. Zhang, W.-H. Zhu, Y. Wu, Minimizing buried interfacial defects for efficient inverted perovskite solar cells, Science (80-.). 380 (2023) 404–409. https://doi.org/10.1126/science.adg3755.

[186] H. Bi, B. Liu, D. He, L. Bai, W. Wang, Z. Zang, J. Chen, Interfacial defect passivation and stress release by multifunctional KPF6 modification for planar perovskite solar cells with enhanced efficiency and stability, Chem. Eng. J. 418 (2021) 129375. https://doi.org/10.1016/j.cej.2021.129375.

[187] Z. Yang, B.H. Babu, S. Wu, T. Liu, S. Fang, Z. Xiong, L. Han, W. Chen,

Review on Practical Interface Engineering of Perovskite Solar Cells: From Efficiency to Stability, Sol. RRL 4 (2020). https://doi.org/10.1002/solr.201900257.

[188] C. Luo, G. Zheng, F. Gao, X. Wang, C. Zhan, X. Gao, Q. Zhao, Engineering the buried interface in perovskite solar cells via lattice-matched electron transport layer, Nat. Photonics 17 (2023) 856–864. https://doi.org/10.1038/s41566-023-01247-4.

[189] J. Chen, H. Dong, J. Li, X. Zhu, J. Xu, F. Pan, R. Xu, J. Xi, B. Jiao, X. Hou, K. Wei NG, S.-P. Wang, Z. Wu, Solar Cell Efficiency Exceeding 25% through Rb-Based Perovskitoid Scaffold Stabilizing the Buried Perovskite Surface, ACS Energy Lett. 7 (2022) 3685–3694. https://doi.org/10.1021/acsenergylett.2c01661.

[190] Y. Wang, M. Han, R. Wang, J. Zhao, J. Zhang, H. Ren, G. Hou, Y. Ding, Y. Zhao, X. Zhang, Buried interface passivation strategies for high-performance perovskite solar cells, J. Mater. Chem. A 11 (2023) 8573–8598. https://doi.org/10.1039/D3TA00750B.

[191] X. Yang, D. Luo, Y. Xiang, L. Zhao, M. Anaya, Y. Shen, J. Wu, W. Yang, Y. Chiang, Y. Tu, R. Su, Q. Hu, H. Yu, G. Shao, W. Huang, T.P. Russell, Q. Gong, S.D. Stranks, W. Zhang, R. Zhu, Buried Interfaces in Halide Perovskite Photovoltaics, Adv. Mater. 33 (2021). https://doi.org/10.1002/adma.202006435.

[192] N.-G. Park, K. Zhu, Scalable fabrication and coating methods for

perovskite solar cells and solar modules, Nat. Rev. Mater. 5 (2020) 333–350. https://doi.org/10.1038/s41578-019-0176-2.

[193] A.C. Mendhe, Spin Coating: Easy Technique for Thin Films, in: Simple Chem. Methods Thin Film Depos., Springer Nature Singapore, Singapore, 2023: pp. 387–424. https://doi.org/10.1007/978-981-99-0961-2_9.

[194] K.R. Gbashi, A.K. Hussein, Cu-doped ZnS coatings for optoelectronics with enhanced protection for UV radiations, J. Mater. Sci. Mater. Electron. 31 (2020) 17258–17268. https://doi.org/10.1007/s10854-020-04280-z.

[195] J. Ávila, C. Momblona, P.P. Boix, M. Sessolo, H.J. Bolink, Vapor-Deposited Perovskites: The Route to High-Performance Solar Cell Production?, Joule 1 (2017) 431–442. https://doi.org/10.1016/j.joule.2017.07.014.

[196] C. Liu, Y.B. Cheng, Z. Ge, Understanding of perovskite crystal growth and film formation in scalable deposition processes, Chem. Soc. Rev. 49 (2020) 1653–1687. https://doi.org/10.1039/c9cs00711c.

[197] J. Li, P. Du, Q. Guo, L. Sun, Z. Shen, J. Zhu, C. Dong, L. Wang, X. Zhang, L. Li, C. Yang, J. Pan, Z. Liu, B. Xia, Z. Xiao, J. Du, B. Song, J. Luo, J. Tang, Efficient all-thermally evaporated perovskite light-emitting diodes for active-matrix displays, Nat. Photonics 17 (2023) 435–441. https://doi.org/10.1038/s41566-023-01177-1.

[198] Y. Vaynzof, The Future of Perovskite Photovoltaics—Thermal Evaporation or Solution Processing?, Adv. Energy Mater. 10 (2020). https://doi.org/10.1002/aenm.202003073.

[199] Z. Liu, D. Liu, H. Chen, L. Ji, H. Zheng, Y. Gu, F. Wang, Z. Chen, S. Li, Enhanced Crystallinity of Triple-Cation Perovskite Film via Doping NH4SCN, Nanoscale Res. Lett. 14 (2019) 304. https://doi.org/10.1186/s11671-019-3134-4.

[200] S. Sidhik, Y. Wang, M. De Siena, R. Asadpour, A.J. Torma, T. Terlier, K. Ho, W. Li, A.B. Puthirath, X. Shuai, A. Agrawal, B. Traore, M. Jones, R. Giridharagopal, P.M. Ajayan, J. Strzalka, D.S. Ginger, C. Katan, M.A. Alam, J. Even, M.G. Kanatzidis, A.D. Mohite, Deterministic fabrication of 3D/2D perovskite bilayer stacks for durable and efficient solar cells, Science (80-.). 377 (2022) 1425–1430. https://doi.org/10.1126/science.abq7652.

[201] C. Xiang, L. Wu, Z. Lu, M. Li, Y. Wen, Y. Yang, W. Liu, T. Zhang, W. Cao, S.-W. Tsang, B. Shan, X. Yan, L. Qian, High efficiency and stability of ink-jet printed quantum dot light emitting diodes, Nat. Commun. 11 (2020) 1646. https://doi.org/10.1038/s41467-020-15481-9.

[202] S.J. Clark, M.D. Segall, C.J. Pickard, P.J. Hasnip, M.I.J. Probert, K. Refson, M.C. Payne, First principles methods using CASTEP, Zeitschrift Für Krist. - Cryst. Mater. 220 (2005) 567–570. https://doi.org/10.1524/zkri.220.5.567.65075.

[203] J.P. Perdew, K. Burke, M. Ernzerhof, Generalized Gradient Approximation Made Simple, Phys. Rev. Lett. 78 (1997) 1396–1396. https://doi.org/10.1103/PhysRevLett.78.1396.

[204] K. Momma, F. Izumi, VESTA 3 for three-dimensional visualization of crystal, volumetric and morphology data, J. Appl. Crystallogr. 44 (2011) 1272–1276. https://doi.org/10.1107/S0021889811038970.

[205] A.D. Rakić, Algorithm for the determination of intrinsic optical constants of metal films: application to aluminum, Appl. Opt. 34 (1995) 4755. https://doi.org/10.1364/AO.34.004755.

[206] C. Cho, B. Zhao, G.D. Tainter, J.-Y. Lee, R.H. Friend, D. Di, F. Deschler, N.C. Greenham, The role of photon recycling in perovskite light-emitting diodes, Nat. Commun. 11 (2020) 611. https://doi.org/10.1038/s41467-020-14401-1.

[207] C. Cho, N.C. Greenham, Computational Study of Dipole Radiation in Re-Absorbing Perovskite Semiconductors for Optoelectronics, Adv. Sci. 8 (2021) 2003559. https://doi.org/10.1002/advs.202003559.

[208] L. Lei, D. Seyitliyev, S. Stuard, J. Mendes, Q. Dong, X. Fu, Y.A. Chen, S. He, X. Yi, L. Zhu, C.H. Chang, H. Ade, K. Gundogdu, F. So, Efficient Energy Funneling in Quasi-2D Perovskites: From Light Emission to Lasing, Adv. Mater. 32 (2020) e1906571. https://doi.org/10.1002/adma.201906571.

[209] Y. Jiang, M. Cui, S. Li, C. Sun, Y. Huang, J. Wei, L. Zhang, M. Lv, C. Qin, Y.

Liu, M. Yuan, Reducing the impact of Auger recombination in quasi-2D perovskite light-emitting diodes, Nat. Commun. 12 (2021) 336. https://doi.org/10.1038/s41467-020-20555-9.

[210] L. Krückemeier, B. Krogmeier, Z. Liu, U. Rau, T. Kirchartz, Understanding Transient Photoluminescence in Halide Perovskite Layer Stacks and Solar Cells, Adv. Energy Mater. 11 (2021) 2003489. https://doi.org/10.1002/aenm.202003489.

[211] M.U. Rothmann, J.S. Kim, J. Borchert, K.B. Lohmann, C.M. O'Leary, A.A. Sheader, L. Clark, H.J. Snaith, M.B. Johnston, P.D. Nellist, L.M. Herz, Atomic-scale microstructure of metal halide perovskite, Science (80-.). 370 (2020). https://doi.org/10.1126/science.abb5940.

[212] S.-J. Woo, J.S. Kim, T.-W. Lee, Characterization of stability and challenges to improve lifetime in perovskite LEDs, Nat. Photonics 15 (2021) 630–634. https://doi.org/10.1038/s41566-021-00863-2.

[213] L. Zhao, K. Roh, S. Kacmoli, K. Al Kurdi, S. Jhulki, S. Barlow, S.R. Marder, C. Gmachl, B.P. Rand, Thermal Management Enables Bright and Stable Perovskite Light-Emitting Diodes, Adv. Mater. 32 (2020) 2000752. https://doi.org/10.1002/adma.202000752.

[214] L. Kong, X. Zhang, Y. Li, H. Wang, Y. Jiang, S. Wang, M. You, C. Zhang, T. Zhang, S. V. Kershaw, W. Zheng, Y. Yang, Q. Lin, M. Yuan, A.L. Rogach, X. Yang, Smoothing the energy transfer pathway in quasi-2D perovskite films using methanesulfonate leads to highly efficient

light-emitting devices, Nat. Commun. 12 (2021) 1246. https://doi.org/10.1038/s41467-021-21522-8.

[215] S. Liu, S. Ho, Y. Chen, F. So, Passivation of Metal Oxide Surfaces for High-Performance Organic and Hybrid Optoelectronic Devices, Chem. Mater. 27 (2015) 2532–2539. https://doi.org/10.1021/acs.chemmater.5b00129.

[216] C. Liang, H. Gu, Y. Xia, Z. Wang, X. Liu, J. Xia, S. Zuo, Y. Hu, X. Gao, W. Hui, L. Chao, T. Niu, M. Fang, H. Lu, H. Dong, H. Yu, S. Chen, X. Ran, L. Song, B. Li, J. Zhang, Y. Peng, G. Shao, J. Wang, Y. Chen, G. Xing, W. Huang, Two-dimensional Ruddlesden–Popper layered perovskite solar cells based on phase-pure thin films, Nat. Energy 6 (2021) 38–45. https://doi.org/10.1038/s41560-020-00721-5.

[217] Y. Guo, Y. Jia, N. Li, M. Chen, S. Hu, C. Liu, N. Zhao, Degradation Mechanism of Perovskite Light-Emitting Diodes: An In Situ Investigation via Electroabsorption Spectroscopy and Device Modelling, Adv. Funct. Mater. 30 (2020) 1910464. https://doi.org/10.1002/adfm.201910464.

[218] Y.H. Kim, S. Kim, A. Kakekhani, J. Park, J. Park, Y.H. Lee, H. Xu, S. Nagane, R.B. Wexler, D.H. Kim, S.H. Jo, L. Martínez-Sarti, P. Tan, A. Sadhanala, G.S. Park, Y.W. Kim, B. Hu, H.J. Bolink, S. Yoo, R.H. Friend, A.M. Rappe, T.W. Lee, Comprehensive defect suppression in perovskite nanocrystals for high-efficiency light-emitting diodes, Nat.

Photonics 15 (2021) 148–155. https://doi.org/10.1038/s41566-020-00732-4.

[219] B. Zhang, S. Ding, X. Zhang, L. Qian, C. Xiang, Enhancing the performance of Quasi-2D perovskite blue light emitting diodes via a WS2 energy matching layer, Chem. Phys. Lett. 826 (2023) 140671. https://doi.org/10.1016/j.cplett.2023.140671.

[220] H. Li, J. Song, W. Pan, D. Xu, W. Zhu, H. Wei, B. Yang, Sensitive and Stable 2D Perovskite Single-Crystal X-ray Detectors Enabled by a Supramolecular Anchor, Adv. Mater. 32 (2020). https://doi.org/10.1002/adma.202003790.

[221] T. Matsushima, S. Hwang, A.S.D. Sandanayaka, C. Qin, S. Terakawa, T. Fujihara, M. Yahiro, C. Adachi, Solution-Processed Organic–Inorganic Perovskite Field-Effect Transistors with High Hole Mobilities, Adv. Mater. 28 (2016) 10275–10281. https://doi.org/10.1002/adma.201603126.

[222] L. Lei, D. Seyitliyev, S. Stuard, J. Mendes, Q. Dong, X. Fu, Y. Chen, S. He, X. Yi, L. Zhu, C. Chang, H. Ade, K. Gundogdu, F. So, Efficient Energy Funneling in Quasi-2D Perovskites: From Light Emission to Lasing, Adv. Mater. 32 (2020) 1906571. https://doi.org/10.1002/adma.201906571.

[223] J.C. Hamill, J. Schwartz, Y.-L. Loo, Influence of Solvent Coordination on Hybrid Organic–Inorganic Perovskite Formation, ACS Energy Lett. 3

(2018) 92–97. https://doi.org/10.1021/acsenergylett.7b01057.

[224] G. Jang, H. Kwon, S. Ma, S. Yun, H. Yang, J. Moon, Cold Antisolvent Bathing Derived Highly Efficient Large-Area Perovskite Solar Cells, Adv. Energy Mater. 9 (2019). https://doi.org/10.1002/aenm.201901719.

[225] D.S. Sholl, J.A. Steckel, Density Functional Theory, John Wiley & Sons, Inc., Hoboken, NJ, USA, 2009. https://doi.org/10.1002/9780470447710.

[226] J. Li, J. Wang, J. Ma, H. Shen, L. Li, X. Duan, D. Li, Self-trapped state enabled filterless narrowband photodetections in 2D layered perovskite single crystals, Nat. Commun. 10 (2019) 806. https://doi.org/10.1038/s41467-019-08768-z.

[227] E. Kashani-Amin, H. Faraji, S. Nouriyengejeh, A. Ebrahim-Habibi, Structure-Sweetness Relationship of Sweet Proteins: A Systematic Review on “Sweet Protein” Studies as a Sub-Group of “Sweetener” Investigations, Moscow Univ. Biol. Sci. Bull. 76 (2021) 175–190. https://doi.org/10.3103/S0096392521440012.

[228] S. Ding, Z. Kong, Y. Shen, P. Shen, C. Wu, L. Qian, X. Zhang, L. Hu, H. Chen, C. Xiang, Phase stabilization via A-site ion anchoring for ultra-stable perovskite light emitting diodes, Mater. Horizons (2024). https://doi.org/10.1039/D4MH00701H.

[229] S. Chen, C. Wu, B. Han, Z. Liu, Z. Mi, W. Hao, J. Zhao, X. Wang, Q. Zhang,

K. Liu, J. Qi, J. Cao, J. Feng, D. Yu, J. Li, P. Gao, Atomic-scale imaging of CH3NH3PbI3 structure and its decomposition pathway, Nat. Commun. 12 (2021) 5516. https://doi.org/10.1038/s41467-021-25832-9.

[230] D. Seebach, Organic Synthesis—Where now?, Angew. Chemie Int. Ed. English 29 (1990) 1320–1367. https://doi.org/10.1002/anie.199013201.

[231] X. Li, W. Zhang, X. Guo, C. Lu, J. Wei, J. Fang, Constructing heterojunctions by surface sulfidation for efficient inverted perovskite solar cells, Science (80-.). 375 (2022) 434–437. https://doi.org/10.1126/science.abl5676.

[232] L. Kong, X. Zhang, Y. Li, H. Wang, Y. Jiang, S. Wang, M. You, C. Zhang, T. Zhang, S. V. Kershaw, W. Zheng, Y. Yang, Q. Lin, M. Yuan, A.L. Rogach, X. Yang, Smoothing the energy transfer pathway in quasi-2D perovskite films using methanesulfonate leads to highly efficient light-emitting devices, Nat. Commun. 12 (2021) 1246. https://doi.org/10.1038/s41467-021-21522-8.

[233] L. Yang, B. Fu, X. Li, H. Chen, L. Li, Poly(vinylidene fluoride)-passivated CsPbBr 3 perovskite quantum dots with near-unity photoluminescence quantum yield and superior stability, J. Mater. Chem. C 9 (2021) 1983–1991. https://doi.org/10.1039/D0TC05103A.

[234] J. Zhang, C. Yin, F. Yang, Y. Yao, F. Yuan, H. Chen, R. Wang, S. Bai, G. Tu, L. Hou, Highly Luminescent and Stable CsPbI3Perovskite Nanocrystals with Sodium Dodecyl Sulfate Ligand Passivation for Red-Light-

Emitting Diodes, J. Phys. Chem. Lett. 12 (2021) 2437–2443. https://doi.org/10.1021/acs.jpclett.1c00008.

[235] F. Wang, X. Jiang, H. Chen, Y. Shang, H. Liu, J. Wei, W. Zhou, H. He, W. Liu, Z. Ning, 2D-Quasi-2D-3D Hierarchy Structure for Tin Perovskite Solar Cells with Enhanced Efficiency and Stability, Joule 2 (2018) 2732–2743. https://doi.org/10.1016/j.joule.2018.09.012.

[236] F. Li, J. Zhang, S. Jo, M. Qin, Z. Li, T. Liu, X. Lu, Z. Zhu, A.K. -Y. Jen, Vertical Orientated Dion–Jacobson Quasi-2D Perovskite Film with Improved Photovoltaic Performance and Stability, Small Methods 4 (2020). https://doi.org/10.1002/smtd.201900831.

[237] S. Yang, W. Liu, L. Zuo, X. Zhang, T. Ye, J. Chen, C.-Z. Li, G. Wu, H. Chen, Thiocyanate assisted performance enhancement of formamidinium based planar perovskite solar cells through a single one-step solution process, J. Mater. Chem. A 4 (2016) 9430–9436. https://doi.org/10.1039/C6TA02999J.

[238] Yukta, R.D. Chavan, D. Prochowicz, P. Yadav, M.M. Tavakoli, S. Satapathi, Thiocyanate-Passivated Diaminonaphthalene-Incorporated Dion–Jacobson Perovskite for Highly Efficient and Stable Solar Cells, ACS Appl. Mater. Interfaces 14 (2022) 850–860. https://doi.org/10.1021/acsami.1c19546.

[239] J.L. Miró-Zárate, M.C. Elías-Espinosa, F. Cervantes-Sodi, C.J. Diliegros-Godines, Effects of NH4SCN Additive in the FAPbI3 Perovskite Films in

a Sequential Deposition Method, Crystals 13 (2023) 795. https://doi.org/10.3390/cryst13050795.

[240] Y. Dong, W. Shen, W. Dong, C. Bai, J. Zhao, Y. Zhou, F. Huang, Y. Cheng, J. Zhong, Chlorobenzenesulfonic Potassium Salts as the Efficient Multifunctional Passivator for the Buried Interface in Regular Perovskite Solar Cells, Adv. Energy Mater. 12 (2022). https://doi.org/10.1002/aenm.202200417.

[241] G. Yang, H. Lei, H. Tao, X. Zheng, J. Ma, Q. Liu, W. Ke, Z. Chen, L. Xiong, P. Qin, Z. Chen, M. Qin, X. Lu, Y. Yan, G. Fang, Reducing Hysteresis and Enhancing Performance of Perovskite Solar Cells Using Low-Temperature Processed Y-Doped SnO 2 Nanosheets as Electron Selective Layers, Small 13 (2017) 1601769. https://doi.org/10.1002/smll.201601769.

[242] B. Tu, Y. Shao, W. Chen, Y. Wu, X. Li, Y. He, J. Li, F. Liu, Z. Zhang, Y. Lin, X. Lan, L. Xu, X. Shi, A.M.C. Ng, H. Li, L.W. Chung, A.B. Djurišić, Z. He, Novel Molecular Doping Mechanism for n-Doping of SnO 2 via Triphenylphosphine Oxide and Its Effect on Perovskite Solar Cells, Adv. Mater. 31 (2019). https://doi.org/10.1002/adma.201805944.

[243] L. Liu, S. Chen, Y. Qu, X. Gao, L. Han, Z. Lin, L. Yang, W. Wang, N. Zheng, Y. Liang, Y. Tan, H. Xia, F. He, Nanographene–Osmapentalyne Complexes as a Cathode Interlayer in Organic Solar Cells Enhance Efficiency over 18%, Adv. Mater. 33 (2021).

https://doi.org/10.1002/adma.202101279.

[244] S. Shao, M.A. Loi, The Role of the Interfaces in Perovskite Solar Cells, Adv. Mater. Interfaces 7 (2020). https://doi.org/10.1002/admi.201901469.

[245] T.Y. Hou, J.S. Lowengrub, M.J. Shelley, Removing the stiffness from interfacial flows with surface tension, J. Comput. Phys. 114 (1994) 312–338. https://doi.org/10.1006/jcph.1994.1170.

[246] P. Kung, M. Li, P. Lin, Y. Chiang, C. Chan, T. Guo, P. Chen, A Review of Inorganic Hole Transport Materials for Perovskite Solar Cells, Adv. Mater. Interfaces 5 (2018). https://doi.org/10.1002/admi.201800882.

[247] G. Yang, C. Wang, H. Lei, X. Zheng, P. Qin, L. Xiong, X. Zhao, Y. Yan, G. Fang, Interface engineering in planar perovskite solar cells: energy level alignment, perovskite morphology control and high performance achievement, J. Mater. Chem. A 5 (2017) 1658–1666. https://doi.org/10.1039/C6TA08783C.

[248] M. Hu, C. Bi, Y. Yuan, Y. Bai, J. Huang, Stabilized Wide Bandgap MAPbBr x I 3– x Perovskite by Enhanced Grain Size and Improved Crystallinity, Adv. Sci. 3 (2016). https://doi.org/10.1002/advs.201500301.

[249] Q. Jiang, Z. Chu, P. Wang, X. Yang, H. Liu, Y. Wang, Z. Yin, J. Wu, X. Zhang, J. You, Planar-Structure Perovskite Solar Cells with Efficiency beyond 21%, Adv. Mater. 29 (2017).

https://doi.org/10.1002/adma.201703852.

[250] A. Merdasa, A. Kiligaridis, C. Rehermann, M. Abdi-Jalebi, J. Stöber, B. Louis, M. Gerhard, S.D. Stranks, E.L. Unger, I.G. Scheblykin, Impact of Excess Lead Iodide on the Recombination Kinetics in Metal Halide Perovskites, ACS Energy Lett. 4 (2019) 1370–1378. https://doi.org/10.1021/acsenergylett.9b00774.

[251] X. Jiang, F. Wang, Q. Wei, H. Li, Y. Shang, W. Zhou, C. Wang, P. Cheng, Q. Chen, L. Chen, Z. Ning, Ultra-high open-circuit voltage of tin perovskite solar cells via an electron transporting layer design, Nat. Commun. 11 (2020) 1–7. https://doi.org/10.1038/s41467-020-15078-2.

[252] P. Zhu, S. Gu, X. Luo, Y. Gao, S. Li, J. Zhu, H. Tan, Simultaneous Contact and Grain-Boundary Passivation in Planar Perovskite Solar Cells Using SnO 2 -KCl Composite Electron Transport Layer, Adv. Energy Mater. 10 (2020). https://doi.org/10.1002/aenm.201903083.

[253] S.W. Lee, M. Jeong, D.R. Whang, J.H. Kim, D.W. Chang, Effect of Fluorine Atom on Photovoltaic Properties of Triphenylamine-Substituted Quinoxaline-Based D-A Type Polymers, Macromol. Res. 28 (2020) 1297–1303. https://doi.org/10.1007/s13233-020-8167-0.

[254] S. Han, H. Zhang, Y. Li, R. Wang, Q. He, Solution-processed amino acid modified SnO2 electron transport layer for carbon-based CsPbIBr2 perovskite solar cells, Mater. Sci. Semicond. Process. 133 (2021) 105964. https://doi.org/10.1016/j.mssp.2021.105964.

[255] E.H. Jung, B. Chen, K. Bertens, M. Vafaie, S. Teale, A. Proppe, Y. Hou, T. Zhu, C. Zheng, E.H. Sargent, Bifunctional Surface Engineering on SnO 2 Reduces Energy Loss in Perovskite Solar Cells, ACS Energy Lett. 5 (2020) 2796–2801. https://doi.org/10.1021/acsenergylett.0c01566.

[256] T. Bu, J. Li, F. Zheng, W. Chen, X. Wen, Z. Ku, Y. Peng, J. Zhong, Y.-B. Cheng, F. Huang, Universal passivation strategy to slot-die printed SnO2 for hysteresis-free efficient flexible perovskite solar module, Nat. Commun. 9 (2018) 4609. https://doi.org/10.1038/s41467-018-07099-9.

[257] K. Deng, Q. Chen, L. Li, Modification Engineering in SnO 2 Electron Transport Layer toward Perovskite Solar Cells: Efficiency and Stability, Adv. Funct. Mater. 30 (2020). https://doi.org/10.1002/adfm.202004209.

[258] S. Ahmadnia-Feyzabad, A.A. Khodadadi, M. Vesali-Naseh, Y. Mortazavi, Highly sensitive and selective sensors to volatile organic compounds using MWCNTs/SnO2, Sensors Actuators B Chem. 166–167 (2012) 150–155. https://doi.org/10.1016/j.snb.2012.02.024.

[259] Z. Li, W. Zeng, Q. Li, SnO2 as a gas sensor in detection of volatile organic compounds: A review, Sensors Actuators A Phys. 346 (2022) 113845. https://doi.org/10.1016/j.sna.2022.113845.

[260] M.H. Jung, Hydrophobic perovskites based on an alkylamine compound for high efficiency solar cells with improved

environmental stability, J. Mater. Chem. A 7 (2019) 14689–14704. https://doi.org/10.1039/c9ta01569h.

[261] Z. Qin, M. Pols, M. Qin, J. Zhang, H. Yan, S. Tao, X. Lu, Over-18%-Efficiency Quasi-2D Ruddlesden–Popper Pb–Sn Mixed Perovskite Solar Cells by Compositional Engineering, ACS Energy Lett. 8 (2023) 3188–3195. https://doi.org/10.1021/acsenergylett.3c00853.

[262] Q. Jiang, J. Tong, Y. Xian, R.A. Kerner, S.P. Dunfield, C. Xiao, R.A. Scheidt, D. Kuciauskas, X. Wang, M.P. Hautzinger, R. Tirawat, M.C. Beard, D.P. Fenning, J.J. Berry, B.W. Larson, Y. Yan, K. Zhu, Surface reaction for efficient and stable inverted perovskite solar cells, Nature 611 (2022) 278–283. https://doi.org/10.1038/s41586-022-05268-x.

[263] G. Wu, T. Yang, X. Li, N. Ahmad, X. Zhang, S. Yue, J. Zhou, Y. Li, H. Wang, X. Shi, S. (Frank) Liu, K. Zhao, H. Zhou, Y. Zhang, Molecular Engineering for Two-Dimensional Perovskites with Photovoltaic Efficiency Exceeding 18%, Matter 4 (2021) 582–599. https://doi.org/10.1016/j.matt.2020.11.011.

[264] X. Zhao, T. Liu, A.B. Kaplan, C. Yao, Y.-L. Loo, Accessing Highly Oriented Two-Dimensional Perovskite Films via Solvent-Vapor Annealing for Efficient and Stable Solar Cells, Nano Lett. 20 (2020) 8880–8889. https://doi.org/10.1021/acs.nanolett.0c03914.

[265] J. Zhou, L. Tan, Y. Liu, H. Li, X. Liu, M. Li, S. Wang, Y. Zhang, C. Jiang, R. Hua, W. Tress, S. Meloni, C. Yi, Highly efficient and stable perovskite

solar cells via a multifunctional hole transporting material, Joule (2024). https://doi.org/10.1016/j.joule.2024.02.019.

[266] T. Niu, Q. Xue, H.-L. Yip, Advances in Dion-Jacobson phase two-dimensional metal halide perovskite solar cells, Nanophotonics 10 (2021) 2069–2102. https://doi.org/10.1515/nanoph-2021-0052.

[267] M. Hao, Y. Bai, S. Zeiske, L. Ren, J. Liu, Y. Yuan, N. Zarrabi, N. Cheng, M. Ghasemi, P. Chen, M. Lyu, D. He, J.-H. Yun, Y. Du, Y. Wang, S. Ding, A. Armin, P. Meredith, G. Liu, H.-M. Cheng, L. Wang, Ligand-assisted cation-exchange engineering for high-efficiency colloidal Cs1−xFAxPbI3 quantum dot solar cells with reduced phase segregation, Nat. Energy 5 (2020) 79–88. https://doi.org/10.1038/s41560-019-0535-7.

[268] Q. Zhao, A. Hazarika, X. Chen, S.P. Harvey, B.W. Larson, G.R. Teeter, J. Liu, T. Song, C. Xiao, L. Shaw, M. Zhang, G. Li, M.C. Beard, J.M. Luther, High efficiency perovskite quantum dot solar cells with charge separating heterostructure, Nat. Commun. 10 (2019) 2842. https://doi.org/10.1038/s41467-019-10856-z.

[269] L. Liu, A. Najar, K. Wang, M. Du, S. (Frank) Liu, Perovskite Quantum Dots in Solar Cells, Adv. Sci. 9 (2022). https://doi.org/10.1002/advs.202104577.

[270] W. Li, S. Ding, J. Xu, C. Wu, X. Li, L. Qian, H. Chen, X. Zhang, K. Kang, C. Xiang, Ammonium Thiocyanate Enhanced High-Performance Quasi-

Two-Dimensional Perovskite Solar Cells, ACS Appl. Energy Mater. 7 (2024) 1120–1127. https://doi.org/10.1021/acsaem.3c02624.

[271] Z. Chu, Q. Ye, Y. Zhao, F. Ma, Z. Yin, X. Zhang, J. You, Perovskite Light-Emitting Diodes with External Quantum Efficiency Exceeding 22% via Small-Molecule Passivation, Adv. Mater. 33 (2021) 2007169. https://doi.org/10.1002/adma.202007169.

[272] X. Peng, X. Yang, D. Liu, T. Zhang, Y. Yang, C. Qin, F. Wang, L. Chen, S. Li, Targeted Distribution of Passivator for Polycrystalline Perovskite Light-Emitting Diodes with High Efficiency, ACS Energy Lett. 6 (2021) 4187–4194. https://doi.org/10.1021/acsenergylett.1c01753.

[273] Z. Liu, W. Qiu, X. Peng, G. Sun, X. Liu, D. Liu, Z. Li, F. He, C. Shen, Q. Gu, F. Ma, H. Yip, L. Hou, Z. Qi, S. Su, Perovskite Light-Emitting Diodes with EQE Exceeding 28% through a Synergetic Dual-Additive Strategy for Defect Passivation and Nanostructure Regulation, Adv. Mater. 33 (2021) 2103268. https://doi.org/10.1002/adma.202103268.

[274] A. Sadhu, M. Rai, T. Salim, X. Jin, J.M.R. Tan, S.W. Leow, M.G. Ahmed, S. Magdassi, S.G. Mhaisalkar, L.H. Wong, Dual Role of Cu-Chalcogenide as Hole-Transporting Layer and Interface Passivator for p–i–n Architecture Perovskite Solar Cell, Adv. Funct. Mater. 31 (2021) 2103807. https://doi.org/10.1002/adfm.202103807.

[275] J. Zhu, D.H. Kim, J.D. Kim, D.G. Lee, W. Bin Kim, S. wang Chen, J.Y. Kim, J.M. Lee, H. Lee, G.S. Han, T.K. Ahn, H.S. Jung, All-in-One Lewis Base for

Enhanced Precursor and Device Stability in Highly Efficient Perovskite Solar Cells, ACS Energy Lett. 6 (2021) 3425–3434. https://doi.org/10.1021/acsenergylett.1c01465.

[276] W. Zhang, X. Li, S. Fu, X. Zhao, X. Feng, J. Fang, Lead-lean and MA-free perovskite solar cells with an efficiency over 20%, Joule 5 (2021) 2904–2914. https://doi.org/10.1016/j.joule.2021.09.008.

[277] S. Yu, M. Abdellah, T. Pullerits, K. Zheng, Z. Liang, Asymmetric Spacer in Dion–Jacobson Halide Perovskites Induces Staggered Alignment to Direct Out-of-Plane Carrier Transport and Enhances Ambient Stability Simultaneously, Adv. Funct. Mater. 31 (2021) 2104342. https://doi.org/10.1002/adfm.202104342.

[278] J. Kim, Y.R. Kim, B. Park, S. Hong, I. Hwang, J. Kim, S. Kwon, G. Kim, H. Kim, K. Lee, Simultaneously Passivating Cation and Anion Defects in Metal Halide Perovskite Solar Cells Using a Zwitterionic Amino Acid Additive, Small 17 (2021) 2005608. https://doi.org/10.1002/smll.202005608.

[279] X. Li, M. Ibrahim Dar, C. Yi, J. Luo, M. Tschumi, S.M. Zakeeruddin, M.K. Nazeeruddin, H. Han, M. Grätzel, Improved performance and stability of perovskite solar cells by crystal crosslinking with alkylphosphonic acid ω-ammonium chlorides, Nat. Chem. 7 (2015) 703–711. https://doi.org/10.1038/nchem.2324.

[280] H. Tsai, W. Nie, J.-C. Blancon, C.C. Stoumpos, R. Asadpour, B.

Harutyunyan, A.J. Neukirch, R. Verduzco, J.J. Crochet, S. Tretiak, L. Pedesseau, J. Even, M.A. Alam, G. Gupta, J. Lou, P.M. Ajayan, M.J. Bedzyk, M.G. Kanatzidis, A.D. Mohite, High-efficiency two-dimensional Ruddlesden–Popper perovskite solar cells, Nature 536 (2016) 312–316. https://doi.org/10.1038/nature18306.

[281] J. Zhang, L. Zhang, P. Cai, X. Xue, M. Wang, J. Zhang, G. Tu, Enhancing stability of red perovskite nanocrystals through copper substitution for efficient light-emitting diodes, Nano Energy 62 (2019) 434–441. https://doi.org/10.1016/j.nanoen.2019.05.027.

[282] H. Wang, Y. Dou, P. Shen, L. Kong, H. Yuan, Y. Luo, X. Zhang, X. Yang, Molecule-Induced p-Doping in Perovskite Nanocrystals Enables Efficient Color-Saturated Red Light-Emitting Diodes, Small 16 (2020) 2001062. https://doi.org/10.1002/smll.202001062.

[283] W.J. Mir, A. Alamoudi, J. Yin, K.E. Yorov, P. Maity, R. Naphade, B. Shao, J. Wang, M.N. Lintangpradipto, S. Nematulloev, A.-H. Emwas, A. Genovese, O.F. Mohammed, O.M. Bakr, Lecithin Capping Ligands Enable Ultrastable Perovskite-Phase CsPbI 3 Quantum Dots for Rec. 2020 Bright-Red Light-Emitting Diodes, J. Am. Chem. Soc. 144 (2022) 13302–13310. https://doi.org/10.1021/jacs.2c04637.

[284] Y.-F. Lan, J.-S. Yao, J.-N. Yang, Y.-H. Song, X.-C. Ru, Q. Zhang, L.-Z. Feng, T. Chen, K.-H. Song, H.-B. Yao, Spectrally Stable and Efficient Pure Red CsPbI 3 Quantum Dot Light-Emitting Diodes Enabled by Sequential

Ligand Post-Treatment Strategy, Nano Lett. 21 (2021) 8756–8763. https://doi.org/10.1021/acs.nanolett.1c03011.

[285] F. Yuan, X. Zheng, A. Johnston, Y.-K. Wang, C. Zhou, Y. Dong, B. Chen, H. Chen, J.Z. Fan, G. Sharma, P. Li, Y. Gao, O. Voznyy, H.-T. Kung, Z.-H. Lu, O.M. Bakr, E.H. Sargent, Color-pure red light-emitting diodes based on two-dimensional lead-free perovskites, Sci. Adv. 6 (2020). https://doi.org/10.1126/sciadv.abb0253.

[286] L. Yang, Y. Zhang, J. Ma, P. Chen, Y. Yu, M. Shao, Pure Red Light-Emitting Diodes Based on Quantum Confined Quasi-Two-Dimensional Perovskites with Cospacer Cations, ACS Energy Lett. 6 (2021) 2386–2394. https://doi.org/10.1021/acsenergylett.1c00752.

[287] J. Qing, S. Ramesh, Q. Xu, X. Liu, H. Wang, Z. Yuan, Z. Chen, L. Hou, T.C. Sum, F. Gao, Spacer Cation Alloying in Ruddlesden–Popper Perovskites for Efficient Red Light-Emitting Diodes with Precisely Tunable Wavelengths, Adv. Mater. 33 (2021). https://doi.org/10.1002/adma.202104381.

Appendix

Appendix 1. Supplementary Information for Chapter 4.

Table A1-1 | Performance of recently reported green perovskite LEDs with EQE exceeding 20%.

Perovskites	EQE_{max} (%)	CE_{max} (cd/A)	L_{max} (cd/m²)	Operational lifetime (T_{50}, min, reported)	Operational lifetime (T_{50}, min, equivalent at 100 cd/m², n=-1.65)	Ref.
FPEABr:$CsPbBr_3$, quasi-2D	20.36	64	8.2×10^4	6.5 (L_0=10,000 cd/m²)	12969.2	[209]
BABr: $CsPbBr_3$, quasi-2D	20.5	63	1.3×10^4	25 (L_0=1,000 cd/m²)	1116.7	[214]
PEABr:(Cs, FA)$PbBr_3$, quasi-2D	21.4	80	1.7×10^4	117 (L_0=100 cd/m²)	117	[42]
PEABr:($CsPbBr_3$, quasi-2D	22.49	59.2	0.5×10^4	52 (L_0=144 cd/m²)	94.9	[271]

PEABr:$FAPbBr_3$, quasi-2D	22.9	98	2.0×10^4	390 (L_0=100 cd/m^2)	390	[272]
$FA_{0.9}GA_{0.1}PbBr_3$, nanocrystals	23.4	108	2.4×10^4	132 (L_0=100 cd/m^2)	132	[40]
PEABr:(Cs, MA)$PbBr_3$, quasi-2D	25.6	88	5.2×10^4	115 (L_0=7,200 cd/m^2)	133,443.2	[72]
PEABr:$CsPbBr_3$, Quasi-core/shell nanoparticles	28.1	95.8	4.1×10^4	242.4 (L_0=100 cd/m^2)	242.4	[273]
$((FA_{0.7}MA_{0.1}GA_{0.2})_{0.87}Cs_{0.13}PbBr_3)$ core/shell	28.9	150.1	4.7×10^5	31,200 (L_0=1,000 cd/m^2)	1,393,652.8	[67]
PEABr:$FAPbBr_3$, quasi-2D	**29.5**	**127.4**	**1.48×10^5**	**1,120 (L_0=12,000 cd/m^2)**	**3,019,027.6**	**This work**

Table A1-2 Storage lifetime of PePVs and this work in the ambient.

Remaining efficiency (%)	Storage time (hour)	Ref.
95	336	[274]
90	1000	[275]
81	2352	[276]
81	700	[277]
72	3200	[278]
67.8	1000	[279]
60	2250	[280]
91.7	**336**	**This work**
85.3	**672**	
80.1	**2400**	

Appendix 2. Supplementary Information for Chapter 5.

Table A2-1 | Performance of recently reported green perovskite LEDs with EQE exceeding 20%.

Perovskites	EQE_{max} (%)	CE_{max} (cd/A)	L_{max} (cd/m²)	Operational lifetime (T_{50}, min, reported)	Operational lifetime (T_{50}, hour, equivalent at 100 cd/m², n=-1.72)	Ref.
FPEABr:$CsPbBr_3$, RDP	20.36	64	8.2×10^4	6.5 (L_0=10,000 cd/m²)	298.4	[209]
BABr:$CsPbBr_3$, RDP	20.5	63	1.3×10^4	25 (L_0=1000 cd/m²)	21.9	[232]
PEABr:(Cs, FA)$PbBr_3$, RDP	21.4	80	1.7×10^4	117 (L_0=100 cd/m²)	1.95	[42]
PEABr:($CsPbBr_3$, RDP	22.49	59.2	0.5×10^4	52 (L_0=144 cd/m²)	1.62	[271]

PEABr:$FAPbBr_3$, RDP	22.9	98	2.0×10^4	390 (L_O=100 cd/m^2)	6.5	[272]
$FA_{0.9}GA_{0.1}PbBr_3$, nanocrystals	23.4	108	2.4×10^4	132 (L_O=100 cd/m^2)	2.2	[40]
PEABr:(Cs, MA)$PbBr_3$, RDP	25.6	88	5.2×10^4	115 (L_O=7,200 cd/m^2)	3000.3	[72]
PEABr:$CsPbBr_3$, Quasi-core/shell nanoparticles	28.1	95.8	4.1×10^4	242.4 (L_O=100 cd/m^2)	4.0	[273]
$((FA_{0.7}MA_{0.1}GA_{0.2})_{0.87}Cs_{0.13}PbBr_3)$ core/shell	28.9	150.1	4.7×10^5	31,200 (L_O=1,000 cd/m^2)	27,290.0	[67]
PEABr:$FAPbBr_3$, RDP	**31.3**	**132.1**	**2.8×10^5**	**4615 (L_O=10,000 cd/m^2)**	**211,846.1**	**This work**

Table A2-2 | Performance summary of pure red PeLEDs (625-635nm).

Perovskites	EL Peak (nm)	FWHM (nm)	EQE_{max} (%)	L_{max} (cd m^{-2})	Ref.
Cu^{2+}-$CsPbBrI_2$ QDs	~630	~20	5.1	~2500	[281]
BI-$CsPb(Br/I)_3$ QDs	625	~31	12.9	3382	[282]
$CsPbI_3$ QDs	634	21	7.1	1391	[283]
$CsPbI_3$ QDs	630	42	6.4	1212	[284]
$(PEA)_2SnI_4$ RDP	632	21	4.97	170	[285]
PEA/NMA RDP	635	42	12.41	1452	[286]
PBA/MBZA RDP	632	43	7.0	1927	[287]
Our work	**635**	**41**	**16.1**	**1508**	**This work**

Appendix 3. Supplementary Information for Chapter 6.

Table A3-1 | Performance of recently reported green perovskite LEDs with EQE exceeding 20% without optical outcoupling.

Perovskites	**EQE_{max} (%)**	**CE_{max} (cd/A)**	**L_{max} (cd/m²)**	**Operational lifetime (T_{50}, min, reported)**	**Operational lifetime (T_{50}, hour, equivalent at 100 cd/m², n=-1.75)**	**Ref.**
FPEABr:$CsPbBr_3$, quasi-2D	20.36	64	8.2×10^4	6.5 (L_0=10,000 cd/m²)	342.6	[209]
BABr:$CsPbBr_3$, quasi-2D	20.5	63	1.3×10^4	25 (L_0=1000 cd/m²)	23.4	[232]
PEABr:(Cs, FA)$PbBr_3$, quasi-2D	21.4	80	1.7×10^4	117 (L_0=100 cd/m²)	1.95	[42]
PEABr:($CsPbBr_3$, quasi-2D	22.49	59.2	0.5×10^4	52 (L_0=144 cd/m²)	1.6	[271]

PEABr:$FAPbBr_3$, quasi-2D	22.9	98	2.0×10^4	390 (L_0=100 cd/m^2)	6.5	[272]
$FA_{0.9}GA_{0.1}PbBr_3$, nanocrystals	23.4	108	2.4×10^4	132 (L_0=100 cd/m^2)	2.2	[40]
PEABr:(Cs, MA)$PbBr_3$, quasi-2D	25.6	88	5.2×10^4	115 (L_0=7,200 cd/m^2)	3,410.9	[72]
PEABr:$CsPbBr_3$, Quasi-core/shell nanoparticles	28.1	95.8	4.1×10^4	242.4 (L_0=100 cd/m^2)	4.0	[273]
$((FA_{0.7}MA_{0.1}GA_{0.2})_{0.87}$ $Cs_{0.13}PbBr_3$) core/shell	28.9	150.1	4.7×10^5	31,200 (L_0=1,000 cd/m^2)	29,241	[67]
FPEABr:$FAPbBr_3$, quasi-2D	**27.1**	**115.8**	**8.1×10^4**	**6,190 (L_0=10,000 cd/m^2)**	**326,252**	**This work**

Appendix 4. Other Contributed Works

Other works of Shuo Ding during the Ph. D. program are listed below:

1. Z. Tang, S. Ding, X. Zhang, C. Wu, N.E. Stott, C. Xiang, L. Qian, Quantum Dots for Display Applications, in: Phosphor Handb., CRC Press, Boca Raton, 2021: pp. 191–214. https://doi.org/10.1201/9781003098676-6.
2. Z. Tang, S. Ding, K. Kang, T. Zhang, C. Xiang, L. Qian, Application of inkjet printing in the large area display of organic light-emitting diode, Chinese Sci. Bull. 66 (2021) 2117–2128. https://doi.org/10.1360/TB-2020-1350.
3. S. Ding, W. Gu, X. Zhang, C. Xiang, L. Qian, 23.2: Invited Paper: Progresses in High - Efficiency Air - Stable Solution - processed Perovskite Light Emitting Diodes for Display, SID Symp. Dig. Tech. Pap. 52 (2021) 302 – 302. https://doi.org/10.1002/sdtp.15101.
4. S. Yin, F. So, S. Ding, L. Zhu, Q. Dong, C.H.Y. Ho, Enhanced lead sulfide quantum dots infrared photodetector performance through ligand exchange, in: R. Shinar, I. Kymissis, E.J. List-Kratochvil (Eds.), Org. Hybrid Sensors Bioelectron. XIV, SPIE, 2021: p. 31. https://doi.org/10.1117/12.2603399.
5. S. Yin, C.H.Y. Ho, S. Ding, X. Fu, L. Zhu, J. Gullett, C. Dong, F. So, Enhanced Surface Passivation of Lead Sulfide Quantum Dots for Short-Wavelength Photodetectors, Chem. Mater. 34 (2022) 5433–5442. https://doi.org/10.1021/acs.chemmater.2c00293.

6. C. Wu, S. Ding, L. Zhang, F. Huang, G. Qiu, J. Yang, F. Yu, T. Sun, L. Qian, C. Xiang, Enhancing the Absorbance and Carrier Extraction of Lead Sulfide Quantum Dot Solar Cells by the Bilayer ZnO with a Self - Assembly Optical Structure, Sol. RRL 7 (2023) 2300019. https://doi.org/10.1002/solr.202300019.
7. J. Yang, C. Wu, T. Huang, F. Yu, S. Ding, L. Qian, T. Sun, C. Xiang, Lithium Salt - Doped Organic Conjugated Hole Transport Layer for High - Performance PbS Quantum Dot Solar Cells, Sol. RRL 7 (2023). https://doi.org/10.1002/solr.202300293.
8. J. Chen, Z. Tang, Y. Zhou, S. Ding, L. Li, L. Qian, C. Xiang, Glutamine Induced High - Quality Perovskite Film to Improve the Efficiency of NIR Perovskite Light - Emitting Diodes, Small 19 (2023). https://doi.org/10.1002/smll.202207520.
9. Z. Zeng, Y. Wang, S. Ding, Y. Li, C. Xiang, C. Lee, Y. Cheng, S. Tsang, Imbalanced Surface Charge Induced Phase Segregation in Mixed Halide Perovskites, Adv. Funct. Mater. (2024). https://doi.org/10.1002/adfm.202404255.
10. M. Deng, Y. Li, X. Zhang, C. Wu, S. Ding, T. Zhang, M. Zhou, R. Li, C. Xiang, Mitigating Perovskite Light-Emitting Diode Degradation Mechanisms through Forward Electrical Pulses, ACS Photonics (2024). https://doi.org/10.1021/acsphotonics.4c00220.

11. P. Shen, S. Ding, Z. Tang, L. Qian, T. Zhang, P. Xiao, T. Chen, H. Chen, X. Zhang, Y. Ren, D. Zhao, C. Xiang, High - n Phase Suppression for Efficient and Stable Blue Perovskite Light - Emitting Diodes, Adv. Sci. (2024). https://doi.org/10.1002/advs.202306167.